

8-1-2024

Characterizing GSK3 β Interaction and Kinetics via Isothermal Titration Calorimetry

W A Bhagya De Silva

Follow this and additional works at: <https://digitalscholarship.unlv.edu/thesesdissertations>



Part of the [Analytical Chemistry Commons](#), [Biochemistry Commons](#), and the [Biophysics Commons](#)

Repository Citation

De Silva, W A Bhagya, "Characterizing GSK3 β Interaction and Kinetics via Isothermal Titration Calorimetry" (2024). *UNLV Theses, Dissertations, Professional Papers, and Capstones*. 5108.
<https://digitalscholarship.unlv.edu/thesesdissertations/5108>

This Dissertation is protected by copyright and/or related rights. It has been brought to you by Digital Scholarship@UNLV with permission from the rights-holder(s). You are free to use this Dissertation in any way that is permitted by the copyright and related rights legislation that applies to your use. For other uses you need to obtain permission from the rights-holder(s) directly, unless additional rights are indicated by a Creative Commons license in the record and/or on the work itself.

This Dissertation has been accepted for inclusion in UNLV Theses, Dissertations, Professional Papers, and Capstones by an authorized administrator of Digital Scholarship@UNLV. For more information, please contact digitalscholarship@unlv.edu.

CHARACTERIZING GSK3 β INTERACTIONS AND KINETICS VIA ISOTHERMAL
TITRATION CALORIMETRY

By

W A Bhagya De Silva

Bachelor of Science – Biochemistry & Molecular Biology
University of Colombo
2011

Master of Science – Biochemistry
Kansas State University
2015

A dissertation submitted in partial fulfillment
of the requirements for the

Doctor of Philosophy – Chemistry

Department of Chemistry and Biochemistry
College of Science
The Graduate College

University of Nevada, Las Vegas
August 2024

Dissertation Approval

The Graduate College
The University of Nevada, Las Vegas

May 2, 2024

This dissertation prepared by

W A Bhagya De Silva

entitled

Characterizing GSK3 β Interaction and Kinetics via Isothermal Titration Calorimetry

is approved in partial fulfillment of the requirements for the degree of

Doctor of Philosophy – Chemistry
Department of Chemistry and Biochemistry

Ronald Gary, Ph.D.
Examination Committee Chair

Gary Kleiger, Ph.D.
Examination Committee Member

Paul Forster, Ph.D.
Examination Committee Member

Boo Shan Tseng, Ph.D.
Graduate College Faculty Representative

Alyssa Crittenden, Ph.D.
*Vice Provost for Graduate Education &
Dean of the Graduate College*

Abstract

Glycogen synthase kinase 3 β (GSK3 β) is a multifunctional serine/threonine kinase involved in several key signaling pathways, including glycogen metabolism, WNT/ β -catenin, and Hedgehog signaling. Hyperactivity of GSK3 β has been linked to Alzheimer's disease, bipolar disorder, type II diabetes, and some cancers. Therefore, GSK3 β is of interest as a target for therapeutics. Lithium ion (Li⁺) is a classical inhibitor of GSK3 β . Structurally similar beryllium ion (Be²⁺) is ~1000-fold more potent. Lithium and beryllium have demonstrated pathway-specific and cell type-specific inhibition of GSK3 β , prompting an investigation into the inhibitory mechanisms and thermodynamic characteristics of the metal-enzyme interaction.

Isothermal titration calorimetry (ITC) is a label-free technique that measures the heat absorbed or released during binding interactions. Be²⁺ is hypothesized to inhibit GSK3 β by competing with magnesium ions (Mg²⁺) for binding sites rich in acidic residues like aspartic acid. ITC binding studies utilizing model chelators and peptides featuring carboxylate groups revealed that Be²⁺ has a higher binding affinity than Mg²⁺ for carboxylate-rich binding sites.

ITC can be extended to studying enzyme kinetics by measuring the heat released or absorbed during enzymatic reactions. This allows for real-time observation of reaction kinetics. This study reports the first use of an ITC enzyme assay for the kinetic analysis of a protein kinase. The ITC enzyme assay facilitates continuous monitoring of the enzyme reaction and provides mechanistic insights into the enzymatic process that may remain uncovered in conventional kinase assays. An ITC assay was developed using the single-injection method for the kinetic characterization of human GSK3 β kinase activity. The assay was utilized to study the phosphorylation of a primed GSK3 β substrate, the GSM phosphopeptide. The GSM phosphopeptide contains three tandem phosphorylation sites. Mutated forms of GSM, where

specific phosphorylation sites were altered to alanine, were created to produce mono-site and zero-site GSM substrates. Phosphorylation of the mono-site GSM by GSK3 β was an exothermic reaction and followed Michaelis-Menten kinetics, with a K_M of 59 μ M and k_{cat} of 6.3 s⁻¹. The intrinsic enthalpy of the reaction was -16 kJ/mol. The kinetic analysis for triple-site GSM phosphorylation did not conform to classical Michaelis-Menten kinetics and instead displayed a biphasic behavior.

GSK3 β sequentially phosphorylates substrates with multiple phosphorylation sites in tandem. A comparative analysis of reaction enthalpies and the shapes of the raw ITC thermograms for mono-site and triple-site GSM demonstrated that tandem multi-site phosphorylation by GSK3 β follows a processive mechanism. The processive phosphorylation by GSK3 β displays two modes: fast kinetics for ES complex formation and phosphorylation of the first site and slow kinetics for the phosphorylation of secondary and subsequent sites. This observation shows that once GSK3 β initiates phosphorylation, it remains associated with the substrate to ensure complete modification of all tandem phosphorylation sites, following a mechanism designed to ensure reliability rather than speed. This provides insight into how the need for complete sequential phosphorylation by GSK3 β plays a role in tightly controlled signaling pathways.

Acknowledgments

I want to express my deepest appreciation to all who made it possible for me to complete this dissertation.

I am grateful for the support and encouragement from my doctoral advisor, Dr. Ronald Gary. This project was particularly challenging, and I appreciate his continuous faith in me through the years. His kindness, understanding, and encouragement helped me continue this project and do my best. I sincerely appreciate the training and mentorship I received from him in shaping this dissertation and his wisdom in general, which will guide me in my life and career.

I want to express my sincere thanks to the members of my Advisory Committee: Dr. Gary Kleiger, Dr. Paul Forster, and Dr. Boo Tseng, for their continued support, encouragement, and understanding. Their insightful comments and expertise were beneficial to this study. Special thanks to Dr. Gary Kleiger and Dr. Chutima Rattanasopa for their generous assistance with the preparation of recombinant human GSK3 β and for sharing their experiences, knowledge, and resources, which was immensely helpful for the progress of this study.

I would also like to thank Dr. Rebecca Lim, with whom I spent a significant portion of my doctoral years. She was an excellent lab mate and a wonderful friend for life. I'm deeply grateful and lucky to have her continued support, whether to discuss experiments, share life experiences, or give emotional support. Gaining her friendship and support was a highlight of coming to UNLV.

I want to thank Dr. Dong-Chan Lee, Dr. Kathleen Robins, and Mr. Jung Jae Koh (JJ) for their assistance and teaching opportunities. JJ has been the best organic chemistry lab coordinator and has made teaching organic chemistry labs a great experience. Additionally, I

would like to thank Mrs. Bianca Rideout, Ms. Jazmyne Taitano Simmons, and Ms. Susun Yunkes from the Chemistry Department Office for their administrative assistance and kind support.

Many thanks to all the health professionals and staff of the Student Counseling and Psychological Services (CAPS) of UNLV, including Dr. Joseph Kithas, Dr. Suzie Hong, Dr. Hadley Johnson, and Dr. Kelly Webber, for their gracious support and kindness in helping me through difficult times.

My deepest gratitude extends to my dearest father, the late Mr. Sarath De Silva; mother, Mrs. Kumudini Fernando; brother, Dr. Amila De Silva; and extended family for loving and protecting me and being wonderful role models. Thank you so much for all you have done and sacrificed to help me come this far.

Finally, I am deeply grateful to my loving husband, Mr. Sidath Kapukotuwa, who has been a pillar of positivity and resilience. Although I have not been the happiest person to live with during the past few years, he has been unbelievably gracious with his kindness, understanding, and constant encouragement. He has continuously believed in me and helped me through each day. I would not have made it this far without his encouragement and emotional support, and I am truly grateful.

The U.S. Army Research Laboratory and the U.S. Army Research Office supported this work under grant numbers W911NF-15-1-0043 and W911NF-15-1-0216. The UNLV GPSA (Graduate and Professional Student Association) also provided support through the research sponsorship program.

Table of Contents

Abstract	iii
Acknowledgments	v
Table of Contents	vii
List of Tables	xiv
List of Figures	xvi
List of Schemes	xxiii
Chapter 1: Project Overview	1
Chapter 2: Motivations for Investigating GSK3 β Inhibition by Lithium and Beryllium: A Prelude to Isothermal Titration Calorimetry Studies	5
GSK3 β is a Unique Serine/Threonine Kinase	5
Regulation of GSK3 β	7
Lithium and Beryllium as GSK3 β Inhibitors	10
Isothermal Titration Calorimetry (ITC) for GSK3 β Ligand Binding and Kinetic Study	16
ITC Instrument	18
Aqueous Solubility of Beryllium for ITC Experiments in Biological Buffers	20
Chapter 3: Preferential Interaction of Beryllium Ions with Carboxylate-Rich Peptides	22
Introduction	22
Competitive Binding Dynamics of Magnesium, Lithium, and Beryllium with GSK3 β : Influence on Carboxylate-Rich Binding Sites	23

Experimental Strategy	28
Microscale Thermophoresis (MST).....	34
Materials and Methods	37
Materials	37
Isothermal Titration Calorimetry – Binding Experiments	38
Baseline Correction for Analysis of ITC Raw Plots.....	39
Microscale Thermophoresis – Binding Experiments	39
Results and Discussion.....	40
Beryllium Ions Show Greater Affinity for Carboxylate-Rich Chelators than Magnesium Ions	40
Beryllium Ions Show a Greater Affinity for Carboxylate-Rich Peptides	48
MicroScale Thermophoresis (MST) Results	59
Chapter 4: Expression and Purification of Full-length Human GSK3 β for Isothermal Titration Calorimetry Experiments	68
Introduction	68
Materials and Methods	71
Materials	71
Bacterial Expression in BL21-CodonPlus E. coli	73
Protein Expression in Sf9 Cells via Baculovirus Expression System	74
Protein Expression in Hi5 Cells via Baculovirus Expression System.....	79

Results and Discussion.....	83
GST-GSK3 β Expressed in BL21(Gold)CodonPlus E. coli was Predominantly Degraded ...	83
Utilization of the Sf9-ET Reporter Cell Line for Baculovirus Titer Estimation	87
Amplified Baculovirus Stocks could be Concentrated by 10-fold using PEG (Polyethylene glycol).....	90
Full-length GST-GSK3 β Expression via Baculovirus Expression in Sf9 Cells	92
Analysis of GST-GSK3 β Purification Yields from Sf9 Cell Cultures using FPLC.....	93
Experimental Challenges Associated with GST-GSK3 β Expression, Extraction, and Purification from Sf9 Cells.....	96
Recombinant GSK3 β Production and Purification from Hi5 Cells Allowed Higher Protein Yields.....	101
Chapter 5: Isothermal Titration Calorimetry (ITC) Ligand Binding Experiments for Glycogen Synthase Kinase3 β (GSK3 β)	107
Introduction	107
Materials and Methods	108
Materials	108
ITC Binding Experiments.....	109
Results and Discussion.....	110
ITC Thermograms for ATP vs. GSK3 β	110
ITC Thermograms for AMP-PNP vs. GSK3 β	112
Hypothesis: Protein Adsorption.....	114

ITC Thermograms for AMP-PNP vs. Concentrated GSK3 β Samples	115
Chapter 6: Kinetic Characterization of GSK3 β Phosphorylation using Isothermal Titration	
Calorimetry (ITC)	121
Background and Introduction.....	121
Kinetic Characterization of Enzymes	121
Isothermal Titration Calorimetry (ITC) in Studying Enzyme Kinetics	125
Phosphorylation Reaction of Glycogen Synthase Kinase 3 β (GSK3 β).....	131
Materials and Methods	137
Materials	137
Isothermal Titration Calorimetry – Single Injection Assay	140
Baseline Correction for Analysis of ITC Raw Plots.....	142
Michaelis – Menten Studies for the Phosphorylation of Triple-site GSM Peptide [RG42]	142
Michaelis – Menten Analysis for the Phosphorylation of Mono-site GSM Peptide [RG43]	144
Analysis of Apparent Reaction Enthalpy (ΔH_{app}) for the Phosphorylation of GSM Peptides	144
Determining the Buffer-Independent ΔH_{app} for GSK3 β Phosphorylation of Mono-site GSM Peptide	145
Effect of Inhibitors: BeSO ₄ and LiCl.....	146
Inhibitor Reversibility Study	146
Results and Discussion.....	148

Detection of GSK3 β Phosphorylation Activity via ITC Single-Injection Assay.....	148
Effect of Different Enzyme Concentrations on GSK3 β Phosphorylation Reaction.....	150
ITC Thermogram for the Effect of Different Peptide Concentrations.....	152
Analysis of Triple-site GSM Phosphorylation by GSK3 β Suggests a Deviation from the Michaelis-Menten Model	154
Michaelis – Menten Analysis for the Phosphorylation of Mono-site GSM Peptide	168
Comparative Analysis of ΔH_{app} and ITC Curve Shapes for Mono- and Triple-Site GSM Suggests a Processive Phosphorylation Mechanism by GSK3 β on Multi-Site Substrates .	175
Determining Buffer-Independent Reaction Enthalpy for the Phosphorylation of Mono-site GSM Peptide by GSK3 β	186
Single-injection Analysis for Dose-Dependent Inhibition of GSK3 β Phosphorylation by Inhibitors LiCl and BeSO ₄	195
Reversibility of LiCl and BeSO ₄ Inhibition of GSK3 β Phosphorylation.....	198
Chapter 7: Summary and Future Directions	202
Summary	202
Future Directions.....	206
Enhancing Kinetic Analysis in ITC: Implementing the Empirical Response Model for Rapid Reaction Dynamics.....	206
Exploring the ITC Multiple-Injection Assay for the Kinetic Analysis for Multi-site Phosphorylation.....	207
Using MALDI-TOF MS to Support Processive Kinetics by GSK3 β	208

Appendix I	210
Capillary Electrophoresis Analysis of Phosphorylation in β -catenin and Ser9 Phosphorylation in GSK3 β Following the Treatment of Lithium and Beryllium in A172 Cells.	210
Appendix II	218
ITC Runs for Chapter 3	218
Appendix III.....	223
GST-GSK3 β Extraction and Purification from Sf9 Cells and Experimental Challenges	223
Experiment 1.....	223
Experiment 2.....	225
Experiment 3.....	227
Experiment 4.....	228
Experiment 5.....	230
Experiment 6.....	232
Experiment 7.....	234
Experiment 8.....	236
Appendix IV	238
Part A: ITC Experiments Exploring GSK3 β Ligand Binding.....	238
Part B: ITC Runs for Chapter 5 and Appendix IV	245
Appendix V	249
Part A.....	249

ITC Single-injection Thermograms for GSK3 β Kinase Reaction in the Presence and Absence of Known GSK3 β Inhibitors.....	249
GSK3 β Kinase Reaction in Different Buffers and pH.....	251
Part B.....	253
Analysis 1: An Example of Determining the Maximum Initial Rate of ITC (Rate _{ITC}) for an ITC Single-injection Assay using Excel.....	253
Analysis 2: Example of DP Correction for the Instrument Response Time for GSK3 β Catalyzed Phosphorylation of the Triple-site GSM peptide.....	257
Analysis 3: Example of DP Correction for the Instrument Response Time for GSK3 β Catalyzed Phosphorylation of the Mono-site GSM peptide.....	258
Analysis 4: Michaelis-Menten Analysis for Mono-site GSM Phosphorylation Catalyzed by GSK3 β Using Excel	259
Appendix VI.....	261
ITC Runs for Chapter 6.....	261
References.....	267
Curriculum Vitae.....	295

List of Tables

Table 3.1: Properties of Lithium, Beryllium, Magnesium, and Their Ions	24
Table 3.2: Thermodynamic Parameters and Stoichiometry for Metal-EDTA Binding.....	43
Table 3.3: Thermodynamic Parameters and Stoichiometry for Be^{2+} -4,5-IDA Binding.....	45
Table 3.4: Thermodynamic Parameters and Stoichiometry for Be^{2+} -NTA Binding	46
Table 3.5: Thermodynamic Parameters and Stoichiometry for Be^{2+} -SA Binding	47
Table 3.6: Stoichiometry for BeSO_4 vs. DDDD Binding	57
Table 6.1: The Apparent Reaction Enthalpy from the Single-injection Analysis of Various Concentrations of Triple-site GSM Peptide (RG42).....	153
Table 6.2: Michaelis-Menten Analysis: Phosphorylation of Mono-Site GSM Peptide by GSK3 β Using Excel	173
Table 6.3: Michaelis-Menten Analysis: Phosphorylation of Mono-Site GSM Peptide by GSK3 β Using MicroCal PEAQ-ITC Analysis Software	174
Table 6.4: Average Michaelis-Menten Parameters for Mono-Site GSM Phosphorylation from MicroCal PEAQ-ITC Analysis	174
Table 6.5: The Apparent Reaction Enthalpy from the Single-injection Analysis Comparing Triple-site GSM (RG42) vs. Mono-site GSM peptide (RG43) Phosphorylation by GSK3 β ...	179
Table 6.6: GSK3 β Substrates Featuring Multiple Tandem Phosphorylation Sites	185

Table 6.7: ΔH_{app} Values for Mono-site GSM Phosphorylation by GSK3 β and ΔH_{ion} in Different Buffers at pH 7	189
Table 6.8: The Association Constant for H_2PO_4^- and the Fully Deprotonated ATP and ADP .	194
Table 6.9: Dose-dependent Decrease in ΔH_{app} for GSK3 β Phosphorylation in the Presence of LiCl and BeSO_4	197
Table Appendix III.A: The Effect of Various Treatments on Cell Lysate Viscosity	229
Table Appendix V.A: Determining Rate_{ITC} for ITC Run R3247	255

List of Figures

Figure 2.1: Capillary Electrophoresis Electropherograms Showing Dose-dependent Effect of Lithium on β -catenin Phosphorylation	13
Figure 2.2: Schematic of the ITC Instrument	18
Figure 3.1: Typical ITC Binding Thermogram	30
Figure 3.2: Illustration of MicroScale Thermophoresis (MST) Process.....	36
Figure 3.3: Carboxylate-Rich Chelators	41
Figure 3.4: ITC Binding for Metal-EDTA	42
Figure 3.5: Thermodynamic Profiles for Metal-EDTA Binding.....	43
Figure 3.6: ITC Binding for Metal-4,5-IDA.....	44
Figure 3.7: ITC Binding for Metal-NTA	46
Figure 3.8: ITC Binding for Metal-SA	47
Figure 3.9: ITC Binding for Be^{2+} vs. Mg^{2+} Against DDDD Peptide	49
Figure 3.10: ITC Binding for Be^{2+} vs. Mg^{2+} Against KKKK Peptide	50
Figure 3.11: ITC Binding for Be^{2+} vs. Mg^{2+} Against GGGG Peptide	50
Figure 3.12: ITC Binding for Be^{2+} , Mg^{2+} , and Li^+ vs. DDDD Peptide.....	51
Figure 3.13: Thermodynamic Profile for Be^{2+} vs. DDDD Binding.....	52
Figure 3.14: ITC Binding for Mg^{2+} and Li^+ vs. DDDD Peptide at pH 7	53

Figure 3.15: ITC Binding for Be^{2+} vs. Tetrapeptides with Varying Number of Aspartic Acid (D) Residues	54
Figure 3.16: ITC Binding for Be^{2+} vs. Tetrapeptides with Aspartic Acid (D) or Glutamic Acid (E) Residues	55
Figure 3.17: ITC Binding for Be^{2+} vs. Various DDDD Peptides	56
Figure 3.18: Model of Be^{2+} Coordination with DDDD Peptide	57
Figure 3.19: MST Binding for Be^{2+} vs. Mg^{2+} Against FITC-DDDD	62
Figure 3.20: MST Binding for Be^{2+} vs. Mg^{2+} Against FITC-GGGG	63
Figure 3.21: MST Binding for Be^{2+} vs. Mg^{2+} Against FITC-KKKK	64
Figure 3.22: Increasing Ionic Strength Counteracts BeSO_4 -Induced FITC-KKKK Fluorescence Increase	65
Figure 3.23: MST Binding for Be^{2+} vs. FITC-DDDD and FITC-GGGGDDDD	66
Figure 3.24: MST Binding for Be^{2+} vs Various Tetrapeptides	67
Figure 4.1: GST-GSK3 β Expression in BL21(Gold) vs. Re-transformed BL21(CodonPlus) <i>E. coli</i> Analyzed on SDS-PAGE	86
Figure 4.2: eGFP Expression in Sf9-ET Reporter Cell line Infected with P2 Baculovirus	88
Figure 4.3: Analysis of eGFP Expression in Sf9-ET Cells Infected with Baculovirus at Varying M.O.I.	89
Figure 4.4: Analysis of eGFP Expression in Sf9-ET Cells Infected with P3 Baculovirus	90

Figure 4.5: GST-GSK3 β Expression in Sf9 Cells Infected with P3 Baculovirus Analyzed on SDS-PAGE.....	93
Figure 4.6: GST-GSK3 β Expression in Sf9 Cells Compared Against GST-GSK3 β Expression in BL21 (Gold) <i>E. coli</i> Cells Analyzed on SDS-PAGE	94
Figure 4.7: GST-GSK3 β Extracted and Purified from Sf9 Cells Infected with P3 via Glutathione-Sepharose Column on FPLC.....	95
Figure 4.8: Analysis of YFP Expression in Sf9 Cells to Monitor Baculovirus Amplification and Recombinant Protein Expression in Hi5 Cells.....	102
Figure 4.9: Hi5 Cultures Expressed Significantly Higher Amount GST-GSK3 β than Sf9 Cultures	103
Figure 4.10: GST-GSK3 β Extraction and Purification from Hi5 Cells Infected with P3 via Glutathione-batch Bead Purification.....	104
Figure 4.11: Purification of GSK3 β by TEV-His Cleavage of GST tag, Ion-Exchange Purification, and His-Bind Resin Purification	105
Figure 5.1: ITC Thermograms for AMP-PNP vs. GSK3 β	118
Figure 5.2: ITC Thermograms for AMP-PNP vs. GSK3 β	119
Figure 5.3: ITC Thermograms for AMP-PNP vs. GSK3 β	120
Figure 6.1: ITC Single-injection Analysis Thermogram for GSK3 β Kinase Reaction	149
Figure 6.2: ITC Single-injection Analysis for the Phosphorylation of Triple-site GSM Peptide (RG42) Catalyzed with Various Concentrations of GSK3 β	151

Figure 6.3: ITC Single-injection Analysis of Various Triple-site GSM (RG42) Peptide Concentrations with GSK3 β	153
Figure 6.4: Initial Rate _{ITC} vs. GSM (RG42) Peptide Concentrations Plot.....	155
Figure 6.5. ITC Single-injection Analysis of Various Triple-site GSM (RG42) Peptide Concentrations with GSK3 β	157
Figure 6.6: Michaelis-Menten Analysis for Triple-site GSM (RG42) Peptide with 0.5 μ M GSK3 β	158
Figure 6.7: Example of a Graphical Analysis of Lag and Linear Phases	161
Figure 6.8: The Initial Rate _{ITC} Determination from Linear DP Range	164
Figure 6.9: Comparison of Observed and Calculated Initial Rates for GSK3 β Catalysis of Triple-site GSM Peptide via IrCal: Poor Fit to Michaelis-Menten Model	165
Figure 6.10: Mechanistic Models for Multi-Site Phosphorylation by GSK3 β	167
Figure 6.11: Comparing ITC Thermograms for the Phosphorylation of Triple-site GSM vs. Mono-site GSM Peptide Catalyzed by GSK3 β	169
Figure 6.12: Rate of GSK3 β Activity vs. Increasing Mono-site GSM Peptide Concentrations	169
Figure 6.13: Sample Enzyme Marker Selection for the Single-injection Assay Analysis.....	171
Figure 6.14: Michaelis-Menten Analysis Plots for Single-injection of Various Mono-site GSM Concentrations	172
Figure 6.15: ITC Thermograms for GSK3 β Kinase Reaction with Different GSM Peptides ..	176

Figure 6.16: Comparison of ITC Thermograms for GSK3 β Phosphorylation of GSM Peptides at Varying Concentrations and Phosphorylation Sites.....	178
Figure 6.17: Thermogram Shape Comparison.....	181
Figure 6.18: Comparison of Reaction Rates Demonstrate Biphasic Behavior for Multi-site Phosphorylation by GSK3 β	183
Figure 6.19: ITC thermograms for GSK3 β Kinase Reaction with Mono-site GSM Peptide in Different Buffers at pH 7 and 30 $^{\circ}$ C	187
Figure 6.20: Buffer-independent ΔH for GSK3 β Kinase Reaction with Mono-site GSM peptide	188
Figure 6.21: ITC Thermograms for GSK3 β Phosphorylation with Various LiCl Inhibitor Concentrations	196
Figure 6.22: ITC Thermograms for GSK3 β Phosphorylation with Various BeSO $_4$ Inhibitor Concentrations	197
Figure 6.23: Near Irreversibility of Be $^{2+}$ Inhibition.....	199
Figure 6.24: Single-injection Analysis Testing the Reversibility of GSK3 β Phosphorylation by LiCl and BeSO $_4$	200
Figure 6.25: Enzyme Activity for GSK3 β Phosphorylation Pre- and Post-inhibitor Wash	200
Figure Appendix I.A: Effect of LiCl on P- β -Catenin and Total- β -Catenin Levels.....	212
Figure Appendix I.B: Effect of LiCl on P-Ser9-GSK3 β and Total-GSK3 β Levels.....	213
Figure Appendix I.C: GAPDH Level and Total Protein Panel with LiCl Treatment.....	214

Figure Appendix I.D: Effect of BeSO ₄ on P- β -Catenin and Total- β -Catenin Levels	215
Figure Appendix I.E: Effect of BeSO ₄ on P-Ser9-GSK3 β and Total-GSK3 β Levels.....	216
Figure Appendix I.F: GAPDH Level and Total Protein Panel with BeSO ₄ Treatment.....	217
Figure Appendix III.A: GST-GSK3 β Expression in Sf9 Cells from GenScript compared against GST-GSK3 β expression in BL21 (Gold) <i>E. coli</i> cells	224
Figure Appendix III.B: Extraction and Isolation of GST-GSK3 β from Sf9 via Glutathione- sepharose column on FPLC Lacked the 74kDa Protein Band.....	226
Figure Appendix III.C: Extraction and Isolation of GST-GSK3 β from Sf9 via Glutathione- sepharose Column on FPLC Lacked the 74kDa Protein Band in the GSH-eluted Fractions ...	231
Figure Appendix III.D: Comparing the Glutathione-bound protein profiles in Fresh vs. Old Sf9 Cells Treated With +/- Amplified Baculovirus	233
Figure Appendix III.E: Elution of Glutathione-bound Protein from Sf9 Lysates with Different GSH Concentrations in the Elution Buffer	235
Figure Appendix III.F: SDS-PAGE Analysis of GST-GSK3 β Elution Efficiency with and without 0.1% Triton X-100 in Lysis, Wash, and Elution Buffers	237
Figure Appendix IV.A: ITC Thermograms for ATP vs. GST-GSK3 β Interactions.....	238
Figure Appendix IV.B: ITC Thermograms for ATP vs. GSK3 β Interactions	239
Figure Appendix IV.C: ITC Thermograms for AL vs. GSK3 β Interactions	239
Figure Appendix IV.D: ITC Thermograms for AMP-PNP vs. GSK3 β Interactions.....	240

Figure Appendix IV.E: ITC Thermograms for AMP-PNP vs. GSK3 β Interactions in the Presence of Peptide Substrate	241
Figure Appendix IV.F: Unusual Baseline Shift in ITC Thermograms.....	242
Figure Appendix IV.G: Unusual Baseline Shift in ITC Thermograms for Peptide vs. GSK3 β Interactions.....	243
Figure Appendix IV.H: No Binding Observed Against 10 μ M GSK3 β	244
Figure Appendix V.A: ITC Single-injection Assay Thermograms for GSK3 β Kinase Reaction +/- Inhibitors	250
Figure Appendix V.B: ITC Single-injection Analysis Thermogram for GSK3 β Kinase Reaction in Different Buffers and pH	252
Figure Appendix V.C: The Rate _{ITC} vs. Time for DP Values from the Reaction Course for R3247	256
Figure Appendix V.D: Comparison between the Measured Thermogram and the Tian Equation Corrected Thermogram.....	257
Figure Appendix V.E: Comparison between the Measured Thermogram and the Tian Equation Corrected Thermogram.....	258

List of Schemes

Scheme 3-1.....	31
Scheme 6-1.....	122
Scheme 6-2.....	190
Scheme 6-3.....	190
Scheme 6-4.....	190
Scheme 6-5.....	191
Scheme 6-6.....	192
Scheme 6-7.....	193
Scheme 6-8.....	193

Chapter 1: Project Overview

Protein kinases are enzymes that modify proteins through phosphorylation, which involves transferring a phosphate group from ATP to specific amino acids in a protein, typically serine, threonine, or tyrosine. This phosphorylation process modulates the activity, stability, complex formation, localization, and functions of these substrate proteins, playing a crucial role in cellular signaling and regulatory mechanisms. Protein kinases are central to signaling pathways that govern vital processes such as cell division, growth, apoptosis, and metabolism. Dysregulation in protein kinase activity is linked to a range of diseases, including cancers, diabetes, and neurodegenerative disorders. Therefore, protein kinases have become significant targets for therapeutic interventions (Cohen, 2002; Schwartz & Murray, 2011). Understanding the activity of protein kinases, including their kinetic and dynamic interactions with substrates and inhibitors, is essential for designing effective drugs that selectively modulate pathological signaling pathways, improving treatment specificity and reducing side effects. Recent trends in kinase drug discovery emphasize developing inhibitors with improved selectivity and potency through a detailed understanding of kinase kinetics and kinase-ligand interactions (Attwood et al., 2021; Riegel et al., 2022; Srinivasan, 2023).

Glycogen Synthase Kinase 3 β (GSK3 β) is a serine/threonine kinase involved in numerous cellular processes critical for development, metabolism, and disease pathology. GSK3 β is unusual among protein kinases because it is constitutively active and primarily regulated through inhibition rather than activation. GSK3 β prefers substrates that are primed through phosphorylation by other kinases. This behavior is distinct from many protein kinases that require phosphorylation for activation. GSK3 β plays a central role in multiple signaling pathways, including insulin, Wnt/ β -catenin, and Hedgehog pathways, making it a pivotal

regulator of cellular responses to environmental cues and maintaining cellular homeostasis (Beurel et al., 2015; Frame & Cohen, 2001; Jope & Johnson, 2004). Our research group is interested in studying GSK3 β -ligand/inhibitor binding and kinetics due to its critical role in various diseases, including diabetes, Alzheimer's, bipolar disorder, and cancer (Sayas & Ávila, 2021; Takahashi-Yanaga, 2013).

Lithium and beryllium are of significant interest for inhibiting GSK3 β due to their unique modes of action and implications for treating diseases like Alzheimer's and bipolar disorder. Lithium, a classical mood stabilizer FDA-approved for treating bipolar disorder, has shown potential therapeutic benefits in Alzheimer's disease models (Klein & Melton, 1996; Stambolic & Woodgett, 1994). It acts as a competitive inhibitor of GSK3 β by competing with magnesium ions at a low-affinity site, which does not affect the enzyme's interaction with ATP (Ryves & Harwood, 2001). This action disrupts GSK3 β catalytic function and has been associated with reduced amyloid-beta levels and tau phosphorylation in Alzheimer's disease models, suggesting potential neuroprotective effects (Eldar-Finkelman & Martinez, 2011; Snitow et al., 2021). While structurally similar to lithium, beryllium inhibits GSK3 β through a different mechanism. It competes with magnesium ions and ATP binding (Ryves et al., 2002). This dual inhibition mechanism makes beryllium a potent GSK3 β inhibitor, approximately 1000-fold more effective than lithium in cellular models (Mudireddy et al., 2014). Lithium and beryllium have also demonstrated pathway-specific and cell-type-specific inhibition of GSK3 β (Abdul et al., 2018; Mudireddy et al., 2014). These distinctive inhibitory mechanisms make lithium and beryllium compelling subjects for further research. Comprehending the GSK3 β -inhibitor interactions at a molecular level and understanding the thermodynamics and kinetics involved are important for rational drug design.

Isothermal titration calorimetry (ITC) is invaluable for studying enzyme-inhibitor interactions because it provides thermodynamic and kinetic data. This technique allows the measurement of binding constants, enthalpy changes, and other interaction parameters directly from a binding event without the need for any labeling, offering a clear advantage over other conventional methods. ITC reveals how ligand binding affects a system's free energy, enthalpy, and entropy, allowing researchers to understand the driving forces behind ligand association. ITC can also measure the kinetics of ligand binding and the kinetics of an enzyme reaction with various substrates in the presence or absence of inhibitors and could provide mechanistic insights into the mode of enzyme activity (Harris & Keshwani, 2009; Su & Xu, 2018; Y. Wang et al., 2019). This study aimed to investigate the interaction of GSK3 β with its inhibitors, beryllium, and lithium, using ITC to obtain quantitative data on binding affinity, stoichiometry, enthalpy, and entropy changes. It also aimed to follow a kinetic analysis of the GSK3 β phosphorylation reaction using ITC. Building upon these aims, the dissertation is organized into several chapters, exploring different aspects contributing to the overall theme of the study. Following is an overview of each chapter and its contribution to the study's aims.

Chapter 1: Project Overview

Chapter 2: Motivations for investigating GSK3 β inhibition by lithium and beryllium: A prelude to isothermal titration calorimetry studies. This chapter provides an overview of GSK3 β and its regulation, highlights the action of beryllium and lithium following pathway-specific and cell type-specific inhibition of GSK3 β , and provides an overview of isothermal titration calorimetry.

Chapter 3: Preferential interaction of beryllium ions with carboxylate-rich peptides. This chapter investigates the preference of beryllium for carboxylate-rich groups using ITC. Despite its structural similarities to magnesium and lithium, beryllium's smaller ionic radius and higher

charge density may allow it to interact especially tightly with acidic residues. This chapter explores these interactions through ITC titrations with model chelators and peptides containing carboxylate groups.

Chapter 4: Expression and purification of full-length human GSK3 β for ITC experiments. This chapter details the expression and purification of recombinant human GSK3 β for ITC experiments, utilizing bacterial strains and baculovirus expression systems with Sf9 and Hi5 insect cell lines. It also addresses the challenges in producing the high quantities of GSK3 β required for effective ITC binding studies.

Chapter 5: ITC ligand binding experiments for GSK3 β . This chapter discusses the ITC binding experiments, which attempted to explore GSK3 β -ligand binding using the non-hydrolyzable ATP analog AMP-PNP and associated technical challenges.

Chapter 6: Kinetic characterization of GSK3 β phosphorylation using ITC. This chapter highlights the first-ever kinetic analysis followed for a protein kinase using ITC. The ITC single-injection assay was utilized to explore the kinetic behavior of GSK3 β for the phosphorylation of the GSM peptide with a single phosphorylation site or multiple tandem phosphorylation sites. This study uncovered mechanistic insights into the kinetic behavior of GSK3 β involving the phosphorylation of multiple tandem sites that had not been discovered through conventional kinase assays. In addition to kinetic analysis, the chapter reports additional analysis, including the determination of intrinsic reaction enthalpy of GSK3 β -catalyzed phosphorylation of GSM and GSK3 β activity in the presence of inhibitors lithium and beryllium.

Chapter 7: Research summary and future directions

Chapter 2: Motivations for Investigating GSK3 β Inhibition by Lithium and Beryllium: A Prelude to Isothermal Titration Calorimetry Studies

GSK3 β is a Unique Serine/Threonine Kinase

Glycogen synthase kinase 3 (GSK3) is a serine/threonine kinase first discovered as one of the protein kinases that regulate the rate-limiting step of glycogen synthesis by phosphorylating glycogen synthase (Embi et al., 1980). Further research involving peptide sequencing of the enzyme from skeletal muscle and screening a rat brain cDNA library revealed that in mammals, GSK3 exists as two isoforms encoded by two independent genes, GSK3 α and GSK3 β , which have molecular weights of 51 and 47 kDa, respectively (Embi et al., 1980; Woodgett, 1990). Analysis shows that GSK3 is highly conserved in all eukaryotes, and the two GSK3 isoforms show 85% overall identity in their sequences, with 93% identity within the catalytic domains (Ali et al., 2001; Woodgett, 1990). The primary difference between the two isoforms is due to the glycine-rich stretch at the N-terminus of GSK3 α (Woodgett, 1990). In mammals, GSK3 expression is widely distributed across various tissues, with the most significant concentrations observed in the brain (Frame & Cohen, 2001; Kaidanovich-Beilin & Woodgett, 2011). Experimental deletion of the GSK3 β gene in mice results in embryonic death due to liver apoptosis or heart development issues. Deleting the GSK3 α gene leads to viable, fertile mice with body masses similar to their regular counterparts (Hoeftlich et al., 2000). These outcomes indicate differing roles for the two isoforms. Nonetheless, there is evidence of considerable overlap in their functions, particularly within the canonical Wnt signaling pathway, suggesting they may share similar functions across multiple signaling pathways (Asuni et al., 2006; Doble et al., 2007).

Although first discovered as a kinase regulating glycogen synthase, subsequent studies have revealed that GSK3 orchestrates many cellular processes critical for development, metabolism, and disease pathology. GSK3 operates at the nexus of multiple signaling pathways, including insulin, Wnt/ β -catenin, and Hedgehog pathways, thereby regulating cellular responses to environmental cues and maintaining cellular homeostasis (Frame & Cohen, 2001; Jope & Johnson, 2004).

GSK3 is unique because it is constitutively active in cells and is primarily regulated by inhibiting its activity. It prefers substrates pre-phosphorylated by another kinase, known as primed substrates. Similar to other protein kinases, GSK3 features a conserved catalytic domain organized into a dual-lobed structure, where the smaller N-terminal lobe facilitates ATP binding and the larger, spherical C-terminal lobe encompasses the "activation loop" that is crucial for kinase activity (Hanks & Hunter, 1995). The study of GSK3 β crystal structure demonstrated that GSK3 β typically resides in an active conformation without needing activation via phosphorylation, unlike most protein kinases. The priming phosphate binding site on GSK3 β includes a positively charged area formed by the basic side chains of Arg96, Arg180, and Lys205, which can interact with the negatively charged phosphate group. (Dajani et al., 2001; Frame & Cohen, 2001). The binding of a primed substrate to the substrate binding site stabilizes the catalytic site of GSK3 β , facilitating the phosphorylation reaction to proceed, which explains why GSK3 prefers pre-phosphorylated substrates (Beurel et al., 2015; Dajani et al., 2001).

Various stimuli trigger different kinases to perform primed phosphorylation on GSK3 substrates. GSK3 phosphorylates many substrates, including metabolic enzymes, signaling proteins, structural proteins, and transcription factors. Some of the well-characterized substrates of GSK3, in addition to glycogen synthase, include β -catenin, tau protein, Cyclin D1,

transcription factors such as c-Myc, c-Jun, CREB, NF- κ B, eIF2B and apoptotic proteins in BCL-2 family (Ali et al., 2001; Beurel et al., 2015; Doble & Woodgett, 2003; Frame & Cohen, 2001; Jope & Johnson, 2004; Kaidanovich-Beilin & Woodgett, 2011; Pap & Cooper, 1998; Sutherland, 2011; Takahashi-Yanaga, 2013).

Regulation of GSK3 β

GSK3 is distinguished by its unique regulatory mechanisms and substrate specificity, ensuring its precise role in cellular signaling and function. GSK3 activity is modulated by tyrosine (Tyr216 for GSK3 β and Tyr279 for GSK3 α) phosphorylation for maximal kinase activity (Dajani et al., 2003; Hughes et al., 1993).

GSK3 is inhibited following stimulation of growth factor receptors, as demonstrated in the insulin signaling pathway (Cross et al., 1995, 1997; Sutherland et al., 1993) and the Wnt signaling pathway (Metcalf & Bienz, 2011; Stambolic et al., 1996). In the insulin signaling pathway, GSK3 inhibition is achieved through phosphorylation at a conserved N-terminal serine, Ser21 for GSK3 α , and Ser9 for GSK3 β by Protein Kinase B (PKB/Akt) (Cross et al., 1995; Shaw et al., 1997; Sutherland et al., 1993). The phosphorylation of the N-terminal serine inhibits its activity by creating a pseudo substrate that competes for binding, thereby controlling the phosphorylation of actual substrates (Dajani et al., 2001). The GSK3-dependent PP1/I-2 complex is also involved in regulating the N-terminal inhibitory phosphorylation. GSK3 β can activate PP1 by phosphorylating I-2, an inhibitory subunit of PP1. This activation leads to the dephosphorylation of Ser9 on GSK3 β , thereby reversing the inhibitory effect and modulating its activity (Zhang et al., 2003).

Unlike insulin, Wnt/ β -catenin signaling does not influence the phosphorylation of the inhibitory serine. (Ding et al., 2000; Ng et al., 2009). Without Wnt ligands, β -catenin is confined in a formation called the " β -catenin destruction complex," alongside the scaffolding protein Axin, Adenomatous Polyposis (APC), casein kinase I, and GSK3 β . This setup enables GSK3 to phosphorylate β -catenin consecutively at Thr41, Ser37, and Ser33. (Behrens et al., 1998; McCubrey et al., 2014; Stamos et al., 2014) and target β -catenin for ubiquitination and proteasomal degradation. In response to Wnt ligands, the phosphorylation of β -catenin by GSK3 is prevented by destabilizing the β -destruction complex. Studies have shown that this destabilization can be achieved via interrupting GSK3 interaction with Axin through LRP5/6 phosphorylation, which can sequester GSK3 and Axin (Bilic et al., 2007; Stamos et al., 2014), or by promoting GSK3 complexation with phosphorylated FRAT1 (Li et al., 1999; Thomas et al., 1999).

While both the insulin and Wnt/ β -catenin signaling pathways result in reduced GSK3 activity, their downstream effects differ. Insulin activates glycogen synthase, whereas Wnt elevates the cytosolic β -catenin level. The phosphorylation of Ser9 in GSK3 β and the activity of PKB/Akt are controlled by insulin but not by Wnt, suggesting that these pathways modulate GSK3 via separate mechanisms, thus leading to distinct downstream outcomes. (Ding et al., 2000; Ng et al., 2009). This suggests that different groups of GSK3 could be present within cells: one linked with Axin that is unaffected by PKB/Akt phosphorylation and another group that is regulated by PKB/Akt. (McCubrey et al., 2014).

Furthermore, the subcellular localization of GSK3 and its association with protein complexes also modulate GSK3 activity in cells. GSK3 is primarily considered a cytosolic protein. However, GSK3 is also found in the mitochondria, nucleus, and other subcellular

structures, where localized signaling activities can regulate the GSK3 activation state. This distribution allows GSK3 to influence a wide range of cellular processes, including oxidative stress responses, gene expression, receptor signaling, and ion channel regulation (Beurel et al., 2015; Meares & Jope, 2007; Taelman et al., 2010; Wood-Kaczmar et al., 2009).

Axin is a scaffold protein and a component of the β -catenin destruction complex. However, Axin has been shown to facilitate selective GSK3 phosphorylation of substrates such as Smad3, TSC1/TSC2, and Tip60 (Beurel et al., 2015), thereby regulating GSK3 substrate specificity. While Axin facilitates the GSK3 β reaction against select substrates, GSK3 β can phosphorylate Axin to stabilize their complex, thereby showing mutual regulation. The Axin scaffold helps with GSK3 β substrate specificity by protecting GSK3 β from phosphorylation at Ser9 by upstream kinases. This prevents the accumulation of pS9-GSK3 β in the Axin-GSK3 β complex, allowing GSK3 β to specifically target Wnt-associated substrates without affecting other GSK3 β -dependent pathways (Gavagan et al., 2020, 2023). These sophisticated regulatory mechanisms ensure that GSK3 selectively phosphorylates its targets, maintaining tight control over various signaling pathways and underpinning its essential role in cellular physiology and disease (Beurel et al., 2015).

Dysregulation of GSK3 activity has been implicated in metabolic disorders (diabetes, atherosclerosis), psychiatric and neurological disorders (Alzheimer's disease, Parkinson's disease, bipolar disorder, schizophrenia, major depressive disorder), inflammatory diseases, cancer, and others (Gao et al., 2011; Juhaszova et al., 2009; Maqbool et al., 2016; Sayas & Ávila, 2021; Shimura, 2011; Takahashi-Yanaga, 2013; Valvezan & Klein, 2012). GSK3 is a crucial kinase contributing to abnormal phosphorylation of the microtubule-binding protein tau, leading to neurofibrillary tangles, a characteristic pathology in Alzheimer's disease (Hanger et al., 1992;

Mandelkow et al., 1992; Rankin et al., 2007). GSK3 β has been shown to enhance the activity of β -secretase (BACE1) and mediate the toxicity of amyloid-beta (A β) aggregates, a hallmark pathology of Alzheimer's disease (Ly et al., 2013). Therefore, the therapeutic importance of GSK3 has been recognized, and GSK3 has emerged as a potential therapeutic target for developing drugs to treat these diseases (Beurel et al., 2015; Takahashi-Yanaga, 2013). Given the complex regulation of GSK3 and its interaction with various signaling pathways, developing inhibitors that can selectively target GSK3 within specific signaling contexts is crucial. Such targeted inhibition would allow for precise modulation of GSK3 activity, potentially minimizing side effects and enhancing therapeutic efficacy in treating diseases linked to its dysregulation.

Lithium and Beryllium as GSK3 β Inhibitors

Several small-molecule inhibitors of GSK3 have been developed, including lithium, the classical mood stabilizer used in the treatment of bipolar disorder. The FDA approved lithium for the treatment of mood disorders in 1970 in the United States, and several studies demonstrated that lithium targeted GSK3 activity (Klein & Melton, 1996; Stambolic et al., 1996). Lithium treatment has exhibited potential benefits in animal models of Alzheimer's disease, highlighting its therapeutic promise. Research indicates chronic dietary lithium intake can ameliorate spatial memory deficits, as observed in tasks like the Morris water maze. Furthermore, lithium has been effective in lowering amyloid-beta levels and mitigating tau phosphorylation, both critical indicators of Alzheimer's pathology. The treatment also promotes neurogenesis and diminishes inflammation within the brain, contributing to enhanced cognitive functions (Eldar-Finkelman & Martinez, 2011; Snitow et al., 2021). Collectively, these findings suggest that lithium could play a

significant role in improving cognitive decline and addressing the pathological hallmarks of Alzheimer's disease in animal models (King et al., 2014).

Despite lithium therapy being effective in managing bipolar disorder and showing potential as a therapeutic for Alzheimer's disease, it is also associated with significant side effects and toxicity since treatment often requires high doses in the millimolar range to maintain therapeutic efficacy. Common adverse effects of lithium therapy include gastrointestinal issues such as nausea, vomiting, and diarrhea, as well as neurological symptoms like tremors and seizures. Lithium toxicity poses risks of renal damage, hypothyroidism, and potentially fatal cardiovascular issues. Therefore, lithium treatment should be carefully monitored and managed (Gitlin, 2016; Oruch et al., 2014)

Lithium has been shown to interact with and inhibit GSK3 directly (Klein & Melton, 1996; Stambolic et al., 1996). Additionally, the administration of lithium indirectly increases the inhibitory serine-phosphorylation of GSK3 (De Sarno et al., 2002; Jope, 2003; Zhang et al., 2003). Lithium acts as a competitive inhibitor of GSK3 by competing with magnesium (Mg^{2+}) ions without affecting the enzyme's interaction with ATP or its substrate. This inhibition mechanism, which disrupts GSK3's catalytic function by binding to a low-affinity Mg^{2+} site, is consistent across mammalian and Dictyostelium GSK3 isoforms (Ginger et al., 2000). Beryllium was also discovered as a potent inhibitor of GSK3 and shown to inhibit through a different mechanism, as it competes with both Mg^{2+} and ATP by binding to the magnesium and Mg: ATP binding sites on GSK3. This dual inhibition contrasts with lithium, which does not interfere with ATP binding. The interaction between beryllium and ADP highlights the competition at the ATP binding site, underscoring the distinct inhibitory mechanisms of lithium and beryllium on GSK3,

with lithium targeting magnesium ions and beryllium affecting both magnesium ions and ATP (Ryves et al., 2002).

Studies followed by our research group explored beryllium as a potential GSK3 inhibitor in more physiologically relevant conditions and cultured cells. Beryllium was a more potent inhibitor of GSK3 β in human cells than lithium, showing approximately 1000-fold greater efficacy. Like lithium, beryllium directly inhibited GSK3 β activity; however, unlike lithium, it does not promote phosphorylation of GSK3 β at Ser9 in A172 and HFL cells, indicating different feedback inhibition mechanisms. Beryllium's inhibition of GSK3 β exhibited less cytotoxicity than lithium, suggesting superior therapeutic potential. The study highlighted beryllium as a robust GSK3 inhibitor in cellular research, potentially affecting GSK3 β regulatory mechanisms differently from lithium, as evidenced by its distinct impact on Ser9 phosphorylation and GSK3 β activity modulation (Mudireddy et al., 2014).

Another study by our research group found that lithium treatment unexpectedly caused an increase in phosphorylation at Ser33/Ser37 of β -catenin in the A172 glioblastoma cell line, which contradicts the conventional view that GSK3 inhibition should decrease phospho- β -catenin levels due to its role in the canonical Wnt signaling pathway. Beryllium treatment did not elicit an increase in Ser33/Ser37 phosphorylation in A172 cells (Abdul et al., 2018). The phosphorylation of β -catenin at Ser33/Ser37 in A172 glioblastoma cells in response to lithium and beryllium treatment was quantitatively analyzed via a capillary electrophoresis method¹. This method offered improved quantitation and reproducibility over traditional Western blotting. Capillary electrophoresis analysis of the phosphorylation of β -catenin at Ser33/Ser37 in A172 glioblastoma cells showed a dose-dependent increase in phosphorylation in response to lithium treatment (**Figure 2.1**). The electropherograms for the capillary electrophoresis analysis of phosphorylation

in β -catenin and Ser9 phosphorylation in GSK3 β following the treatment of A172 cells with lithium and beryllium are shown in **Appendix I**.

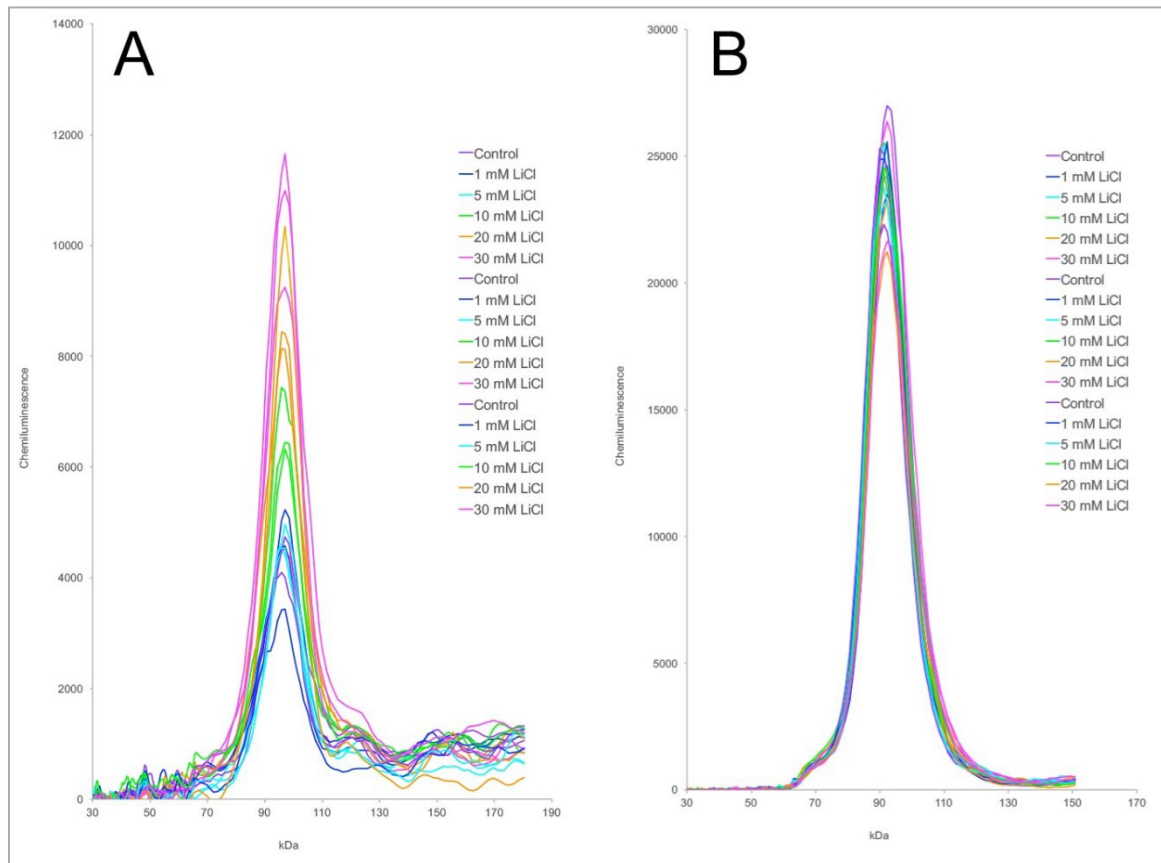


Figure 2.1: Capillary Electrophoresis Electropherograms Showing Dose-dependent Effect of Lithium on β -catenin Phosphorylation. A172 cells treated with 0mM (purple), 1mM (blue), 5mM (cyan), 10mM (green), 20mM (orange), or 30mM (pink) LiCl for 24h (n=3/group) resolved via capillary electrophoresis and stained with antibodies for (A) phospho-Ser33/Ser37- β -catenin or (B) total β -catenin.

¹Capillary electrophoresis data adapted from a published work.

Abdul A.U.R.M., De Silva B., Gary R.K. (2018). The GSK3 kinase inhibitor lithium produces unexpected hyperphosphorylation of β -catenin, a GSK3 substrate, in human glioblastoma cells. Biol Open. 7(1):bio030874. doi: 10.1242/bio.030874.

This study also revealed that lithium's effect on β -catenin phosphorylation varies across different cell types: U251 and U87MG glioblastoma cells showed a significant increase in β -catenin phosphorylation, similar to A172 cells, indicating a common response among glioma cell types. Conversely, RKO human colon carcinoma cells experienced increased total and phosphorylated β -catenin, aligning more with the expected outcomes of GSK3 inhibition through canonical Wnt signaling. The response in HT-1080 human fibrosarcoma cells was intermediate, illustrating variability in lithium's impact across cell types. This underscores how cellular context significantly influences β -catenin phosphorylation following GSK3 inhibition by lithium, highlighting the complexity of using a single model to predict drug effects. In summary, the study suggests that the mechanisms of GSK3 inhibition and subsequent effects on β -catenin phosphorylation by lithium and beryllium could differ significantly, highlighting the complexity of these signaling interactions and the potential for cell-type-specific responses (Abdul et al., 2018).

Understanding the interactions between GSK3 and its inhibitors, such as lithium and beryllium, is important since lithium is commonly used to treat bipolar disorder and may eventually be used for Alzheimer's disease therapeutics because of its potential benefits. Beryllium, being 1000-fold more potent than lithium and displaying cell-type-specific responses, could help uncover novel therapeutic approaches. Knowledge of the binding sites and mechanisms of action of lithium and beryllium on GSK3 can guide the design of new drugs that target GSK3 more efficiently or selectively and help understand drug-induced side effects. This could lead to the development of drugs with improved efficacy and reduced toxicity.

It should be noted that the study of beryllium-GSK3 interactions is not aimed at developing beryllium itself as a therapeutic but at using beryllium's unique inhibition of GSK3 as

a method to investigate a potent and potentially selective mechanism of inhibiting GSK3 activity. Beryllium is toxic when inhaled and responsible for chronic beryllium disease (CBD), an inflammatory lung condition primarily observed in industrial workers carrying the major histocompatibility complex class II (MHC class II) allele HLA-DP2 (Clayton et al., 2014).

HLA (Human leukocyte antigen) genes play a critical role in the immune system by presenting small peptides derived from pathogens, such as viruses and bacteria, to helper T cells (CD⁺ cells). This presentation helps the immune system recognize and respond to foreign molecules. MHC class II molecules, including HLA-DP, are primarily expressed on the surface of antigen-presenting cells like dendritic cells, macrophages, and B cells. Individuals with the HLA-DP2 allele are at an increased risk of developing CBD. Instead of presenting pathogenic peptides in CBD, HLA-DP2 binds beryllium ions via acidic amino acid residues. When beryllium is inhaled and enters the lungs, it can bind to the peptide-binding groove of HLA-DP2, which features a glutamic acid residue at position 69 of its β -chain. It is hypothesized that beryllium ions form a tight complex with this key acidic residue along with other coordination partners, leading to conformational changes in HLA-DP2 that are seen as foreign by CD4⁺ cells, leading to an inappropriate immune response characterized by inflammation and tissue damage in the lungs. Thus, the Be²⁺/peptide complex triggers the CBD disease response rather than the ion or peptide alone. This response is not typical for other MHC class II molecules, which highlights the specificity of HLA-DP2 in its interaction with beryllium and the subsequent immune response that leads to CBD (Buchner, 2020; Clayton et al., 2014). An analysis of genetic markers associated with CBD disease risk found that the prevalence of glutamic acid at position 69 was 30% in the general population but 97% in CBD patients (Richeldi et al., 1993). Obviously, the presence of glutamic acid alone is insufficient to direct high-affinity interaction

with Be^{2+} because this common amino acid is a constituent of virtually every peptide and protein within the body. Rather, these studies demonstrate that acidic residues, such as aspartic acid and glutamic acid, when part of a larger peptide structure that possesses the proper coordination partners arranged with the proper geometry in 3D space, can exhibit stable, highly selective, high-affinity associations with the Be^{2+} ion.

Isothermal Titration Calorimetry (ITC) for GSK3 β Ligand Binding and Kinetic Study

ITC is a highly effective technique for studying interactions between proteins and small molecules or metal ions. It provides precise, quantitative data on binding affinity, stoichiometry, enthalpy, and entropy changes, offering comprehensive insights into the molecular mechanisms driving these interactions. ITC directly measures the heat released or absorbed during a binding event, allowing for the direct calculation of the binding constant (K_d), which quantifies the affinity between the inhibitor and GSK3. The stoichiometry (n) of the interaction, or the ratio of lithium or beryllium ions needed to bind one molecule of GSK3, can be precisely determined from ITC data.

This information is essential for understanding the molecular basis of the inhibition mechanism and whether multiple ions are required to achieve inhibition. ITC uniquely provides direct enthalpy (ΔH) measurements, a valuable parameter for correlating structure and thermodynamics in developing new drug-like compounds. Additionally, ITC provides a complete thermodynamic profile of the interaction, including entropy (ΔS) changes and the Gibbs free energy change (ΔG) calculation. This profile helps distinguish between different binding modes, such as whether the interaction is driven more by enthalpic or entropic changes. It provides insights into the forces driving the interaction, such as hydrogen bonding, ionic interactions, or

hydrophobic effects. ITC experiments can be conducted under various pH, temperature, and ionic strength conditions (Draczkowski et al., 2016; Su & Xu, 2018; Y. Wang et al., 2020), offering insights into how environmental factors affect the interaction between lithium/beryllium and GSK3. This is important for understanding how physiological conditions influence the efficacy of lithium or beryllium as inhibitors. Since ITC does not require any modification or labeling of the protein or the ions, ensuring that the interaction is studied under near-native conditions without any potential interference from labels or tags helps maintain the integrity of the studied biological interaction.

Additionally, ITC methods have been expanded to assay enzyme activity (Frasca, 2016; Hagedoorn, 2022; Todd & Gomez, 2001). ITC measurements capture the heat generated in enzymatic reactions in real time, offering a unique ability to uncover mechanisms or modes of enzymatic reactions that may not be observable through conventional enzymatic assays. Developing an ITC-based kinase assay to study the phosphorylation reaction of GSK3 against various substrates in the absence or presence of lithium/beryllium or other GSK3 inhibitors will provide insight into how the kinase reaction is affected.

In summary, ITC offers a comprehensive and detailed examination of the thermodynamic and kinetic interactions between lithium/beryllium and GSK3, providing invaluable insights for elucidating the molecular mechanisms of inhibition and guiding the development of therapeutic agents targeting GSK3.

ITC Instrument

ITC measures the heat released or absorbed during a biomolecular interaction or enzymatic reaction. This technique operates on the fundamental principles of thermodynamics, where the interaction between two molecules—whether a macromolecule and a ligand, a protein and a small molecule, or chemical conversions during enzymatic reactions—results in a thermal change. These changes are due to heat generated or absorbed from the binding events and chemical reactions, including enzymatic processes, thereby reflecting the overall energetics of these interactions. This thermal change indicates whether the interaction or reaction is exothermic (heat releasing) or endothermic (heat absorbing).

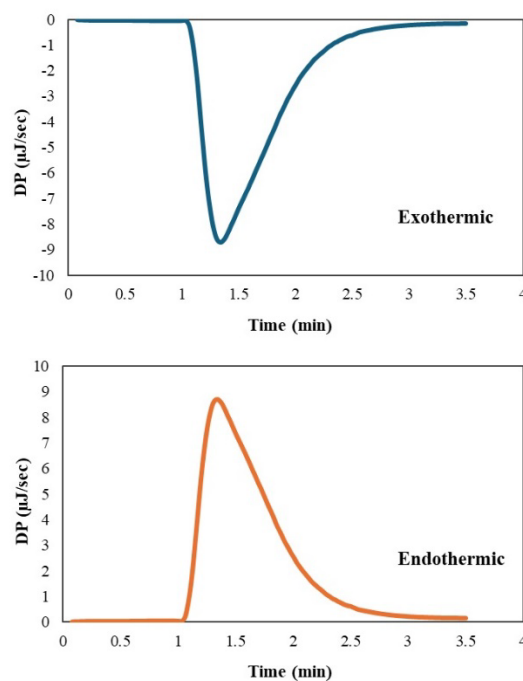
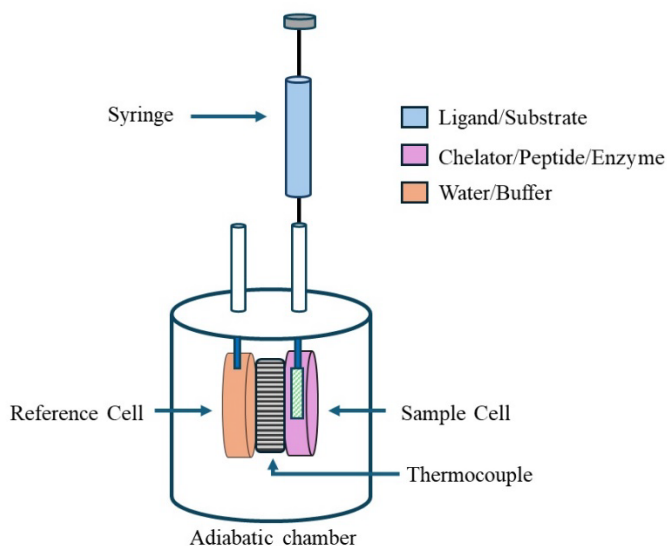


Figure 2.2: Schematic of the ITC Instrument. Examples of ITC thermograms for an exothermic reaction (blue curve) and an endothermic reaction (orange curve) are shown.

Figure 2.2 shows a schematic of the ITC instrument setup. The ITC apparatus consists of a sample cell, where the macromolecule/enzyme is generally placed, and a reference cell, typically filled with water or buffer, to maintain control conditions. Both cells are maintained at constant temperature and pressure. During an ITC experiment, a ligand (for binding experiments) or a substrate (for enzymatic reactions) is gradually injected into the sample cell via a syringe. The injection syringe has a rotation assembly at the end, continuously stirring the solutions in the sample cell to efficiently mix molecules. The thermocouple can detect temperature differences between the reference and sample cells.

The interaction between the ligand and the macromolecule or chemical conversions by enzymatic reactions in the sample cell either absorbs or releases heat, altering the temperature inside the sample cell. However, the instrument is designed to keep the temperature of the sample cell consistent with that of the reference cell by adjusting the power supplied to a heater in the sample cell. The entire system, enclosed in an adiabatic chamber, ensures minimal heat exchange with the environment.

The differential power (DP) required to maintain equal temperature in both cells directly measures the heat in the biomolecular interactions or reactions. This setup helps determine the binding affinity and thermodynamic properties of molecular interactions and understand the kinetic aspects of the binding process or determine the kinetics for an enzyme-catalyzed reaction. An exothermic reaction will decrease the DP output, and an endothermic reaction will increase the DP output. Once the binding interaction reaches equilibrium, the DP will return to the baseline. Otherwise, for an enzymatic reaction, the DP will return to the baseline once all the substrate is consumed or the reaction has reached equilibrium. Chapter 3 will describe how

binding parameters are interpreted through the DP output, and Chapter 6 will describe how kinetic parameters are derived from the DP output.

Aqueous Solubility of Beryllium for ITC Experiments in Biological Buffers

Studies in the biochemical mechanism of action using ITC require preparing beryllium salt solutions in aqueous buffers to evaluate metal-protein interactions under physiological pH. However, the relatively low aqueous solubility of Be^{2+} near physiological pH introduces specific technical challenges that are generally not encountered with most other biologically relevant metal ions. A fluorescence-based HBQS (10-hydroxybenzo[h]quinoline-7-sulfonate) assay (Matsumiya et al., 2001) was used to quantify soluble beryllium in various buffers and pH. Although this assay was introduced as a sensitive assay to quantify beryllium, we found the assay was also sensitive to slight pH changes². Multiple approaches to improving the aqueous solubility of beryllium near physiological pH were attempted, such as adding salts or incorporating ligands that weakly associate with beryllium (Data not shown). These approaches led to a marginal increase in beryllium solubility near physiological pH. However, they also led to a decreased affinity between beryllium and other chelators or peptides when beryllium was titrated against them in ITC. Lim showed that including SO_4^{2-} as a counter ion during solution preparation or adding BSA improved beryllium solubility (R. Lim, 2022).

² The pH sensitivity of HBQS assay for beryllium quantification included in published work. Lim, R. C., De Silva, B., Park, J. H., Hodge, V. F., & Gary, R. K. (2020). Aqueous solubility of beryllium(II) at physiological pH: effects of buffer composition and counterions. *Preparative Biochemistry & Biotechnology*, 50(6), 585–591. <https://doi.org.ezproxy.library.unlv.edu/10.1080/10826068.2020.1719514>

However, these approaches could not be effectively used for ITC experiments involving beryllium in this dissertation due to the presence of the counter-ion resulting in decreased affinity between beryllium and chelators or peptides in ITC binding experiments or technical issues associated with using BSA, such as increased viscosity and frothing (Data not shown).

Therefore, the ITC binding experiments in this dissertation involving beryllium were followed at pH 5.8-6.0 (for 1-5mM concentrations). In cell culture studies, beryllium salt at concentrations ranging from 10 to 100 μ M inhibited GSK3 β kinase activity in A172 cells while showing a minimal impact on cell viability (Mudireddy et al., 2014). A FRET-based in vitro assay also determined that the IC₅₀ for GSK3 β inhibition by BeSO₄ is 5 μ M (Mudireddy et al., 2014). Therefore, beryllium inhibition studies in ITC kinase assays were followed at pH 6.5 (for 1-100 μ M concentrations).

Chapter 3: Preferential Interaction of Beryllium Ions with Carboxylate-Rich Peptides

Introduction

Beryllium and lithium are potent Glycogen synthase kinase 3 β (GSK3 β) metal ion inhibitors that have demonstrated cell type-specific and pathway-specific inhibition in particular signaling pathways in cells (Abdul et al., 2018; Mudireddy et al., 2014). Magnesium is an important cofactor essential for GSK3 β activity. Lithium has been shown to compete for a magnesium ion binding site on GSK3 β , while beryllium has been shown to compete with both magnesium and ATP binding sites (Ryves et al., 2002). Beryllium, lithium, and magnesium are all positively charged ions. Therefore, it is reasonable to hypothesize that beryllium and lithium binding sites on GSK3 β carry acidic groups facilitating the binding. Acidic amino acids have a side chain containing a carboxyl group, which can release a hydrogen ion (H^+) in solution and present a negatively charged binding site for positively charged groups. Aspartic acid (Asp, D) and Glutamic acid (Glu, E) are the acidic amino acid residues in proteins, and each has a carboxyl group on the side chain. This chapter follows a comparative analysis of the preferences of beryllium, lithium, and magnesium ions towards carboxylate-rich groups. The metal ions are prepared in buffered solutions and titrated against model chelators with carboxylate groups and model peptides using isothermal titration calorimetry (ITC).

Competitive Binding Dynamics of Magnesium, Lithium, and Beryllium with GSK3β: Influence on Carboxylate-Rich Binding Sites

Beryllium ions (Be^{2+}) in aqueous solutions exhibit interesting coordination chemistry due to their unique properties. Be^{2+} has a significantly small ionic radius (**Table 3.1**), resulting in a high charge density. This high charge density influences its behavior in solutions and how it coordinates with ligands. Be^{2+} typically forms tetrahedral coordination complexes with water and other ligands. The most common coordination number for Be^{2+} in aqueous solutions is four. Be^{2+} can form very stable complexes with water due to the ion's high charge density, leading to strong electrostatic attraction with the oxygen atoms of H_2O . Be^{2+} is surrounded by 4 water molecules forming $[\text{Be}(\text{H}_2\text{O})_4]^{2+}$ complex in water. Under acidic conditions (pH 3.5 or less), this aquo complex $[\text{Be}(\text{H}_2\text{O})_4]^{2+}$ is predominant. However, hydroxide ions can replace H_2O molecules as the pH increases, forming $[\text{Be}(\text{OH})(\text{H}_2\text{O})_3]^+$ or $[\text{Be}_3(\text{OH})_3(\text{H}_2\text{O})_6]^+$ (pH 4.5-5.5) and predominantly $[\text{Be}(\text{OH})_2]$, nearing physiological pH, which also has poor aqueous solubility (Alderighi et al., 2000; R. C. Lim et al., 2020; L. Scott et al., 2008; Mederos et al., 2001; Naglav et al., 2016) The limited aqueous solubility of Be^{2+} near physiological pH presented significant challenges in this research project. Consequently, the ITC experiments were conducted at a pH range of 5.8-6.0 to ensure adequate solubility. A study by our research group highlighted the impact of sulfate ions as a counterion that enhances Be^{2+} solubility (Lim et al., 2020). The presence of sulfate introduced either through the use of H_2SO_4 for pH adjustment or added as Na_2SO_4 was found to increase the solubility of beryllium considerably. This was attributed to the “Diverse Ion Effect,” where sulfate interacts with solvated Be^{2+} , promoting higher solubility through ion pairing. The diverse ion effect and the addition order were considered when preparing beryllium solutions for this study.

Lithium, the lightest alkali metal, exhibits distinctive behavior in aqueous solutions, mainly due to its small ionic size and strong charge density. In water, lithium ions (Li^+) are present as hydrated cations. Due to lithium's high charge density, these ions tend to be highly solvated, which leads to a strong attraction to the polar water molecules. In aqueous solutions, lithium (Li^+) commonly forms simple aquo complexes $[\text{Li}(\text{H}_2\text{O})_n]^+$, where n typically ranges from 4 to 6, exhibiting tetrahedral coordination with four ligands and octahedral coordination with six ligands. Lithium's interactions are particularly strong with hard base donor atoms (e.g., oxygen in the water and other oxygen-containing groups) (Olsher et al., 1991; Schweitzer & Pesterfield, 2010). The interaction of lithium with bio-relevant molecules like carboxylic acids and water in aqueous environments is critical for its pharmacological activity, especially in the treatment of bipolar disorder and other psychiatric conditions (Marmol, 2008).

Table 3.1: Properties of Lithium, Beryllium, Magnesium, and Their Ions. Be^{2+} cation has a smaller ionic radius compared to Mg^{2+} and Li^+ (Ahrens, 1952)

Metal	Atomic number	Mass (g/mol)	Electron Configuration	Cation	Ionic radii (6-fold coordination) (Å)
Li	3	6.938	$[\text{He}] 2\text{S}^1$	Li^+	0.68
Be	4	9.012	$[\text{He}] 2\text{S}^2$	Be^{2+}	0.35
Mg	12	24.304	$[\text{Ne}] 3\text{S}^2$	Mg^{2+}	0.66

Magnesium ion (Mg^{2+}) is the fourth most abundant cation in living organisms. It has indispensable roles across numerous cellular functions due to its physiochemical properties, particularly its ability to form stable complexes. Mg^{2+} is crucial for over 300 enzymatic reactions, often as a cofactor necessary for activation and proper enzyme function. Magnesium typically coordinates with six water molecules in an octahedral configuration, a stable form contributing to its bioactivity. Mg^{2+} has a smaller ionic radius than other Alkali and Alkaline metals, except for Be^{2+} (Cowan, 1998). The small ionic size and high hydration energy allow for stable and significant interactions with various ligands, particularly those with oxygen donors such as carboxylates and phosphates. Mg^{2+} , as a divalent cation, can effectively neutralize the negative charges on these groups, leading to stable complex formations. This characteristic is essential for its biological roles, as it interacts with the phosphate groups of ATP, facilitating various biochemical processes, including energy transfer and enzyme activation. (Case et al., 2020; Dudev et al., 1999; Wolf & Cittadini, 2003).

Mg^{2+} binds ATP primarily by coordinating with the oxygen atoms of the γ or β phosphate groups. In the context of kinase reactions, the Mg^{2+} -ATP complex is essential to stabilizing the negative charges of the phosphates in ATP, facilitating ATP binding to the kinases for phosphotransfer. The complexation of Mg^{2+} with ATP significantly enhances the binding affinity of ATP for kinases several-fold because the stabilized Mg^{2+} -ATP complex can form more favorable interactions with the kinase binding sites than the unbound form of ATP. Mg^{2+} also helps orient the phosphate groups of ATP in the catalytic site for better nucleophilic attack by the substrate, thereby making the phosphotransfer reaction more efficient (Forstner et al., 1999).

Carboxylate groups commonly found in the side chains of aspartate and glutamate residues are expected to play an important role in coordinating the binding of cations such as

Mg²⁺ in proteins. These groups can bind Mg²⁺ using one or both oxygen atoms, leading to monodentate or bidentate coordination. The negative charge of the carboxylate group helps neutralize the positive charge of Mg²⁺, enhancing the stability and specificity of the interaction. This coordination is essential for enzymatic functions where Mg²⁺ is a cofactor (Dudev & Lim, 2011).

GSK3 β is an Mg²⁺-dependent enzyme. Ryves & Harwood (2000) demonstrated that Li⁺ acts as a competitive inhibitor of GSK3 β with respect to Mg²⁺, not with respect to the substrate or ATP. The inhibition potency of Li⁺ on GSK3 β depended on Mg²⁺ concentration. At lower Mg²⁺ concentrations, Li⁺ was more effective in inhibiting GSK3 β . This indicated that Li⁺ directly competes with Mg²⁺ ions for binding sites essential for the enzymatic activity of GSK3 β (Ryves & Harwood, 2001). Be²⁺ appeared to act as a more potent inhibitor of GSK3 β by competing for both Mg²⁺ and ATP binding sites (Ryves et al., 2002). This dual competitive nature was demonstrated through dual inhibition studies. When Be²⁺ and ADP (the product of ATP hydrolysis) are present together, they interfere with each other's actions, suggesting they target overlapping sites associated with ATP binding. Dual inhibition studies with Li⁺ and Be²⁺ suggested that they target separate but specific Mg²⁺ binding sites, where one site is sensitive to both Li⁺ and Be²⁺ and another sensitive to Be²⁺, which interacts with the Mg²⁺-ATP complex binding site (Ryves et al., 2002).

The catalytic site of GSK3 β contains several aspartic acid residues: Asp133, Asp181, and Asp200. Asp133 is primarily involved in binding and stabilizing the adenosine ring of ATP. Mg²⁺ binding is closely associated with ATP binding (Bertrand et al., 2003; SUN et al., 2011). A molecular dynamics simulation study identified two key magnesium ions referred to as **Mg1** and **Mg2**: **Mg1** coordinating four oxygen atoms, including those from the α - and γ - phosphates of

ATP and the backbone carbonyl of Asn186 and the carboxylate group of Asp200, and **Mg2** showing octahedral coordination involving six oxygen atoms, one each from β - and γ -phosphates of ATP and carboxylate oxygens of Asp200 side chain, and two water molecules (SUN et al., 2011). Asp181 was also involved in the orientation of the Mg^{2+} -ATP complex. Sun et al. (2011) demonstrated that both Mg^{2+} ions were essential for correctly positioning ATP phosphate groups with key catalytic residues like Lys85 and Lys183 for efficient phosphotransfer. The study found that in the absence of both Mg^{2+} ions, ATP forms intramolecular hydrogen bonds, adopting a folded conformation unfavorable for phosphorylation. GSK3 β structure bound to both Mg^{2+} and Mg^{2+} -ATP showed the lowest RMSF (Root Mean Square Fluctuation), indicating the GSK3b structure involving the binding of two Mg^{2+} is the most rigid and assists in maintaining the specific shape to ensure efficient interaction with substrates.

A computational analysis utilizing experimental stability constants of Mg^{2+} and Li^+ complexes and computed free energies for replacing hexacoordinated Mg^{2+} with tetracoordinate Li^+ in Mg^{2+} binding sites involving carboxylate groups showed Li^+ is more likely to compete with and displace Mg^{2+} ions from the **Mg2** site which involves more solvation (water molecules participating in the coordination), and unlikely to compete with the **Mg1** site that is not solvated (Dudev & Lim, 2011). Since experimental evidence suggests that Be^{2+} can compete with two distinct Mg^{2+} binding sites of GSK3 β (Ryves et al., 2002), that implies Be^{2+} can occupy both solvated and less solvated Mg^{2+} binding sites involving carboxylate groups in GSK3 β .

Be^{2+} has a considerably smaller ionic radius than Mg^{2+} and Li^+ ions (**Table 3.1**). Due to this small ionic radius and +2 charge, Be^{2+} has a high charge density. This high charge density enhances its ability to form strong electrostatic and coordination bonds with negatively charged

carboxylate groups, more than Mg^{2+} and Li^+ . The stronger electrostatic attraction between beryllium and the carboxylate groups could lead to more stable complexes. Beryllium typically exhibits a coordination number of four, favoring a tetrahedral geometry in its complexes. Therefore, compared to Mg^{2+} , beryllium ions are coordinated with fewer water molecules in aqueous solutions. The lower solvation shell of Be^{2+} means that it can approach closer to the carboxylate groups with fewer intervening water molecules. The combination of preferential coordination geometry, high charge density, reduced solvation, and ability to form strong electrostatic interactions with negatively charged groups, such as carboxylate groups, provides a theoretical basis to hypothesize that Be^{2+} would display higher affinity towards carboxylate-rich binding sites compared to Mg^{2+} or Li^+ . This study intended to experimentally evaluate this by conducting binding experiments between Be^{2+} and Mg^{2+} (and Li^+) against carboxylate-rich model chelators and model peptides.

Experimental Strategy

Our study explored the binding dynamics between beryllium, magnesium, and lithium ions using model chelators and peptides enriched with carboxylate groups. We selected a suite of model chelators, including EDTA, NTA (nitriloacetic acid), 4,5-IDA (imidazole dicarboxylic acid), and SA (salicylic acid), to evaluate their metal-binding affinities through Isothermal Titration Calorimetry (ITC) experiments. To maximize carboxylate presence, we designed tetrapeptides composed entirely of aspartic acid residues for the peptide models. Control peptides included sequences of four lysine residues and four glycine residues, respectively, to assess the specificity of metal ion binding to carboxylate groups. Each peptide was tagged with a fluorescein isothiocyanate (FITC) label at the N-terminus. While ITC, a label-free technique, was

employed to measure binding affinity and thermodynamics, we also intended to utilize Microscale Thermophoresis (MST) for these studies. MST requires fluorescence to track interaction changes and was intended to validate our ITC findings. This dual-methodological strategy aimed to enhance the robustness of our investigation into how these metal ions interact with carboxylate-rich environments.

Isothermal Titration Calorimetry (ITC) for Binding Interactions

ITC measures the heat changes that occur when molecules interact. Typically, in an ITC binding experiment, a chelator or macromolecule solution is placed in the sample cell, and the ligand is loaded into the syringe. The ligand and sample cell solutions are prepared in compatible buffers and pH. During the experiment, the ligand is incrementally injected into the sample cell, and the ITC measures the heat released or absorbed by monitoring the power adjustments needed to keep the sample and reference cells at the same temperature. The reference cell is typically filled with water or buffer. The power adjustment is expressed as differential power (DP), calibrated against the reference power. Suppose the binding interactions result in an overall release of heat (exothermic). In that case, the DP value decreases relative to the reference, and if the binding interactions result in overall heat absorption (endothermic), the DP value increases relative to the reference (Wiseman et al., 1989).

The exothermic or endothermic nature depends on the molecular interactions between the molecules involved in binding. Bond formation typically releases heat, and bond breaking usually absorbs heat. Hydrogen bonding, ionic interactions, hydrophobic interactions, and Vander Waals forces, including dipole-dipole interactions, are among the non-covalent interactions that could occur during binding between molecules. Molecules can undergo

conformational changes upon binding (folding or unfolding, for instance), which can involve both making and breaking intermolecular interactions and changes in solvent interactions leading to heat changes. The heat change measured during an ITC experiment reflects the sum of all these interactions. The heat released or absorbed during a binding interaction equals the enthalpy (ΔH_{app}) when the system is at constant pressure (Falconer et al., 2021; Ghai et al., 2012; Kalidas & Sangaranarayanan, 2023; Velazquez-Campoy et al., 2015; Wiseman et al., 1989).

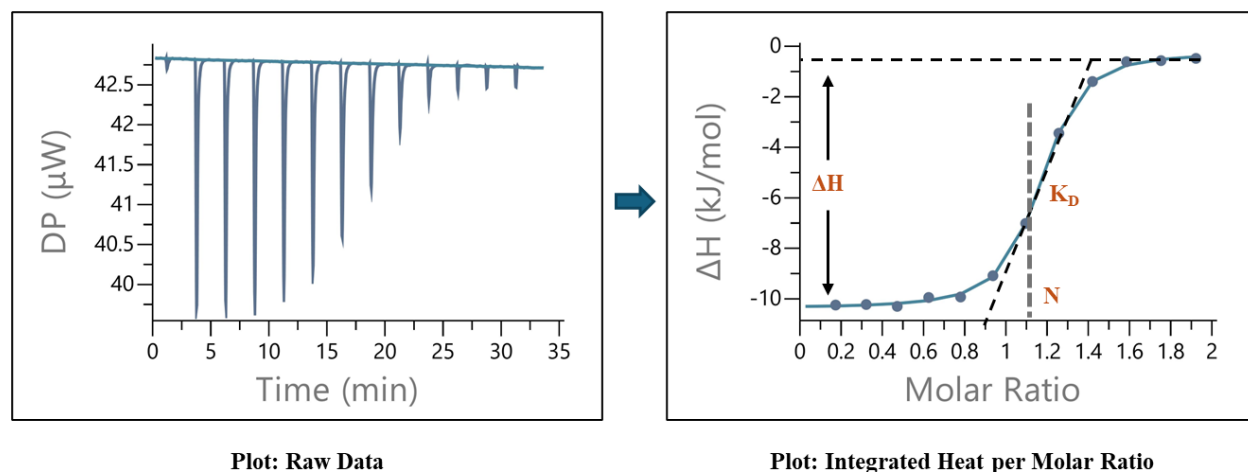
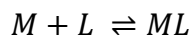


Figure 3.1: Typical ITC Binding Thermogram. (Plot: Raw Data) This is the raw ITC thermogram for an exothermic binding reaction. The ligand is incrementally injected into the sample cell containing the macromolecule in a series of injections. The differential potential (DP) change following each injection is recorded. The DP change gradually decreases as the macromolecule gets saturated with the ligand. (Plot: Integrated Heat per Molar Ratio) The integrated heat change derived from each injection peak is plotted against the Ligand: Macromolecule molar ratio, deriving a binding isotherm. In a one-site binding model, the curve is fitted to derive a stoichiometry (N) close to 1, and the dissociation constant (K_D) is obtained from the slope. The overall heat change represents the enthalpy (ΔH) of the binding reaction.

In a typical ITC binding experiment, the ligand is incrementally injected into the sample cell. With each injection, the resulting heat change peaks gradually decrease as the chelator or macromolecule reaches saturation (**Figure 3.1, Plot: Raw Data**). Beyond this point, the peaks stabilize, reflecting only the heat involved in dilution. After titration, the heat change peaks corresponding to each injection are integrated and plotted against the ligand: macromolecule molar ratio (**Figure 3.1, Plot: Integrated Heat per Molar Ratio**). The integrated heat vs. molar ratio, known as the Wiseman plot, represents the binding curve. The binding isotherm is analyzed by fitting it to an appropriate binding model (one-site binding or two-site binding, etc). By applying a suitable binding model to the Wiseman plot, values for binding enthalpy (ΔH_{app}), dissociation constant (K_D), and stoichiometry (n) are derived.

In binding studies, K_D is defined as the concentration of ligand at which half of the available binding sites are occupied. It represents the equilibrium between the bound and unbound states when the rates of association and dissociation are the same. For a 1:1 binding interaction between a ligand (L) and macromolecule (M), the K_D can be mathematically expressed as:

Scheme 3-1:



Equation 3.1:

$$K_A = \frac{[ML]}{[M][L]}$$

Where:

K_A = Association constant

Equation 3.2:

$$K_D = \frac{[M][L]}{[ML]}$$

A lower K_D value indicates a higher affinity between the ligand and the macromolecule because a lower ligand concentration is needed to occupy the binding sites significantly. Conversely, a higher K_D indicates a lower affinity, requiring a higher ligand concentration to achieve the same occupancy level. In ITC binding studies, K_D is the equilibrium constant for dissociating the ligand-macromolecular complex into its constituent parts. This constant calculates the binding reaction's Gibbs free energy change (ΔG) using equation 3.3.

Equation 3.3:

$$\Delta G = -RT \ln K_A = -RT \ln\left(\frac{1}{K_D}\right)$$

Where:

R = the universal gas constant (8.314 J. mol⁻¹. K⁻¹)

T = Temperature in Kelvin (K)

Applying the ΔH_{app} directly measured from the binding reaction and the ΔG derived from equation 3.3, the reaction entropy (ΔS) can also be derived via the Gibbs-Helmholtz equation (equation 3.4) to provide a complete thermodynamic profile of the binding reaction. This fundamental equation is a cornerstone of thermodynamics and helps understand the spontaneity and feasibility of a binding reaction.

Equation 3.4:

$$\Delta G = \Delta H - T\Delta S$$

A negative ΔG value indicates that the binding process is spontaneous, with the magnitude of ΔG giving an idea of the strength and stability of the binding. The lower the K_D , the more negative ΔG becomes, indicating a stronger and more favorable binding interaction. The exothermic or endothermic nature and the magnitude of ΔH indicate whether the reaction is enthalpically favorable. The magnitude and sign of ΔS indicate whether or not the binding interaction is entropically favorable. Increased change in disorder or randomness in the system implies the binding is entropically favorable. For a binding reaction to be feasible, the changes in ΔH and ΔS often offset each other. This phenomenon is known as enthalpy-entropy compensation. Typically, bond formation between ligand and macromolecule leads to the structuring of these molecules, thus decreasing the entropy. However, typically, the solvent molecules involved in the solvation of ligands and macromolecules in solution get displaced during ligand-macromolecule interactions, leading to increased entropy. Burying hydrophobic groups away from water upon binding or folding reduces system entropy. However, it can be enthalpically favorable due to reduced disruption of the hydrogen-bond network in water (Malvern Instruments; TA Instruments).

Microscale Thermophoresis (MST)

MST is an analytical technique to study molecular interactions between biomolecules or small molecules vs. biomolecules in an immobilization-free environment. This technique utilizes a microscopic temperature gradient induced by an infrared laser to cause molecules to move – a phenomenon known as thermophoresis. The movement of a molecule in a temperature gradient depends on the properties of the molecule being studied, such as its charge, size, and hydration shell. When a molecule interacts with another molecule, these factors change, leading to altered thermophoretic behavior (Entzian & Schubert, 2016; Jerabek-Willemsen et al., 2011; Mao et al., 2015; Shao et al., 2020). MST allows for the quantification of molecular interactions by measuring these changes. The setup and data collection from an MST are depicted in **Figure 3.2** (NanoTemper Technologies, Munich).

The target molecule, typically the macromolecule, must be labeled with a fluorescent dye for an MST experiment. This labeling allows the detection of the target molecule's thermophoresis following ligand binding. The ligand is prepared at various concentrations in matching buffer conditions. This ligand can be unlabeled since the detection is based on changes in the fluorescence of the labeled target. A fixed concentration of the fluorescently labeled target is mixed with varying ligand concentrations. These samples are loaded into capillaries. The temperature control and the appropriate excitation and emission wavelengths for the fluorescent label can be set on the MST instrument. An initial capillary scan is followed for each capillary to test the initial fluorescence of the samples before applying the thermal gradient. The initial fluorescence should typically remain similar ($\pm 10\%$) across all capillaries. The fluorophore is excited by adjusting the LED power by 5-90% to obtain fluorescent counts within the 500-2000 range (For Nanotemper Monolith MST). An infrared laser is used at 20-60% power to create a

precise temperature gradient within the capillary solution. As the target molecules move in the temperature gradient, their concentration changes lead to changes in fluorescent intensity. The movement of molecules from warmer to cooler regions or vice versa is captured by detecting the fluorescence. Normalized fluorescence is calculated to assess the relative change in fluorescence due to thermophoresis. This involves comparing the fluorescence intensity in different parts of the temperature gradient (hot vs. cold) using equation 3.5.

Equation 3.5:

$$F_{norm} = \left(\frac{F_{hot}}{F_{cold}} \right)$$

Normalized fluorescence changes are plotted against the ligand concentration to obtain a binding curve. The curve can be fitted to binding models to extract the dissociation constant (K_D), the primary output of an MST experiment. The binding stoichiometry (n) can also be obtained, and thermodynamic parameters ΔG , ΔH , and ΔS can be obtained by performing the MST experiment at different temperatures.

In cases where the initial fluorescence (fluorescence prior to applying a thermal gradient) is different among the sample capillaries, an MST experiment can not be performed. If the change in initial fluorescence depends on the ligand concentration, this dose-dependent change in initial fluorescence can be directly utilized to obtain a binding curve.

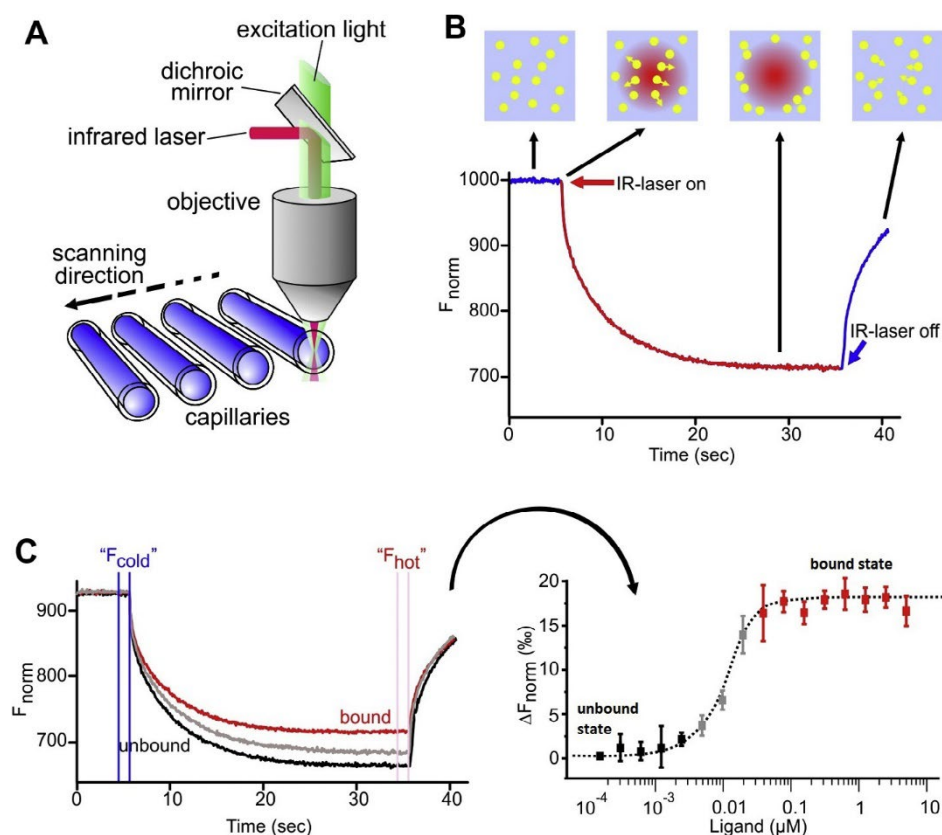


Figure 3.2: Illustration of MicroScale Thermophoresis (MST) Process. (A) In the MST setup, the optical system is focused at the center of the glass capillaries containing the binding molecules to capture the movement of the molecules. The temperature gradients are created by an infrared (IR) laser and fluorescent species excited by an LED light source (B) The MST time trace shows the movement profile of molecules within a temperature gradient (C) The results from a typical MST experiment are depicted: time traces from 16 capillaries, each containing the same concentration of the fluorescent-tagged macromolecule and varying concentrations of ligand, are collected and displayed on a graph (left side). The normalized fluorescence from these traces is then plotted against the ligand concentration (right side) to analyze and determine binding parameters, such as binding affinity. Image from NanoTemper Technologies, Munich and Entzian & Schubert (2016).

Materials and Methods

Materials

The study used chelators EDTA (Ethylene diamine tetra acetic acid) (Sigma #ED2SS), NTA (Nitrilotriacetic acid) (Sigma Aldrich #N9877), 4,5-IDA (4,5-imidazole dicarboxylic acid) (Sigma Aldrich #246115), and SA (Salicylic acid) (Sigma Aldrich #C3771). The metal ions used for the study were Beryllium sulfate hydrate (Fluka #14270), Lithium Chloride (Sigma #L-8895), Magnesium Sulfate (Sigma Aldrich #746452), and Calcium sulfate (Sigma Alrich #C3771). The stock solutions of the chelators and metal ions were prepared in ultra-pure water. The solutions for ITC experiments were prepared in 100mM MES buffer (Sigma #SLBT0247) at pH 6.

The model peptides for the study were custom-made by GenScript. The model peptides were designed as tetrapeptides carrying Aspartic acid (D), Glutamic acid (E), Lysine (K), or Glycine (G) with a fluorescein isothiocyanate (FITC) tagged at the N-terminus. The C-terminus of the peptides were amidated. The tetrapeptides used in the study were FITC-DDDD, FITC-KKKK, FITC-GGGG, FITC-GDDD, FITC-GGDD, and FITC-EEEE. A peptide with a spacer between the N-terminal fluorescent tag and the tetrapeptide portion was designed for the DDDD peptide, FITC-GGGGDDDD. Two additional peptides for DDDD and KKKK were designed with a Cyanine5 at the N-terminus, replacing the FITC tag, Cy5-CDDDD, and Cy5-CKKKK. The Cysteine residue (C) is used to help conjugate the peptide with the Cy5 tag. The peptides with the spacer and Cy5 tag were obtained to test whether the initial fluorescence emitted by the FITC tag was explicitly sensitive to Be^{2+} concentrations. The peptides with charged amino acids were water-soluble. Peptides with increasing Glycine (G) residues were solubilized in ultra-pure water and DMSO (Sigma Aldrich #27043). Peptide and ligand solutions for ITC binding

experiments were prepared in 100mM MES buffer at pH 5.8-6.0. For an experiment at pH 7, the peptide and ligand (only MgCl_2 and LiCl) solutions were prepared in 100mM HEPES buffer (Sigma Aldrich #246115). The peptides and ligand solutions were prepared in 100mM MES buffer at pH 5.5-6.0 for MST experiments. Sodium Chloride (Amresco #0241) was added to the buffer to observe the effect of ionic strength over the MST signal.

Isothermal Titration Calorimetry – Binding Experiments

For all ITC binding experiments, MicroCal PEAQ-ITC (PEAQ-ITC Instrument Cell Serial #MAL1122596 and PEAQ-WM Serial #29061559-0047) was used with the 13-injection method. The ligand and chelator/peptide solutions were prepared in matching buffers and pH to avoid pH mismatch and minimize dilution heat. For each experiment, the ITC syringe is loaded with 75 μL of the ligand solution, and the ITC sample cell is loaded with 280 μL of chelator/peptide solution. The final reaction volume in the adiabatic cell is 200 μL . The binding reactions were performed by incrementally injecting the ligand into the sample cell via 13 injections. The first injection of 0.4 μL is followed as a priming injection. The subsequent 12 injections will inject 4 μL of ligand into the sample cell, incrementally increasing the ligand concentration in the cell. The reactions were performed at 25 °C with 750 rpm stir speed. Once the sample cell solution had equilibrated to the assigned temperature and the baseline was stable, the substrate in the ITC syringe was first injected at $t = 1$ min, and each subsequent injection was spaced appropriately to allow the ITC peaks to return to the baseline. The default injection-spacing time is 150 sec.

Baseline Correction for Analysis of ITC Raw Plots

The baseline in a raw ITC thermogram is influenced by the set reference power, the constituents of the buffer solutions, and the exact volume loaded into the sample cell. Minor air pockets or bubbles and particulates in the cell can lead to slight fluctuations in the baseline between each ITC run. To directly compare various ITC experiments within the same graph, each thermogram's baseline was normalized to a DP of 0. This was achieved by deducting the starting baseline DP value and utilizing Microsoft Excel software to adjust.

Microscale Thermophoresis – Binding Experiments

All MST binding experiments were performed using a Monolith NT.115 MST instrument from NanoTemper Technologies. Preliminary experiments were performed with various concentrations of the fluorescence-tagged peptides in buffers. Initial fluorescence scans of the fluorescence-tagged molecule help set the appropriate fluorescence intensity between 200 and 1500 fluorescence units. The LED power can be adjusted between 5% and 95% to obtain the ideal fluorescence intensity. The Nano BLUE detector (Excitation wavelength: 460-490 nm) is selected for the analysis of FITC-tagged peptides, and for Cy5-tagged peptides, the Pico RED detector (Excitation wavelength: 600-650 nm) is selected. A 1:1 dilution series of the ligand in 16 concentrations was prepared for the binding analysis. Preliminary experiments demonstrated that at least 2.5mM BeSO₄ was needed as the highest concentration to observe a sufficient signal-to-noise ratio. Beginning with 20μL of 5mM BeSO₄ in 100mM MES pH 5.5-6.0 in the first tube, a serial dilution was prepared across the tubes by transferring 10μL from one to the next and mixing well. Each tube, starting from tube #2, contained 10μL of 100mM MES buffer for

dilution. After discarding 10 μ L from the #16 tube to maintain volume consistency, 10 μ L of the doubly concentrated fluorescent-labeled peptides (prepared in matching buffer) was added to each tube and mixed well. After mixing, the samples were incubated for ~5 min at room temperature before being loaded into capillaries for MST data capture and analysis. The instrument setup follows a scan of the 16 capillaries to measure the initial fluorescence. Thermophoresis can be measured by applying a thermal gradient if the initial fluorescence is uniform across all samples ($\pm 10\%$). In the Monolith NT.115 MST instrument, thermophoresis is measured at 20% and 40% MST power. If the initial fluorescence changes as a function of ligand concentration, the thermophoresis analysis can not be performed, and instead, the initial fluorescence measurements can be directly analyzed for binding. The data can be fitted to an appropriate binding model to obtain the dissociation constant.

Results and Discussion

Beryllium Ions Show Greater Affinity for Carboxylate-Rich Chelators than Magnesium Ions

This study compared the raw ITC thermograms and thermodynamic parameters, primarily for the interactions between Be²⁺ and Mg²⁺ ions and chelators featuring carboxylate groups (**Figure 3.3**). Both Be²⁺ and Mg²⁺ ions exhibited endothermic binding interaction with EDTA, while Ca²⁺ exhibited exothermic binding interaction (**Figure 3.4**). The Be²⁺-EDTA complexation reaction absorbs heat. This suggests that breaking existing bonds in the system (like water-metal interactions) requires more energy than is released by forming new bonds between Be²⁺ and EDTA. Like Be²⁺, the Mg²⁺-EDTA binding reaction absorbs heat for breaking

water-metal bonds, which are less strong or extensive than those in Be^{2+} due to the larger size and lower charge density of Mg^{2+} . Conversely, the formation of the Ca^{2+} -EDTA complex releases more energy than is absorbed in breaking the initial interactions in the system. The larger ionic radius of Ca^{2+} compared to Mg^{2+} and Be^{2+} likely allows EDTA to form a more stable complex, releasing more energy. Be^{2+} and Mg^{2+} binding with EDTA are entropically driven (**Figure 3.5**). A significant increase in entropy likely results from the release of water molecules that previously coordinated the metal ion. Since Be^{2+} is a smaller ion with a higher charge density, it tends to be more tightly solvated with water, which leads to greater entropy when displaced by EDTA. The increase in entropy for Mg^{2+} -EDTA binding is less than that of Be^{2+} , suggesting that fewer water molecules are released upon binding of EDTA to Mg^{2+} compared to Be^{2+} . This is consistent with the higher affinity (lower K_D) of Be^{2+} for EDTA than Mg^{2+} , indicating stronger complexation (**Table 3.2**).

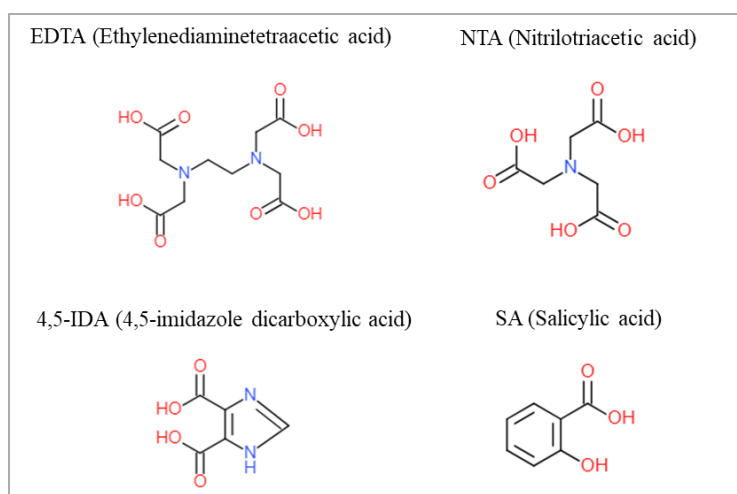


Figure 3.3: Carboxylate-Rich Chelators. Illustration of the molecular structures of four carboxylate-rich chelators used in the study: EDTA (Ethylenediaminetetraacetic acid), NTA (Nitrilotriacetic acid), 4,5-IDA (4,5-imidazole dicarboxylic acid), and SA (Salicylic acid). This figure demonstrates the functional groups involved in metal binding.

The larger ionic radius of Mg^{2+} compared to Be^{2+} results in a less tightly packed solvation shell, leading to a smaller change in entropy. Ca^{2+} and EDTA binding was an exothermic reaction that appeared enthalpically and entropically favored (**Figure 3.5**). However, the smaller change in entropy suggests that fewer water molecules are displaced upon chelation compared to Be^{2+} and Mg^{2+} . This is likely due to the lower charge density of Ca^{2+} , which results in weaker or fewer initial water interactions disrupted by EDTA binding.

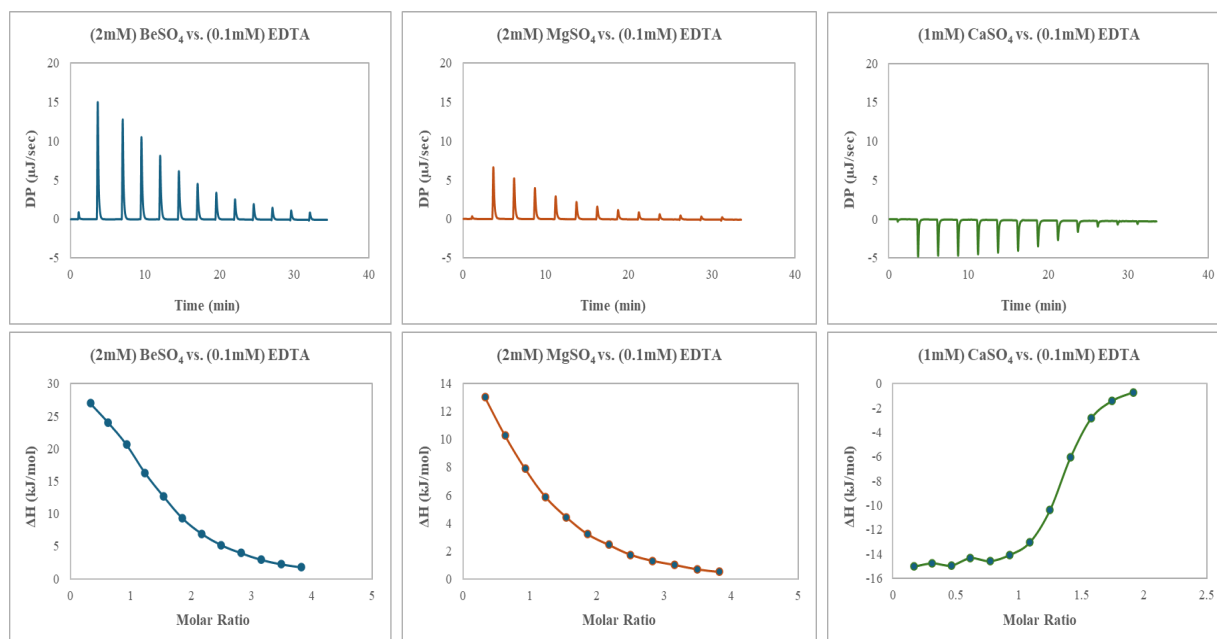


Figure 3.4: ITC Binding for Metal-EDTA. (Top panel) The raw ITC thermograms show the binding between 2mM Be^{2+} , 2mM Mg^{2+} , 1mM Ca^{2+} , and EDTA in 100mM MES pH 6. The binding interaction between Be^{2+} and Mg^{2+} and EDTA is endothermic, while the Ca^{2+} vs. EDTA binding interaction is exothermic. (Bottom panel) The integrated heat change against the ligand:chelator molar ratio is illustrated.

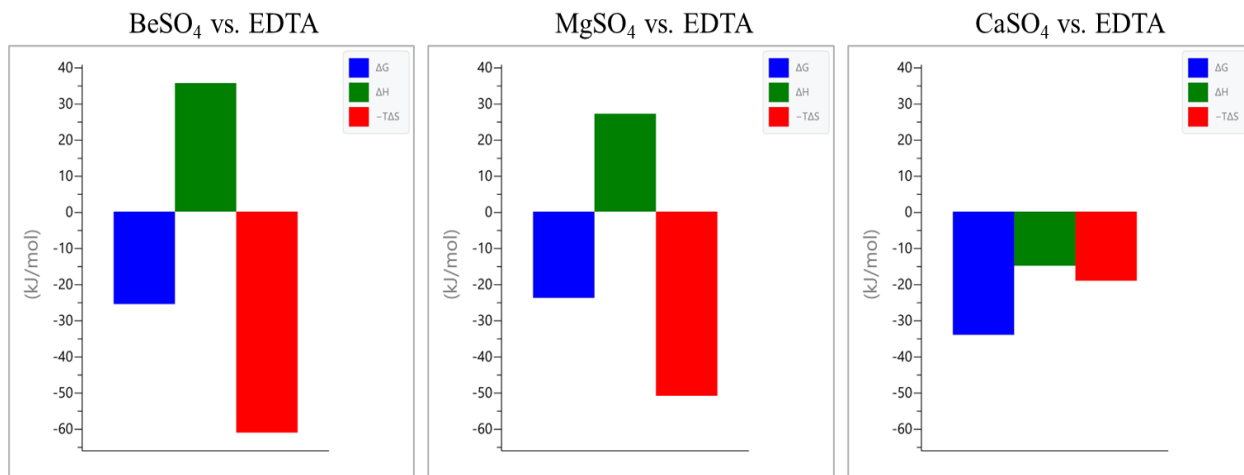


Figure 3.5: Thermodynamic Profiles for Metal-EDTA Binding. The thermodynamic profiles for the EDTA titrations with Be²⁺, Mg²⁺, and Ca²⁺ in 100mM MES pH 6 are shown. The ΔG (blue), ΔH (green), and ΔS (red) are shown. The Ca²⁺ vs. EDTA binding reaction is both enthalpically and entropically favorable. Be²⁺ and Mg²⁺ vs. EDTA binding reactions are entropically driven.

Table 3.2: Thermodynamic Parameters and Stoichiometry for Metal-EDTA Binding. The thermodynamic parameters are obtained for Metal-EDTA binding experiments in 100mM MES pH 6, as shown in **Figure 3.4**. Ca²⁺-EDTA complexation is enthalpically and entropically favored. Be²⁺-EDTA complexation is more entropically favored than Mg²⁺-EDTA complexation. The dissociation constants (K_D) for each binding interaction reflect the affinity between Metal-EDTA with K_D values Ca²⁺ < Be²⁺ < Mg²⁺.

Run#	Metal ion	N (sites)	K_D (μ M)	ΔH (kJ/mol)	ΔG (kJ/mol)	$-T\Delta S$ (kJ/mol)
R133	2mM Be ²⁺	1.36 ± 0.0098	33.3 ± 1.61	35.6 ± 0.625	-25.6	-61.2
R224	2mM Mg ²⁺	0.865 ± 0.014	66.3 ± 3.09	27.1 ± 0.903	-23.9	-51.0
R348	1mM Ca ²⁺	1.29 ± 0.0067	1.08 ± 0.104	-15.0 ± 0.225	-34.1	-19.1

The interaction of Be²⁺ with 4,5-IDA was exothermic, indicating that the energy released by bond formation is more than the energy absorbed upon breaking existing bonds with solvent

molecules (**Figure 3.6**). The 4,5-IDA molecules have two carboxylate groups, and the oxygen atoms in these groups can form strong interactions with Be^{2+} with a high charge density. In comparison, Mg^{2+} did not display a discernible binding curve with 4,5-IDA, suggesting weak or negligible interaction (**Figure 3.6**). The Be^{2+} and 4,5-IDA binding is also entropically favored (**Table 3.3**). The stoichiometry of approximately 0.5 (**Table 3.3**) suggests that each Be^{2+} ion is chelated by two molecules of 4,5-IDA, forming a 2:1 ligand-to-metal ratio. This coordination pattern reflects the preferred geometry of the Be^{2+} ion for optimal stability, potentially influenced by both enthalpic and entropic factors in forming a more ordered and solvent-displacing complex.

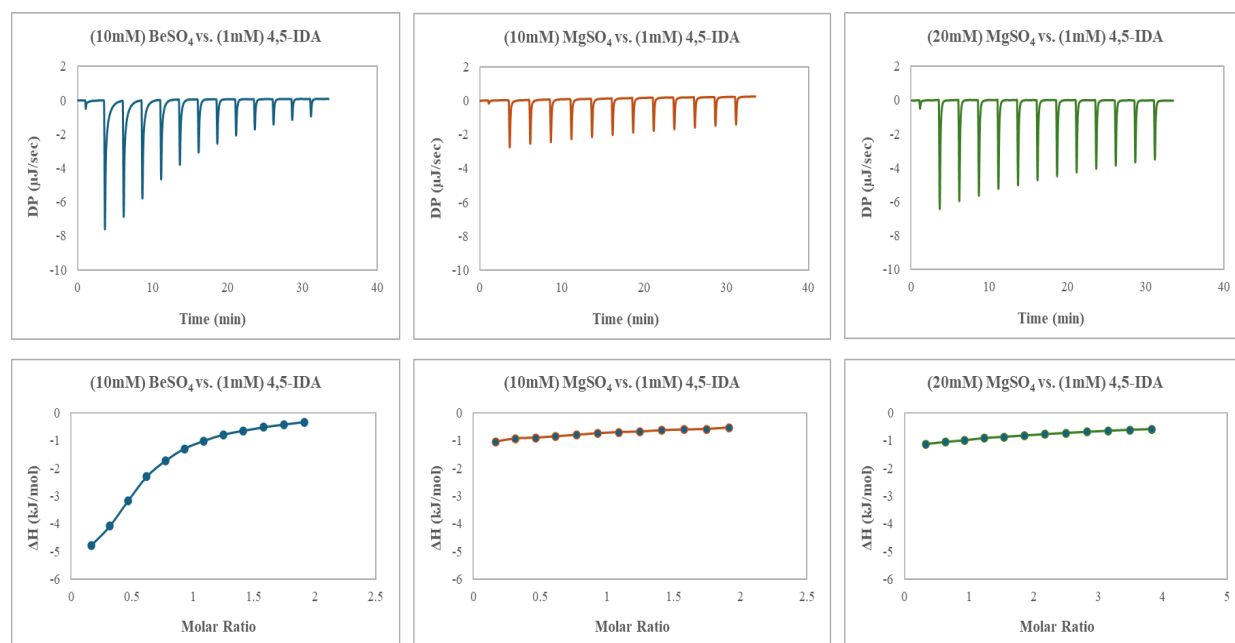


Figure 3.6: ITC Binding for Metal-4,5-IDA. (Top panel) The raw ITC thermograms show the binding between 10mM Be^{2+} , 10mM, and 20mM Mg^{2+} vs 4,5-IDA in 100mM MES pH 6. Both metal ions display exothermic peaks for the interaction with 4,5-IDA. (Bottom panel) The integrated heat change against the ligand: chelator molar ratio is illustrated. Be^{2+} vs. 4,5-IDA interaction produced a binding curve; however, Mg^{2+} did not display a discernable binding curve with 4,5-IDA, even at increased concentrations.

Table 3.3: Thermodynamic Parameters and Stoichiometry for Be²⁺-4,5-IDA Binding.

Run#	Metal ion	N (sites)	K _D (μM)	ΔH (kJ/mol)	ΔG (kJ/mol)	-TΔS (kJ/mol)
R074	10mM Be ²⁺	0.509 ± 0.0012	172 ± 20.2	-6.77 ± 0.347	-21.5	-14.7

The interaction of Be²⁺ with NTA was exothermic, indicating that the energy released by bond formation is more than the energy absorbed upon breaking existing bonds with solvent molecules (**Figure 3.7**). The NTA molecules feature multiple carboxylate groups, and the oxygen atoms in these groups can form strong interactions with Be²⁺ with a high charge density. In comparison, Mg²⁺ did not display a discernible binding curve with NTA, suggesting weak or negligible interaction (**Figure 3.7**), which is potential because the charge density of Mg²⁺ is less than that of Be²⁺. The increase in entropy associated with Be²⁺ and NTA binding favors the interaction (**Table 3.4**). The stoichiometry for Be²⁺-NTA complexation is approximately 0.5 (Average 0.46) (**Table 3.4**). The NTA molecule contains three carboxyl groups. The pK_a values for NTA: pK_{a1} = 3.03, pK_{a2} = 3.07, and pK_{a3} = 10.70 at 20 °C (<https://pubchem.ncbi.nlm.nih.gov/compound/Nitrilotriacetic-acid>). Therefore, under the experimental conditions at pH 6, we can expect the first two carboxyl groups to be predominantly deprotonated, and the third carboxyl group will remain primarily protonated. This suggests that under the experimental conditions, the Be²⁺ ion is chelated by two NTA molecules, forming a stable tetrahedral geometry preferred by the Be²⁺ ion, which will be both enthalpically favorable and entropically favorable by the displacement of water molecules.

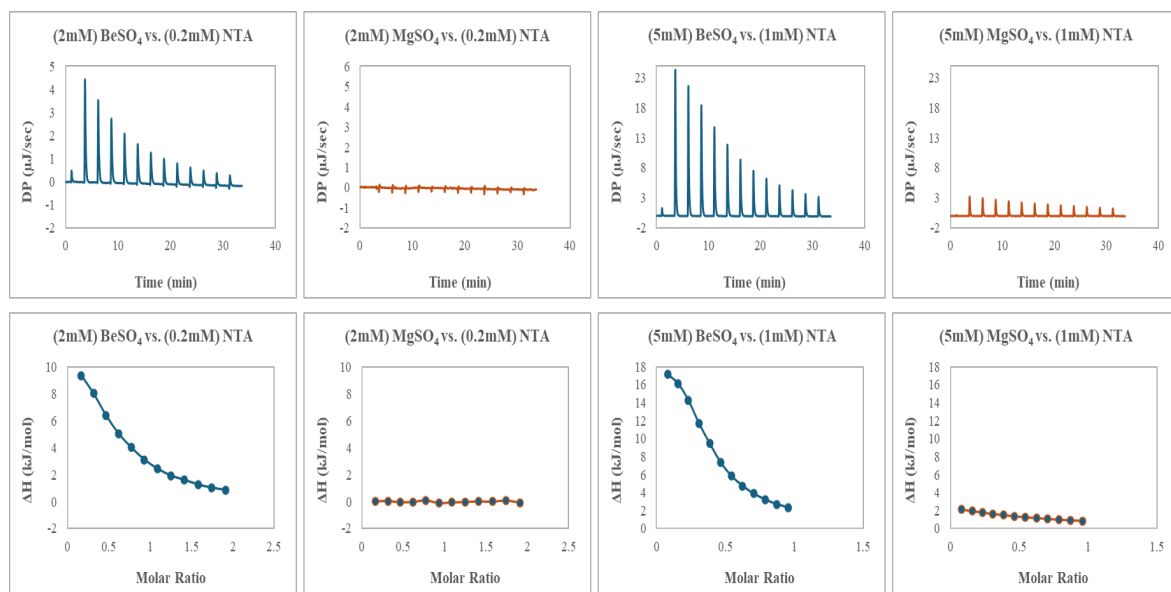


Figure 3.7: ITC Binding for Metal-NTA. (Top panel) The raw ITC thermograms show the binding between 2mM and 5mM Be^{2+} , 2mM, and 5mM Mg^{2+} vs NTA in 100mM MES pH 6. Be^{2+} displays endothermic peaks for the interaction with NTA. Mg^{2+} did not show binding with NTA (Bottom panel). The integrated heat change against the ligand: chelator molar ratio is illustrated. Be^{2+} vs. NTA interaction produced a binding curve.

Table 3.4: Thermodynamic Parameters and Stoichiometry for Be^{2+} -NTA Binding.

Run#	Metal ion	N (sites)	K_D (μM)	ΔH (kJ/mol)	ΔG (kJ/mol)	$-T\Delta S$ (kJ/mol)
R291	2mM Be^{2+}	0.551 ± 0.01	59.1 ± 5.32	15.7 ± 0.780	-24.2	-39.8
R130	5mM Be^{2+}	0.369 ± 0.0057	70.7 ± 7.67	19.9 ± 0.705	-23.7	-43.6

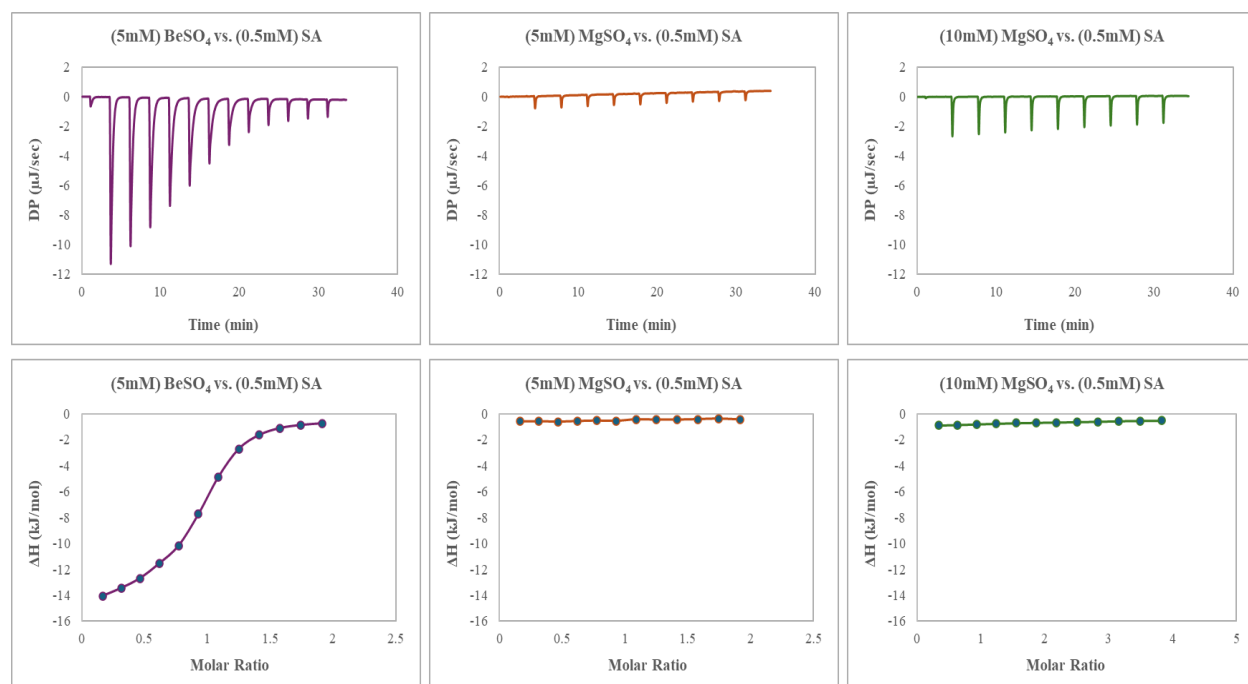


Figure 3.8: ITC Binding for Metal-SA. (Top panel) The raw ITC thermograms show the binding between 5mM Be^{2+} and 5mM Mg^{2+} vs Salicylic acid (SA) in 100mM MES pH 6. Be^{2+} displayed exothermic peaks for the interaction with SA. Mg^{2+} did not show binding with SA (Bottom panel). The integrated heat change against the ligand: chelator molar ratio is illustrated. Be^{2+} vs. SA interaction produced a binding curve.

Table 3.5: Thermodynamic Parameters and Stoichiometry for Be^{2+} -SA Binding.

Run#	Metal ion	N (sites)	K_D (μM)	ΔH (kJ/mol)	ΔG (kJ/mol)	$-T\Delta S$ (kJ/mol)
R189	2mM Be^{2+}	0.981 ± 0.0053	9.16 ± 0.47	-14.2 ± 0.152	-28.8	-14.6
R190	5mM Be^{2+}	0.915 ± 0.012	20.1 ± 2.58	-14.5 ± 0.361	-26.8	-12.3

The interaction of Be^{2+} with SA was exothermic, indicating favorable enthalpy changes (**Figure 3.8**). Mg^{2+} did not bind SA even at higher concentrations, indicating weak interactions. The stoichiometry for Be^{2+} -SA complexation was close to 1 (**Table 3.5**). These observations are reasonable because, unlike the previous chelators, the carboxyl group has less freedom of movement. Therefore, the metal ion should be able to approach the existing conformation of the chelator. Be^{2+} has a smaller ionic radius than Mg^{2+} and could occupy this binding site. While present, the entropic contributions were less significant than the interactions of Be^{2+} with EDTA or NTA, suggesting that fewer water molecules are displaced during this binding event.

Beryllium Ions Show a Greater Affinity for Carboxylate-Rich Peptides

This study investigates the binding interactions between the metal ions Be^{2+} , Mg^{2+} , and Li^+ against a series of tetrapeptides using ITC. The peptides were designed with a fluorescence tag on the N-terminus since we intended to study the metal-peptide binding using MST as a complementary biophysical technique. All peptides were FITC tagged unless specified otherwise. The binding and thermodynamic behavior for metal binding against the DDDD, KKKK, and GGGG peptides was tested. The tested metal ions are all cations and, thus, were expected to demonstrate binding against the DDDD peptide while demonstrating no binding against the KKKK and GGGG peptides, which would serve as controls.

The comparison of raw ITC thermograms for the binding analysis between BeSO_4 and DDDD peptide vs. MgSO_4 and DDDD peptide in 100mM MES pH 5.80 buffer demonstrated a binding interaction with Be^{2+} but no binding with Mg^{2+} (**Figure 3.9**). The comparison of the raw ITC thermograms for metal vs. peptide titration against the buffer vs. buffer, buffer vs. peptide,

and metal vs. buffer controls demonstrate that Be^{2+} displays a clear binding interaction with the DDDD peptide. In contrast, the titration for Mg^{2+} vs. peptide is identical to the Mg^{2+} vs. buffer control (Figure 3.9). Both Be^{2+} and Mg^{2+} demonstrated no binding against the KKKK peptide (Figure 3.10) and GGGG peptide (Figure 3.11).

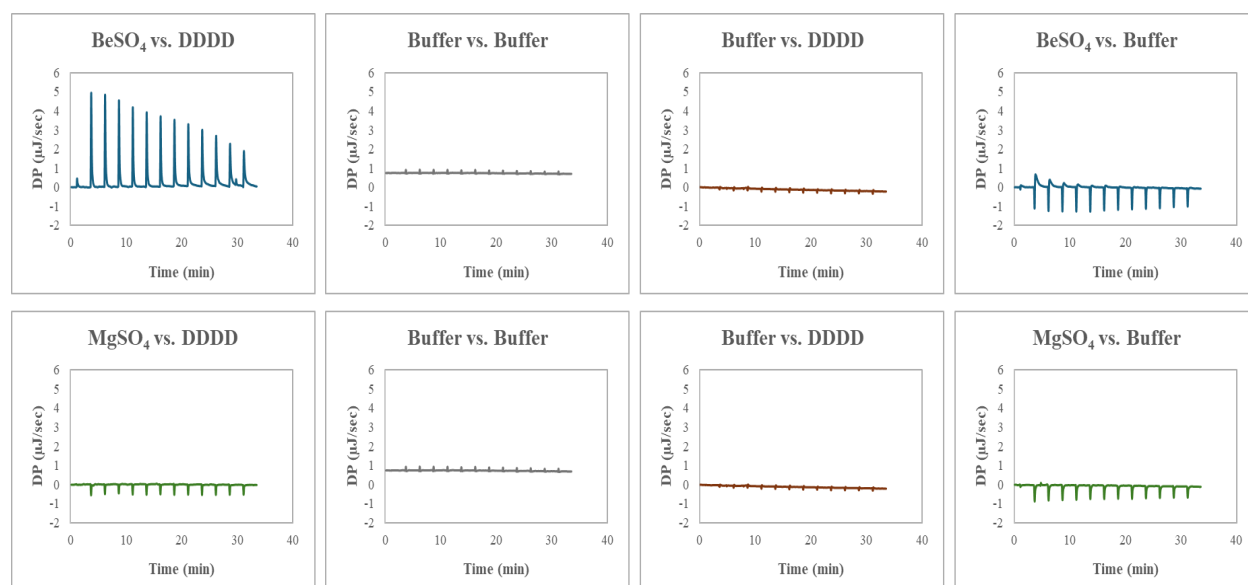


Figure 3.9: ITC Binding for Be^{2+} vs. Mg^{2+} Against DDDD Peptide. (Top panel) The raw ITC thermograms for 5mM BeSO_4 vs. DDDD peptide in 100mM MES pH 5.80. (Bottom panel) The raw ITC thermograms for 5mM MgSO_4 vs. DDDD peptide in 100mM MES pH 5.80. The buffer vs. buffer, buffer vs. peptide, and metal ion vs. buffer controls are shown.

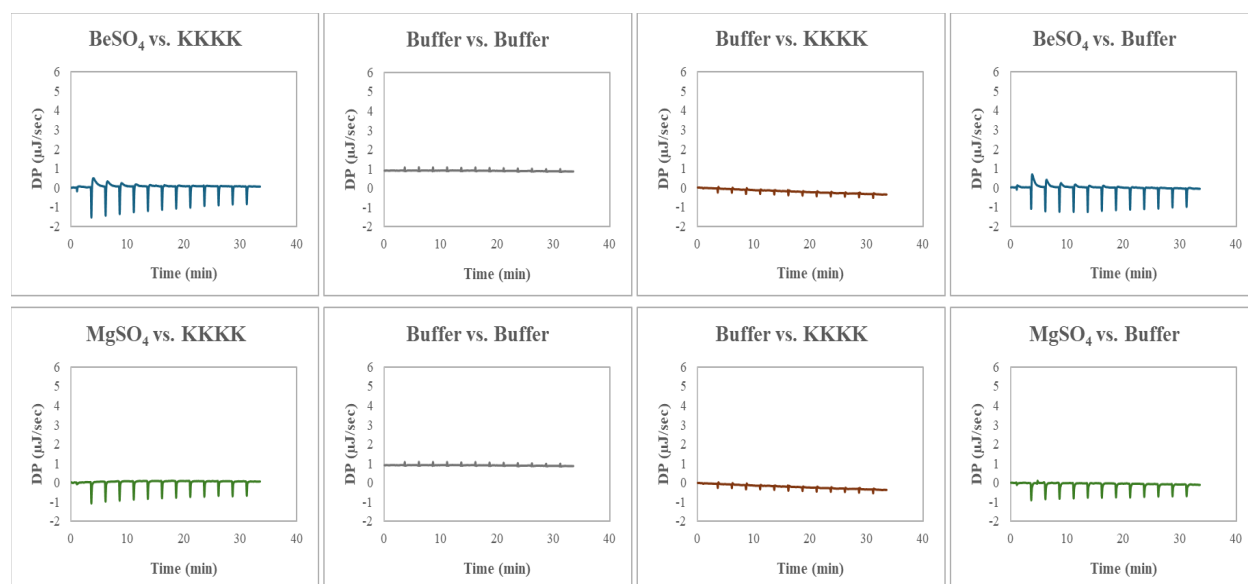


Figure 3.10: ITC Binding for Be^{2+} vs. Mg^{2+} Against KKKK Peptide. (Top panel) The raw ITC thermograms for 5mM BeSO_4 vs. KKKK peptide in 100mM MES pH 5.80. (Bottom panel) The raw ITC thermograms for 5mM MgSO_4 vs. KKKK peptide in 100mM MES pH 5.80. The buffer vs. buffer, buffer vs. peptide, and metal ion vs. buffer controls are shown.

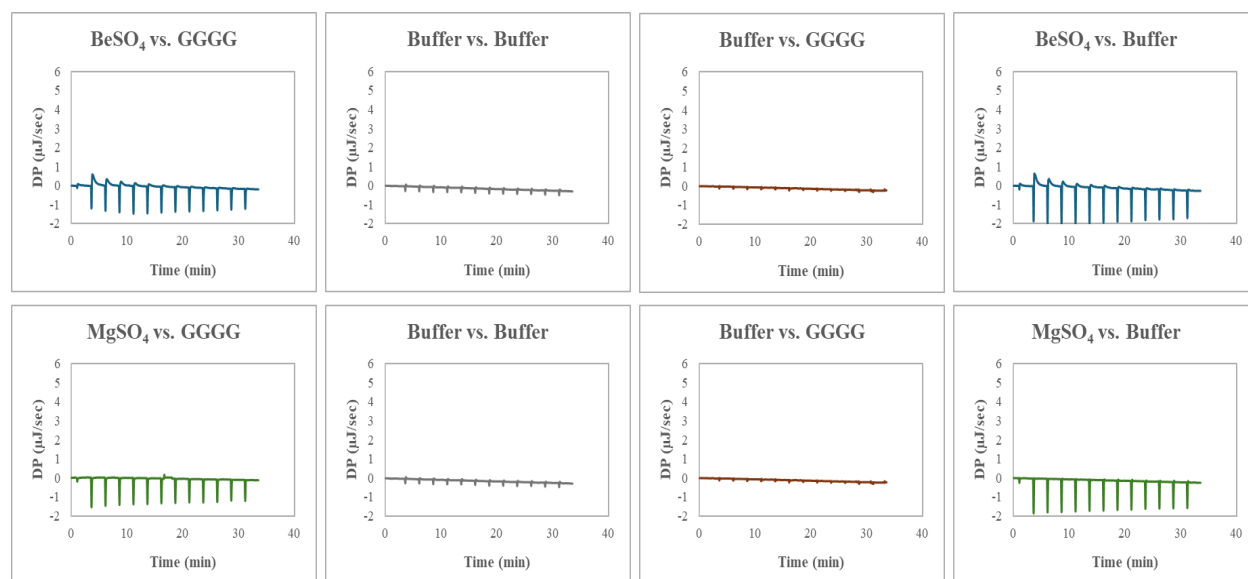


Figure 3.11: ITC Binding for Be^{2+} vs. Mg^{2+} Against GGGG Peptide. (Top panel) The raw ITC thermograms for 5mM BeSO_4 vs. GGGG peptide in 100mM MES pH 5.80. (Bottom panel) The raw ITC thermograms for 5mM MgSO_4 vs. GGGG peptide in 100mM MES pH 5.80. The buffer vs. buffer, buffer vs. peptide, and metal ion vs. buffer controls are shown.

The ITC thermograms and integrated heat plots for Be^{2+} vs. Mg^{2+} vs. Li^+ with DDDD in 100mM MES pH 5.80 were compared (**Figure 3.12**). Be^{2+} showed a significantly stronger interaction with the DDDD peptide, which is rich in carboxylate groups. The binding interaction between Be^{2+} and the DDDD peptide is also endothermic, suggesting that breaking the existing bonds between the metal ion and solvent molecules, as well as bonds between the carboxylate groups and solvent molecules, requires more energy than is released by forming new bonds between Be^{2+} and the peptide. The thermodynamic profile of the Be^{2+} -DDDD binding interaction (**Figure 3.13**) shows that the binding has an enthalpic cost but is primarily favored by a significant increase in entropy.

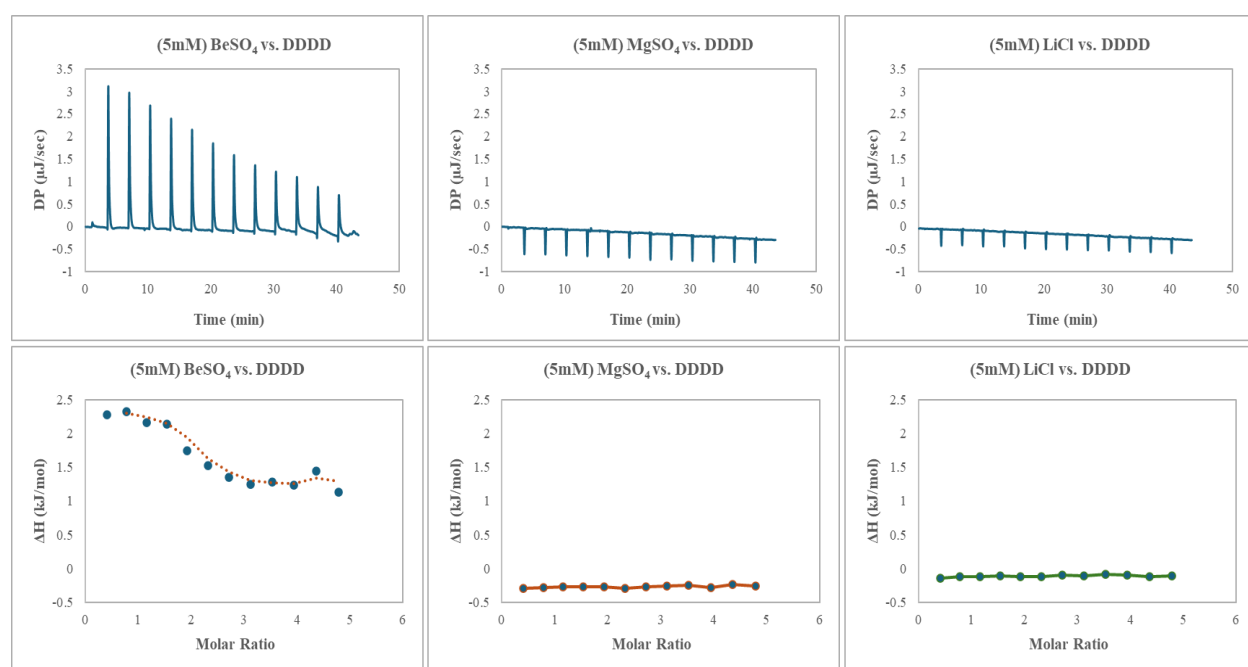


Figure 3.12: ITC Binding for Be^{2+} , Mg^{2+} , and Li^+ vs. DDDD Peptide. (Top panel) The raw ITC thermograms for 5mM BeSO_4 , MgSO_4 , and LiCl vs. DDDD peptide in 100mM MES pH 5.80. (Bottom panel) The integrated heat vs. molar ratio for the respective titrations from the top panel.

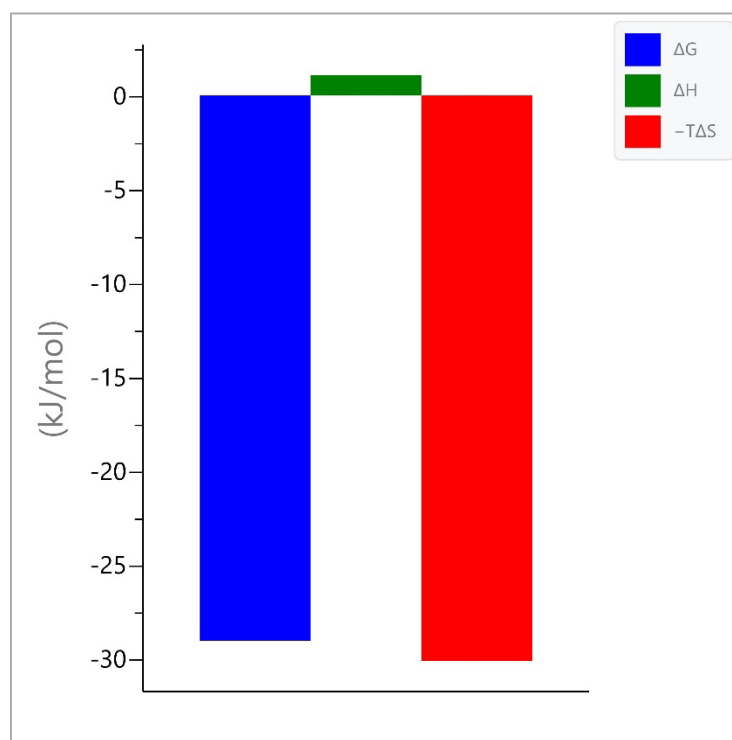


Figure 3.13: Thermodynamic Profile for Be^{2+} vs. DDDD Binding. This is the thermodynamic profile for R#1581. A significant increase in entropy favors the Be^{2+} -DDDD binding reaction, compensating for the enthalpy cost.

As previously described, Be^{2+} ions are highly solvated due to the high charge density. The oxygen atoms in the carboxylate groups in the DDDD peptide would also form strong interactions with water molecules. Therefore, expecting an enthalpic cost associated with breaking solvent interactions is logical for the Be^{2+} and DDDD binding. However, since Be^{2+} has a small ionic radius and, therefore, a high charge density, it could form stable interactions with the oxygen atoms in the carboxylate groups and occupy spaces inaccessible by larger ions. Many solvent molecules will be displaced in this binding process, contributing to a significant increase in entropy (**Figure 3.13**), yielding a favorable binding interaction.

These binding experiments were performed at pH 5.80 due to the solubility constraints of Be^{2+} . However, it is possible that the carboxyl groups are not fully protonated at this pH, and Mg^{2+} and Li^+ ions displayed a weaker interaction due to this fact. Therefore, Mg^{2+} and Li^+ binding with the DDDD peptide were studied at pH 7 in the HEPES buffer (**Figure 3.14**). The raw ITC thermograms for the metal-peptide titrations are compared against the metal-buffer titrations. The Mg^{2+} vs. buffer titration showed exothermic peaks. These peaks were significantly diminished in the Mg^{2+} vs. DDDD peptide titration, implying a weak interaction at pH 7. The Li^+ vs. buffer and Li^+ vs. DDDD peptides yielded similar peaks, demonstrating no binding.

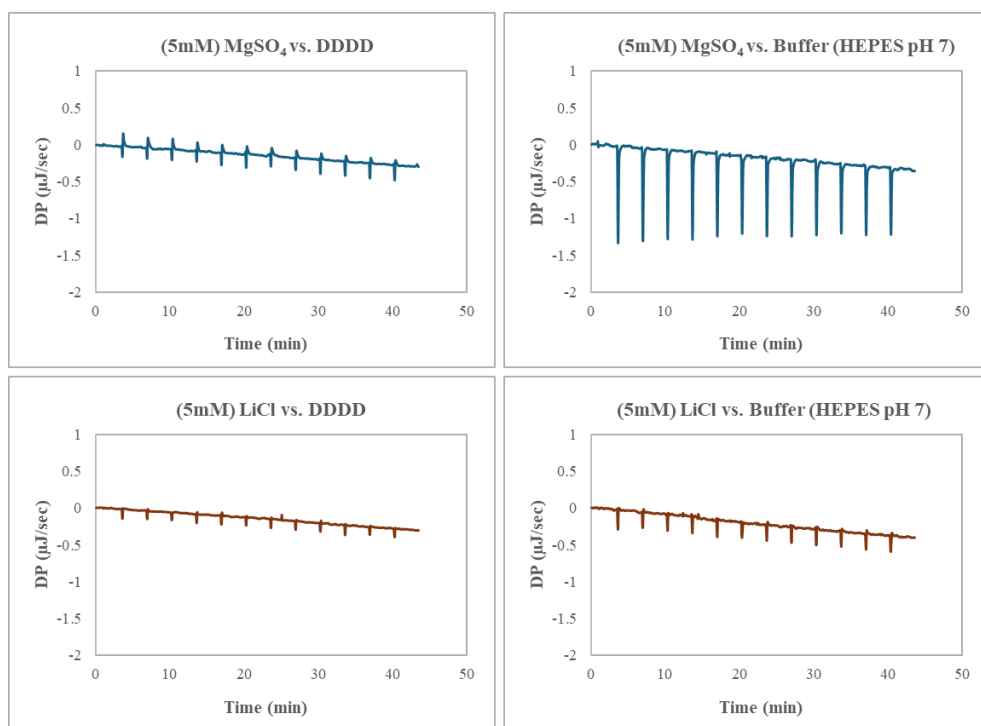


Figure 3.14: ITC Binding for Mg^{2+} and Li^+ vs. DDDD Peptide at pH 7. (Top panel) The raw ITC thermograms for 5mM MgSO_4 vs. DDDD peptide and metal vs. buffer titrations in 100mM HEPES pH 7.0. (Bottom panel) The raw ITC thermograms for 5mM LiCl vs. DDDD peptide and metal vs. buffer titrations in 100mM HEPES pH 7.0.

The interaction between Be^{2+} and the carboxylate groups in the peptides was further explored using peptides with various D residues. The raw ITC thermograms for the Be^{2+} interaction with peptides DDDD, GDDD, and GGDD were compared (**Figure 3.15**). Be^{2+} showed a binding interaction, with each endothermic peak gradually decreasing as the peptide was getting saturated for the DDDD peptide. The titration against the GGDD peptide resembles the Be^{2+} vs. buffer thermogram. The titration against the GDDD peptide is not identical to the titrant vs. buffer control; however, a binding behavior is not observed. The small endothermic peaks typically observed in the first few injections for Be^{2+} mixing with the buffer are not observed in the titration against the GDDD peptide, indicating there must be weak binding occurring. However, the binding is not strong enough to show binding.

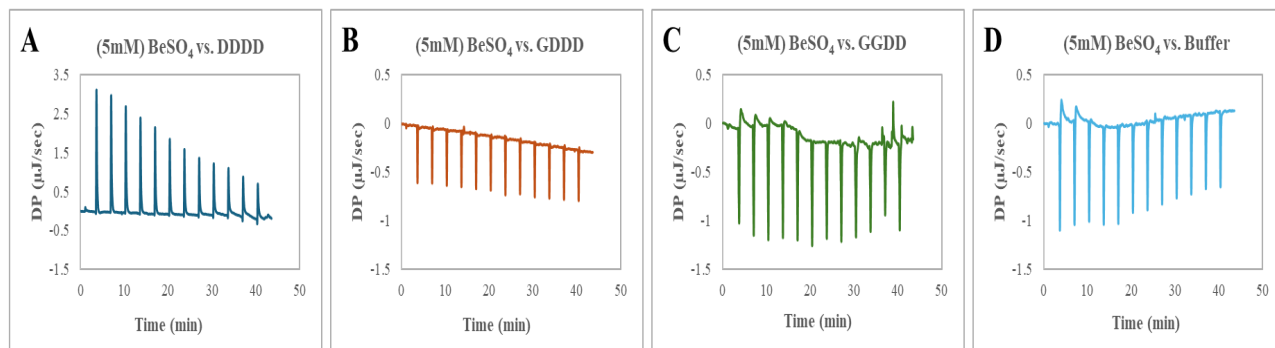


Figure 3.15: ITC Binding for Be^{2+} vs. Tetrapeptides with Varying Number of Aspartic Acid (D) Residues. The raw ITC thermograms shown for 5mM BeSO_4 vs. (A) DDDD peptide (B) GDDD peptide (C) GGDD peptide (D) buffer. All titrations followed in 100mM MES pH 5.80.

Since carboxylate groups are featured in Glutamic acid residues (E), Be^{2+} was titrated against an EEEE peptide to observe binding (**Figure 3.16**). Interestingly, despite Be^{2+} being capable of forming strong interactions with carboxylate oxygens, only a weak interaction was

detected between Be^{2+} and EEEE under conditions comparable to the DDDD titrations. The observed variation in the binding affinity of Be^{2+} towards DDDD versus EEEE peptides likely stems from the structural disposition of the carboxyl groups in these peptides. The side chain of aspartic acid, which is one carbon shorter than that of glutamic acid, positions its carboxyl group closer to the peptide backbone, potentially allowing for a more structured and rigid arrangement that can more effectively coordinate with Be^{2+} ions. This shorter side chain facilitates a closer and more defined spatial arrangement that aligns well with the geometric requirements for optimal Be^{2+} coordination, which prefers tetrahedral structures. In contrast, the longer side chain of glutamic acid in the EEEE peptide introduces additional flexibility, making the carboxyl groups less geometrically favorable for binding with Be^{2+} . This results in weaker interactions as the extended side chains provide a less structured environment, thereby diminishing the effective coordination with the metal ion.

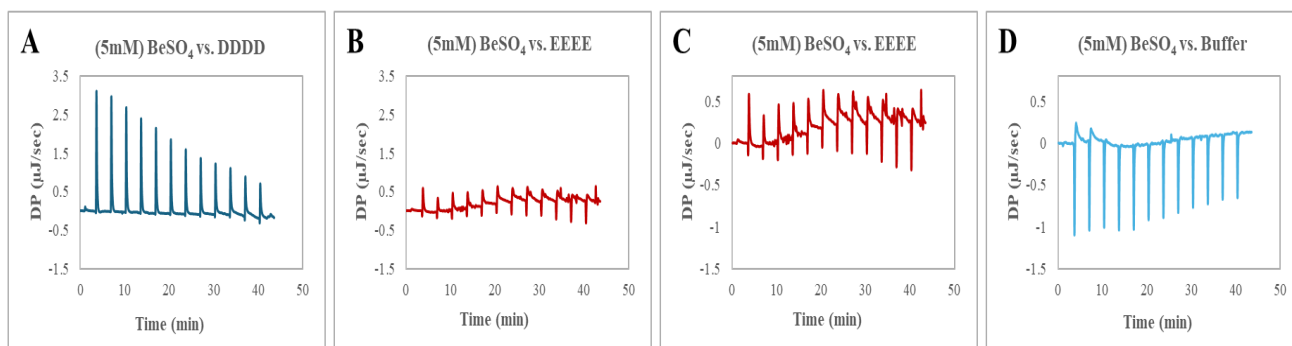


Figure 3.16: ITC Binding for Be^{2+} vs. Tetrapeptides with Aspartic Acid (D) or Glutamic Acid (E) Residues. The raw ITC thermograms for 5mM BeSO_4 vs. (A) DDDD peptide (B) EEEE peptide for titrations followed in 100mM MES pH 5.80. (C) Thermogram for BeSO_4 vs. EEEE shown on a scale comparable to that of (D) BeSO_4 vs. buffer control to compare the nature of the peaks.

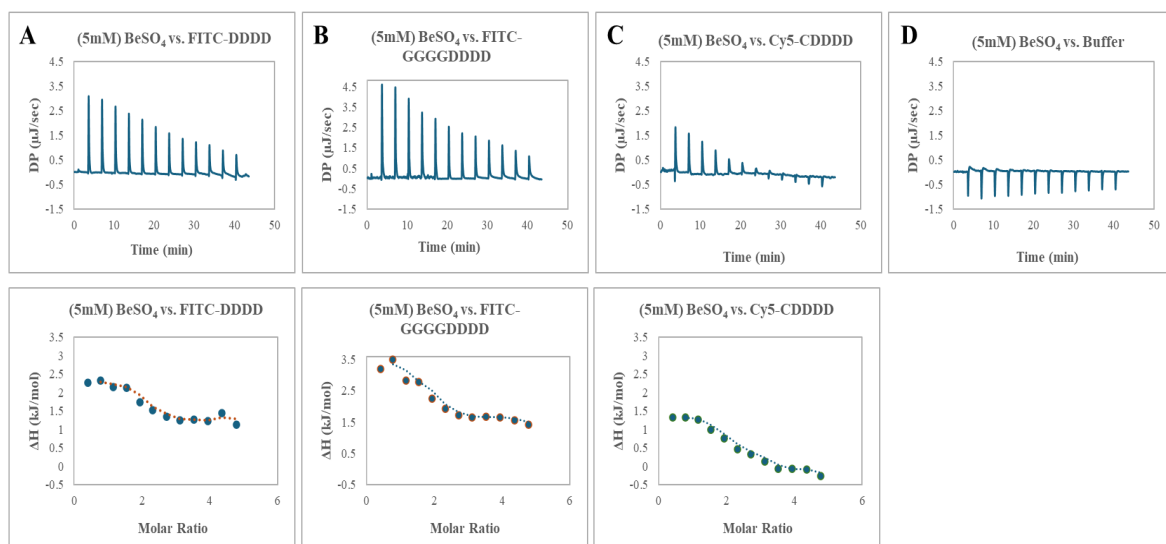


Figure 3.17: ITC Binding for Be^{2+} vs. Various DDDD Peptides. The raw ITC thermograms for 5mM BeSO_4 vs. (A) FITC-DDDD peptide, (B) FITC-GGGGDDDD peptide, (C) Cy5-CDDDD and (D) Buffer. All titrations followed in 100mM MES pH 5.80.

The binding reaction between Be^{2+} and DDDD was analyzed for several different DDDD peptides: FITC-DDDD, FITC-GGGGDDDD, and Cy5-DDDD (**Figure 3.17**). The reason for using peptides with a different fluorescence tag or a spacer between the fluorescence tag is explained under MST results. All peptides displayed binding, showing that the fluorescence tag is not involved in the binding interaction. The different fluorescence tags may affect the heat of dilution, which would explain the slightly different peak sizes. All DDDD peptides showed an endothermic reaction, and the stoichiometry obtained from the integrated heat vs. molar ratio plots was close to 2 (**Table 3.6**). This result indicated that two Be^{2+} ions are coordinated to one DDDD peptide. Be^{2+} ions, with their small ionic radius and +2 charge, exhibit a high charge density that favors tetrahedral coordination geometry due to their electronic configuration and

size. This specific geometry involves the ion seeking four donor atoms, ideally positioning them to form a tetrahedral shape around the metal. In the case of the DDDD peptide, composed of four aspartic acid residues, each residue contributes a carboxylate group that can interact with Be^{2+} . The linear arrangement of these residues affords the peptide a degree of flexibility in how the carboxylate groups are presented to the metal ions.

Table 3.6: Stoichiometry for BeSO_4 vs. DDDD Binding. The stoichiometry for Be^{2+} and DDDD binding was obtained from the titration of various peptides, including DDDD with a FITC tag or Cy5 tag at the N-terminus or a GGGG spacer between the FITC tag and the DDDD sequence. All ITC experiments yielded a binding curve; the average stoichiometry was 1.76 (~ 2)

Run#	Peptide	N (sites)
R1581	FITC-DDDD	1.78 ± 0.095
R1710	FITC-GGGGDDDD	1.66 ± 0.125
R1712	Cy5-CDDDD	2.18 ± 0.099
R1714	FITC-GGGGDDDD	1.32 ± 0.093
R2360	FITC-DDDD	1.88 ± 0.095

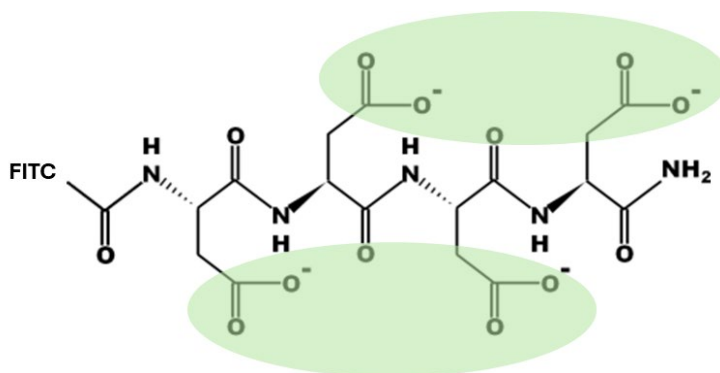


Figure 3:18: Model of Be^{2+} Coordination with DDDD Peptide: This illustration shows that carboxylate groups from alternating aspartic acid residues could potentially coordinate the Be^{2+} ion in a tetrahedral geometry.

If two Be^{2+} ions bind to the DDDD peptide, a likely coordination mode would see each ion interacting with two carboxylates from alternate aspartic acids. This arrangement optimizes the spatial orientation necessary for tetrahedral coordination and might require the peptide to flex or rotate slightly to accommodate the preferred geometry. Such an orientation would allow Be^{2+} ions to form a stable tetrahedral complex with the peptide (**Figure 3.18**). The notable increase in entropy observed for the Be^{2+} vs. DDDD ITC binding experiments can be linked to the displacement of water molecules originally solvating both the carboxylate groups and the Be^{2+} ions. The released water molecules increase the system's disorder as the Be^{2+} ions bind to the carboxylates. Furthermore, the inherent flexibility of the peptide backbone likely aids in making the necessary conformational adjustments, allowing two alternate carboxylates to coordinate each Be^{2+} ion effectively. This flexibility is crucial for aligning the donor atoms into the tetrahedral geometry preferred by Be^{2+} .

The results of this ITC binding study demonstrated that Be^{2+} ions show a higher affinity towards carboxylate-rich groups than Mg^{2+} or Li^+ ions. The results also showed that Be^{2+} can occupy structured binding sites, likely due to its small ionic size and preference for tetrahedral coordination. Also, its high charge density compared to Mg^{2+} or Li^+ ions allows Be^{2+} to form strong electrostatic interactions with carboxylate groups.

Be^{2+} could compete for both of the Mg^{2+} binding sites on GSK3 β , while Li^+ could compete for only one of the Mg^{2+} binding sites (Ryves et al., 2002). Computational studies showed Li^+ can not approach the less solvated Mg^{2+} binding site on GSK3 β (Dudev & Lim, 2011). The results of this study support these prior observations and the higher potency of Be^{2+} ion-induced inhibition of GSK3 β relative to that of Li^+ ions. Since the Mg^{2+} binding sites on GSK3 β feature aspartic acid residues (Asp181 and Asp200), and because Be^{2+} ions have a higher

affinity for carboxylate groups and prefer a tetrahedral geometry and are typically less solvated, it suggests that Be^{2+} ions can occupy both solvated and non-solvated Mg^{2+} binding sites of GSK3 β .

MicroScale Thermophoresis (MST) Results

This study aimed to complement the observations from the ITC binding experiments by investigating the interactions between Be^{2+} and Mg^{2+} with various fluorescently labeled peptides using MST. In order to utilize the thermophoretic properties of the molecules to detect binding, the fluorescence of each sample before applying the thermal gradient should be uniform ($\pm 10\%$). The initial fluorescence of the FITC-DDDD peptide decreased with increasing BeSO_4 concentrations (**Figure 3.19**). Therefore, the binding of Be^{2+} vs. FITC-DDDD was analyzed based on initial fluorescence change against ligand concentration. In contrast, MgSO_4 exhibited uniform initial fluorescence across the samples and could be analyzed via thermophoresis. The F_{norm} (%) plotted against the Mg^{2+} concentrations indicated minimal to no binding (**Figure 3.19**). The initial fluorescence scans for BeSO_4 and MgSO_4 vs. FITC-GGGG peptide did not fluctuate with the ligand concentration, and therefore, the respective samples could be analyzed via thermophoresis. The change in F_{norm} (%) with ligand concentration was minimal for both metal ions, showing no binding with FITC-GGGG (**Figure 3.20**).

The initial fluorescence scans for MgSO_4 vs. FITC-KKKK peptide did not fluctuate with the ligand concentration, and therefore, the respective samples could be analyzed via thermophoresis. The change in F_{norm} (%) with ligand concentration was minimal for both metal ions, showing no binding with FITC-GGGG (**Figure 3.20**). An unexpected increase in initial

fluorescence was observed with increasing BeSO₄ concentration for the FITC-KKKK peptide (**Figure 3.21**). The initial fluorescence for FITC-KKKK was uniform across the MgSO₄ samples except for the two capillaries with the highest ligand concentration, and thermophoretic analysis for Mg²⁺ vs. FITC-KKKK showed no binding (**Figure 3.21**). The increase in initial fluorescence with increasing BeSO₄ concentration (and to a slight degree with increasing MgSO₄ concentration) was hypothesized due to charge repulsion effects. The KKKK peptide, rich in lysine residues, carries a positive charge at physiological and slightly acidic pH levels due to the amino group on the side chain of lysine. When BeSO₄ is introduced, the Be²⁺ ions being highly charged might cause electrostatic repulsion against positively charged amino groups, which could alter the environment around the FITC tag and potentially lead to changes in fluorescence emission. This effect was mitigated by increasing the ionic strength in the buffer with NaCl, effectively counteracting the increase in BeSO₄-induced fluorescence (**Figure 3.22**). This confirms that the initial fluorescence changes were primarily driven by electrostatic interactions rather than specific binding events.

The introduction of a GGGG spacer in the FITC-GGGGDDDD peptide did not prevent the BeSO₄-induced decrease in initial fluorescence, indicating that the primary factor affecting fluorescence was not spatial separation but the direct interaction of Be²⁺ with D (**Figure 3.23**). Replacing the FITC tag with a Cy5 tag to see whether FITC is particularly sensitive to this phenomenon showed that the BeSO₄-induced decrease in initial fluorescence persisted (Data not shown), again showing the change in initial fluorescence is due to binding between Be²⁺ and D residues. This was further supported by different patterns observed in FITC-DDDD, FITC-GDDD, and FITC-GGDD peptides (**Figure 3.24**). The experiments in **Figure 3.24** were performed in 100mM Bis-TRIS pH 5.5, and an increase in initial fluorescence was observed for

FITC-DDDD with increasing BeSO_4 concentration. Binding curves were derived from the change in initial fluorescence vs. ligand concentration. The strongest binding and most significant fluorescence changes were associated with the highest density of D residues (as in FITC-DDDD), confirming that the number of carboxylate groups directly influences Be^{2+} binding affinity.

The MST results complement the observations from the ITC experiments demonstrating that Be^{2+} has a strong preference for binding to carboxylate groups in peptides. Be^{2+} can form complexes primarily with peptides that offer multiple carboxylate groups, such as DDDD, and this binding capability decreases with fewer D residues (**Figure 3.24**). However, the MST experiments between Be^{2+} and these model peptides were highly sensitive to slight pH changes, buffer composition, and ionic strength, making it difficult to obtain reliable binding parameters. Additionally, the thermophoretic function of MST could not be applied for Be^{2+} vs. DDDD experiments due to the dramatic change in initial fluorescence induced by BeSO_4 concentration. These observations also show that MST experiments utilizing thermophoresis function can be technically challenging due to the sensitivity of fluorescent tags to various factors such as binding environment, pH, buffer composition, and ionic strength, limiting their successful application across all experimental contexts.

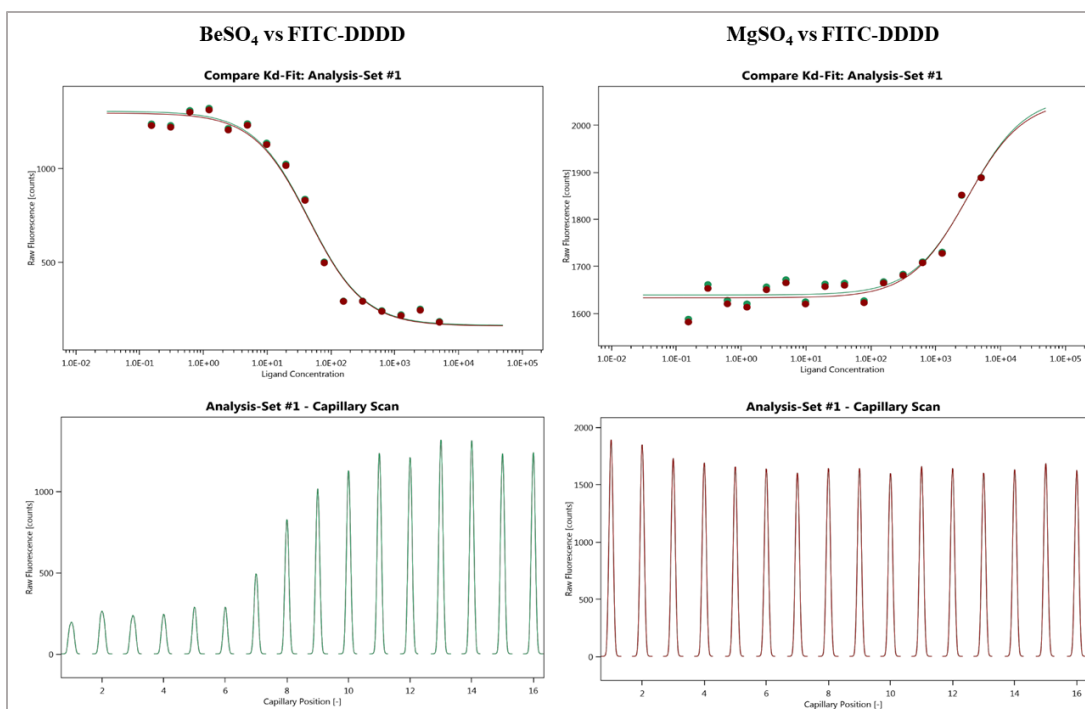


Figure 3.19: MST Binding for Be^{2+} vs. Mg^{2+} Against FITC-DDDD. BeSO_4 and MgSO_4 were diluted 1:1 in 16 samples with 5mM as the highest concentration and mixed with a final concentration of $0.75\mu\text{M}$ FITC-DDDD in 100mM MES pH 6.0. The samples were loaded onto 16 capillaries and analyzed in the MST at room temperature. The bottom panels show the Capillary scan at various ligand concentrations. The initial fluorescence for FITC-DDDD decreases with the ligand concentration for BeSO_4 , while the initial fluorescence is generally uniform across the samples with MgSO_4 . The top left panel shows the binding curve by fitting the initial fluorescence change with the BeSO_4 concentration. The top right panel shows the thermophoresis data ($F_{\text{norm}} \%$) plotted against the MgSO_4 concentration.

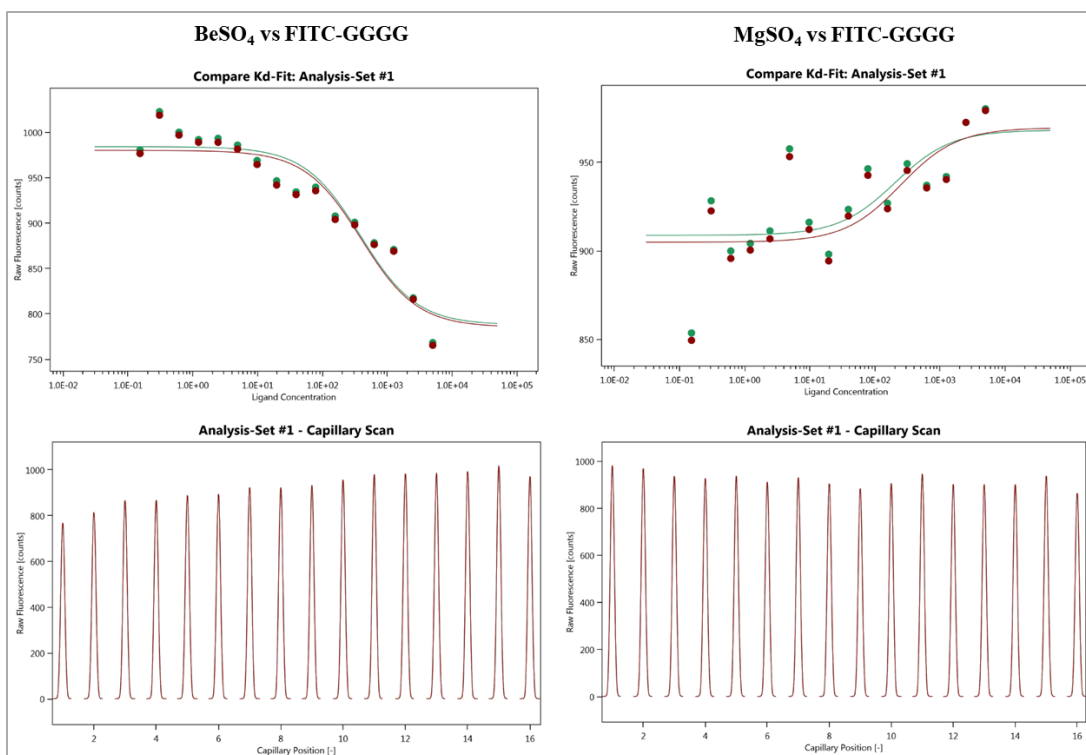


Figure 3.20: MST Binding for Be²⁺ vs. Mg²⁺ Against FITC-GGGG. BeSO₄ and MgSO₄ were diluted 1:1 in 16 samples with 5mM as the highest concentration and mixed with a final concentration of 0.75μM FITC-GGGG in 100mM MES pH 6.0 + 5% DMSO. The samples were loaded onto 16 capillaries and analyzed in the MST at room temperature. The bottom panels show the Capillary scan at various ligand concentrations. The initial fluorescence for FITC-GGGG is generally uniform across the samples with BeSO₄ and MgSO₄. The top panels show the thermophoresis data as a function of ligand concentration. They show subtle differences in F_{norm} % and do not fit the binding model.

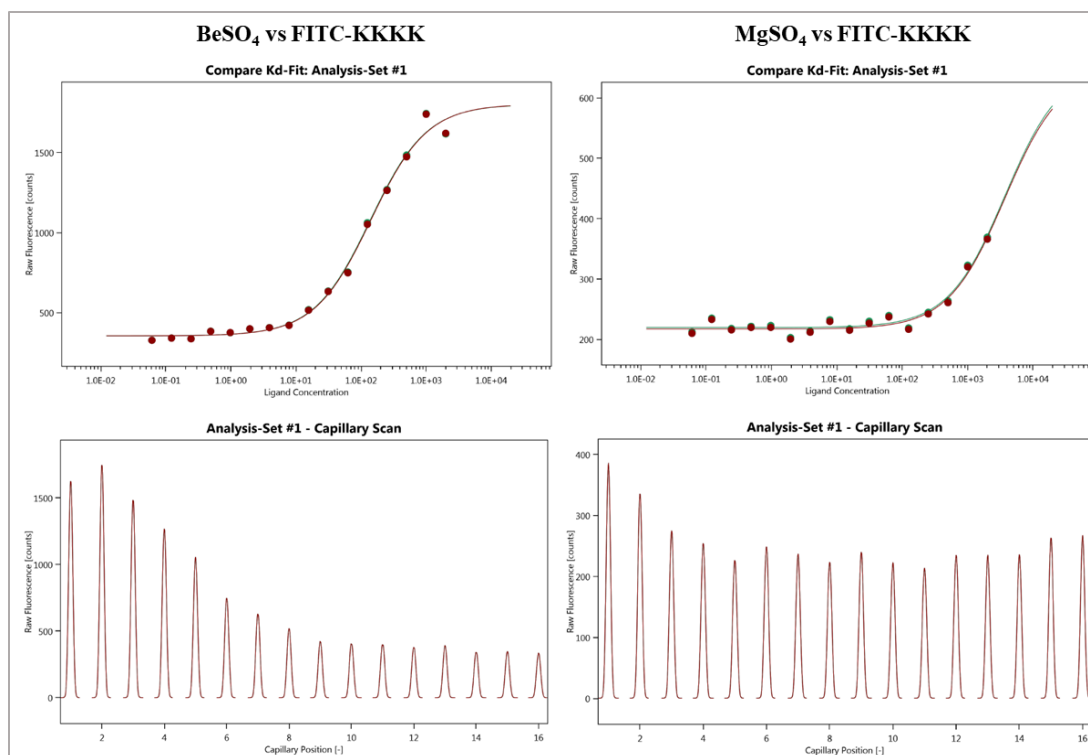


Figure 3.21: MST Binding for Be^{2+} vs. Mg^{2+} Against FITC-KKKK. BeSO_4 and MgSO_4 were diluted 1:1 in 16 samples with 5mM as the highest concentration and mixed with a final concentration of $2\mu\text{M}$ FITC-KKKK in 100mM MES pH 6.0. The samples were loaded onto 16 capillaries and analyzed in the MST at room temperature. The bottom panels show the Capillary scan at various ligand concentrations. The initial fluorescence for FITC-KKKK increases with the ligand concentration for BeSO_4 , while the initial fluorescence is relatively uniform across the samples with MgSO_4 . The top left panel shows the binding curve by fitting the initial fluorescence change with the BeSO_4 concentration. The top right panel shows the thermophoresis data ($F_{\text{norm}} \%$) plotted against the MgSO_4 concentration.

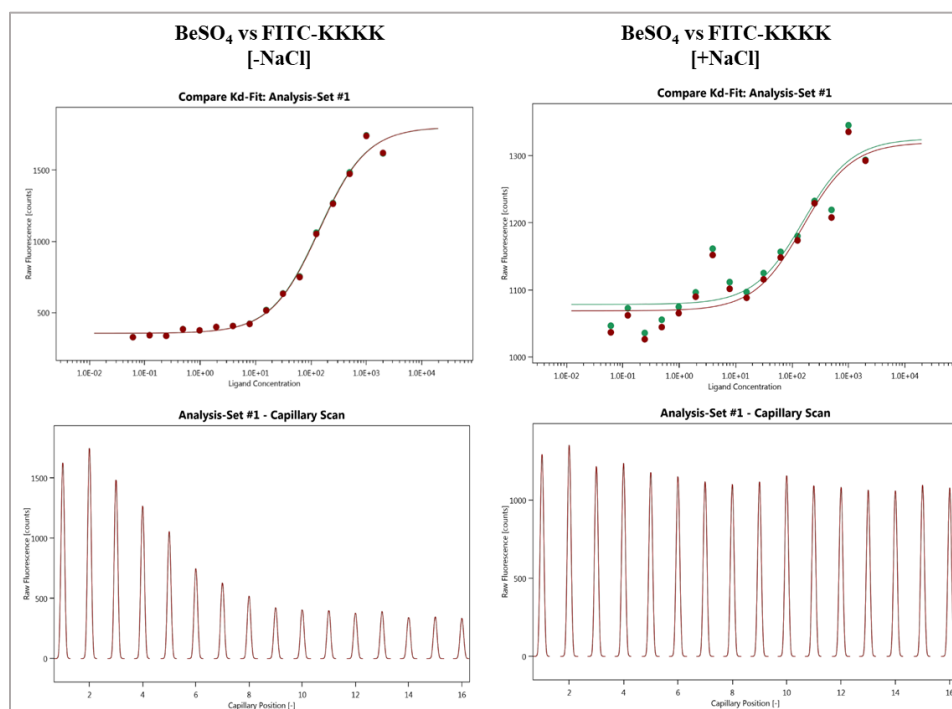


Figure 3.22: Increasing Ionic Strength Counteracts BeSO₄-Induced FITC-KKKK Fluorescence Increase: BeSO₄ was diluted 1:1 in 16 samples with 5mM as the highest concentration and mixed with a final concentration of 2μM FITC-KKKK in 100mM MES pH 6.0 with or without 100mM NaCl. The samples were loaded onto 16 capillaries and analyzed in the MST at room temperature. The left panels show a BeSO₄-induced increase in the initial fluorescence of FITC-KKKK. The right panels show that increasing the ionic strength of the solution by adding NaCl counteracts the BeSO₄-induced increase in FITC-KKKK initial fluorescence. The top right panel shows the thermophoresis data plotted against the BeSO₄ concentration, with minimal change in F_{norm} %.

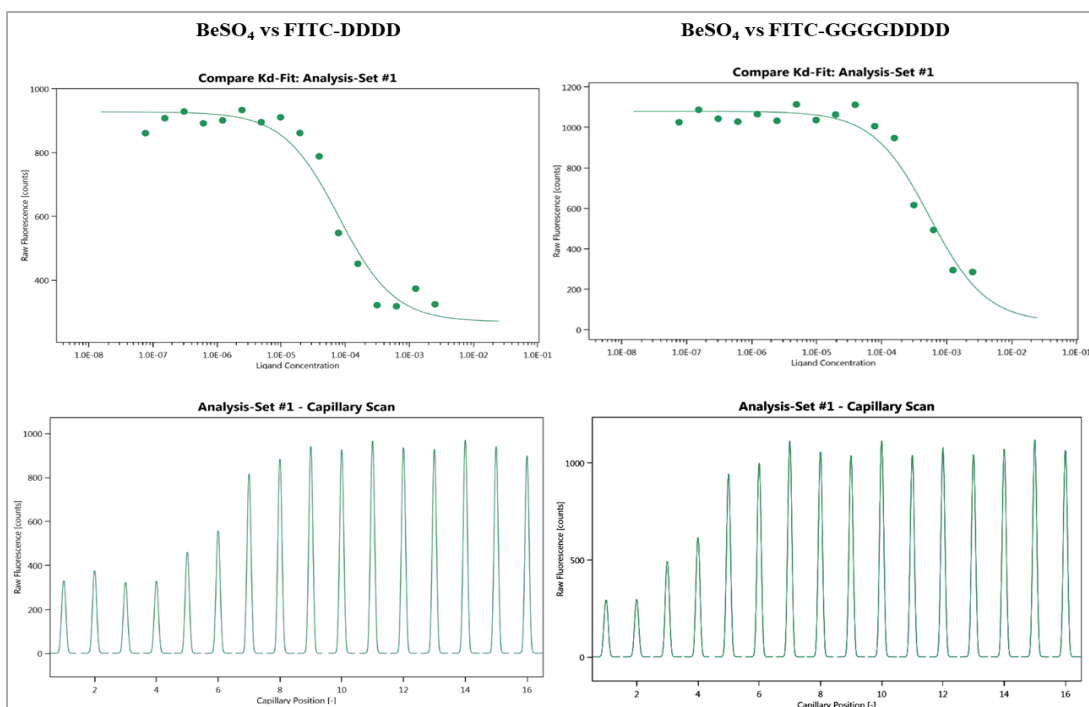


Figure 3.23: MST Binding for Be²⁺ vs. FITC-DDDD and FITC-GGGGDDDD. BeSO₄ was diluted 1:1 in 16 samples with 2.5mM as the highest concentration and mixed with a final concentration of 1μM FITC-DDDD or 0.4μM FITC-GGGGDDDD in 100mM MES pH 5.7 and 5% DMSO (I =0.1M). The samples were loaded onto 16 capillaries and analyzed in the MST at room temperature. The bottom panels show the BeSO₄-induced decrease in the initial fluorescence of FITC-DDDD and FITC-GGGGDDDD. The top panels show the binding curve by fitting the initial fluorescence change with the BeSO₄ concentration.

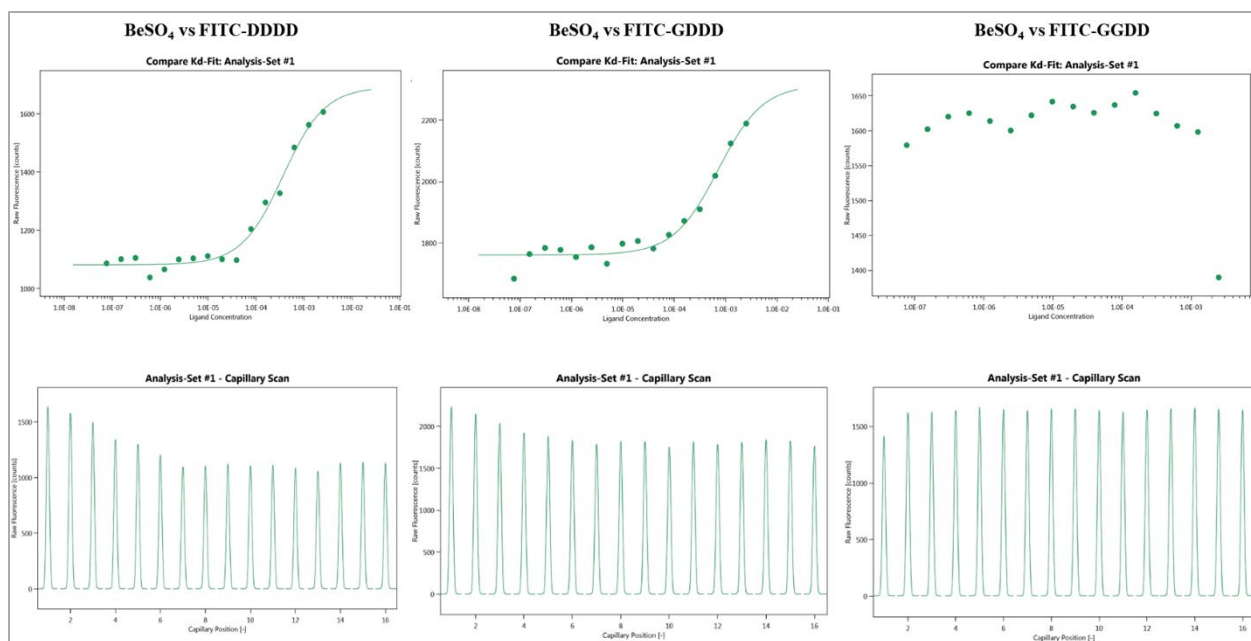


Figure 3.24: MST Binding for Be^{2+} vs. Various Tetrapeptides. BeSO_4 was diluted 1:1 in 16 samples with 2.5mM as the highest concentration and mixed with a final concentration of 0.4 μM FITC-DDDD, 0.8 μM FITC-GDDD or 0.4 μM FITC-GGDD in 100mM Bis-TRIS pH 5.5 and 1% DMSO ($I=0.1\text{M}$). The samples were loaded onto 16 capillaries and analyzed in the MST at room temperature. The binding curves were obtained by fitting the thermophoretic data across BeSO_4 concentrations for FITC-DDDD (Left panel), FITC-GDDD (Middle panel), and FITC-GGDD (Right panel).

Chapter 4: Expression and Purification of Full-length Human GSK3 β for Isothermal Titration Calorimetry Experiments

Introduction

Glycogen Synthase Kinase 3 (GSK3), a serine/threonine kinase, originally identified for its role in glycogen synthesis regulation, has emerged as a critical player in various cellular processes affecting development, metabolism and disease pathology through its involvement in multiple signaling pathways such as insulin, Wnt/ β -catenin, and Hedgehog. Existing in two isoforms, GSK3 α and GSK3 β , it displays high sequence homology and is characterized by sophisticated regulatory mechanisms that include phosphorylation and control through substrate pre-phosphorylation. GSK3's dysregulation is linked to numerous diseases, including diabetes, neurological disorders, and cancer, positioning it as a key target for therapeutic interventions. Notably, lithium, a classical mood stabilizer approved for treating bipolar disorder, inhibits GSK3 and has shown promise in mitigating Alzheimer's disease symptoms in animal models by affecting tau protein phosphorylation and amyloid-beta levels. Recent research has also explored beryllium as a more potent GSK3 inhibitor, suggesting potential for investigating more selective and enhanced modes for GSK3 inhibition. Our study aimed to investigate GSK3's interactions using Isothermal Titration Calorimetry (ITC) to study both GSK3 ligand binding and kinase activity. This method allows for precise measurement of binding constants, enzyme kinetics, and thermodynamics of interactions, offering valuable insights into the molecular mechanisms by which ligands like lithium and beryllium inhibit GSK3 (Beurel et al., 2015; Frame & Cohen, 2001; Kaidanovich-Beilin & Woodgett, 2011).

Our laboratory has predominantly focused on cell-based studies of GSK3 β rather than GSK3 α because more extensive research and a wide range of experimental tools are available for GSK3 β compared to GSK3 α . Therefore, we endeavored to express and purify recombinant GSK3 β for Isothermal Titration Calorimetry (ITC) experiments. Expressing and purifying GSK3 β is crucial for studying its interaction with substrates and inhibitors in ITC. Purified GSK3 β allows for precise measurement of binding affinities and thermodynamic parameters using ITC, providing insight into the enzyme's regulation and potential therapeutic targeting. This specificity is essential for identifying how GSK3 β interacts with various molecules, which can lead to the development of selective inhibitors with clinical applications.

Having a less pure protein sample for ITC studies can introduce several challenges. Impurities can contribute to non-specific binding, altering the heat signal and leading to inaccurate measurements of binding constants and kinetic parameters. Additionally, contaminants might compete with the intended interaction, affecting the data. These factors can obscure the accurate binding profile between GSK3 β and its substrates or inhibitors, making it challenging to derive precise mechanistic insights and potentially leading to erroneous conclusions about the protein's function or inhibition.

Traditional GSK3 β studies predominantly utilized immunoassays or kinase activity assays requiring minimal protein quantities. ITC necessitates considerably more significant amounts of protein to study the binding and kinetic interactions of GSK3 β with substrates and inhibitors, such as lithium and beryllium. This is because ITC measures the heat released or absorbed when molecules interact, and to generate a sufficient heat signal, we would need higher concentrations of the binding partners. This distinction underscores the necessity for expressing and purifying GSK3 β in high quantities. Previous efforts to express and purify GSK3 β have

varied widely, ranging from bacterial expression systems to more complex mammalian and insect cell-based expressions, each with its inherent challenges and advantages:

Bacterial Expression Systems: GSK3 β has been successfully expressed in *E. coli* and purified for use in kinase activity assays against specific substrates, indicating the potential for high-yield protein production but often resulting in protein folding issues and inclusion body formation (Klein & Melton, 1996; Murai et al., 1996; Primot et al., 2000; Q. M. Wang et al., 1994).

Mammalian Expression Systems: Using mammalian cell lines for expressing human GSK3 β tagged with epitopes, such as HA and Myc, facilitates post-translational modifications and proper folding. These systems have been utilized for immunoprecipitation and subsequent kinase activity assays (Hagen et al., 2002; Mudireddy et al., 2014; Tejeda-Muñoz et al., 2016).

However, mammalian cells grow slower than prokaryotic cells and often have lower protein yields, extending the duration of experiments and increasing the cost, especially when a large quantity of protein is required.

Insect Cell Expression Systems: The Bac-to-Bac baculovirus expression system has been employed for expressing GSK3 β . It offers an advantage regarding post-translational modifications and functional protein yield, albeit with potentially increased complexity and cost.

Across these methods, challenges such as achieving high yield, maintaining protein solubility and activity, and the complexity of purification protocols are recurrent themes. The purification processes often involve affinity chromatography, ion exchange, and size exclusion steps, each requiring optimization to ensure high purity and functionality of GSK3 β (Dajani et al., 2001; Kim et al., 2015). Notably, Wang and Young et al. (2016) reported the use of ITC to screen synthetic drugs against GSK3 β , highlighting the significant quantities of purified protein

required for ITC experiments (Y. Wang et al., 2016). This underscores the critical need for efficient and scalable protein expression and purification methods to meet the demands of ITC studies.

In summary, the expression and purification of GSK3 β for ITC analysis presents a unique set of challenges that demand a comprehensive understanding of previous methods and their limitations. Selecting an expression system and purification strategy is crucial to producing GSK3 β in sufficient quantity and purity to facilitate detailed analyses of its interactions with substrates and inhibitors. This research contributes to this field by addressing these challenges, aiming to provide new insights into GSK3 β 's role and interactions that surpass what has been achievable through more conventional biochemical assays.

Materials and Methods

Materials

Reagents used for bacterial expression included Luria-Bertani (LB) broth (Sigma #L7658) and LB Agar (Sigma #L7533) for bacterial cell culture, Ampicillin (Sigma-Aldrich #A9518) and Chloramphenicol (Sigma #C7795) for antibiotic selection, and Isopropyl β -D-1-thiogalactopyranoside (IPTG) (VWR Life Sciences #N679) for inducing protein expression under the control of the lac operator.

Reagents used for insect cell culture work included ESF 921 (Expression Systems #96-001-01), Gibco sf-900 III SFM (Gibco #12658-019) as cell culture media, FBS to supplement ESF 921 media, and Geneticin (Gibco #11811-023) for antibiotic selection of Sf9-ET cells.

Cell lines for insect cell culture: Sf9-ET (CRL-3357) was purchased from ATCC, and Sf9 cells were purchased from ATCC/Expression Systems/Millipore Sigma. Collaborators Dr. Gary Kleiger and Dr. Chutima Rattanasopa of the University of Nevada, Las Vegas, shared Sf9 and Hi5 cells used in later protein preparation work.

Reagents used to prepare buffers for cell lysis and protein purification included TRIS Base (J.T. Baker #4099-02), HCl (Sigma #920-1), NaCl (Amresco #0241), EDTA (Sigma #ED2SS), 100x Protease and Phosphatase inhibitor cocktail (Thermo Scientific #78442) or 100x Protease inhibitor cocktail (Abcam #ab271306), PMSF (OmniPur #7110), NP-40 (Fluka #74385), Triton x-100 (Sigma #T9284), Lysozyme (Sigma #L-7651), Glycerol (Sigma #G-6279), PEI 50% (w/v) solution in H₂O (Supleco #P3143), HEPES (Sigma #H3375), DTT (Roche Diagnostics #10197777001), β -Mercaptoethanol (OmniPur #6010), Reduced L-Glutathione (Sigma-Aldrich #G4251). Glutathione dry beads (Sigma #G4510) were used to prepare Glutathione slurries for batch-bead purification of Glutathione fusion proteins. GSTrap 4B (GE Healthcare #28-4017-47) and HiTrap SP XL (Cytiva #17516001) 1mL columns were used for affinity and ion-exchange purification on FPLC. His-Bind buffer kit (Novagen #69755-1) was used to remove His tagged TEV from GSK3 β protein samples following ion-exchange purification.

SDS-PAGE analysis of protein purification was followed on NuPAGE 4-12% Bis-TRIS gels (Invitrogen NP0322) with NuPAGE MES 1x SDS running buffer (Invitrogen NP0002) or homemade 10-12% TRIS-based gels with TRIS-Glycine 1x running buffer. Page Ruler Pre-Stained Protein Ladder (Thermo Scientific #815-968-0747) was used as the molecular marker. The gels were stained with Coomassie SimplyBlue Safe Stain (Invitrogen #465034) according to manufacturer protocol. Purified protein samples were quantified using a Qubit Protein Assay kit

(Invitrogen #Q33211) or Pierce BCA Protein Assay kit (Thermo Scientific #23225).

Bacterial Expression in BL21-CodonPlus E. coli

A pGEX-4T-3 vector cloned with human GSK3 β variant 2 (420 amino acids) was obtained from AddGene (Plasmid #15898) and transformed into BL21-Gold (DE3) *E. coli* to produce a GST-GSK3 β fusion protein with an N-terminal GST tag. The sequence was confirmed by UNLV Genomics Core using pGEX primers. An unmodified vector expressing plain GST was a negative control for GST-fusion proteins. The *E. coli* expressing GST-GSK3 β was cultured overnight in LB broth with Ampicillin at 34 °C, and the plasmid was isolated using Wizard Plus SV Minipreps (Promega #A1330), with quantification by Nanodrop. Following Agilent Technologies guidelines, the plasmid was re-transformed into BL21-CodonPlus (DE3)-RIPL *E. coli* (#230280), plated on LB Agar with Ampicillin and Chloramphenicol, and two single colonies were selected, cultured, and stored as glycerol stocks at -80 °C.

Overnight cultures of *E. coli* strains for GST, GST-GSK3 β (BL21-Gold), and GST-GSK3 β (BL21-CodonPlus) were grown at 34 °C in LB supplemented with respective antibiotics (0.1mg/mL Ampicillin and 50 μ g/mL Chloramphenicol). Each culture was expanded by inoculating 50mL fresh LB supplemented with antibiotics as earlier and allowed to grow at 34 °C or 37 °C shaker for 3h (~ 0.6 O.D.). IPTG was added to the cultures at a 0.1mM final concentration to induce protein expression and harvested after incubating the cultures for 4h. To analyze, each pellet was lysed on ice for 30 min with lysis buffer (50mM TRIS pH 8, 50mM NaCl, 1mM EDTA, 1x Lysozyme, 1x Protease inhibitor cocktail, 1x PMSF, and 1% NP-40) and sonicated at 0.5 power setting for 15 sec (Misonix sonicator 3000). Each lysate was centrifuged at 4 °C and 10,000 rpm for 10 minutes to remove crude debris and at 12,500 rpm for 10 minutes

to obtain a clarified lysate. Each lysate was incubated and rotated for 2 h at 4 °C with 40% Glutathione bead slurry. The beads were rinsed with cold wash buffer (50mM TRIS pH 8, 50mM NaCl, 1mM EDTA, and 1% NP-40) and eluted with Glutathione elution buffer (10mM GSH, 50mM TRIS pH 8, 50mM NaCl). The eluted protein fractions, respective soluble lysates (input), and unbound lysates were analyzed on SDS-PAGE.

Protein Expression in Sf9 Cells via Baculovirus Expression System

P2 baculovirus stock:

GenScript prepared a P2 baculovirus stock to express human GSK3 β isoform 1, N-GST. The human GSK3 β isoform 1 cDNA was synthesized and subcloned into a pFastBacGST expression vector. This vector was transformed into a DH10Bac strain to generate a recombinant bacmid. Using PCR, the positive recombinant bacmid containing human GSK3 β isoform 1 was confirmed. Sf9 cells were transfected with the recombinant bacmid, and the supernatant collected was designated as P1 viral stock. P2 viral stock was generated using P1 to verify protein expression. SDS-PAGE and Western Blot confirmed the expression of GST-GSK3 β . The estimated titer for the P2 baculovirus stock received from GenScript was 3.35×10^8 PFU/mL.

Fluorescence microscopy method using Sf9-ET reporter cell line:

Sf9-ET cells were cultured in ESF 921 medium supplemented with 10% FBS and 50 μ g/mL Geneticin in T75 flasks at 27 °C. After the cultures reached 60-80% confluency, the cells were treated with 0.25% Trypsin and suspended in ESF 921 medium. 0.1mL of the cell

suspension was mixed with 9.9mL of isotone II solution, and the cell numbers were measured on the Beckman Coulter Particle Counter. The estimated cell density was used to determine the approximate number of Sf9-ET cells to seed in T75 flasks. After adding the desired volume of cell stock each to 3 x T75 flasks, the volume was brought up to 25mL with ESF 921 medium supplemented with 10% FBS and 50 µg/mL Geneticin. To test the Sf9-ET cells for eGFP expression upon infection with the P2 virus, the three prepared Sf9-ET cultures were treated with an M.O.I (Multiplicity of Infection) of 0, 0.1, or 1 and incubated for 72h at 27 °C. The cells were harvested and analyzed via flow cytometry for eGFP expression.

The following demonstrates calculating the baculovirus stock volume added to an Sf9-ET culture according to the M.O.I. of choice.

Titer of 1:2 diluted P2 baculovirus stock = 3.35×10^7 PFU/mL

Cells added in each T75 flask = 6.7×10^6 cells

$$M.O.I = \frac{\text{infectious baculovirus particles}}{\text{number of cells}}$$

To infect the Sf9-ET cells in the above T75 flask with an M.O.I of 1

$$1 = \frac{\text{infectious baculovirus particles (PFU)}}{6.7 \times 10^6 \text{ cells}}$$

$$\text{infectious baculovirus particles} = 6.7 \times 10^6 \text{ PFU}$$

$$\text{Volume of P2 stock} = \frac{6.7 \times 10^6 \text{ PFU}}{3.35 \times 10^7 \frac{\text{PFU}}{\text{mL}}}$$

$$\text{Volume of P2 stock} = 0.2\text{mL}$$

Sf9-ET cells were grown in T25 flasks cultured in ESF 921 medium supplemented with 10% FBS and 50 µg/mL Geneticin at 27 °C. These cultures were infected with P2 baculovirus stocks with an M.O.I of 0, 0.1, 1, 5, and 10 and incubated at 27 °C for 72h. Each culture was analyzed for eGFP-expressing cells under the fluorescence microscope (Nikon Eclipse TE2000-U). Images were captured at 10x magnification from the eGFP and brightfield channels to compare eGFP⁺ cells/total cells in the captured images. The number of eGFP⁺ cells and total cells were counted using ImageJ 1.53k. The average eGFP⁺ ratios for each M.O.I tested were plotted to obtain a standard curve that can be used to obtain approximate estimations of amplified baculovirus titers.

Baculovirus amplification in Sf9 cells:

In a shaker, sf9 cells were grown as 50 mL suspension cultures in ESF 921 medium supplemented with 10% FBS at 27 °C /100 rpm. Once the cell density reached $\sim 3 \times 10^5$ cells/mL, the cultures were treated with P2 baculovirus at an M.O.I of 0.1 or 0.5. One culture was left uninfected as the negative control. The cultures were incubated in a 27 °C /100 rpm shaker. Media from each culture was collected at 24h, 48h, 72h, 96h, and 120h post-injection. The collected samples were centrifuged at 5000 rpm, and 4 °C for 5 min, and the supernatant was collected and filtered through a 0.45µm syringe filter and stored in sterile tubes at 4 °C. These baculovirus stocks would be designated as P3 stocks. Sf9-ET cultures were seeded at $\sim 3 \times 10^5$ cells in T25 flasks in ESF 921 medium supplemented with 10% FBS and 50 µg/mL Geneticin and 1:10 dilutions of each collected baculovirus sample. These cultures were incubated at 27 °C for 72h and analyzed by fluorescence microscopy for eGFP-expressing cells.

Using PEG (Polyethylene glycol) for the concentration of amplified P3 baculovirus stocks:

Amplified P3 baculovirus stocks needed to be concentrated for protein production. A (5x) PEG virus precipitation kit (Abcam #ab102538) was obtained for baculovirus concentration. One part of the PEG stock solution was mixed with 4 parts of baculovirus samples and incubated overnight at 4 °C. Following overnight incubation, the baculovirus particles precipitated as an off-white pellet, which was collected by centrifugation at 3200 x g and 4 °C for 30 min. The supernatant was carefully removed, and the pellet was resuspended in a smaller volume of ESF 921 supplemented with 10% FBS. To estimate the titer, sf9-ET cultures were infected with the concentrated baculovirus stocks and observed under the fluorescence microscope for eGFP-expressing cells. The use of PEG allowed ~10-fold concentration of the baculovirus samples. A similar protocol was followed to concentrate amplified baculovirus P3 stocks using a homemade PEG stock: 40% (w/v) PEG with 1.2M NaCl and 1x PBS pH 7.2.

Expression of GST-GSK3b in Sf9 cells with P3 baculovirus:

In a shaker, sf9 cells were grown as 50 mL suspension cultures in ESF 921 medium supplemented with 10% FBS at 27 °C/100 rpm. Once the cell density reached 1×10^6 cells/mL, the cultures were infected with P3 baculovirus at an M.O.I of 10 and incubated at 27 °C in a shaker. Cultures were harvested at 24h, 48h, or 72h post-infection by centrifugation at 5000 rpm and 4 °C for 10 min. The pellets were rinsed with 1x PBS, centrifuged, and stored at -80 °C. Each pellet was thawed and resuspended on ice in lysis buffer (50mM TRIS pH 8, 50mM NaCl, 1x EDTA, and 1x Protease inhibitors). Each cell lysate was sonicated at 0.5 power setting for 30 sec. Lysates were centrifuged at 14 000 rpm and 4 °C for 20 min. The clarified lysates were

mixed with 0.2mL of 40% Glutathione bead slurry for 2h at 4 °C. Following the incubation, the beads were spun down, and the unbound lysate was saved for analysis. The Glutathione beads were rinsed 5x with cold wash buffer (50mM TRIS pH 8, 50mM NaCl) and eluted with 10mM GSH elution buffer (10mM GSH, 50mM TRIS pH 8, 50mM NaCl). The collected eluents were analyzed on SDS-PAGE.

Protein purification from Sf9 cell cultures using Fast Protein Liquid Chromatography (FPLC):

Sf9 cells were grown as 250 mL suspension cultures in ESF 921 medium supplemented with 10% FBS at 27 °C /100 rpm in a shaker. Once the cell density reached 2×10^6 cells/mL, the cultures were infected with P3 baculovirus at an M.O.I of 10 and incubated at 27 °C /100 rpm in a shaker. Cultures were harvested at 72h post-infection by centrifugation at 5000 rpm and 4 °C for 10 min. The pellets were rinsed with 1x PBS, centrifuged, and stored at -80 °C. Each 250mL pellet was lysed with 4mL lysis buffer (50mM TRIS pH 8, 50mM NaCl, 1mM EDTA, and 1x Protease and Phosphatase inhibitors) and sonicated with 2 pulses at 0.5 power setting for 30 sec. The cell lysates were centrifuged at 4000 rpm at 4 °C for 15 min to remove crude debris, and the partially clarified supernatant was centrifuged at 14 000 rpm at 4 °C for 10 min. The clarified supernatant was filtered by passing through a 0.45 µm syringe filter. A 1mL Glutathione-sepharose column on FPLC was washed with 10x column volumes or more with wash buffer (50mM TRIS pH 8, 50mM NaCl) at 0.5mL/min, and then the lysate was loaded onto the column at 0.3mL/min. The column was rinsed with more than 10x column volume with the wash buffer at 0.5mL/min. The FPLC pumps were rinsed with the elution buffer, and the elution buffer (10mM GSH, 50mM TRIS pH 8, 50mM NaCl) was passed through the Glutathione-sepharose

column at 0.3mL/min to elute bound protein. 1mL fractions were collected and analyzed on SDS-PAGE.

Protein Expression in Hi5 Cells via Baculovirus Expression System

Re-cloning human GSK3 β isoform 1, N-GST into EMbacY bacmid and for protein expression in Hi5 cells

The human GSK3 β isoform 1, previously subcloned into a pFastBacGST expression vector via custom contract work by the GenScript company, was transposed with an EMbacY bacmid. PCR analysis was performed to confirm the recombinant bacmid. Sf9 cells were transfected with the recombinant bacmid, and the supernatant was collected on day 6. This supernatant was designated as P1 viral stock, which was used to generate P2 stock. Sf9 cells were infected with P2 stock to amplify baculovirus and generate P3 stocks, which were then used for protein expression in Hi5 cells.

Our collaborator, Dr. Chutima Rattanasopa (University of Nevada, Las Vegas), performed re-cloning GSK3 β into EMbacY, generation of P1, P2, and P3 in Sf9 cells, protein expression, and purification from 4L of Hi5 cultures. Collaborators Dr. Rattanasopa and Dr. Gary Kleiger (University of Nevada, Las Vegas) shared P2 baculovirus stocks, Sf9, and Hi5 strains. Sf9 and Hi5 cell culture protocols, protein extraction, and purification protocols shared by our collaborators were adapted to our lab conditions, as explained next.

Sf9 cell culture and baculovirus amplification

Sf9 cultures were grown as 25mL suspension cultures in Gibco sf-900 III SFM media at 27 °C /125 rpm. Sf9 cultures were seeded to reach $2.2 - 2.5 \times 10^6$ cells/mL, and 25×10^6 cells were transferred to a 250mL flask, which was topped to 25mL with Gibco sf-900 III SFM media. The culture was infected with 0.3mL of P2 baculovirus stock and incubated at 27 °C /125 rpm. On day 6, the culture was centrifuged at 1200 x g, 4 °C for 5 min, and the supernatant was collected. The collected supernatant was passed through a 0.45µm syringe filter and stored at 4 °C. Cells from the pellet were observed under the fluorescence microscope to determine YFP expression. The amplified baculovirus stocks were designated P3 stocks and used for protein expression in Hi5 cells.

Hi5 cell culture and protein expression

Hi5 cultures were grown as 50mL suspension cultures in ESF 921 media at 27 °C /125 rpm. Cells were allowed to reach $4-5 \times 10^6$ cells/mL density and then used to prepare cultures for protein expression. 2-Days before infection with baculovirus, 250mL cultures with ESF 921 media were seeded with 0.4×10^6 cells/mL Hi5 cells and incubated at 27 °C /125 rpm (Cultures were prepared in 500mL or 1L flasks). These cultures would expand to $2.0-2.5 \times 10^6$ cells/mL by the infection day. Half of each culture was centrifuged in sterile 50mL tubes at 1200 x g, room temperature for 10 min. The supernatant was removed, and the cell pellets were resuspended in the remaining half of the culture media. This step would double the cell density. P3 baculovirus stocks were mixed with the Hi5 cultures at 5mL virus:250mL culture, and the cultures were incubated at 27 °C for 1h at 75 rpm to allow the baculoviruses to settle into the Hi5 cells.

Following the 1h incubation, the total volume of each culture was topped to 250mL with fresh ESF 921 media, and the cultures were incubated at 27 °C /125 rpm for 72h to allow protein expression. Cultures were harvested by centrifugation at 1500 x g, 4 °C for 10 min. Cells from the pellet were observed under the fluorescence microscope to determine YFP expression. The pellets were washed with 1x PBS, centrifuged, and stored at -80 °C.

Protein purification from Hi5 cells via Glutathione-affinity purification

Cell pellets of Hi5 cultures expressing recombinant protein were thawed on ice and resuspended in lysis buffer (30mM TRIS pH 7.5, 200mM NaCl, 10% Glycerol, 5mM DTT, 5mM EDTA, 1x Protease inhibitors, 0.1mM PMSF, 0.1% (w/v) PEI, 0.1% (v/v) Triton x-100) added at a volume to culture ratio of 5mL to 50mL pellet. Resuspended pellets were sonicated with 2 pulses at a 3.5 power setting for 15 sec. The lysates were centrifuged twice at 12,500 rpm, 4 °C for 15 min. The clarified lysates were mixed with 50% Glutathione slurry (0.2mL of Glutathione slurry for 10-12mL clarified lysate in 15mL tubes) and incubated tumbling at 4 °C for 2h. The lysates were centrifuged at 2000 rpm, 4 °C for 2 min. The supernatants were collected as the “unbound” lysate. The Glutathione slurries were washed 4x with ice-cold wash buffer (30mM TRIS pH 7.5, 200mM NaCl, 1mM DTT, 0.5mM EDTA). After washing, the Glutathione slurries were pooled into 2x eppendorfs and eluted with GSH elution buffer (20mM GSH, 50mM TRIS pH 7.5, 200mM NaCl, 1mM DTT, 0.5mM EDTA). The eluted protein samples were analyzed with Bradford reagent to monitor protein concentrations. Each eluent was analyzed on SDS-PAGE.

Enzymatic cleavage to remove GST affinity tag and Ion-exchange purification.

TEV protease with a C-terminal His tag was purchased from New England Biolabs or GenScript and additionally shared by collaborators Dr. Gary Kleiger and Dr. Chutima Rattanasopa (University of Nevada, Las Vegas). A TEV protease cleavage site ENLYFQG was included in the Poly-linker between the GST tag and GSK3 β . The glutathione-eluted protein samples were pooled and incubated at 4 °C for 24h with TEV protease. The cleaved GSK3 β was purified using ion-exchange chromatography. A 1mL HiTrap SP XL cation-exchange column on FPLC was washed with 10x column volumes or more with Buffer A (20mM HEPES pH 7.5, 50mM NaCl, 2mM β -Mercaptoethanol) at 1mL/min. The TEV-cleaved protein sample was diluted 4x with the buffer with no salt (20mM HEPES pH 7.5, 2mM β -Mercaptoethanol) and filtered through a 0.45 μ m syringe filter before loading onto the column. The protein sample was loaded onto the column at 0.5mL/min. The column was rinsed with more than 10x column volume with Buffer A at 1mL/min. The FPLC pumps were rinsed with Buffer B/elution buffer (20mM HEPES pH 7.5, 1.0M NaCl, 2mM β -Mercaptoethanol), and a linear gradient of Buffer B was used to elute GSK3 β collecting 1mL fractions. Each fraction was analyzed on SDS-PAGE. Fractions with GSK3 β and TEV-His co-elution were pooled, and TEV-His was removed using His-bind resin purification according to the manufacturer's protocol. A final purified GSK3 β sample was obtained by pooling purified GSK3 β fraction from ion exchange (including TEV cleared fractions) and concentrating the sample via centrifugation in centricon tubes. The purified GSK3 β sample was analyzed on SDS-PAGE, and the protein concentration was estimated using the BCA assay and BSA as the standard. The protein samples collected this way were dialyzed into appropriate buffers for isothermal titration calorimetry experiments or stored at -80 °C following flash-freezing in liquid N₂.

Results and Discussion

*GST-GSK3 β Expressed in BL21(Gold)CodonPlus *E. coli* was Predominantly Degraded*

Our research group previously used the pGEX-4T-3 vector cloned with human GSK3 β variant 2 (420 amino acids) to prepare N-terminal GST fused recombinant GSK3 β in BL21-Gold(DE3) *E. coli* for a FRET-based kinase assay. SDS-PAGE analysis showed that the purified protein sample was a heterogeneous mixture of the full-length protein of 74kDa (27kDa GST tag and 47kDa GSK3 β) and degraded protein (Data not shown). The quantity of full-length protein in the purified protein samples contained sufficient activity, as detected by the FRET-based kinase assay (Mudireddy et al., 2014). However, a heterogeneous protein sample would not be ideal for ITC binding experiments to study the specific interactions between GSK3 β and particular substrates or inhibitors.

Expressing heterologous proteins in *E. coli* faces several challenges, primarily due to codon bias, which can significantly hinder the efficient production of these proteins (Kane, 1995). “BL21 Codon Plus Cells Correct Expression Problems Caused by Codon Bias” by Carstens et al. for Stratagene outlines the main issues related to this problem:

Codon Bias: The genomes of certain organisms prefer sequences with codons that occur infrequently in *E. coli*. This mismatch can lead to inefficient translation of heterologous genes in *E. coli*, as the bacterium may lack sufficient tRNAs that recognize these rare codons.

Forced High-Level Expression Issues: Attempting to force the high-level expression of genes containing rare codons can deplete *E. coli*'s limited pool of corresponding tRNAs. This depletion

disrupts translation, resulting in truncated or no protein expression and potential frameshifts, codon skipping, and misincorporations.

Protein Expression Limitations: A deficit of tRNA molecules can slow or completely halt protein expression, leading to mRNA degradation. This problem is particularly acute when expressing proteins derived from AT—and GC-rich genomes.

The sequence for GSK3 β contained a significant number of all 5 rare *E. coli* codons: 22 out of the 420 amino acid residues, which is 5.2%. Our protein sequence's rare *E. coli* codons included two rare Arg and rare Ile, Pro, and Leu codons. BL21(Gold)CodonPlus cells are specially engineered to contain extra copies of tRNA genes, which are rare in *E. coli* but more frequently used in genes from other organisms. By supplying additional tRNA copies, these modified *E. coli* strains can effectively mitigate the problems caused by codon bias, allowing for the efficient and high-level expression of heterologous proteins that would otherwise be difficult or impossible to achieve in conventional *E. coli* hosts.

This approach can dramatically improve the expression of heterologous proteins within these *E. coli* expression systems. Therefore, we re-transformed the pGEX-4T-3 vector cloned with the human GSK3 β variant 2 into BL21(Gold)Codon Plus (DE3)-RIPL cells, which contain extra copies of the *argU*, *ileY*, and *leuW* as well as the *proL* tRNA genes. We expected this strain would allow the expression of full-length GST-GSK3 β protein with less or no degradation. The resultant protein product was predominantly degraded (**Figure 4.1**), particularly affecting the GSK3 β portion of the fusion construct. This was inferred from the intact GST binding to glutathione beads, indicating that degradation likely occurred at the C-terminal end of the fusion protein where GSK3 β resides. Since the GST tag is still bound to the glutathione beads, indicating that the GST portion remained intact, and considering GST's small size and high

solubility, it is reasonable to conclude that the degradation affected the GSK3 β portion rather than the GST tag. The presence of rare codons within the GSK3 β sequence and the challenges associated with their efficient translation in *E. coli*, despite the codon-optimization strategies employed by the BL21(Gold)CodonPlus (DE3)-RIPL cells, might contribute to this degradation. Protein instability in bacterial expression systems can be attributed to several factors, even in *E. coli* strains that lack proteases.

These factors include improper folding, misincorporation of amino acids due to rare codon usage (even in codon-optimized strains), formation of insoluble aggregates, or intrinsic sequences within the protein that make it susceptible to degradation. The absence of specific chaperones or post-translational modifications in bacterial systems can contribute to protein instability. Some residual proteolytic activity or stress-induced proteases might still cause degradation even with protease-deficient strains (Harper & Speicher, 2011). Although the bacterial expression system was more convenient and cost-effective, the challenge of resolving codon bias and protein degradation led us to transition to a eukaryotic expression system to prepare full-length GSK3 β for use in ITC studies.

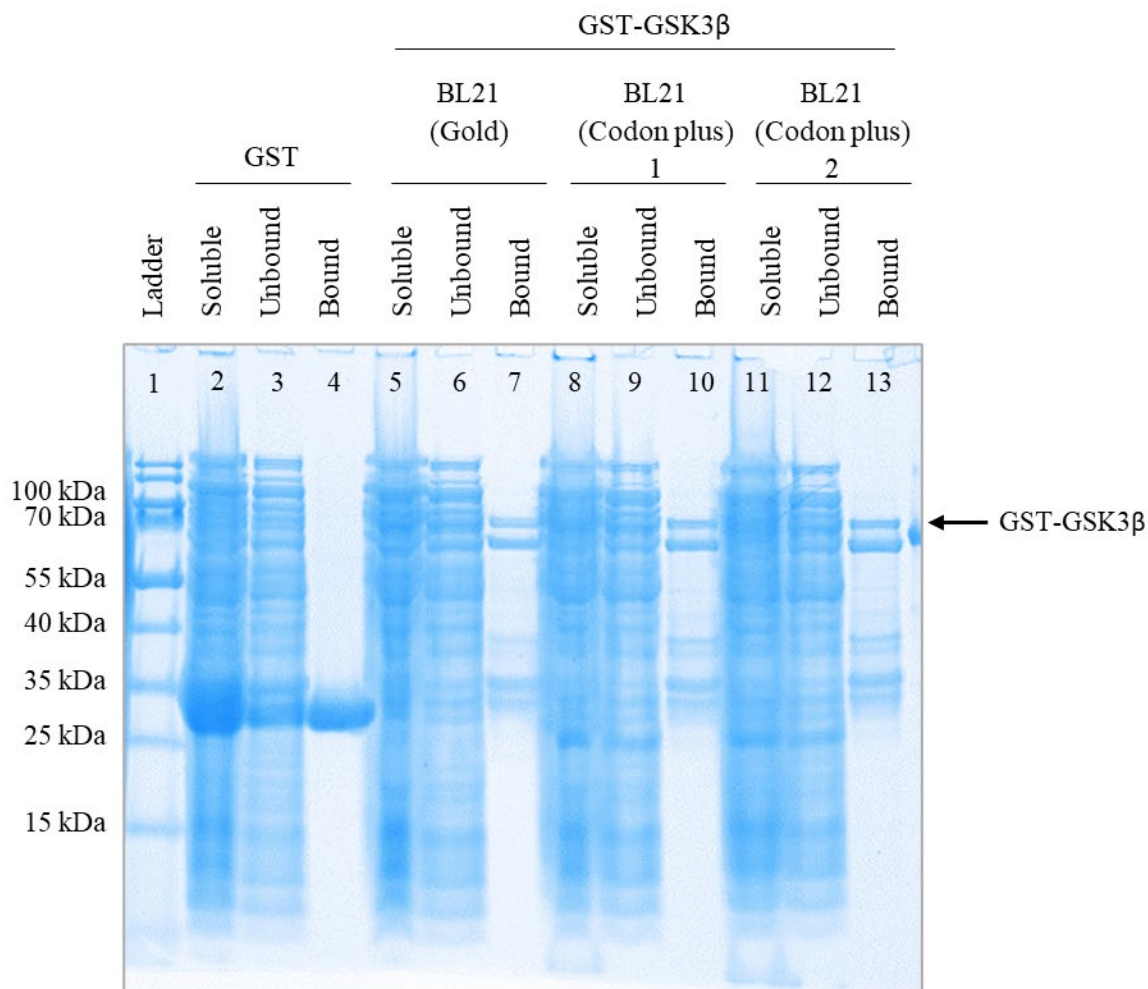


Figure 4.1: GST-GSK3 β Expression in BL21(Gold) vs. Re-transformed BL21(CodonPlus) *E. coli* Analyzed on SDS-PAGE. Soluble lysate (input) and the Glutathione bead-unbound and bound samples isolated from each bacterial strain are compared. ~65% of the expressed GST-GSK3 β in the BL21(CodonPlus) strains were degraded (lanes 10 and 13). The degradation of expressed GST-GSK3 β was not improved in BL21(CodonPlus) cells(lanes 10 and 13) compared to that of BL21(Gold) (lane 7).

Utilization of the Sf9-ET Reporter Cell Line for Baculovirus Titer Estimation

Sf9-ET cells are a stable cell line with plasmid DNA containing the enhanced green fluorescent protein (eGFP) under the control of the baculovirus polyhedrin promoter. Early viral gene products act as activators for the polyhedrin promoter. The plasmid also contains the neomycin resistance gene, which allows the selection of transfectants when grown in a medium containing Geneticin. Uninfected Sf9-ET cells do not express detectable GFP, while infection with baculovirus particles produces early viral proteins, which turn on GFP expression from the integrated polyhedrin promoter. Virus titers are determined in three days by measuring the GFP-expressing cells under the fluorescence microscope (Hopkins & Esposito, 2009). Our study demonstrated the effective use of the Sf9-ET reporter cell line in estimating baculovirus titers through eGFP expression in response to baculovirus infection.

The eGFP expression in Sf9-ET cells after infection with the P2 baculovirus at M.O.I of 0, 0.1, and 1, incubated at 27 °C for 72h, was observed. The analysis via flow cytometry confirmed eGFP expression, with eGFP-positive cells constituting 0.21%, 0.79%, and 4.71% of the total cell population for M.O.I. of 0, 0.1, and 1, respectively(**Figure 4.2**). This incremental increase in eGFP expression relative to the M.O.I highlights the Sf9-ET cells' capability to serve as an effective tool for baculovirus titer estimation. The relationship between baculovirus infection intensity and eGFP expression was further explored by infecting Sf9-ET cells with P2 baculovirus stocks at varying M.O.I. (0, 0.1, 1, 5, and 10) (**Figure 4.3**). The subsequent examination under fluorescence microscopy revealed a proportional increase in eGFP expression with the M.O.I., demonstrating the utility of Sf9-ET cells in reflecting the degree of baculovirus infection and potential titers.

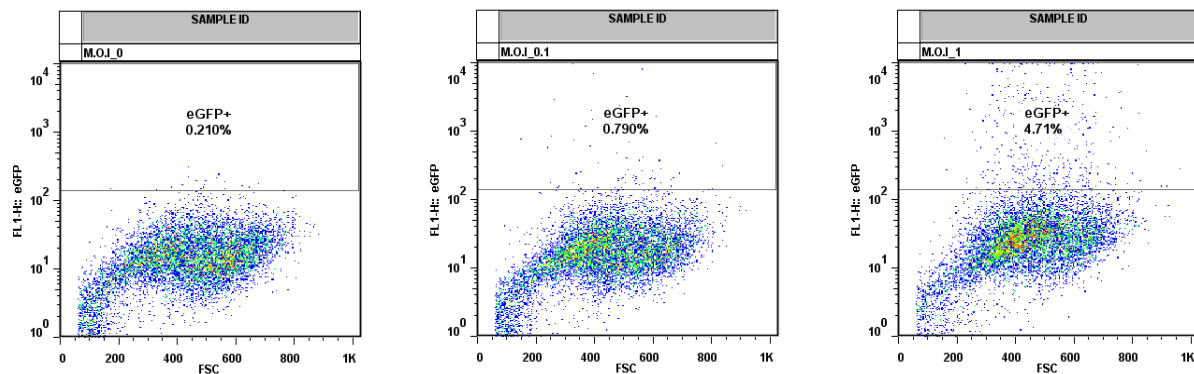


Figure 4.2: eGFP Expression in Sf9-ET Reporter Cell line Infected with P2 Baculovirus. Sf9-ET cells grown in T75 flasks were infected with P2 baculovirus at an M.O.I of 0, 0.1, or 1 and incubated at 27 °C for 72h. Harvested cells were analyzed via flow cytometry to confirm eGFP expression with the baculovirus for the expression of GST-GSK3 β and observe eGFP expression against M.O.I. The eGFP+ cells were 0.210%, 0.79%, and 4.71%, respectively, in cultures without baculovirus infection, and M.O.I of 0.1 and 1, showing Sf9-ET cells can be utilized to estimate the titers for amplified baculovirus stocks.

Sf9 cultures infected with P2 baculovirus at an M.O.I of 0.1 or 0.5 yielded P3 baculovirus samples that, upon harvesting at 72, 96, and 120 hours, induced eGFP expression in Sf9-ET cells (Figure 4.4). Firstly, this experiment showed that we could successfully amplify baculovirus under our lab conditions, and the homemade baculovirus induced eGFP expression in Sf9-ET reporter cells. Notably, P3 samples derived from cultures infected at an M.O.I of 0.1 and incubated for 96 or 120 hours exhibited the highest ratios of eGFP-expressing cells. The results showed that the optimal conditions for baculovirus amplification would be infection at an M.O.I. of 0.1 and incubation at 27 °C for 96-120h. Sf9 cells infected at an M.O.I of 0.5 with P2 displayed similar amplification to 0.1 infections for the 72h incubation. However, lower eGFP+ ratios were observed for 96h and 120h. This makes sense because at a higher M.O.I., more cells

will be infected initially. However, once a cell is infected with the baculovirus, that cell will no longer divide, which limits the number of cells available to be newly infected as the culture is incubated longer. The number of Sf9 cells available for infection becomes limited, ultimately leading to a lower yield of amplified baculovirus P3.

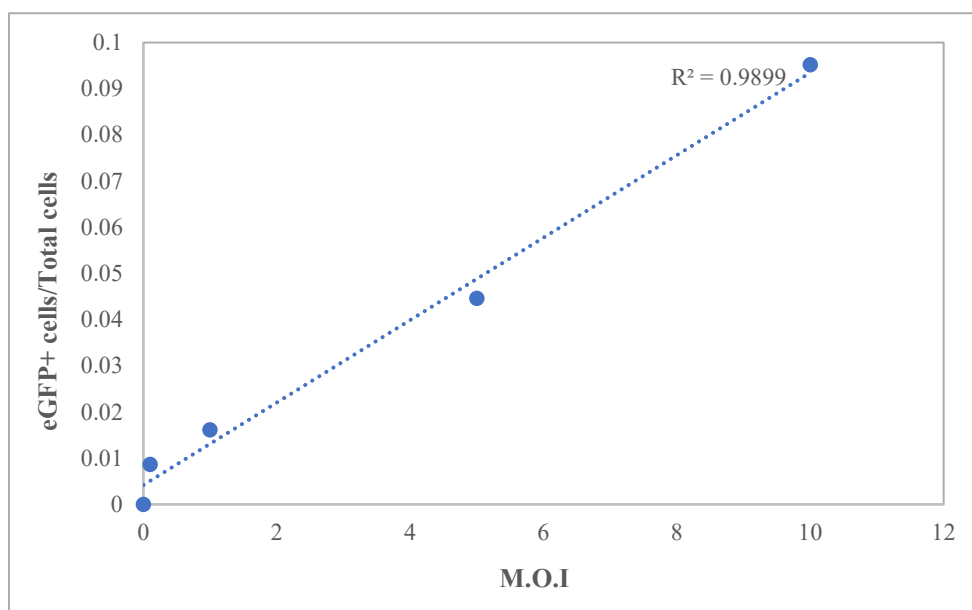


Figure 4.3: Analysis of eGFP Expression in Sf9-ET Cells Infected with Baculovirus at Varying M.O.I. The quantification of eGFP expression in Sf9-ET cells following infection with P2 baculovirus stocks at M.O.I of 0 (uninfected control), 0.1, 1, 5, and 10, and incubated for 72 hours at 27 °C. Post-incubation, cells were examined using a fluorescence microscope for eGFP fluorescence, indicative of baculovirus infection. Both eGFP and brightfield channel images were captured to assess eGFP-expressing cells' (eGFP+) ratio to total cells.

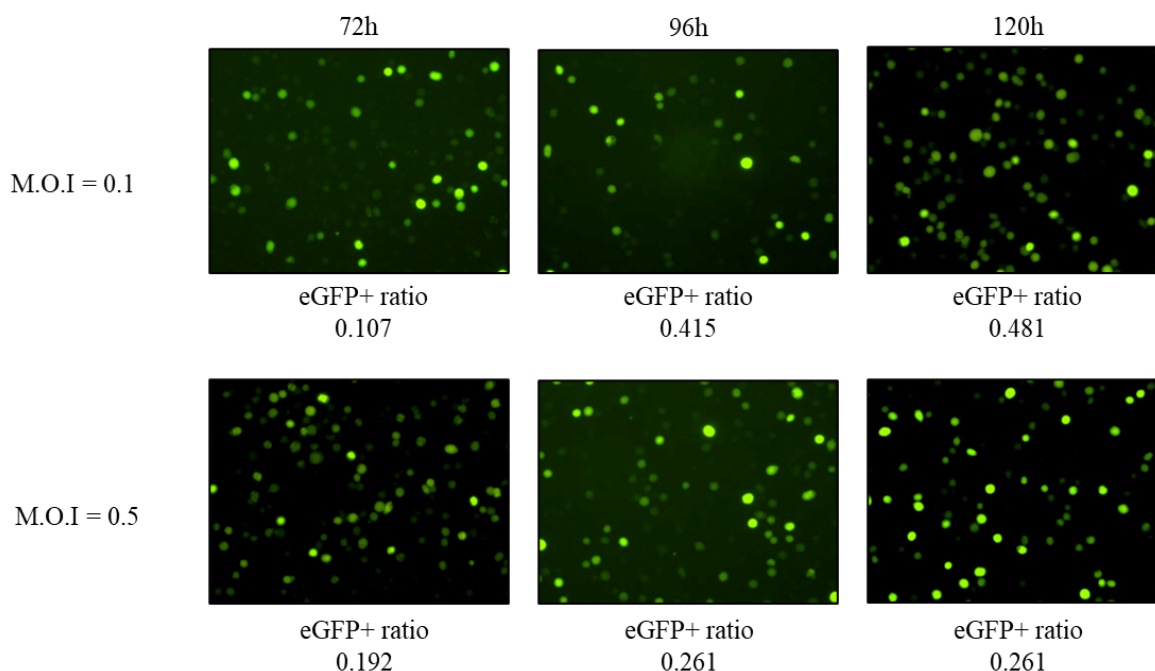


Figure 4.4: Analysis of eGFP Expression in Sf9-ET Cells Infected with P3 Baculovirus. Amplified baculovirus samples were harvested at varying time points from Sf9 cultures post-infection with P2 baculovirus at an M.O.I of 0.1 or 0.5. Significant eGFP expression was induced by P3 baculovirus samples harvested at 72h, 96h, and 120h. P3 baculovirus harvested from Sf9 cultures infected at an M.O.I of 0.1 and incubated for 96h or 120h yielded a higher ratio of eGFP-expressing cells in Sf9-ET cultures.

Amplified Baculovirus Stocks could be Concentrated by 10-fold using PEG (Polyethylene glycol)

To upscale protein production, it was necessary to intensify the concentration of amplified baculovirus P3 stocks for high M.O.I. infection in Sf9 cells. A PEG-based approach offered a straightforward and efficient alternative to ultracentrifugation for virus concentration. We successfully demonstrated a 10-fold concentration of amplified baculovirus P3 stocks using PEG. The PEG-based precipitation process leverages PEG's property to exclude water molecules, thereby aggregating virus particles and causing the virus particles to precipitate. Once

precipitated, the pellet with the baculovirus particles can be isolated via centrifugation and resuspended in a smaller media volume to obtain a concentrated baculovirus stock. The PEG-based virus precipitation method provides an easy, convenient method to concentrate viruses without ultracentrifugation (Colombet et al., 2007). Initially, the PEG-based baculovirus concentration was tested with the Abcam (5x) PEG virus precipitation kit, as explained in the methods. 170mL of amplified baculovirus P3 was concentrated to 34mL (concentrating the sample by a factor of 5). The estimated titer of the P3 stock prior to concentration was 2.82×10^7 PFU/mL. Based on volume reduction, if 100% recovered, the titer of the concentrated P3 stock would be 1.41×10^8 PFU/mL. The titer of the PEG-concentrated P3 stock determined by eGFP expression in Sf9-ET cells was 1.61×10^8 PFU/mL. The observed results showed an almost 100% recovery and a 10-fold concentration of the amplified baculovirus P3 stocks. Repeated experiments with homemade PEG virus precipitation solution yielded 60-100% recovery and 10-20-fold concentration (data not shown).

Polyethylene glycol (PEG) can improve virus infection efficiency in insect cells by enhancing viral entry. PEG induces a mild dehydration of the virus and cell surface, leading to closer contact and possibly fusion between the virus and cell membrane. This promotes viral uptake, improving the efficiency of virus infection and potentially increasing the delivery of the viral genetic material into the host cell. This could explain the instances in which we observed almost 100% recovery. So, ultimately, the true titer might be lower than estimated in the presence of PEG. However, our purpose was to obtain an approximate estimation of the baculovirus titers to infect Sf9 cultures with a sufficient M.O.I.

Full-length GST-GSK3 β Expression via Baculovirus Expression in Sf9 Cells

The GST-GSK3 β expressed and purified from Sf9 cells by GenScript was compared against protein expression in BL21(Gold) *E. coli* in (**Figure Appendix III.A**) – Lane 7 shows a prominent 74kDa protein band for the full-length GST-GSK3 β , in contrast to the primarily degraded protein observed in the bacterial expression system in lane 6. This demonstrates the potential of the Sf9 baculovirus expression system in producing intact, full-length protein, alleviating the degradation issues encountered with the bacterial system. However, repeating this observation in our lab and optimizing expression conditions was necessary. The optimal incubation time for GST-GSK3 β expression in Sf9 cells infected with amplified P3 baculovirus was examined (**Figure 4.5**). By comparing the glutathione-bound and GSH-eluted GST-GSK3 β at various post-infection incubation times (24h, 48h, and 72h), it was observed that a 72h incubation period yielded the highest level of GST-GSK3 β expression.

SDS-PAGE analysis of glutathione affinity-purified protein samples for GST-GSK3 β expressed in Sf9 cells with that expressed in BL21(Gold) *E. coli* underscores a significant degradation (> 90%) of the bacterially expressed GST-GSK3 β (**Figure 4.6**). Conversely, the Sf9-expressed protein displayed no notable degradation, highlighting the superiority of the eukaryotic expression system in maintaining the integrity of GST-GSK3 β . This improvement is likely attributable to the eukaryotic nature of Sf9 cells, which offer a more compatible environment for the folding and processing of eukaryotic proteins, thereby minimizing degradation. The degradation of GST-GSK3 β in bacterial systems (even in codon-optimized *E.coli* strains) compared to its stability in Sf9 cells shows that this protein is better suited to eukaryotic expression systems, especially when expressing and purifying for utilization in biophysical assays such as ITC.

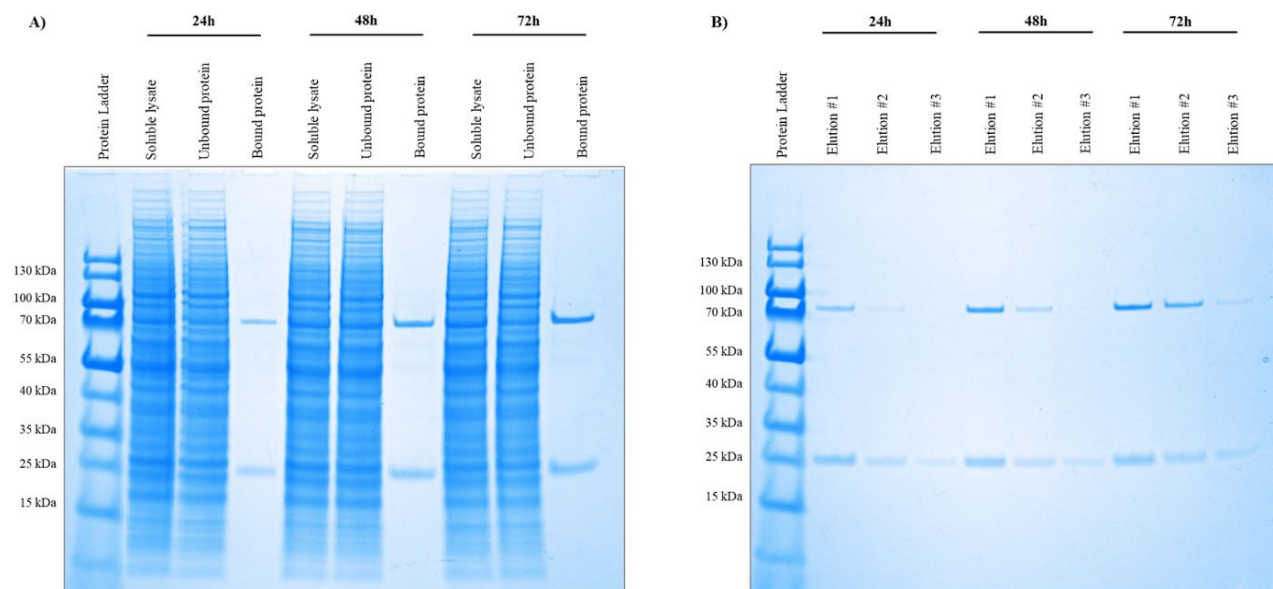


Figure 4.5: GST-GSK3 β Expression in Sf9 Cells Infected with P3 Baculovirus Analyzed on SDS-PAGE. Sf9 cultures infected with P3 baculovirus were incubated at 27 °C for 24h, 48h, or 72h. A) Comparison of glutathione bound GST-GSK3 β in Sf9 cultures harvested at different incubation times. B) Comparison of GSH eluted GST-GSK3 β collected for Sf9 cultures at different incubation times. Results show that a 72h incubation time yielded the highest GST-GSK3 β expression. 25kDa band is an endogenous glutathione-binding protein.

Analysis of GST-GSK3 β Purification Yields from Sf9 Cell Cultures using FPLC

In order to purify sufficient quantities of GST-GSK3 β for ITC experiments, we needed to scale up expression in Sf9 cells. Sf9 cultures were grown as 250mL cultures in ESF 921 medium to a 2×10^6 cells/mL density with > 90% cell viability. These cultures were infected with PEG-concentrated P3 baculovirus at an M.O.I. of 10 and incubated at 27 °C /100rpm for 72h. The harvested pellets were rinsed with 1x PBS and stored at -80 °C until used for protein extraction.

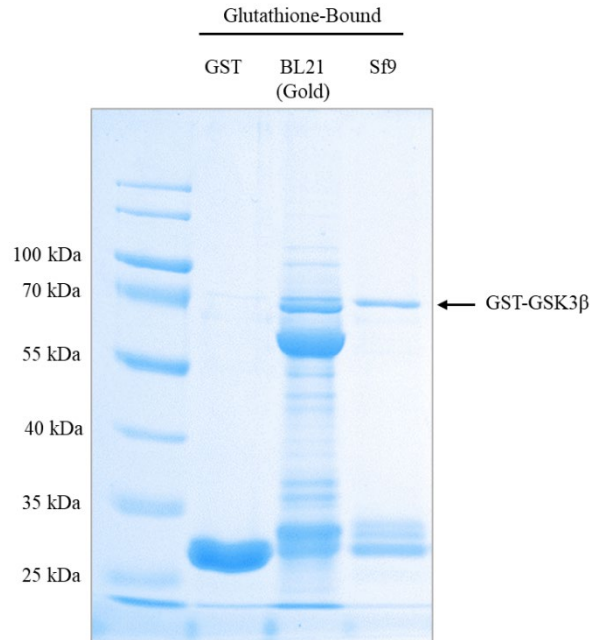


Figure 4.6: GST-GSK3 β Expression in Sf9 Cells Compared Against GST-GSK3 β Expression in BL21 (Gold) *E. coli* Cells Analyzed on SDS-PAGE. GST and GST-GSK3 β were expressed in BL21(Gold) *E. coli*, and GST-GSK3 β was expressed in Sf9 cells. Batch-bead purification with Glutathione resin was followed for each cell lysate and eluted with Glutathione elution buffer. 0.2 μ g from each Glutathione affinity purified protein sample was analyzed on SDS-PAGE for comparison. GST alone is expressed well, but the full-length GST-GSK3 β expressed in bacterial cells is more than > 90% degraded. The full-length GST-GSK3 β expressed in Sf9 does not show degradation compared to the bacterially expressed fusion protein.

Multiple 250mL Sf9 pellets were lysed and combined during purification to purify more protein. Cell lysates were purified via affinity purification using a Glutathione-sepharose column on FPLC (**Figure 4.7A**). Quantitative analysis demonstrates variances in protein yield between the two preparations (**Figure 4.7B**), with 0.12 mg/mL for pooled fractions (F2 + F3 + F4) of prep 1 and 0.37 mg/mL for pooled fractions (F2 + F3 + F4) of prep 2, indicating an approximate threefold difference. This difference is apparent when observing the gel band densities of the 74kDa protein bands on SDS-PAGE.

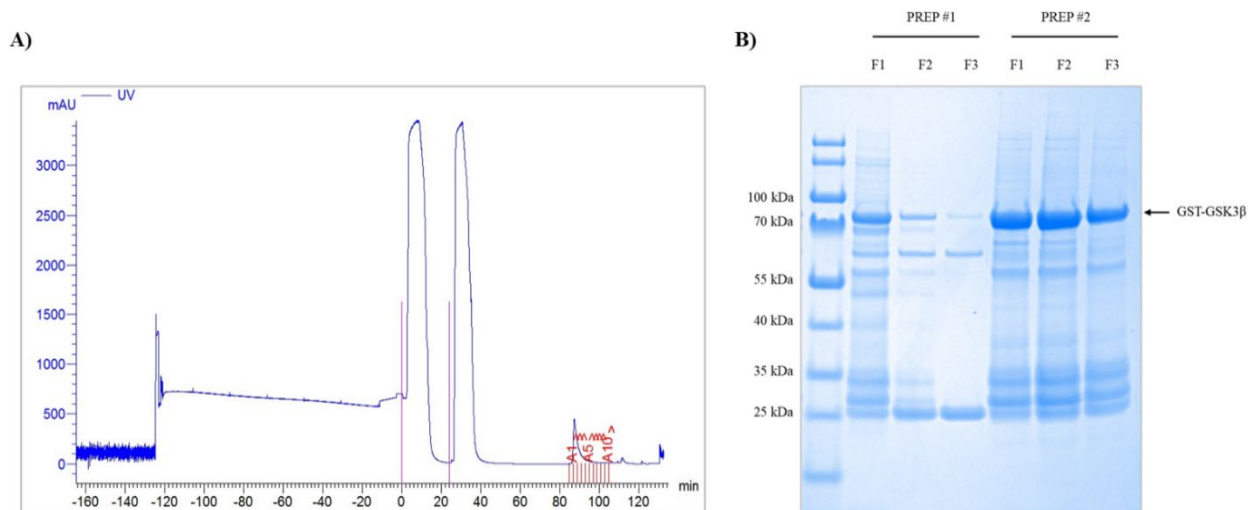


Figure 4.7: GST-GSK3 β Extracted and Purified from Sf9 Cells Infected with P3 via Glutathione-Sepharose Column on FPLC. Each prep utilized 5 x 250mL of Sf9 cultures (total 1.25L) grown to a density of 2×10^6 cells/mL, infected with P3 at an M.O.I. = 10, and incubated at 27 °C /100rpm for 72h. A) Representative UV trace for affinity protein purification and elution on Glutathione-sepharose column for GST-GSK3 β purification from clarified Sf9 cell lysates (Prep #2) The peaks at 0 and 20mL marks represent unbound protein and the smaller peak at 84mL is GSH-eluted protein. B) SDS-PAGE analysis of GSH-eluted fractions F1, F2, and F3 collected from two independent protein extractions (equivalent to 1.25L). Each lane represents 13.5 μ L from a 1mL fraction of GSH-eluted protein (=1.35% total). The concentration of GST-GSK3 β in the pooled fractions from prep 1 and 2 was $\sim 10\mu$ M.

The disparity in protein yield between the two preparations suggests variability in baculovirus expression levels across cultures, which could be attributed to differences in cell viability or other biological variations inherent to the cultures. The estimated molarity of GST-GSK3 β in the pooled and concentrated FPLC fractions from prep 1 and 2 was approximately 10 μ M. The subsequent use of this protein sample in ITC experiments to assess binding affinity with ATP and a substrate peptide was hindered by insufficient heat signatures (Discussed in Chapter 5), indicating a low signal-to-noise ratio that prevented the acquisition of a binding curve. This outcome suggests that, despite successful purification, the concentration and purity of

the protein were not optimal for ITC measurements, necessitating further optimizations of the purification protocols to enhance the yield and purity.

Experimental Challenges Associated with GST-GSK3 β Expression, Extraction, and Purification from Sf9 Cells

In expressing and purifying GST-GSK3 β from Sf9 cells, our lab encountered several significant challenges that impacted the efficiency and outcome of the protein purification process. This section discusses the challenges arising from various stages of expression, extraction, and purification, as well as the methods adopted to overcome them, as referenced in Appendix III.

Initially, the project was constrained by a limited supply of P2 stock received from GenScript, necessitating the amplification of baculovirus in large quantities to express the GST-GSK3 β . This led to the generation of P3 from P2 and, subsequently, P4 from P3, given the scarcity of the initial P2 stock. However, a notable decline in protein expression levels was observed over time, particularly in the P4 generations. This decrease can be attributed to several factors, including a reduction in virus titer, the emergence of defective interfering particles (DIPs), selective pressure leading to genetic instability, the condition of the Sf9 cells, and suboptimal infection parameters. These factors may have contributed to diminished yields of the desired protein over successive baculovirus generations.

Another significant challenge was the increased viscosity observed in Sf9 cell lysates during protein extraction, complicating the filtration process essential for preventing column clogging during Fast Protein Liquid Chromatography (FPLC). High viscosity during protein

extraction is usually due to host-cell DNA, necessitating a DNase treatment step during cell lysis and protein extraction. However, the activation of DNase requires Mg^{2+} , which in turn can activate metalloproteases that could degrade the expressed protein. The cell lysis buffers contained EDTA, added to chelate metal ions such as Mg^{2+} to prevent metalloprotease activation and inadvertent degradation of the recombinant protein of interest. To follow the DNase treatment for DNA degradation, Mg^{2+} was added in excess over EDTA to activate DNase, followed by the addition of EDTA to chelate Mg^{2+} and inhibit protease activity after the DNase treatment. Despite these measures, protein degradation remained a concern, particularly under suboptimal expression levels.

The absence of the expected 74kDa protein band for GST-GSK3 β in the GSH-eluted fractions from the FPLC, as well as the in the Glutathione-Mini-pulldown tests performed over the input and FPLC flow-through (**Figure Appendix III.B**), indicated possible degradation of the target protein. The contrast between the outcomes of the Glutathione-Mini-Pulldown assay followed on a smaller sample saved from the same Sf9 culture but without the DNase treatment against the FPLC purification experiment suggests that the DNase treatment, while necessary for reducing the lysate viscosity, might also contribute to protein degradation by unintentional activation of metalloproteases.

Applying polyethyleneimine (PEI) emerged as a promising strategy for addressing these challenges. PEI is a cationic polymer that effectively precipitates DNA from cell lysates. This ability is attributed to its high density of amine groups, which can protonate under physiological conditions, providing a positive charge. DNA, negatively charged due to its phosphate backbone, interacts strongly with the positively charged PEI. This interaction neutralizes the DNA's charge, causing it to aggregate and precipitate out of solution. (Sami et al., 2016; Sun et al., 2018). PEI

effectively precipitated DNA from cell lysates, reducing viscosity and enhancing filtration. PEI effectively reduced lysate viscosity by precipitating DNA, facilitating easier filtration and reducing the risk of column clogging during FPLC. This method demonstrated significant advantages over traditional DNase treatment, highlighting the importance of exploring alternative techniques for improving lysate processing (**Table Appendix III.A**).

Despite improving lysate processing and mitigating potential protein degradation, GST-GSK3 β could not be purified via the Glutathione-sepharose column on FPLC. GST-GSK3 β was not bound to the GSTrap HP column but was present in the input and the FPLC flow-through (**Figure Appendix III.C**). Another significant observation was the high expression of non-specific endogenous Glutathione-binding proteins (GBPs), complicating the purification process. A 25kDa endogenous GBP, which is usually observed in Sf9 lysates (Bichet et al., 2000), appeared to bind the GSTrap HP column and elute with GSH elution buffer in the FPLC fractions, implying the affinity column was working. A highly expressed ~35kDa GBP was also present in the Sf9 lysates. Initially, we suspected this could be a truncated version of the recombinant protein, or else the Sf9 cell stocks might be inadvertently infected with a bacmid expressing a truncated version. However, analysis of Sf9 cell lysates via the Glutathione-Mini-pulldown assay for existing and fresh Sf9 cultures infected with and without baculovirus identified the 35kDa protein as an endogenous GBP (**Figure Appendix III.D**), complicating the purification of GST-GSK3 β . Bichet et al. (2000), demonstrated that employing a linear GSH gradient elution could allow the separation of co-eluting GST-fusion and endogenous GBPs. Protein elution with different GSH concentrations in a Glutathione-Mini-Pulldown assay showed (**Figure Appendix III.E**) that GST-GSK3b and the 35kDa endogenous GBP can be separately eluted.

Another observation was the significant retention of GST-GSK3 β recombinant protein on Glutathione beads in the Glutathione-Mini-pulldown experiments, which highlighted challenges in elution efficiency. Glutathione is a dimeric protein, and its crystal structure reveals 4 exposed cysteine residues that can contribute to protein aggregation by oxidation under certain conditions. DTT was added to lysis, wash, and elution buffers to maintain a reducing environment and prevent potential protein aggregation in this way. However, adding DTT did not improve GSH-elution efficiency for GST-GSK3 β (Data not shown). Protein aggregation is also possible through non-specific hydrophobic interactions, which could be exacerbated during sonication or other lysis conditions, and including 0.1% Triton X-100, a non-ionic detergent, in the lysis, wash, and elution buffers significantly improved GST-GSK3 β elution from Glutathione beads (**Figure Appendix III.F**). This suggests that Triton X-100's role in reducing sonication-induced aggregation and possibly altering protein-membrane interactions or the protein's conformation is crucial for enhancing solubility and elution efficiency.

Despite many optimization attempts to improve protein expression and purification from Sf9, the overall yield of GST-GSK3 β derived from Sf9 cultures was not sufficiently high for ITC work. Low protein expression levels could explain why no GST-GSK3 β was observed in Glutathione-sepharose column FPLC elution fractions in the cultures infected with P4 generation baculovirus. The likelihood of the GST-tagged protein interacting with the glutathione ligands on the column is proportional to its concentration in the lysate. If the concentration is too low, the chances of binding events occurring during the flow-through can significantly decrease, especially if the flow rate is not adjusted to allow longer interaction times.

Also, when the lysate is diluted, the protein might not be presented to the column matrix in a concentrated enough form to facilitate effective binding. In a dilute lysate, other proteins—

even in small amounts—might compete with GST-GSK3 β for binding sites on the glutathione resin, especially if those proteins have higher affinity interactions with the column matrix or are present in relatively higher concentrations, which was the case in many of our Sf9 lysates where the band intensities of the 25kDa or 35kDa endogenous GBPs were larger than GST-GSK3 β . The evidence implied that without re-cloning the baculovirus and generating new P1 and subsequent new amplified baculovirus stocks, it would be challenging to obtain the high amounts of recombinant GSK3 β required, especially to attempt ITC binding experiments.

Some sources report that Sf9 cells are better for baculovirus amplification at high titers, while Hi5 insect cell lines are better at heterologous protein production. Some studies have reported higher-per-cell expression levels for various recombinant proteins in Hi5 cell lines compared to Sf9 cell lines, specifically, the expression of recombinant β -galactosidase (Wickham et al., 1992), soluble tissue factor (Wickham et al., 1995), and secreted alkaline phosphatase (Davis et al., 1993) in Hi5 cell lines were observed to be 7 times, 28 times and 20 times higher, respectively than those achieved with Sf9 cells (Saarinen et al., 1999).

High baculovirus titers in Sf9 cell cultures can complicate protein expression and purification in several ways. For expression, high virus levels might lead to cell lysis or altered cellular metabolism, potentially reducing the yield of the desired recombinant protein. During purification, high amounts of baculovirus mean that additional steps or more stringent conditions are needed to separate the virus particles from the target protein, complicating the process and possibly affecting protein quality or yield.

High virus levels in Sf9 cells can lead to an increase in cell lysate viscosity. This happens because the large quantities of baculovirus particles and cell debris from lysed cells thicken the solution, making it more difficult to handle during downstream processes such as purification.

This increased viscosity can hinder efficient purification and recovery of the desired recombinant protein. When lysate viscosity increases due to high levels of baculovirus particles in Sf9 cell cultures, it is possible to lose the target protein in the pellet during centrifugation. This could happen because the thickened lysate may not properly separate, causing some soluble proteins to co-precipitate with the cell debris and baculovirus particles. This leads to a lower recombinant protein yield following purification. A high baculovirus titer in Sf9 cell cultures could have contributed to the low yield of GST-GSK3 β . Switching to Hi5 cells, known for producing fewer baculovirus titers and higher recombinant protein yields, could likely mitigate these issues, resulting in a better yield of GSK3 β for ITC work.

Recombinant GSK3 β Production and Purification from Hi5 Cells Allowed Higher Protein Yields

The re-cloning of human GSK3 β isoform 1 into the EMbacY bacmid and subsequent expression in Hi5 cells appeared to mitigate the issues associated with GST-GSK3 β expression in Sf9 cells. The new protocol adapted for baculovirus amplification allowed us to harvest baculovirus stocks with high titers without following additional concentration steps or estimating titers.

Amplifying baculovirus in Sf9 cultures with a small culture volume of 25mL allowed to obtain high titers and this could be determined by observing YFP expression in the Sf9 cells via fluorescent microscope at the time baculovirus stocks were harvested. Having YFP expression to monitor baculovirus amplification in real-time (**Figure 6.8**) was very useful and saved time since we no longer needed to use a secondary cell line like the Sf9-ET reporter cell line to determine whether baculovirus amplification was successful, which was both time and cost-efficient.

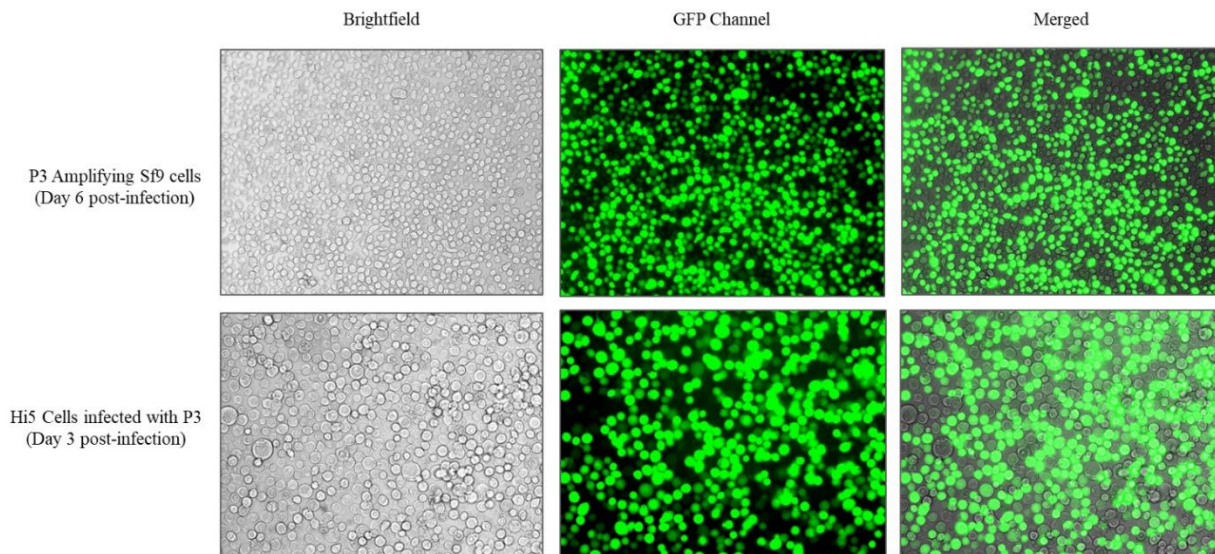


Figure 4.8: Analysis of YFP Expression in Sf9 Cells to Monitor Baculovirus Amplification and Recombinant Protein Expression in Hi5 Cells. The EmBacY bacmid transposed with the pFASTBac vector carrying GST-GSK3 β contained a YFP gene, which would be expressed under the activation of the polyhedrin promoter. YFP expression allowed for real-time monitoring of the efficiency of baculovirus amplification in Sf9 cells and GST-GSK3 β expression in Hi5 cells. For each test, 0.03-0.05mL of Sf9 cell culture amplifying baculovirus (Day 6 post-infection) or Hi5 cell culture infected with P3 (Day 3 post-infection) were observed under brightfield and GFP channels in the fluorescence microscope.

SDS-PAGE analysis revealed that Hi5 cultures expressed significantly higher amounts of GST-GSK3 β than Sf9 cultures, with 74kDa GST-GSK3 β protein band indicating successful expression and purification stages (**Figure 6.9**). The GST-GSK3 β band observed in the GSH-eluted samples from 10mL of Hi5 + P3 culture showed ~4-fold more protein compared to the GST-GSK3 β band from a 100mL Sf9 + P4 pellet. This result confirmed the previously discussed concerns, such as the reduction in infection efficiency of baculovirus from later generations causing issues with successful protein expression, and that Hi5 might be more suited for the expression of this protein than Sf9 cells. The approach of doubling the cell density before infection adapted in the new protocol also enhanced the efficiency of baculovirus infection and

subsequent protein expression, highlighting the critical role of optimizing cell culture conditions in improving protein yield.

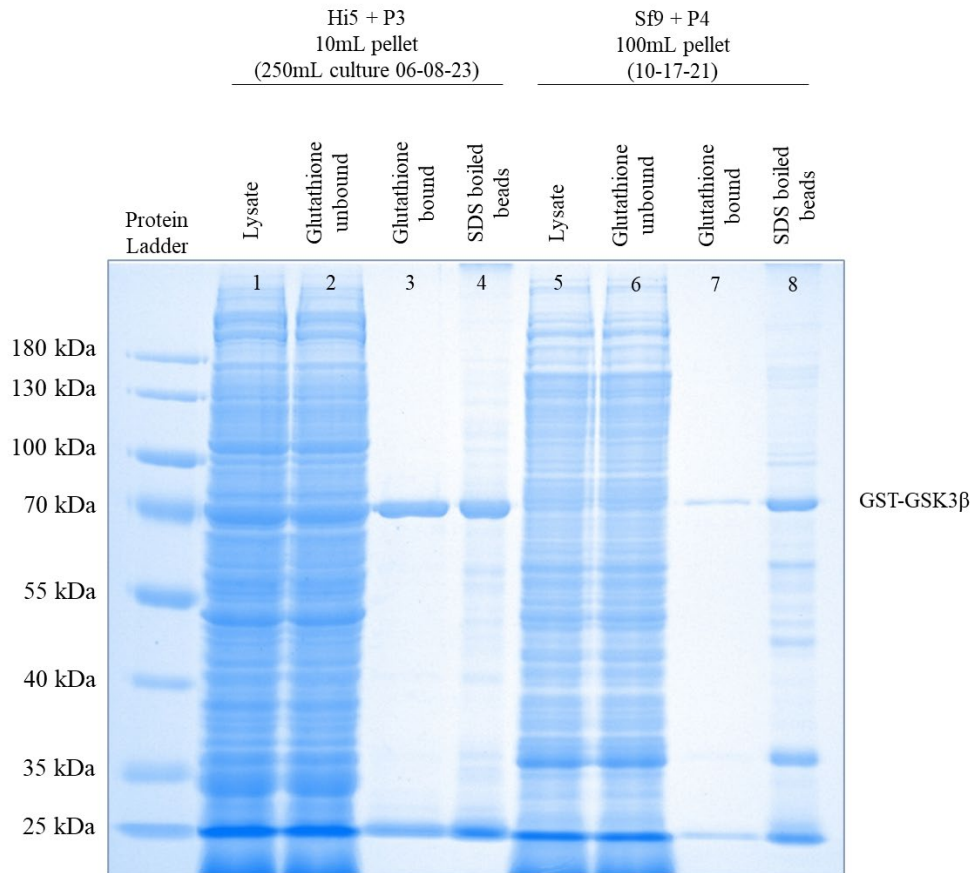


Figure 4.9: Hi5 Cultures Expressed Significantly Higher Amount GST-GSK3 β than Sf9 Cultures. The SDS-PAGE analysis compares the expression levels of GST-GSK3 β in cell lysates derived from 10mL Hi5 cell culture infected with P3 baculovirus (Hi5 + P3) and 100mL Sf9 cell culture infected with P4 baculovirus (Sf9 + P4). Lanes 1-3 represent samples from Hi5 + P3 cell lysates at different stages of the purification process: total lysate, supernatant post-glutathione bead binding, and proteins eluted from the Glutathione beads, respectively. Lanes 5-7 depict corresponding samples from Sf9 + P4 cell lysates. The analysis indicates a higher level of GST-GSK3 β expression in the Hi5 + P3 cell lysate compared to the Sf9 + P4 cell lysate, as evidenced by the intensity of the bands corresponding to GST-GSK3 β . Hi5 Cells were infected with the re-cloned and amplified baculovirus.

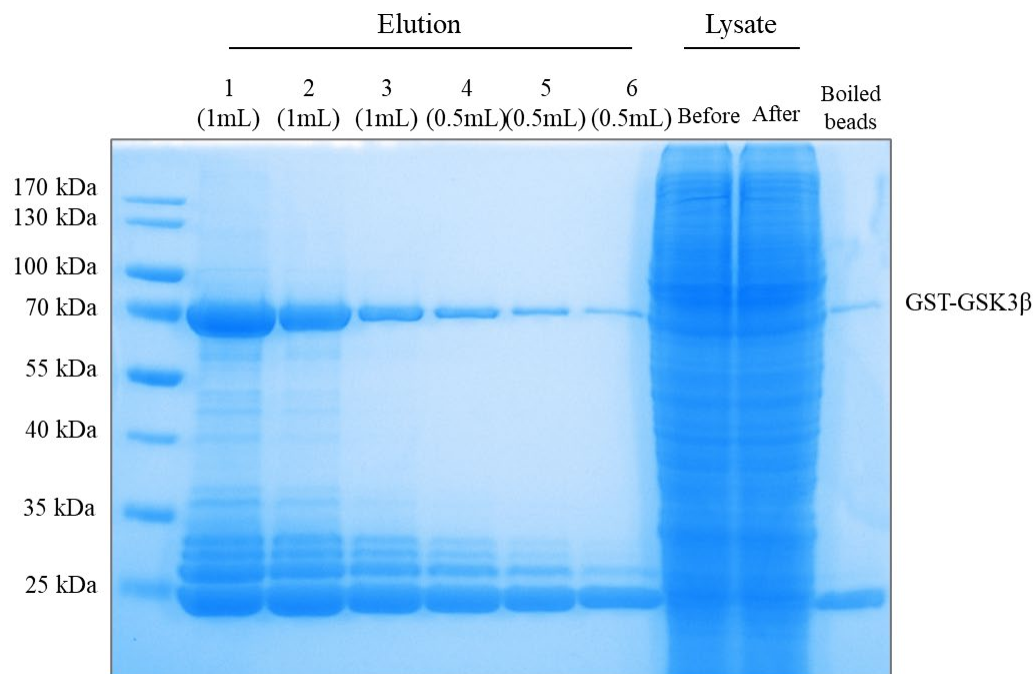


Figure 4.10: GST-GSK3 β Extraction and Purification from Hi5 Cells Infected with P3 via Glutathione-batch Bead Purification. The analyzed prep utilized pooled 250mL and 200mL pellets of Hi5 cultures (total 1.2L) grown to a density of 2-2.5 x 10⁶ cells/mL, infected with P3 at 5mL baculovirus:250mL culture volume ratio and incubated at 27 °C /125rpm for 72h. Lanes 1-6 on SDS-PAGE show GSH-elution from Glutathione beads. Each lane represents protein in 10.5 μ L from the total eluted volumes. The estimated concentration of eluted GST-GSK3 β was determined based on the total protein concentration, and gel band intensities for the GST-GSK3 β band was ~1 mg/mL.

The purification process was optimized, starting with glutathione-affinity purification, enzymatic removal of the GST tag, and final ion-exchange chromatography. The SDS-PAGE analyses (**Figure 6.10 and Figure 6.11**) demonstrated the effectiveness of each step, from the initial extraction of GST-GSK3 β from Hi5 cells to the final purification of GSK3 β with > 90% purity. The TEV protease cleavage site facilitated the efficient removal of the GST tag. At the same time, the ion-exchange chromatography and His-tag purification steps ensured the high purity of the final GSK3 β product.

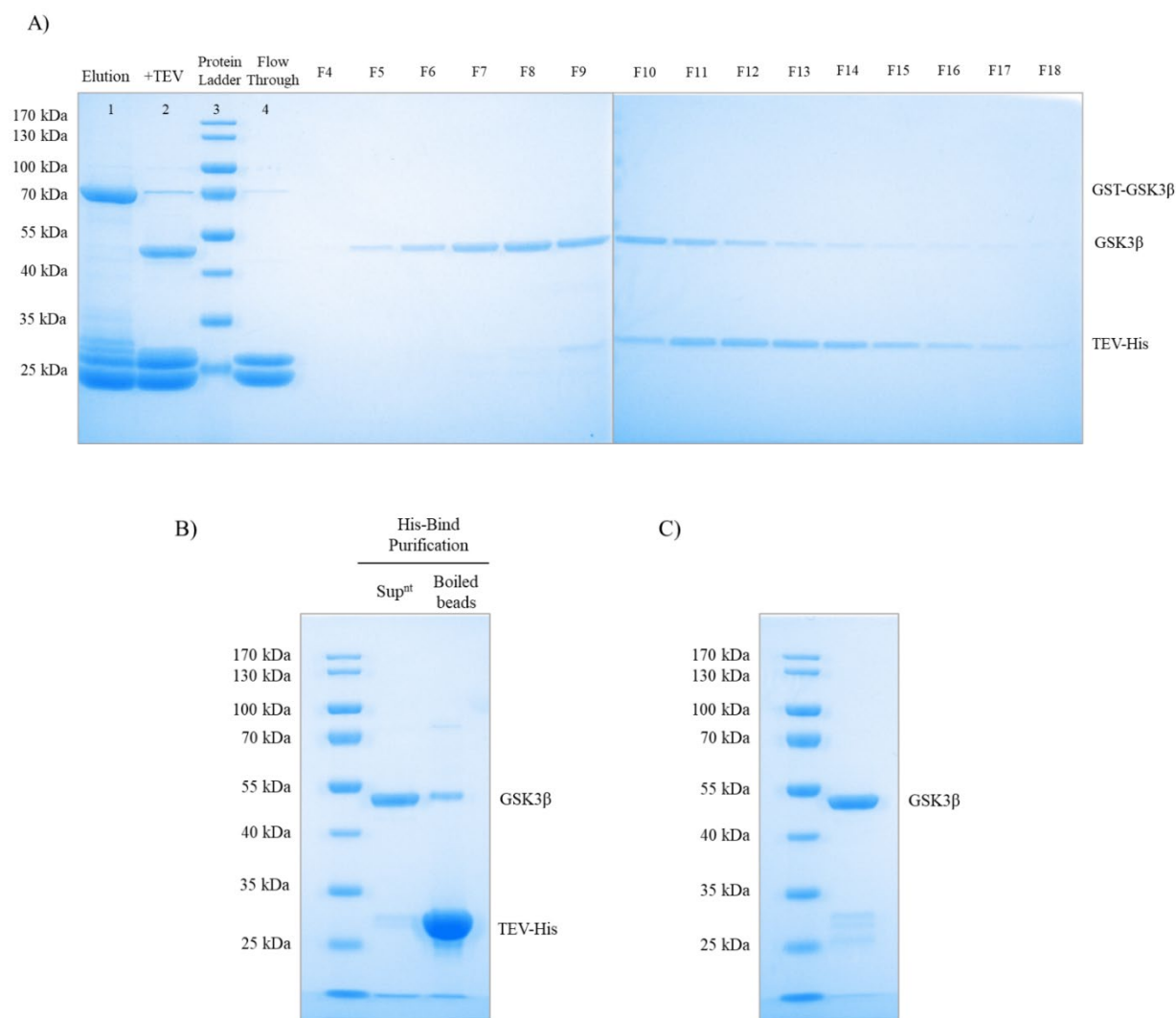


Figure 4.11: Purification of GSK3β by TEV-His Cleavage of GST tag, Ion-Exchange Purification, and His-Bind Resin Purification. A) SDS-PAGE Analysis of GST tag cleavage using TEV-His and ion-exchange purification of GSK3β. Lane 1 shows GST-GSK3β in the pooled GSH-elution samples from the Glutathione batch bead purification of 1.2L of Hi5 cultures infected with P3. Lane 2 shows the efficiency of GST tag cleavage following ~24h incubation of the pooled GSH-eluted protein with TEV-His at 4 °C. The gel band intensities show that a significant amount of GST-GSK3β underwent GST tag cleave. The cleaved GSK3β was purified via the SP (cation exchange) column on FPLC with 20mM HEPES pH 7.5, 50mM NaCl and 2mM β-Mercaptoethanol (Buffer A). Lane 4 shows trace amounts of intact GST-GSK3β and the non-specific endogenous Glutathione binding proteins in SP column flow-through. After washing the column with Buffer A, the bound protein was eluted with a linear NaCl gradient. GSK3β predominantly eluted in fractions F5-F12. TEV-His co-eluted with GSK3β starting from F9. B) SDS-PAGE analysis of the TEV-His purification using His-Bind beads from the GSK3β and TEV-His co-eluted fractions collected during ion-exchange purification. C) SDS-PAGE Analysis of final purified GSK3β protein shows > 90% purity.

Despite the successful implementation of the purification protocol in our lab, the yield and expression levels of GST-GSK3 β in Hi5 cultures were lower than those observed by our collaborators. Our collaborators obtained ~0.7-0.75mL of 84-94 μ M GSK3 β following protein extraction and purification from 2L Hi5 cultures infected with P3. Our lab obtained ~0.5-0.6mL of 10-11 μ M GSK3 β after protein extraction and purification from 1-1.2L batches of Hi5 cultures infected with P3.

This could be due to differences in available lab equipment, such as not having optimal incubators for maintaining 27 °C, which could affect protein expression levels, different centrifugation methods during protein extraction, and differences in SP column elution patterns during ion-exchange purification. For example, our collaborators saw fewer SP column fractions with co-elution of GSK3 β and TEV-His (Data not shown). At the same time, we observed several fractions containing higher amounts of GSK3 β , co-eluting with TEV-His, which required a further purification step involving His-bind bead purification, and every additional purification step leads to loss of final protein yield.

Chapter 5: Isothermal Titration Calorimetry (ITC) Ligand Binding Experiments for Glycogen Synthase Kinase3 β (GSK3 β)

Introduction

ITC is an invaluable technique in drug discovery for studying protein-ligand interactions, as it provides detailed information on binding thermodynamics. ITC can detect the heat changes that occur when a protein binds to a ligand. In a standard ITC experiment, the ligand is gradually added to a solution with the protein, and the heat that is either released or absorbed during the binding process is measured. The measured heat change reflects the energetic contributions to the interaction, such as electrostatic interactions, hydrogen bonding, van der Waals, hydrophobic interactions, and changes in solvent structuring. By analyzing these heat changes, key thermodynamic parameters such as the binding constant (K_A), the stoichiometry of the interaction (n), and the enthalpy of binding (ΔH) can be directly determined. Using the relationship between the Gibbs free energy (ΔG) and equilibrium constant and the relationship between ΔG , ΔH , and entropy (ΔS), the values of ΔG and ΔS for the particular temperature can be calculated. This capability to directly measure all thermodynamic parameters in a single experiment without labeling or immobilizing the protein or ligand makes it an authentic representation of biological interactions. The thermodynamic parameters derived from the heat measurements provide insight into the forces driving the interaction and stability of the resulting protein-ligand complex. Mechanistic binding details, such as the roles of specific amino acids at the binding site and their contributions to the overall binding energy, can also be explored using ITC. This enhances the understanding of molecular recognition and aids in the rational design of

effective therapeutics (Falconer et al., 2021; Y. Liang, 2008; Pierce et al., 1999; Velazquez-Campoy et al., 2015; Ward & Holdgate, 2001; Wiseman et al., 1989).

We aimed to establish an ITC binding assay for GSK3 β using ligands such as ATP and a substrate peptide of GSK3 β known as GSM to advance to study binding interactions between GSK3 β and its metal ion inhibitors, lithium, and beryllium. The study experienced many technical difficulties; some are documented in this chapter. Generally, published work reporting ITC binding data for protein-ligand interactions does not address the optimization work or technical challenges associated with developing an ITC binding assay. Therefore, this chapter will document some factors that can be useful in optimizing and troubleshooting ITC binding assays involving proteins.

Materials and Methods

Materials

The GSK3 β used for ITC binding experiments was derived from several sources. Early studies used GST-GSK3 β expressed in bacteria or Sf9 insect cells and purified via glutathione-affinity purification. The bacterially expressed GST-GSK3 β was a heterogeneous protein sample due to degraded versions of the protein (discussed in Chapter 4). GST-GSK3 β derived from Sf9 contained the full-length protein and displayed kinase activity (data not shown), but the overall protein concentration was low (discussed in Chapter 4). Many ITC experiments documented in this chapter used GSK3 β prepared via baculovirus expression in Hi5 cells and purified by Glutathione-affinity and ion exchange (SP Cation exchange) purification (described in Chapter 4). GSK3 β prepared by our collaborators was suspended in 20mM HEPES pH 7.5, 125mM

NaCl, and 1mM DTT and stored at -80 °C in aliquots following a quick freeze process in liquid N₂. These GSK3 β aliquots were thawed and diluted in the buffer of choice or dialyzed into the buffer of choice for ITC binding experiments. The GSK3 β stock solutions and dialyzed protein samples were quantified using a Qubit Protein Assay kit (Invitrogen #Q33211) or Pierce BCA Protein Assay kit (Thermo Scientific #23225).

The substrates used in the experiments included ATP (Sigma #A2383), non-hydrolyzable ATP analog, adenylyl-imidodiphosphate (AMP-PNP) (Roche Diagnostics #10102547001), GSM, a synthetic substrate peptide of GSK3 β (Millipore Sigma #12-533) and Alsterpaullone (Santa Cruz #sc-202455). The ITC binding experiments were performed in buffers TRIS Base (J.T. Baker #4099-02), HEPES (Sigma #H3375) BIS-TRIS (Sigma #SLBV2468), supplemented with NaCl (Ameresco #0241), MgCl₂ (Sigma #SLBQ9064V), DTT (Roche Diagnostics #10197777001) or, β -Mercaptoethanol (OmniPur #6010). L-arginine (Sigma Aldrich #A5131) and L-glutamic acid (Sigma Aldrich #G1251) were used for improved protein solubility where specified.

ITC Binding Experiments

All binding experiments on MicroCal PEAQ-ITC (PEAQ-ITC Instrument Cell Serial #MAL1122596 and PEAQ-WM Serial #29061559-0047) used the 13-injection method. The GSK3 β solutions were prepared for each ITC experiment as a 300 μ L sample, and 280 μ L was loaded into the ITC cell. The final reaction volume in the adiabatic cell is 200 μ L. The ligand solutions were prepared with matching buffer components, and 75 μ L loaded into the ITC syringe. The reactions were performed at 15 °C or 25 °C with 750 or 500 rpm stir speed. Once

the samples had equilibrated to the assigned temperature and the baseline was stable, the ligand was injected, typically starting at $t = 1$ min. In the first injection, $0.4\mu\text{L}$ is injected as a priming step (this volume can be adjusted to be less if desired), followed by $12 \times 3\mu\text{L}$ injections to obtain a binding isotherm. The injection spacing can be determined during preliminary experiments and adjusted as needed. By default, it is 150 seconds. The baseline in a raw ITC thermogram is influenced by the set reference power, the constituents of the buffer solutions, and the exact volume loaded into the sample cell. To directly compare various ITC experiments within the same graph, each thermogram's baseline was normalized to a DP of 0. This was achieved by deducting the starting baseline DP value and utilizing Microsoft Excel software to adjust or subtract the baseline for each experiment in the MicroCal PEAQ-ITC Analysis software.

Results and Discussion

ITC Thermograms for ATP vs. GSK3 β

Initial experiments were conducted using GST-GSK3 β , which was expressed in bacteria and partially degraded. Titration of ATP against the protein sample in 25mM HEPES pH 7, 150mM NaCl, and 10mM MgCl₂ displayed broad exothermic peaks (**Figure Appendix IV.A**). The peaks produced due to ligand-protein interactions were markedly different from the exothermic peaks observed upon ATP vs. buffer titration, and despite the presence of exothermic peaks indicating potential interactions between ATP and GSK3 β , the heterogeneous nature of the protein preparation likely affected the thermodynamic parameters, making it challenging to fit these data into a standard binding model. Experiments performed with GST-GSK3 β expressed

via baculovirus expression in Sf9 cells did not produce any binding behavior, potentially due to the low protein concentration (data not shown).

Titration with ATP were conducted against GSK3 β expressed in Hi5 cells. The GST tag was cleaved, and the protein was purified via ion exchange chromatography. Therefore, the protein sample was highly pure. The titration of 2mM ATP vs. 10 μ M GSK3 β yielded a similar result as previously observed. After each injection, an exothermic peak was observed, and each peak took approximately 5 minutes to return to the baseline (**Figure Appendix IV.B**, R3093). The titration was continued with 5mM ATP (R3094), and the exothermic peaks gradually declined, although each peak took approximately 5 minutes to return to the baseline. This peak behavior emulated an enzymatic reaction more than a binding event. The integrated heat vs. molar ratio plots give the illusion of a binding curve. However, the data could not be fitted to an appropriate binding model to derive data. Typically, ITC signals for a binding event resolve much faster. Wang et al. (2022) reported a similar-looking result in ITC that was attributed to background ATP hydrolysis, where they demonstrated a bacterial phosphotransferase: aminoglycoside-3'-phosphotransferase-IIIa exhibited low levels of ATP hydrolysis in the absence of the phospho-acceptor substrate (Y. Wang et al., 2022). The consistency of these results across different protein preparations hinted at underlying enzymatic activity rather than direct binding interactions. Therefore, a non-hydrolyzable ATP analog, AMP-PNP, was utilized to follow ITC binding experiments (Bertrand et al., 2003).

Alsterpaullone is an ATP-competitive potent synthetic inhibitor of GSK3 β with an IC₅₀ of 4nM (Kunick et al., 2004; Wei et al., 2022). An IC₅₀ value in the nanomolar range implies a more substantial binding event between Alsterpaullone and GSK3 β . Therefore, 10 μ M Alsterpaullone

was titrated against 10 μ M GSK3 β in the HEPES buffer system; however, no detectable binding was observed (**Figure Appendix IV.C**)

ITC Thermograms for AMP-PNP vs. GSK3 β

Upon switching to the non-hydrolyzable ATP analog, AMP-PNP, the interaction studies (**Figure Appendix IV.D**) continued to show no binding despite observing some changes in the thermogram profiles (R3117). Some exothermic peaks that displayed a slow return to baseline were observed when AMP-PNP was continued to be titrated into the R3117 cell (R3118). This was surprising given AMP-PNP's stability against hydrolysis, suggesting that ATP hydrolysis might not have been the sole issue in previous experiments. Subsequent binding experiments were conducted, including a GSK3 β substrate peptide (20 μ M GSM peptide) both in the syringe solution with 5mM AMP-PNP and the ITC cell with the 10 μ M GSK3 β (**Figure Appendix IV.E**). The binding of the phospho-acceptor substrate to GSK3 β could stabilize the conformation of the catalytic site, making it more favorable for AMP-PNP binding by adopting a more closed or properly aligned conformation that effectively positions critical residues for ATP (or ATP analog) binding. This is a form of allosteric regulation where the binding of one molecule influences the binding site for another molecule. This mode of enhancement of AMP-PNP binding to GSK3 β may produce a more pronounced heat change measurable by ITC. However, in this experiment (R3119), no binding was observed.

The attempted ITC binding experiments were performed in a HEPES buffer system. HEPES contains a sulfonate group, which might be weakly competitive with the phosphate groups on the primed phosphorylated site of the peptide substrate and those in the ATP molecule.

Dajani et al. (2001) crystallized GSK3 β suspended in a HEPES buffer system, and the analysis of the crystal structure revealed the sulfonate group of HEPES occupying phosphate binding sites of GSK3 β (Dajani et al., 2001). Therefore, we decided to perform the binding experiments in TRIS pH 8 buffer instead of HEPES pH 7. The ionization states would be slightly different at pH 8. Additionally, TRIS buffer has a higher ionization enthalpy, which could amplify the strength of the ITC signals corresponding to binding interactions. An ITC kinase activity assay performed for GSK3 β activity in different buffers and pH demonstrated that the reaction in TRIS pH 8 buffer generated the most significant thermal signal (discussed in Chapter 6). In addition to changing the buffer, the ionic strength of the solution was lowered by decreasing the NaCl and MgCl₂ concentrations to provide a less stringent binding environment.

A significant baseline shift was observed when binding experiments were performed in TRIS pH 8 buffer. Typically, the reference cell is maintained at 41.9 μ J/sec, and the baseline in the sample cell is adjusted relative to this. When a binding event occurs, the corresponding exothermic or endothermic signal will deviate from the baseline and resolve. However, we observed that the baseline at the beginning of the ITC experiment was unusually below the typically observed baseline. The ITC thermogram baseline displayed a sigmoidal shape, starting at a low baseline and then shifting to a higher baseline, producing exothermic peaks of the same size. This phenomenon was observed when the nucleotide was titrated into GSK3 β (**Figure Appendix IV.F**) and when the peptide substrate was titrated into GSK3 β (**Figure Appendix IV.G**). In each case, protein was the common factor.

Hypothesis: Protein Adsorption

The ITC cell and syringe are cleaned extensively after every run. However, suppose there is residual GSK3 β protein sticking to the cell wall despite cleaning. In that case, when a fresh protein solution is added to start a new run, the new protein may adsorb to the existing protein film built on the ITC cell walls. This adsorption is an exothermic process, which would result in a low initial baseline. Once most of the protein is depleted from the cell because it has been adsorbed to the walls, the adsorption reaction ceases, and the baseline goes up, explaining the sigmoidal baseline. Also, this hypothesis would explain why a baseline shift is not observed in the titrant-to-buffer or buffer-to-buffer control runs. A stringent cleaning protocol was established to test this hypothesis by soaking the cell in concentrated detergent solution for several hours at 60 °C and additionally soaking the cell in Proteinase K (to degrade any accumulated proteins from the cell) followed by multiple rinses with ultra-pure H₂O. ITC runs conducted following the stringent cleaning did not display the unusual baseline shift. Subsequent ITC runs followed by titrating 0.5mM GSM peptide substrate against 10 μ M GSK3 β , or 5mM AMP-PNP against GSK3 β , or the titrating a combination of peptide and nucleotide against 10 μ M GSK3 β did not show binding (**Figure Appendix IV.H**).

In order to observe binding, the protein concentration in the ITC cell was increased. One study has reported K_D values for GSK3 β vs. ligand binding using ITC. The study reported two K_D values, 600 μ M, and 9 μ M for ligand-GSK3 β interaction between two synthetic pyridinyl amides (0.5-2mM) and GSK3 β (at 50-85 μ M) with 2.5-5% DMSO (DMSO likely added to match conditions of ligand solution)(Wang et al., 2016). Other buffer conditions were not reported. The most prominent peak measured was approximately 1.2 μ W (= μ J/sec). A K_M value of 50.2 μ M is

reported for ATP and GSK3 β (Knight & Shokat, 2005). These values suggest that a higher concentration of GSK3 β is ideally required in the ITC cell to observe potential binding.

ITC Thermograms for AMP-PNP vs. Concentrated GSK3 β Samples

5mM AMP-PNP was titrated against increased concentrations of GSK3 β , approximately 43.9 μ M and 42.45 μ M. These titrations were performed under conditions optimized to potentially enhance binding detection, using a buffer of 50mM TRIS pH 8, 20mM NaCl, and 10mM MgCl₂ at 15 °C (**Figure 5.1**). The overall thermograms for each titration were similar to thermograms from the titrant to buffer control experiments except for the second injection (the first injection is a 0.1 μ L “pre-injection” that serves only to remove looseness in the injector system in preparations for the larger analytical injections to follow). For the second injection there was a distinct small exothermic peak (**Figure 5.1A and C**). The enlarged views (**Figure 5.1B and D**) focus on this initial peak, showing its reproducibility and hinting at a potential binding event. However, subsequent injections did not produce additional notable peaks, limiting our ability to characterize binding interaction further under these conditions.

A notable observation during these experiments was that the protein solution recovered from the ITC cell post-run was opaque. Once the protein samples were centrifuged, a small white pellet could be detected, indicating protein precipitation during the ITC experiment. The clear supernatant was tested for kinase activity (ITC kinase assay) and detected enzyme activity (data not shown). This implies that the protein solution during the ITC experiment was partially aggregated, leading to a heterogeneous protein population of enzymatically active GSK3 β and aggregated GSK3 β . Protein aggregation would effectively lower the GSK3 β availability for

binding, and thus, the overall heat generated from binding events would still be small. Several changes were introduced. The stock GSK3 β was suspended in 25mM HEPES pH 7.5, 125mM NaCl, and 1mM DTT (~80-94 μ M stock). When preparing protein solutions of ~43 μ M concentration in 50mM TRIS pH 8, 20mM NaCl, and 10mM MgCl₂ buffer, there would still be a high concentration of HEPES buffer carried over (~11mM). HEPES may weakly compete for phosphate binding sites on GSK3 β , and the competition would be prevalent at millimolar concentrations, compared to AMP-PNP, which would reach less than 1mM in the cell even after 12 injections. Therefore, the GSK3 β solutions were dialyzed into the binding buffer before use for ITC experiments. Additionally, the stirring speed during the ITC reaction was reduced from 750 rpm (default setting) to 500 rpm because excessive stirring could promote protein aggregation. The AMP-PNP concentration was reduced from 5mM to 2.5mM. If the protein was saturated from the first injection of 5mM AMP-PNP, we may not see a binding pattern other than the small exothermic peak for the first injection. By reducing the nucleotide concentration by half, we expected to see maybe a second or third exothermic peak. Despite having made these changes, the binding experiment yielded similar results as previously observed (**Figure 5.2**). The post-ITC protein solution was opaque and yielded a small white pellet following centrifugation, indicating protein precipitation. Given the persistent issue with protein precipitation, the experimental conditions were further refined.

The pI of GSK3 β is 7.98. Having the protein solution prepared in TRIS pH 8 buffer might not be optimal for GSK3 β at high concentrations. A protein would have a net zero charge at its isoelectric point. At pH 8, GSK3 β would be predominantly a zwitter ion and, at high concentrations, might tend to form aggregates and precipitate. The ITC kinase assay for GSK3 β activity produced the second largest signal in BIS-TRIS pH 6.5 (discussed in Chapter 6). Buffer

conditions optimal for enzymatic reaction would also be optimal for substrate binding. pH 6.5 would be more than 1 pH unit different from the pI of GSK3 β , ensuring a more ionized protein and improving protein solubility. Simultaneous addition of 50mM of the charged amino acids L-arginine and L-glutamate to protein solutions can improve protein solubility at high concentrations (Golovonov et al., 2004). The stock GSK3 β was dialyzed into 50mM BIS-TRIS pH 6.5, 20mM NaCl, and 10mM MgCl₂, 50mM L-Arg, 50mM L-Glu, and 0.5mM β -Mercaptoethanol and used for an ITC binding experiment where 2.5mM AMP-PNP in prepared in matching buffer conditions were titrated against GSK3 β (**Figure 5.3**). Unlike before, the post-ITC cell solution was clear and not opaque, indicating improved protein solubility. However, the result of the binding experiment was not different. The small exothermic peak at the second injection was reproduced, but subsequent injections did not clearly show binding. The exothermic peak at the second injection of the titration was repeatedly observed and is distinct from the peaks measured during the respective titrant-to-buffer controls. Therefore, we can conclude that a binding event is present, but thermodynamic parameters could not be derived since a binding isotherm could not be obtained under the tested experimental conditions. The exothermic peak suggests that the AMP-PNP binding to GSK3 β is an enthalpically favorable binding event.

Highly concentrated GSK3 β solutions are prone to frothing, which complicates the loading of the ITC cell by making it difficult to avoid air bubbles. The presence of these air bubbles can disrupt the accurate measurement of heat changes, leading to fluctuations in the baseline and unwanted spikes in the thermogram. If frothiness leads to the formation of air bubbles during loading, the protein sample must be drawn out and reloaded. However, we observed that GSK3 β is susceptible to precipitation when subjected to multiple loading attempts,

posing an additional technical challenge during ITC binding experiments with highly concentrated GSK3 β samples. Therefore, exploring methods to enhance GSK3 β solubility in highly concentrated solutions would be advantageous, as it could improve binding measurements.

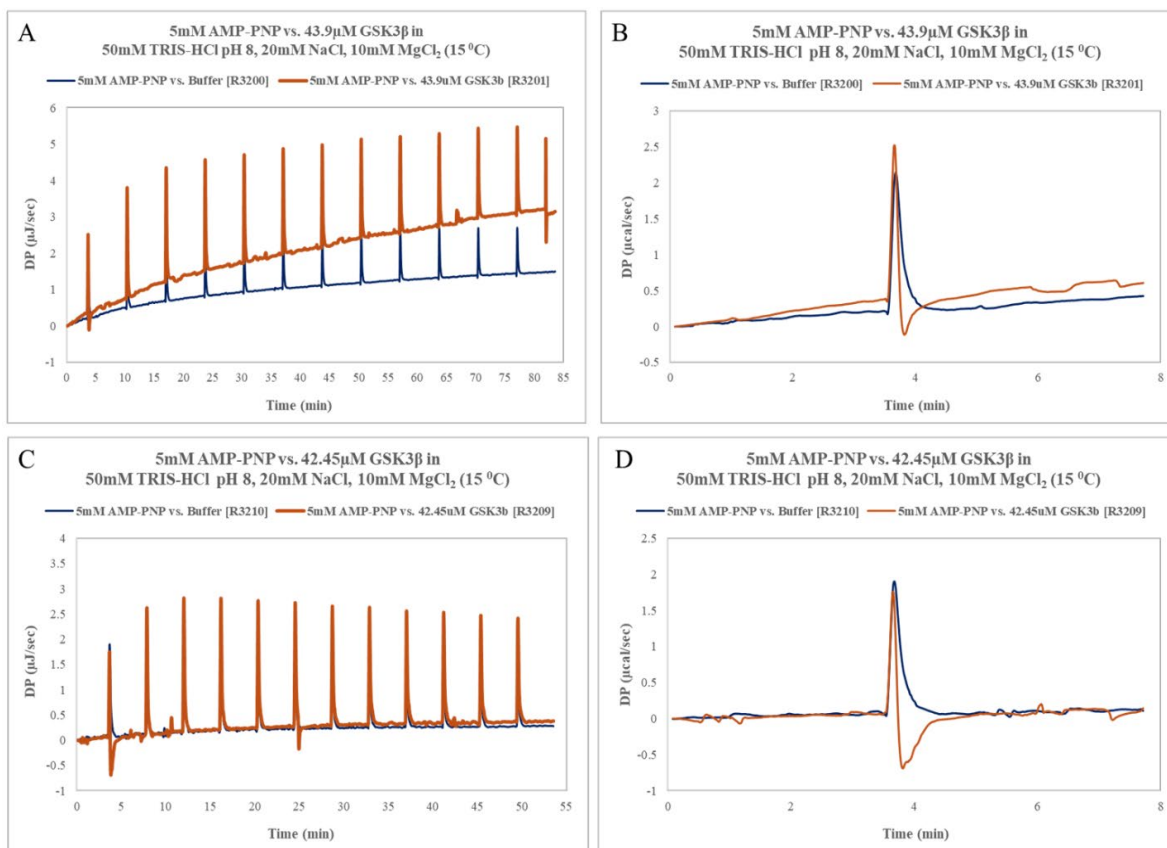


Figure 5.1: ITC Thermograms for AMP-PNP vs. GSK3 β . ITC binding experiments for 5mM AMP-PNP vs. ~ 43 μ M GSK3 β were performed in 50mM TRIS pH 8, 20mM NaCl, and 10mM MgCl₂ at 15 °C. In each titration, the nucleotide is in the syringe and is incrementally injected into the cell containing the protein with 12 x 3 μ L injections. The blue curves show the thermograms for AMP-PNP vs. Buffer, and the orange curves for AMP-PNP vs. GSK3 β . (A) 5mM AMP-PNP vs. 43.9 μ M GSK3 β (B) Enlarged view of the first injection from A (C) 5mM AMP-PNP vs. 42.45 μ M GSK3 β (D) Enlarged view of the first injection from B.

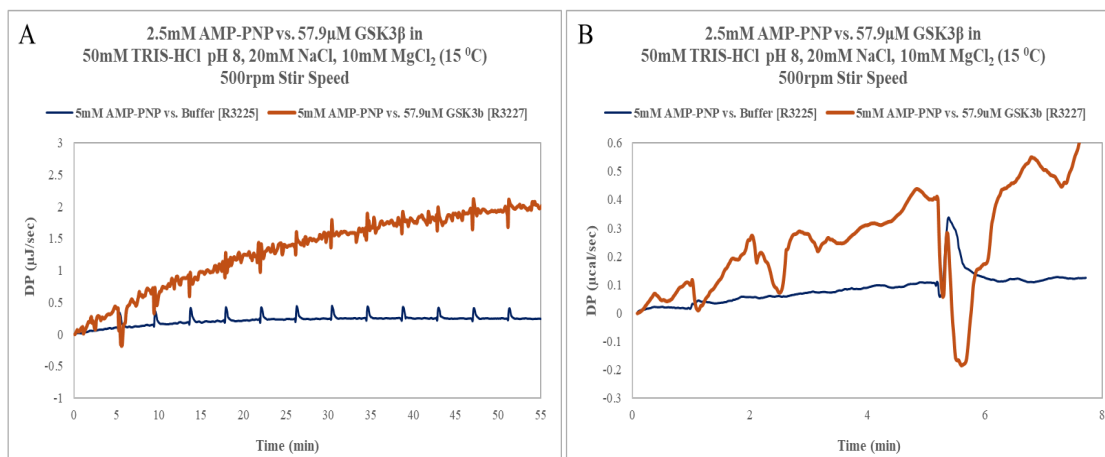


Figure 5.2: ITC Thermograms for AMP-PNP vs. GSK3 β . ITC binding experiments for 2.5mM AMP-PNP vs. $\sim 57.9 \mu\text{M}$ GSK3 β were performed in 50mM TRIS pH 8, 20mM NaCl, and 10mM MgCl₂ at 15 °C and reduced stir speed at 500rpm. The GSK3 β used for the experiment was pre-dialyzed in 50mM TRIS pH 8, 20mM NaCl, and 10mM MgCl₂ at 4 °C to remove carryover HEPES buffer and DTT from the stock GSK3 β solution. In each titration, the nucleotide is in the syringe and is incrementally injected into the cell containing the protein with 12 x 3 μL injections. The blue curves show the thermograms for AMP-PNP vs. Buffer, and the orange curves for AMP-PNP vs. GSK3 β . (A) 5mM AMP-PNP vs. 57.9 μM GSK3 β (B) Enlarged view of the first injection from A.

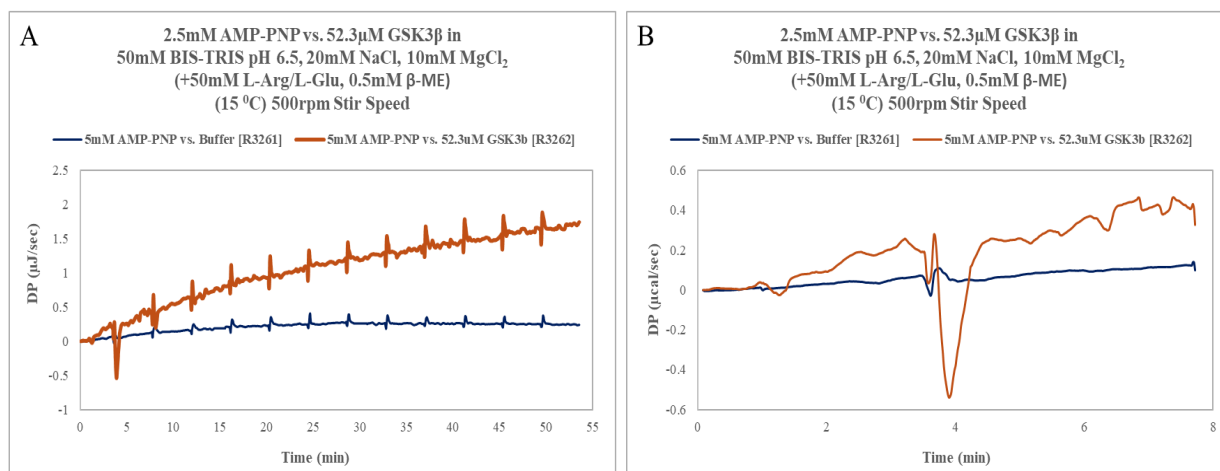


Figure 5.3: ITC Thermograms for AMP-PNP vs. GSK3β. ITC binding experiments for 2.5mM AMP-PNP vs. ~52.3 μM GSK3β were performed in 50mM BIS-TRIS pH 6.5, 20mM NaCl, 10mM MgCl₂, 50mM L-Arginine, 50mM L-Glutamate and 0.5mM β-Mercaptoethanol at 15 °C. The GSK3β used for the experiment was pre-dialyzed in 50mM BIS-TRIS pH 6.5, 20mM NaCl, 10mM MgCl₂, 50mM L-Arginine, 50mM L-Glutamate and 0.5mM β-Mercaptoethanol at 4 °C. In each titration, the nucleotide is in the syringe and is incrementally injected into the cell containing the protein with 12 x 3μL injections. The blue curves show the thermograms for AMP-PNP vs. Buffer, and the orange curves for AMP-PNP vs. GSK3β. (A) 2.5mM AMP-PNP vs. 52.3μM GSK3β (B) Enlarged view of the first injection from A.

Chapter 6: Kinetic Characterization of GSK3 β Phosphorylation using Isothermal Titration Calorimetry (ITC)

Background and Introduction

Kinetic Characterization of Enzymes

Enzyme kinetics is a pivotal area of biochemistry that studies the rates of enzyme-catalyzed reactions. It offers insight into how enzymes, biological catalysts, increase the rate of virtually all cell chemical reactions and how they are regulated. Enzyme kinetics studies can reveal how enzymes bind to substrates (the molecules they act on) and turn them into products, the mechanisms by which enzymes can achieve such remarkable feats of catalysis, and also help understand how enzyme activity is finely controlled by the cell to meet the demands of metabolism.

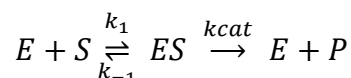
Studying enzyme kinetics involves measuring reaction rates and observing how enzyme concentration, substrate concentration, and the presence of inhibitors or activators affect these rates. This information is essential to understand an enzyme's role in the body and how cells adjust to different conditions. Furthermore, enzyme kinetic studies have significant implications for medical and industrial applications, particularly in drug development, where enzyme inhibition studies are critical for therapeutic design, and in biotechnology, where enzymes are employed to catalyze industrial-scale biochemical reactions (Nagar et al., 2014).

The mathematical modeling of enzyme kinetics, including the derivation of equations such as the Michaelis-Menten equation, allows for the quantitative description of these reactions. These models facilitate the comparison of enzyme activities under different conditions and help

predict the effects of mutations on enzyme function, offering insights into the design of enzyme inhibitors and activators (Johnson & Goody, 2011).

Generally, enzymes exhibit saturation kinetics as explained by the Michaelis-Menten model, depicted in **Scheme 6-1**.

Scheme 6-1:



In this model, an enzyme (E) interacts with a substrate (S), forming a complex (ES) at rate k_1 (association) and k_{-1} (dissociation). The enzyme then converts the substrate into a product (P) at a rate of k_{cat} . This mechanism leads to the well-known Michaelis-Menten equation, where the initial reaction velocity, v_0 , shows a saturation effect as substrate concentration increases. The initial reaction velocity is equal to the rate of substrate consumption or the rate of product formation, as shown in equation 6.1.

Equation 6.1:

$$v_0 = -\frac{d[S]}{dt} = \frac{d[P]}{dt}$$

Applying the steady state assumption, the Michaelis-Menten equation can be derived for the model in **Scheme 6-1**.

Equation 6.2:

$$v_0 = \frac{V_{max} [S]}{K_M + [S]}$$

V_{max} represents the maximum rate of an enzyme-catalyzed reaction when the enzyme is saturated with substrate. K_M is the substrate concentration at which an enzyme-catalyzed reaction proceeds at half its maximum velocity ($V_{max}/2$), indicating the enzyme's affinity for its substrate. K_M can also be explained through the rate constants for the formation and breakdown of the ES complex. Therefore, K_M can be given as the ratio of the sum of the dissociation and catalysis rate constants to the association rate constant reflecting the enzyme's substrate affinity in terms of its forward and reverse reactions.

Equation 6.3:

$$K_M = \frac{k_{-1} + k_{cat}}{k_1}$$

The reaction velocity depends on the rate of product formation, which can also be explained with respect to the rate of ES complex breakdown. The velocity becomes maximum when substrates occupy all the enzyme (or all active sites). Therefore, the maximum velocity can be represented by the catalysis rate multiplied by the total enzyme concentration $[E]_t$, as shown next. This relationship shows how the maximum rate is directly proportional to the total enzyme concentration available.

Equation 6.4:

$$V_{max} = k_{cat} [E]_t$$

The catalysis rate constant, k_{cat} , is also called an enzyme's turnover number. It quantifies how many substrate molecules one enzyme molecule (or the number of active sites participating

in the reaction) can convert into a product per unit of time when the enzyme is fully saturated with substrate.

During enzyme kinetic experiments, measurements primarily focus on the reaction rate at varying substrate concentrations. Typically, the initial reaction velocity (v_0) is measured under different substrate concentrations to ensure that the rate reflects only the early phase of the reaction where the reverse reaction ($P \Rightarrow S$) is negligible. The reaction rate is measured by substrate consumption or product formation over time. Plotting these velocities against the substrate concentrations produces a curve that can be fitted to the Michaelis-Menten equation. This fitting process allows for extracting the crucial kinetic parameters K_M , V_{max} , and k_{cat} . Through this analysis, the Michaelis-Menten model provides insight into the fundamental properties of enzyme-catalyzed reactions, including how quickly an enzyme can work and how tightly it binds its substrate.

Most enzyme-catalyzed reactions are not as straightforward as converting a single substrate into a single product. Such reactions often involve two or more substrates interacting to produce multiple products. This complexity arises from the need to understand how each substrate and product influences the reaction rate, which can complicate the kinetics analysis. Despite these challenges, the fundamental principles of the Michaelis-Menten model can still be applied to these multi-substrate and multi-product reactions, with modifications to reaction conditions to accommodate the additional complexity. A typical practical approach to studying such reactions involves mimicking pseudo-first-order kinetics for a particular substrate of interest. This is achieved by maintaining a high concentration of the other substrates, ensuring their concentrations do not limit the reaction rate. This technique simplifies the kinetic analysis by allowing the focus to remain on how changes in the concentration of the substrate of interest

affect the reaction rate, facilitating the derivation of kinetic parameters similar to those obtained for more straightforward reactions (Seibert & Tracy, 2014; Wharton & Eisenthal, 1981).

Isothermal Titration Calorimetry (ITC) in Studying Enzyme Kinetics

Isothermal Titration Calorimetry (ITC) allows the analysis of enzyme kinetics by directly measuring the heat flow associated with enzymatic reactions. This technique can readily determine whether an enzyme-catalyzed reaction is exothermic or endothermic, facilitating the straightforward calculation of kinetic parameters. Unlike traditional enzyme assays, which often rely on detecting changes in substrate, product, or cofactor concentrations over time through methods such as UV/Vis absorbance, fluorescence, and even secondary detection techniques requiring specialized reporter molecules or post-reaction separations (e.g., FRET assays, ADP-Glo assays, HPLC, GC, MS), ITC measures the enthalpy change directly and derive the kinetic parameters based on the rate of heat flow. This eliminates the need for modified substrates, indirect measurements, or complex setups, allowing for studying enzyme reactions under conditions close to their natural cellular environment. ITC provides a more direct and universally applicable approach to studying enzyme reactions, simplifying the experimental process, and offering insights into the thermodynamics and kinetics of enzyme-catalyzed reactions in conditions that closely mimic the cell's natural environment (Todd & Gomez, 2001; Y. Wang et al., 2020).

Once a reaction is initiated by mixing substrate and enzyme in the ITC cell, the instrument measures the heat flow as a function of time, expressing this as differential power (DP), calibrated against the reference power (equation 6.5). For exothermic reactions, where heat

is released, the DP value decreases relative to the reference, and for endothermic reactions, where heat is absorbed, the DP value increases. The direction and magnitude of DP shifts can provide insight into the reaction's thermodynamic nature and kinetic speed (Bianconi, 2007; Olsen, 2006; Todd & Gomez, 2001; Y. Wang et al., 2020).

Equation 6.5:

$$DP = \frac{dQ}{dt}$$

Where:

dQ/dt = The heat change observed at a given time point ($\mu\text{cal/sec}$ or $\mu\text{J/sec}$)

The ITC determines the reaction's apparent enthalpy (ΔH_{app}) by integrating the area under the curve in the ITC raw plot (equation 6.6). The ΔH_{app} represents the combined heat effects taking place in the ITC cell during a reaction, which includes the intrinsic enthalpy of the reaction (ΔH_{rxn}) and any heat variations associated with buffer ionization (proton uptake or release) and the heats of dilution associated with the mixing of substrates with the enzyme solution in the buffer. The total heat generated from the reaction when a specific amount of substrate moles is converted to the product can be given by equation 6.7 (Todd & Gomez, 2001).

Equation 6.6:

$$\Delta H_{\text{app}} = \frac{(\int_{t=0}^{\infty} DP \, dt)}{V_{\text{cell}} \cdot [S]_0}$$

Where:

$[S]_0$ = the total concentration of substrate injected into the ITC cell (M)

V_{cell} = the reaction volume of the ITC cell (L)

Equation 6.7:

$$Q = n \cdot \Delta H_{\text{app}} = [P] \cdot V_{\text{cell}} \cdot \Delta H_{\text{app}}$$

Where:

Q = heat measured for the complete reaction (kJ)

n = the moles of substrate injected into the ITC cells for the reaction (mol)

ΔH_{app} = The apparent reaction enthalpy obtained by integrating the area under the raw ITC curve (kJ/mol)

[P] = The concentration of product generated by the conversion of n moles of substrate (M)

Since the rate of the reaction is represented by the rate of product formation $[dP]/dt$, and the change in DP is directly proportional to the rate of product formation, the above relationships can be rearranged to show how ITC determines the reaction rate (Rate_{ITC}).

Equation 6.8:

$$DP = \frac{dQ}{dt} = \frac{d[P]}{dt} \cdot V_{\text{cell}} \cdot \Delta H_{\text{app}}$$

Equation 6.9:

$$\text{Rate}_{\text{ITC}} = \frac{DP}{V_{\text{cell}} \cdot \Delta H_{\text{app}}}$$

Enzyme assays for measuring enzyme activity can be categorized as continuous and discontinuous (Harris & Keshwani, 2009). Continuous assays provide real-time monitoring of the reaction, allowing for observing substrate or product concentration changes as the reaction proceeds. This method is advantageous for kinetic studies because it offers instantaneous data, allowing for the calculation of reaction rates concurrently with the catalytic process. On the other hand, discontinuous assays require periodic sampling of the reaction mixture at different time points following quenching of the reaction using specific methods before analysis. Although this approach might not provide the immediacy of continuous assays, it is helpful for conditions under which the reaction cannot be easily monitored in real-time or when multiple samples need to be compared under identical conditions. In ITC experiments, the reaction is monitored in real-time as the assay progresses, with the heat flow being measured continuously as substrate injections are made into the enzyme solution. This allows for the direct and continuous observation of the reaction kinetics and thermodynamics. ITC kinase experiments can be performed in two ways: 1) multi-injection assay and 2) single-injection assay (Todd & Gomez, 2001).

The multiple-injection ITC assay involves the sequential addition of small substrate volumes into an enzyme solution within the ITC cell, allowing for real-time analysis of the reaction rates across a series of injections according to equation 6.9. This design allows for minimal substrate consumption post-injection because the enzyme concentration is chosen to be low enough for minimal substrate depletion but would still produce discernible signals. Since the enzyme concentration is low, the signal will take longer to return to the baseline, and with closely spaced injections, the reaction can be maintained under steady-state conditions. As a result, the DP continues to increase or decrease depending on the type of reaction, forming a

staircase pattern with each step corresponding to a substrate injection. The DP change between the initial baseline and the baseline of each step reflects the reaction rate corresponding to the substrate concentration in the ITC following the respective injection. This strategy allows $[S] \ll K_M$ during the initial injections and $[S] \gg K_M$ towards the final injections. A comprehensive Michaelis-Menten curve can be constructed by plotting the rates determined from the DP change for each injection against the respective substrate concentration in the ITC cell post-injection. The multiple-injection strategy is advantageous since it requires low enzyme concentrations. Since substrate depletion is minimal upon each injection, the product accumulation through the course of the reaction is low; therefore, it is a beneficial assay for enzyme reactions with potent product inhibition (Y. Wang et al., 2019). However, reaching saturation might require numerous injections because each injection provides only a single rate value, and a prolonged time for the assay could impact enzyme stability. The reliance on low enzyme concentration also increases the vulnerability of the signal to noise. Additionally, the multiple-injection method requires an additional experiment to determine the reaction's enthalpy, which makes the data analysis process more complicated (Todd & Gomez, 2001; Transtrum et al., 2015; Y. Wang et al., 2020).

The single-injection ITC assay involves introducing the substrate into the enzyme solution in the ITC cell or vice versa via one injection, which produces a pronounced initial deviation in the DP value due to the catalytic heat release or absorption based on the type of reaction. The enzyme concentration in the ITC cell should be high enough to ensure all injected substrate is converted to product but low enough that the raw ITC peak is broad and the signal returns to the baseline within the order of minutes as the substrate is consumed. The substrate concentration in the ITC cell post-injection should be high enough to saturate the enzyme (Di Trani et al., 2017; Todd & Gomez, 2001; Transtrum et al., 2015; Y. Wang et al., 2020).

The advantage of this method is the ability to measure the enthalpy of the reaction and construct a comprehensive Michaelis-Menten curve with data from a single experiment. The integration of the raw ITC curve provides the ΔH_{app} , which can be utilized to detect the reaction rate at each time point during the reaction course via equation 6.9. These rates can be plotted against the substrate concentrations at each time point. The unreacted substrate concentration at each time point can be calculated with equation 6.10 (Di Trani et al., 2017; Todd & Gomez, 2001; Y. Wang et al., 2020).

Equation 6.10:

$$[S]_t = [S]_0 - \frac{\left(\int_0^t DP \, dt \right)}{V_{cell} \cdot \Delta H_{app}}$$

Where:

$[S]_t$ = The unreacted substrate concentration available for the reaction at each time point (M)

The single-injection assay is particularly effective for studying enzyme-catalyzed reactions that follow Michaelis-Menten kinetics, such as those involving simple substrate-to-product conversions with well-defined stoichiometry. This includes a wide range of hydrolysis reactions, phosphorylations, and other common types of enzymatic activities where the enzyme operates under classical kinetic principles. However, it is important to acknowledge that reactions involving complex mechanisms or multiple steps might present challenges for analysis using single-injection ITC. These include enzyme systems exhibiting allosteric regulation, those that follow cooperative binding models, or reactions that involve transient intermediates with rapid equilibria not easily captured by this technique. Additionally, reactions with very slow

kinetics may not reach equilibrium within a practical timeframe for ITC analysis, and extremely fast reactions might resolve too quickly to measure the entire reaction course accurately.

Phosphorylation Reaction of Glycogen Synthase Kinase 3 β (GSK3 β)

GSK3 β is a serine/threonine kinase that plays a pivotal role in cellular signaling pathways and is highlighted for its therapeutic significance, as discussed in Chapters 2 and 4. GSK3 β is unique in its action, requiring a pre-phosphorylated substrate to function efficiently, allowing it to integrate into complex signaling networks within the cell.

The mechanism by which GSK3 β catalyzes the phosphorylation reaction is precise, targeting substrates that contain a particular sequence motif, Ser/Thr-X-X-X-Ser/Thr(P), where Ser/Thr denotes a serine or threonine residue. X can be any amino acid, and Ser/Thr(P) denotes the prime phosphorylation site. This specificity is crucial for the enzyme's function, as it often acts on substrates already primed by another kinase. Priming occurs through phosphorylating a serine or threonine residue located four residues away (generally towards the C-terminus) from the site GSK3 β phosphorylate (Fiol et al., 1990). This pre-phosphorylation is necessary for substrate recognition by GSK3 β . It enables the substrate to bind effectively to the enzyme and positions the target site precisely for phosphorylation by GSK3 β 's kinase domain (Beurel et al., 2015; ter Haar et al., 2001).

GSK3 β is constitutively active. The enzyme's activity is tightly controlled through the phosphorylation of an inhibitory serine (Ser9) within GSK3 β itself, with regulation from signaling pathways mediated by kinases such as Akt, PKA, protein kinase C, and p70 S6 kinase. Its crystal structure reveals that it occupies a catalytically active configuration even without the

dephosphorylation of Ser9, setting it apart from many kinases. The N-terminal segment with the Ser9 phosphorylation mimics a primed substrate and occupies the substrate binding site (Dajani et al., 2001).

Furthermore, GSK3 β regulates its activity by phosphorylating the PP1 inhibitor I-2, thereby increasing PP1 activity, which leads to dephosphorylating the GSK3 β 's inhibitory serine, enhancing the enzyme's activity (Beurel et al., 2015). GSK3 β also interacts with the scaffolding protein Axin, which is crucial for phosphorylating specific substrates, such as β -catenin in the β -catenin destruction complex in the canonical Wnt signaling pathway (Ikeda et al., 1998). This interaction underscores the sophisticated regulation of GSK3 β 's substrate specificity and activity (Beurel et al., 2015).

GSK3 β is capable of phosphorylating multiple residues initiated by the priming phosphorylation, which allows GSK3 β to sequentially phosphorylate substrates with Ser/Thr pentad repeats. In the enzyme reaction, GSK3 β transfers a phosphate group from ATP to a specific serine or threonine residue on its target substrate. The presence of Mg²⁺ ions is essential as an activator by coordinating with ATP. Once the substrate is correctly positioned, ATP, complexed with Mg²⁺, interacts with GSK3 β , aligning the phosphate group to be transferred directly adjacent to the substrate's target hydroxyl group of the serine or threonine residue (Lu et al., 2011). The reaction proceeds as the gamma phosphate group is transferred to the hydroxyl group of the target amino acid, resulting in the phosphorylated product and the release of ADP. The Mg²⁺ ions play a critical role throughout this process by stabilizing the negative charges of the phosphate groups of ATP, thereby facilitating the nucleophilic attack by the substrate's hydroxyl group on the phosphate to be transferred.

Conventionally, the study of GSK3 β kinase activity has leveraged in vitro biochemical assays that quantitatively measure the enzyme's ability to transfer a phosphate group from ATP to specific substrate peptides or proteins. A common approach is the conventional γ -ATP incorporation assay, which tracks the transfer of the γ -phosphate from γ -P³² labeled ATP to the target. This method involves mixing GSK3 β with a substrate in the presence of γ -P³²-ATP and Mg²⁺ ions to facilitate the reaction in a buffer of choice. The phosphorylation of the substrate by GSK3 β results in the incorporation of the radioactive phosphate, which can be measured by various methods, including scintillation counting or SDS-PAGE, followed by autoradiography or phosphor imaging (Ding et al., 2000; Godemann et al., 1999; Rylatt et al., 1980; Ryves et al., 1998; Q. M. Wang et al., 1994; Yamamoto et al., 1999). This assay has been adapted to explore diverse facets of GSK3 β 's role in cellular processes, enabling comparisons between wild-type and mutant forms of GSK3 β , assessing substrate specificity, and the phosphorylation of various cellular substrates such as Glycogen synthase, Axin, β -catenin, Tau and CREB (Fraser et al., 2002; Godemann et al., 1999; Rylatt et al., 1980; Q. M. Wang et al., 1994; Yamamoto et al., 1999) as well as examining the kinase's response to various signaling stimuli, such as insulin and Wnt pathways. Moreover, these assays have been pivotal in elucidating the activation and inactivation mechanisms of GSK3 β , including its modulation by regulatory proteins and the impact of inhibitors on its activity, thereby offering comprehensive insights into the enzyme's regulation and pivotal role in cellular signaling (Dajani et al., 2001, 2003; Ginger et al., 2000; Ikeda et al., 1998; Sutherland et al., 1993; Thornton et al., 2008; Yamamoto et al., 1999).

Since the γ -P³²-ATP incorporation assays rely on radioactive isotopes, which pose safety, disposal, and regulatory challenges, other methods to study GSK3 β activity have been utilized, such as a SELDI-TOF-MS (Surface Enhanced Laser Desorption/Ionization Time of Flight Mass

Spectrometry) assay to detect kinase activity through molecular weight shifts corresponding to phosphate group addition (Bowley et al., 2005), a FRET (Förster Resonance Energy Transfer) based assay to detect kinase activity through the fluorescence generated proportional to product phosphorylation, an ADP-Glo assay to detect GSK3 β kinase activity by measuring the ADP produced following the phosphorylation reaction by a secondary enzyme-coupled reaction producing luminescence (S. H. Liang et al., 2016).

ITC presents significant advantages for studying the kinase activity of GSK3 β compared to the traditional assays discussed. ITC's non-radioactive detection circumvents the safety, disposal, and regulatory challenges associated with radioactive materials. Conventional assays are discontinuous, whereas ITC allows for real-time observation of the reaction without stopping the assay, offering a dynamic view of enzyme kinetics. This continuous monitoring can reveal transient states or intermediate steps in the kinase reaction that may be missed in endpoint assays. Furthermore, ITC eliminates the need for customized substrate labeling, as is the case for FRET-based kinase assays, avoiding potential alterations to substrate properties and enabling studies under more physiological conditions while being cost-effective. Coupled enzyme assays like the ADP-Glo assay, while useful for indirect kinase activity measurement, are disadvantageous due to the complex multi-step processes and sensitivity of the assay components to reaction buffer components. The experimental setup of ITC reduces artifacts from product inhibition or accumulation, offering a clearer reflection of GSK3 β activity. Furthermore, beyond kinetic parameters, ITC provides insight into the thermodynamics associated with the reaction by measuring the reaction enthalpy. Lastly, ITC is a non-destructive technique; therefore, depending on the stability of the enzyme, it can be recovered and utilized in a secondary technique (Falconer et al., 2021; Todd & Gomez, 2001; Y. Wang et al., 2020).

Although many studies have been published regarding the application of ITC for enzyme kinetics, only 11 kinases have been studied in this regard (Bianconi, 2007; R. Lim, 2022; Lonhienne et al., 2003; Lopez-zavala et al., 2016; Olsen, 2006; Palmer et al., 2013; Rohatgi et al., 2015; Streeter et al., 2014; Todd & Gomez, 2001; Y. Wang et al., 2019). Only two studies utilized a protein kinase. Streeter et al. (2014) employed an ITC single-injection assay to explore the phosphorylation of a peptide by Protein Kinase C- β 1 (PKC- β 1). The peptide substrate was designed based on the potential phosphorylation site of a transmembrane protein known as Nox1. Despite achieving phosphorylation, a kinetic analysis was not conducted due to significant product inhibition, compounded by the observed overlap between the peak of the reaction heat and the heat of dilution, thus limiting the assessment of reaction kinetics (Streeter et al., 2014). Lopez-Zavala et al. (2016) explored an alternative function of Arginine Kinase from *Litopenaeus vannamei*, using ITC, showing that it can phosphorylate deoxythymidine-diphosphate (dTDP) to dTTP using ATP as a phosphate donor, indicating a nucleoside diphosphate kinase-like activity. Although K_M values were reported for dTDP and Arginine, the methodology for obtaining this parameter was not discussed. Additionally, considering the substrates studied were not peptides or proteins, the application of ITC was not strictly relevant to protein kinase activity (Lopez-zavala et al., 2016).

Protein kinases are central to regulating nearly all cell functions, including metabolism, transcription, cell division, and apoptosis, by modulating protein function through phosphorylation. Given their pivotal role in cellular signaling, their dysregulation is closely related to diseases such as cancer, inflammatory disorders, and neurodegenerative diseases, and therefore, they have become crucial targets for therapeutic intervention (Cohen, 2002; Roskoski, 2015). ITC presents a novel approach to dynamically understanding the thermodynamics and

kinetics of protein kinases. ITC enables detailed characterization of interactions between protein kinases with their substrates and inhibitors and their effect on kinase activity that is difficult to obtain from traditional assays. ITC can aid in the rational design of targeted kinase inhibitors, potentially leading to more effective and selective therapeutics (Su & Xu, 2018; Y. Wang et al., 2020). Given this context, it is important to investigate the application of ITC for protein kinase reactions.

GSK3 β 's ability to conduct multiple phosphorylation reactions on a single substrate sets it apart as a catalytically complex protein kinase, presenting a compelling case for ITC-based kinetic studies. This multiplicity in phosphorylation, exemplified by the hyperphosphorylation of Tau, a key pathological feature of Alzheimer's disease, underscores GSK3 β 's significance in biomedical research. Analyzing its phosphorylation mechanism through an ITC assay could yield invaluable insights, particularly in understanding how sequential phosphorylation events influence enzyme activity and substrate specificity. Moreover, given the novelty of applying ITC to study multi-phosphorylation enzyme reactions, investigating GSK3 β 's kinetics using this technique could significantly enrich the current understanding of both the enzyme's intricate catalytic processes and the broader applicability of ITC in detailed enzymatic analyses. Such research could also open new avenues in drug development, especially for diseases where GSK3 β 's activity is a central concern, by providing a deeper comprehension of its regulatory mechanisms and interaction dynamics.

In our study of GSK3 β 's enzyme kinetics through ITC, we chose a single injection assay with the GSM peptide as the substrate. The GSM peptide contains a primed phosphorylation site needed for substrate recognition and binding by GSK3 β . This peptide was selected because it is well-known from previous GSK3 β research (Dajani et al., 2001, 2003; Fraser et al., 2002; Ryves

et al., 1998; Ryves & Harwood, 2001; Thornton et al., 2008), ensuring our results are reliable and comparable. The single injection method was picked for its simplicity, allowing us to measure both enthalpy and kinetic parameters in one experiment. This straightforward approach helps us gather detailed information about how GSK3 β works with the GSM peptide efficiently.

Materials and Methods

Materials

Human Glycogen Synthase Kinase-3 β (GSK3 β) isoform 1, used for all the experiments, was prepared via baculovirus expression in Hi5 cells and purified by Glutathione-affinity and ion exchange (SP Cation exchange) purification (Described in Chapter 4). GSK3 β prepared by our collaborators was suspended in 20mM HEPES pH 7.5, 125mM NaCl, and 1mM DTT and stored at -80 °C in aliquots following a quick freeze process in liquid N₂. These GSK3 β aliquots were thawed and diluted in the reaction buffer of choice or dialyzed into the reaction buffer of choice for ITC kinase experiments. GSK3 β prepared in our lab was dialyzed into the reaction buffer of choice for ITC kinase experiments and used immediately without freezing. The GSK3 β stock solutions were quantified using a Qubit Protein Assay kit (Invitrogen #Q33211) or Pierce BCA Protein Assay kit (Thermo Scientific #23225) following dialysis, and 0.125 – 2 μ M protein concentrations were applied for the various ITC kinase assays. Protein samples were dialyzed using Slide-A-Dialysis Cassette, 10K MWCO, 0.1-0.5mL capacity (Thermo Scientific #66383). Purified protein fractions following ion-exchange purification were concentrated using PES Concentrators, 10K MWCO, 0.5mL (Pierce #88513) when necessary.

The substrate for the GSK3 β kinase assay was a synthetic peptide (GSM) designed based on GSK3 β phosphorylation sites of muscle glycogen synthase 1 (Fiol et al., 1987; Ryves et al., 1998). As previously explained, GSK3 β prefers pre-phosphorylated substrates for specific substrate recognition. This recognition is characterized by a phosphorylated serine (pSer) located four amino acids downstream (Ser/Thr XXX pSer) of the target serine or threonine residue that GSK3 β would phosphorylate. The synthetic GSM peptide modeled on muscle glycogen synthase contains three phosphorylation sites. This GSM peptide will be called Triple-site GSM [RG42] peptide in the text. This peptide with the sequence RRRPASVPPSPSLSRHS{pSer}HQRR and MW of 6231.82 Da was either purchased from Millipore Sigma (#12-533) or custom synthesized from GenScript with > 90% purity. Two variants of this GSM peptide were custom-synthesized by GenScript with > 90% purity.

A Mono-site GSM [RG43] RRRPAAVPPAPSLSRHS{pSer}HQRR where the serine residues in the second and third phosphorylation sites were replaced with alanine and a Ser>Ala mutant GSM peptide [RG44] RRRPASVPPSPSLARHS{pSer}HQRR where an alanine residue replaced the serine residue at the first phosphorylation site.

For a typical ITC kinase experiment, GSK3 β in buffer was loaded onto the ITC cell. The reaction volume in the ITC cell is 200 μ L for the ITC instrument used, so about 300 μ L is needed to fill the cell completely while avoiding the introduction of air pockets. The GSK3 β solutions for loading the ITC cell were prepared in the reaction buffer of choice (50mM TRIS pH 8 or 50mM BIS-TRIS pH 6.5) supplemented with 20mM NaCl, 10mM MgCl₂ and ATP added to maintain at least a 10:1 ratio between ATP in the cell compared to the final peptide concentrations in the ITC cell following injection of the peptide solution from the ITC syringe to the cell. This ensures that the phosphorylation of the GSM peptides depends only on the

concentration of peptide injected into the ITC cell during the reaction. NaCl was included to maintain ionic strength in the reaction buffer. 20mM NaCl was chosen as the optimal concentration to maintain the ionic strength of the reaction buffer, and higher NaCl concentrations did not improve the observed activity (Data not shown). Mg^{2+} ions are necessary for kinase activity because ATP complexes with Mg^{2+} bind protein kinases to serve as a phosphate donor. A non-hydrolyzable ATP analog AMP-PNP was used as a negative control.

The reagents used to prepare the reaction buffers included TRIS Base (J.T. Baker #4099-02), HCl (Sigma #920-1), BIS-TRIS (Sigma #SLBV2468), NaCl (Amresco #0241), $MgCl_2$ (Sigma #SLBQ9064V), ATP (Sigma #A2383), and AMP-PNP (Roche Diagnostics #10102547001). 0.5mM β -Mercaptoethanol (OmniPur #6010) was included in dialysis buffers to maintain a reducing environment to prevent protein oxidization.

The GSM peptides were resuspended in ultra-pure water, and stock solutions were stored at -20 °C until used. The peptide substrates were prepared at a chosen concentration in the same buffer conditions for a typical kinase experiment to match the protein solution in the ITC cell. Typically, 40 μ L of the prepared peptide solution in buffer was loaded into the ITC syringe, and 4 μ L was injected into the ITC cell to initiate the phosphorylation reaction. About 75 μ L of solution is needed to fill and purge the syringe to achieve the 40 μ L loading. The peptide concentration in the syringe would be diluted 50-fold once injected into the cell (4 μ L into 200 μ L final reaction volume in ITC cell).

During some initial studies, ATP was used as the substrate in the ITC syringe, while the GSM peptide was included in the ITC cell. However, increasing the ATP concentration by more than 5mM in the syringe would produce a relatively large heat dilution (Data not shown), which

could obscure the heat associated with the phosphorylation reaction. Therefore, subsequent experiments included the GSM peptide substrate in the ITC syringe.

Isothermal Titration Calorimetry – Single Injection Assay

The Single-Injection method of MicroCal PEAQ-ITC (PEAQ-ITC Instrument Cell Serial #MAL1122596 and PEAQ-WM Serial #29061559-0047) was used for all ITC kinase experiments. GSK3 β in 50mM TRIS pH 8 or BIS-TRIS pH 6.5 with 20mM NaCl, 10mM MgCl₂, and ATP (at least at 10:1 ratio compared to the final concentration of peptide substrate in the ITC cell) was prepared as a 300 μ L sample and 280 μ L was loaded into the ITC cell for each experiment. The final reaction volume in the adiabatic cell is 200 μ L. The GSM substrate peptide solutions were prepared with matched buffer conditions and loaded onto the ITC syringe. The reactions were performed at 25 °C or 30 °C with 750 rpm stir speed. Once the reaction mixtures had equilibrated to the assigned temperature and the baseline was stable, the substrate in the ITC syringe was injected at t = 1min. For each Single-injection assay, 4 μ L of the peptide substrate was injected during 8-sec. Upon injection, the concentration of the peptide substrate will be diluted 50-fold.

The final peptide concentration in the ITC cell would be estimated using equation 6.11.

Equation 6.11:

$$C_2 = \frac{C_1 V_1}{V_2}$$

Where:

C₁ = the concentration of GSM peptide substrate in the ITC syringe

V_1 = the injection volume, 4 μ L

C_2 = the concentration of the GSM peptide substrate available for the phosphorylation reaction

V_2 = the active reaction volume, 200 μ L

If the GSM peptide concentration in the solution prepared and loaded onto the ITC syringe was 1mM, the concentration of the peptide available for phosphorylation by GSK3 β in the ITC cell would be:

$$C_2 = \frac{1mM \times 4\mu L}{200\mu L}$$

$$C_2 = 0.02mM$$

Hence, the ATP concentration in the ITC cell would be maintained at 0.2mM or higher (10:1) compared to the final peptide substrate concentration in this instance.

The reference power was set at 41.85 μ W/sec, and the feedback was set to high. The differential power (DP) deflects from the baseline upon substrate injection and the reaction initiation. DP is reported in units of μ W. Because 1W = 1 joule/sec and 1 calorie = 4.184 joules, the baseline DP corresponding to the reference power is 41.84 μ W. The reaction was considered complete once the DP returned to the baseline. To directly compare multiple runs pertaining to an experiment set, the baseline values were adjusted to DP = 0. The DP values at each 1-second time interval from the point of substrate injection are measured and recorded by the PEAQ-ITC software. The DP values can be exported as CSV Files, and the DP values can be adjusted to DP = 0 for respective runs for comparison using Microsoft Excel. Each ITC run carries a run number R# assigned chronologically as an identifier.

Baseline Correction for Analysis of ITC Raw Plots

The baseline in a raw ITC thermogram is influenced by the set reference power, the constituents of the buffer solutions, and the exact volume loaded into the sample cell. Minor air pockets or bubbles and particulates in the cell can lead to slight fluctuations in the baseline between each ITC run. To directly compare various ITC experiments within the same graph, each thermogram's baseline was normalized to a DP of 0. This was achieved by deducting the starting baseline DP value and utilizing Microsoft Excel software to adjust.

Michaelis – Menten Studies for the Phosphorylation of Triple-site GSM Peptide [RG42]

The Enzyme Kinetics – Single injection fitting model on MicroCal PEAQ analysis software (v.1.0.0.1259) displays the ITC raw data, which is the change in DP over time, and then uses the area under the curve to determine the apparent enthalpy (ΔH_{app}) of the reaction. The software then calculates the reaction rate and substrate consumed for each time point. It constructs a plot for rate vs. substrate concentration and attempts multi-parameter fitting of the data to the Michaelis – Menten enzyme kinetics model.

In this study, the raw ITC data obtained from a single injection assay of the kinase activity of GSK3 β on the triple-site GSM peptide did not conform to the Michaelis-Menten model. One possible explanation for the apparent failure to exhibit Michaelis-Menten kinetics could be that the raw ITC curve failed to remain at the saturation point for an adequate duration before exhibiting a "return-to-baseline" deflection in the DP. Typically, an enzyme reaction that maintains a prolonged presence at the saturation point allows for a more accurate fit to the

Michaelis-Menten model from a single injection assay, providing a comprehensive Michaelis-Menten curve for the reaction.

The behavior of the ITC curves with the triple-site GSM peptide led us to employ multiple single-injection assays using various initial substrate concentrations. The maximum initial rate for each concentration was determined by examining the peak deflection in the ITC curve, explicitly using the change in DP at the deflection point. The Rate_{ITC} at the onset of each reaction, calculated immediately after injecting the substrate into the ITC cell, was determined using equation 6.9 and plotted over the reaction's time duration to pinpoint the maximum initial Rate_{ITC} . An illustration of this analysis, performed using Microsoft Excel, is detailed in **Appendix V (Part B, Analysis 1)**, showcasing the examination of the ITC R#3247 dataset. The substrate concentrations corresponding to these initial rates were then calculated using equation 6.10. The initial Rate_{ITC} values were then plotted against respective substrate concentrations to assess conformity with the Michaelis-Menten equation, facilitating direct extraction and comparison of these rates using the MicroCal PEAQ analysis software.

Furthermore, a secondary approach was introduced to quantify the initial reaction rates based on the early segment of the raw ITC curve following substrate injection. This segment, where the DP change linearly correlates with time, incorporates principles from the initial rate calorimetry (IrCal) method (Honarmand Ebrahimi et al., 2015). We could extract the initial rates at points where the rate change is linear by plotting the reaction rates from the onset post-injection against the elapsed time for each tested substrate concentration. The substrate concentrations corresponding to these initial rates were then calculated using equation 6.10. The initial Rate_{ITC} values were plotted against the substrate concentrations to assess the fit with the Michaelis-Menten model.

Michaelis – Menten Analysis for the Phosphorylation of Mono-site GSM Peptide [RG43]

The Enzyme Kinetics – Single injection fitting model in MicroCal PEAQ analysis software was used to analyze raw ITC data for the phosphorylation of a mono-site GSM peptide by GSK3 β . The Michaelis-Menten model could be applied effectively when the peptide concentration in the ITC syringe was 3mM or higher. The analysis provided quantitative values for the Michaelis-Menten constant (K_M) and the catalytic rate constant (k_{cat}). The kinetic parameters obtained from the MicroCal PEAQ software were also corroborated by manually analyzing the raw ITC data using the Michaelis-Menten model in Microsoft Excel, ensuring the reliability of the software's calculations. **Appendix V** shows an example of the Excel analysis (**Part B, Analysis 4**).

Analysis of Apparent Reaction Enthalpy (ΔH_{app}) for the Phosphorylation of GSM Peptides

The ITC single injection assay was used to compare the ΔH_{app} for the GSK3 β mediated phosphorylation reaction of triple-site GSM [RG42], mono-site GSM [RG43], and Ser>Ala mutant GSM [RG44] peptides. Each GSM peptide was prepared at a concentration of 1 mM in buffer and loaded into the ITC syringe. Additionally, the mono-site GSM peptide was prepared at a concentration of 3mM (to add 3x the substrate) to compare the ΔH_{app} of that reaction against the ΔH_{app} from the 1mM peptide ITC runs. The enzyme GSK3 β was used at 0.5-2 μ M concentrations. The reaction mixture contained 50mM TRIS pH 8, 20mM NaCl, 10mM MgCl₂, and 0.2mM or 1mM ATP. The concentration of the enzyme does not affect the ΔH_{app} of a reaction as long as there is sufficient enzyme activity to convert all substrate to product, which in an ITC single injection assay is indicated by the DP returning to the baseline following the deflection

that corresponds to the reaction. The ΔH_{app} for each reaction was obtained from the MicroCal PEAQ analysis software.

Determining the Buffer-Independent ΔH_{app} for GSK3 β Phosphorylation of Mono-site GSM Peptide

Obtaining the buffer-independent reaction enthalpy is important for observing the intrinsic enthalpy change, which reflects the actual thermodynamic signature of the reaction. The buffer-independent reaction enthalpy for the GSK3 β kinase reaction with the mono-site GSM peptide was obtained by performing the reaction in various buffers at the same pH and analyzing the relationship between apparent enthalpy changes and the enthalpy changes associated with ionization in each buffer. The mono-site peptide was chosen for this study because it provides a more straightforward system with fewer variables and potential interaction sites. It describes the attributes of a single phosphorylation event. Additionally, binding and phosphorylation of the first site is likely the rate-limiting step in the reaction pathway, even for triple-site substrates. For the experiment, 1mM mono-site GSM peptide was prepared in respective buffers at pH 7. GSK3 β was prepared at 1 μ M concentration in the respective buffers at pH 7 (at 50mM buffer concentration), 20mM NaCl, 10mM MgCl₂, and 2mM ATP. The buffer components between the ITC syringe and cell solutions were matched for each experiment. The ITC single injection assay was performed at 30 °C. The reaction was performed in buffers TRIS, BIS-TRIS, MOPS (Sigma #M1254), MES (Sigma #SLBT0247), and HEPES (Sigma #H3375) at 50mM buffer concentration and pH 7. The ΔH_{app} for each reaction was plotted against ΔH_{ion} for each buffer at the respective temperature to obtain the buffer-independent reaction enthalpy and measure the proton exchange associated with the reaction.

Effect of Inhibitors: BeSO₄ and LiCl

A series of single injection assays were conducted to investigate the inhibitory effects of BeSO₄ and LiCl on the enzymatic activity of GSK3 β on ITC. In each experiment, 1 mM triple-site GSM peptide was prepared, loaded in the ITC syringe, and injected into the ITC cell with 0.5 μ M GSK3 β in 50mM BIS-TRIS pH 6.5, 20mM NaCl, 10mM MgCl₂, and 0.2mM ATP containing BeSO₄ (0, 3, 10, 30 and 100 μ M) or LiCl (0, 3, 10, and 30mM) at 30 °C. The inhibitor stock solutions were prepared using Beryllium sulfate hydrate (Fluka #14270) and Lithium Chloride (Sigma #L-8895). The 50mM BIS-TRIS pH 6.5 buffer system was chosen due to Beryllium solubility constraints at higher pH in aqueous solutions.

Inhibitor Reversibility Study

A FRET-based assay (Mudireddy et al., 2014) was performed to investigate the reversibility of Be²⁺ and Li⁺ mediated inhibition on GSK3 β employing GST-GSK3 β fusion protein attached to Glutathione beads and treated with 100 μ M BeSO₄ or 100mM LiCl. The kinase activity of GST-GSK3 β was assessed after the inhibitor-treated protein-bead slurry was washed to remove the inhibitor or left unwashed to retain the inhibitor. The results of this study hinted at the possibility of Be²⁺ exerting a near-irreversible inhibitory effect on GSK3 β (Unpublished results by Dr. Ronald Gary).

The following method was adapted to investigate this phenomenon via ITC. A 300 μ L GSK3 β solution was prepared at 0.5 μ M concentration in 50mM BIS-TRIS pH 6.5, 20mM NaCl, 10mM MgCl₂, and 0.8mM ATP. The solutions with the enzyme were treated with no inhibitor, 30 μ M BeSO₄ or 30mM LiCl, and incubated at room temperature for 15min. These samples were

transferred to 0.5mL Pierce PES Concentrators (10K MWCO), and the inhibitors were washed by exchanging the buffer using fresh 50mM BIS-TRIS pH 6.5, 20mM NaCl, and 10mM MgCl₂ buffer. The buffer exchange was done by adding ~300μL of ice-cold fresh buffer to the PES spin column and centrifugation at 12 500 rpm and 4 °C for 3-4 min. Each time, the sample in the PES spin column was reduced to ~100μL. The washing steps were repeated 5x. Following the final wash, the protein sample was recovered from the column, the volume was estimated, and the final volume was brought to 300μL with buffer. The ATP concentration was adjusted to 0.8mM. These enzyme samples were loaded on the ITC. A single injection assay was performed by titrating 4mM triple-site GSM peptide (in matching buffer conditions without inhibitors). The kinase activity in these samples was compared against the GSK3β activity in samples left unwashed to retain the inhibitor. The initial RateITC was obtained for each experiment, and the enzyme activity for the +inhibitor tests was normalized with respect to the GSK3β activity in pre-wash and post-wash samples with no inhibitor.

Results and Discussion

Detection of GSK3 β Phosphorylation Activity via ITC Single-Injection Assay

The ITC single-injection analysis was utilized to examine the kinase activity of GSK3 β , specifically its phosphorylation of the triple-site GSM peptide. The reaction was initiated by injecting 1mM peptide substrate (the actual concentration in the ITC cell is diluted 1:50, giving 20 μ M) into the ITC cell containing 2 μ M GSK3 β and ATP in excess. Substrate and enzyme solutions were prepared in 50mM TRIS pH 8, 20mM NaCl, and 10mM MgCl₂ buffer. The exothermic nature of the reaction is indicated by the downward deflection of the ITC thermogram, which shows that energy was released during the phosphorylation process. A slight downward peak, only reflecting the heat of dilution, was observed when the same assay was repeated by injecting the substrate peptide into the buffer alone or the enzyme solution where the non-hydrolyzable ATP analog AMP-PNP was present instead of ATP (**Figure 6.1**), confirming the large exothermic peak was generated by the heat released from the phosphorylation of triple-site GSM peptide by GSK3 β . Additionally, in the presence of LiCl, a classical inhibitor of GSK3 β and Alsterpaullone, a potent synthetic inhibitor of GSK3 β the exothermic signal was significantly decreased (**Figure Appendix V.A**), validating the specificity of the ITC measurement for GSK3 β 's kinase action on the GSM peptide.

A reaction's apparent enthalpy (ΔH_{app}) can be quantified by integrating the area under the raw ITC peak. The total area under the peak represents the total heat generated by the reaction process. ΔH_{app} is determined by dividing the total heat measured by the total moles of substrate injected into the ITC cell.

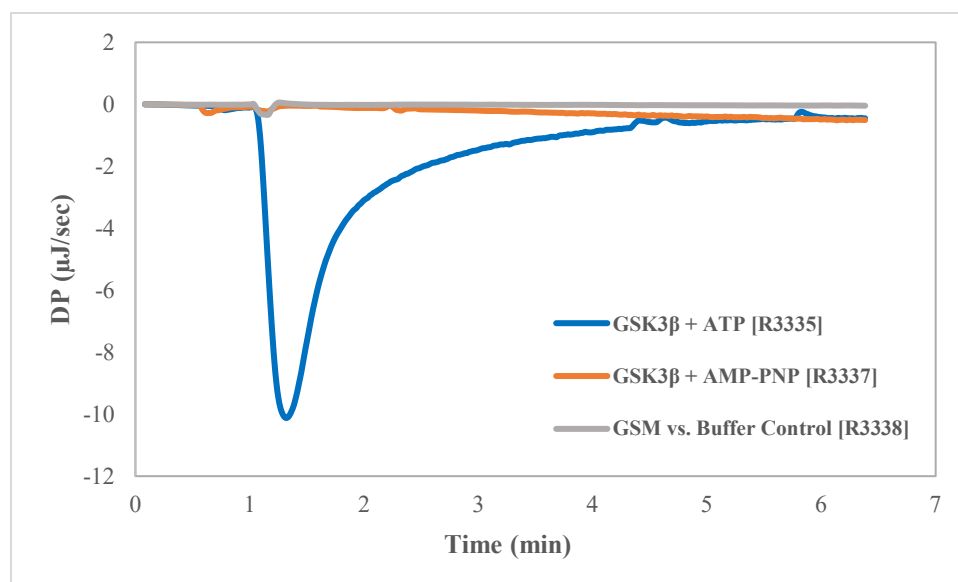


Figure 6.1: ITC Single-injection Analysis Thermogram for GSK3 β Kinase Reaction. The thermogram for the phosphorylation of 1mM Triple-site GSM peptide (RG42) catalyzed by 2 μ M GSK3 β in the reaction buffer: 50mM TRIS pH 8, 20mM NaCl, 10mM MgCl₂, and 0.2mM ATP (blue). The peptide was injected at $t = 1$ min. Two negative controls are compared: control with no GSK3 β (grey) and control where the non-hydrolyzable ATP analog AMP-PNP replaces ATP.

The ΔH_{app} obtained from the integrated peak area in the ITC experiment reflects the cumulative heat released or absorbed due to the substrate's conversion to the product under the assumption of a near-complete reaction. This is a reasonable assumption for serine/threonine protein kinases. For example, $K_{eq} = 3500$ for the phosphorylation of a 15-amino acid peptide substrate by CaM kinase II (Kwiatkowski et al., 1990). The return of the raw ITC curve to baseline after the peak associated with the reaction indicates that the thermal effect of the reaction has ceased. This is expected when the reaction has consumed most of the available substrate and has reached a state of near completion at equilibrium. Under these conditions, the measured ΔH_{app} should closely represent the actual enthalpy change of the reaction per mole of substrate converted (Hagedoorn, 2022; Hansen et al., 2016; Quinn & Hansen, 2019; Transtrum et

al., 2015). The ΔH_{app} quantified for this exothermic reaction (**Figure 6.1**) was -120 kJ/mol in the TRIS buffer system. This significant heat release demonstrates that the reaction is highly enthalpically favorable. Ideally, a secondary technique might demonstrate that all the substrate is consumed during the reaction, unequivocally confirming that the ΔH_{app} measured by ITC represents the true reaction enthalpy.

Effect of Different Enzyme Concentrations on GSK3 β Phosphorylation Reaction

The ITC single-injection assay was performed by injecting 5mM ATP into the ITC cell containing 100 μ M triple-site GSM peptide in 50mM TRIS pH 8, 20mM NaCl, and 10mM MgCl₂, and various concentrations of GSK3 β : 0 μ M, 0.125 μ M, 0.5 μ M, and 2 μ M (**Figure 6.2**). This experiment aimed to observe the effect of different enzyme concentrations on the raw ITC curve and the reaction rates but not to obtain kinetic parameters.

The raw ITC curves provide a qualitative view of the GSK3 β phosphorylation reaction depending on the enzyme concentration, which is the only variable. The control experiment (0 μ M GSK3 β) only produced a small endothermic peak for the ATP dilution (grey curve), and the exothermic peaks corresponding to the GSK3 β phosphorylation reaction became sharper with increasing enzyme concentration (**Figure 6.2A**). The exothermic peaks from the phosphorylation reaction in the presence of 0.5 μ M GSK3 β (orange curve) and 2 μ M GSK3 β are prominent and mask the small endothermic peak for the ATP dilution heat. However, the exothermic peak in the presence of 0.125 μ M GSK3 β (green curve) shows a small endothermic peak before the DP deflects downward. Furthermore, the raw ITC curve for the reaction with 0.125 μ M GSK3 β takes longer to reach the baseline when compared to the other peaks.

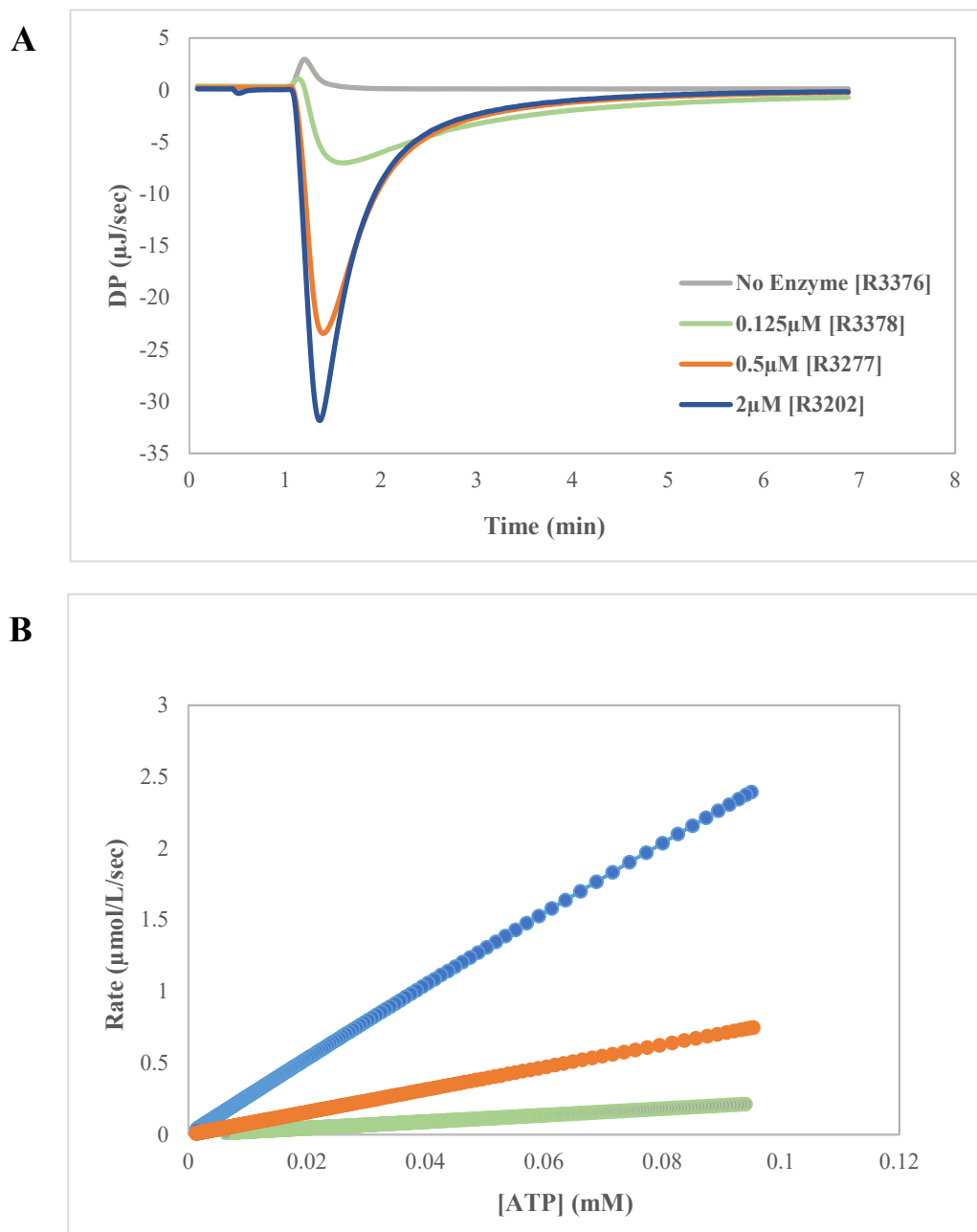


Figure 6.2: ITC Single-injection Analysis for the Phosphorylation of Triple-site GSM Peptide (RG42) Catalyzed with Various Concentrations of GSK3 β . A) 5mM ATP was injected at $t = 1$ min into the ITC cell containing 100 μM GSM in 50mM TRIS pH 8, 20mM NaCl, 10mM MgCl_2 , and various concentrations of GSK3 β 0 μM (grey), 0.125 μM (green), 0.5 μM (orange) and 2 μM (blue) at 30 °C. ITC records the progress of the reaction as DP changes as a function of time. B) The reaction rate (Rate_{ITC}) extracted from the PEAQ ITC analysis software plotted against the respective concentration of unreacted ATP in the ITC cell.

In the single-injection assay, when the enzyme concentration is low, the curve generated takes longer to reach the baseline due to the slower rate of the enzyme-catalyzed reaction. The effect of enzyme concentration on the observed reaction rate is shown (**Figure 6.2B**). This study shows the importance of choosing a sufficiently high enzyme concentration for the ITC single-injection assay. We used 0.5-2 μ M enzyme concentrations in proceeding experiments.

ITC Thermogram for the Effect of Different Peptide Concentrations

A comparison of the ITC thermogram for the triple-site GSM phosphorylation by GSK3 β in four biological buffers: TRIS pH 8, HEPES pH 7, BIS-TRIS pH 6.5, and MES pH 6 demonstrated that the exothermic signal for this reaction was significantly higher in the TRIS pH 8 buffer (**Figure Appendix V.B**). Five different concentrations of the triple-site GSM peptide (0.125mM, 0.25mM, 0.5mM, 0.75mM, and 1mM concentrations in the ITC syringe) were prepared in TRIS and injected into a 2 μ M GSK3 β solution in the ITC cell. As discussed in the methods, a 4 μ L injection is followed into the ITC cell with a 200 μ L active reaction volume, which means the final substrate concentrations in the cell would be diluted 1:50. An exothermic peak was observed for each reaction with an increase in DP change in a concentration-dependent manner (**Figure 6.3**). All reactions were followed in a TRIS pH 8, 20 mM NaCl, and 10 mM MgCl₂ buffer with ATP in excess. The ΔH_{app} values for the ITC thermograms (**Figure 6.3**) with increasing substrate concentration were obtained from MicroCal PEAQ analysis software (**Table 6.1**). The experimental average ΔH_{app} for the phosphorylation of triple-site GSM peptide by GSK3 β in the chosen reaction conditions was -118 kJ/mol. This value is comparable to the ΔH_{app} observed previously (**Figure 6.1**), demonstrating that the ITC single-injection assay can be reproducible.

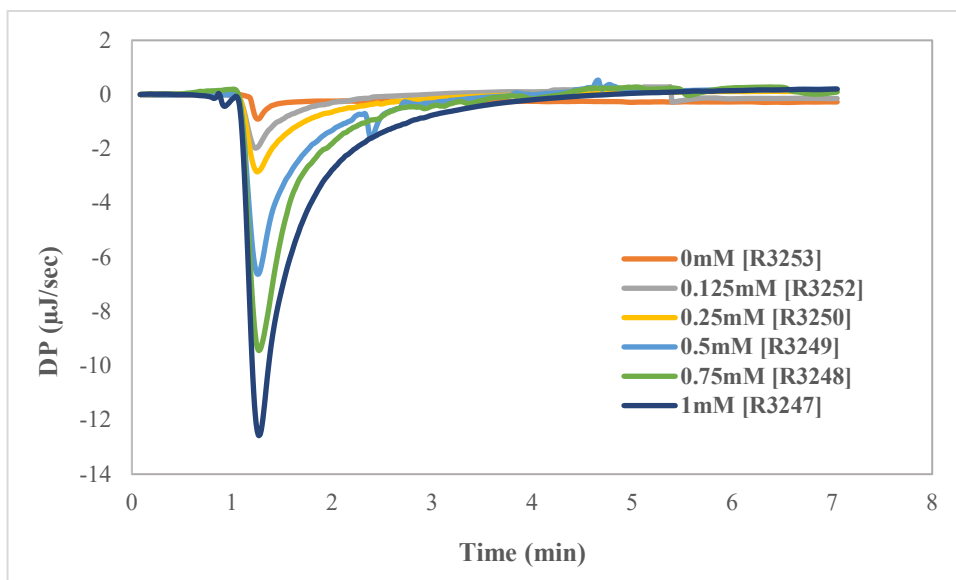


Figure 6.3: ITC Single-injection Analysis of Various Triple-site GSM (RG42) Peptide Concentrations with GSK3 β . 1mM, 0.75mM, 0.5mM, 0.25mM and 0.125mM triple-site GSM peptide was injected at $t = 1$ min into the ITC cell containing 2 μ M GSK3 β and 0.2mM ATP in 50mM TRIS pH 8, 20mM NaCl, 10mM MgCl₂ at 30 °C.

Table 6.1: The Apparent Reaction Enthalpy from the Single-injection Analysis of Various Concentrations of Triple-site GSM Peptide (RG42). The substrate was injected into the ITC cell containing 2 μ M GSK3 β in 50mM TRIS pH 8, 20mM NaCl, 10mM MgCl₂, and 0.2mM ATP. The actual concentrations of peptide present for the reaction are listed (the syringe solution is diluted 1:50 upon injection). The apparent reaction enthalpy values are reported from MicroCal PEAQ ITC analysis software.

[Triple-peptide GSM] (mM)	ΔH (kJ/mol)
0.0025	-116
0.005	-119
0.01	-118
0.015	-120
0.02	-117

Analysis of Triple-site GSM Phosphorylation by GSK3 β Suggests a Deviation from the Michaelis-Menten Model

We investigated whether the triple-site GSM data would fit the Michaelis-Menten model. The data observed with this substrate did not fit the enzyme kinetics model in the MicroCal PEAQ analysis software. One possible explanation stemmed from the raw ITC curve's inability to sustain a saturation point for a sufficient duration before DP deflection occurred, implying that the catalysis of triple-site GSM phosphorylation by GSK3 β displays fast kinetics. Recognizing that the analysis software could not adequately fit data from a single curve to the Michaelis-Menten model, we conducted multiple single-injection assays across a range of substrate concentrations.

A pilot study for urea hydrolysis by jack bean urease was conducted in our lab using the single-injection assay (Lim, 2022). The ITC thermograms observed for the urea hydrolysis reaction also displayed a similarly sharp peak, with a quick decline in DP change over time. By conducting multiple single-injection assays at increasing urea concentrations and fitting the maximum initial rate for each assay with respect to the substrate concentration, the data could be fitted to the Michaelis-Menten model to derive kinetic parameters comparable to those reported in the literature.

First, to observe the change in the reaction rate for increasing substrate concentrations, the maximum initial Rate_{ITC} values were obtained from the raw ITC curves in **Figure 6.3**, using equation 6.9 (**Appendix V, Part B, Analysis 1**). The unreacted substrate concentration in the ITC cell at the time point representing the calculated initial Rate_{ITC} was determined using equation 6.10 (**Table Appendix V.A**). The initial Rate_{ITC} can be plotted as a function of time, and the peak would represent the maximum initial Rate_{ITC} (**Figure Appendix V.C**). The maximum initial

Rate_{ITC} values were plotted against the peptide substrate concentration in the ITC cell to observe the behavior of rate change with respect to substrate concentration. The rate of GSK3 β catalyzed phosphorylation of triple-site GSM peptide increased linearly with increasing substrate concentration (**Figure 6.4**).

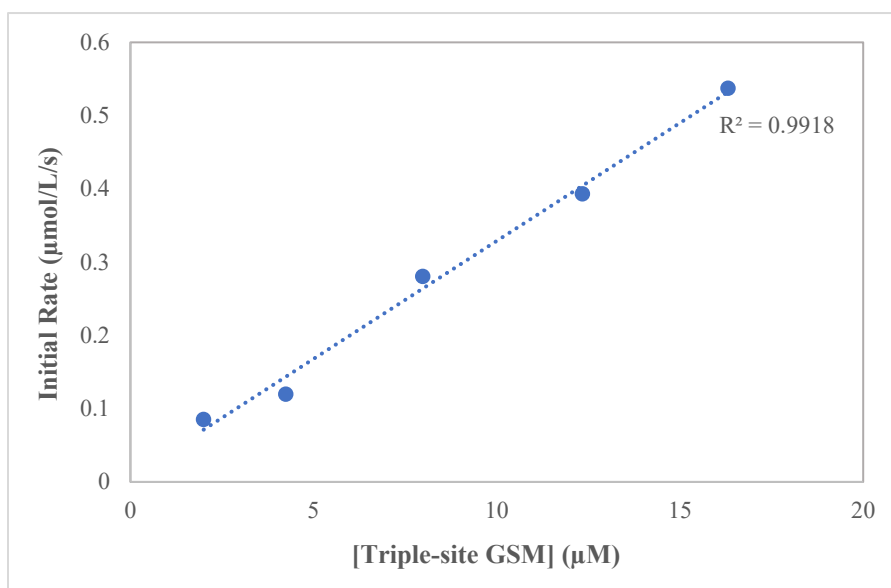


Figure 6.4: Initial Rate_{ITC} vs. GSM (RG42) Peptide Concentrations Plot. The initial Rate_{ITC} increases as the peptide concentration increases, demonstrating a linear relationship. Dots represent the initial Rate_{ITC} extracted from MicroCal PEAQITC analysis software for each experiment, and the dotted line represents the linear line of the best fit.

This observation agrees with the linear part of the Michaelis-Menten model because at concentrations when $[S] \ll K_M$, the reaction rate is directly proportional to the substrate concentration. In this experiment, the highest substrate peptide concentration in the ITC cell was 20μM.

Several studies conducted with γ -P³²-ATP incorporation assay for GSK3 β kinase activity with increasing triple-site GSM peptide aligned with the Michaelis-Menten model (Dajani et al., 2001, 2003; Ryves et al., 1998; Ryves & Harwood, 2001; Thornton et al., 2008). K_M values of 75 μ M and 91.1 μ M were reported for this triple-site GSM peptide phosphorylation by GSK3 β derived from rabbit skeletal muscle (Ryves et al., 1998; Ryves & Harwood, 2001), and K_M values of 60-85 μ M were reported for this reaction by human GSK3 β (Dajani et al., 2001, 2003). This shows that the peptide concentration in the cell was much lower than the expected range for K_M ; therefore, our data would only represent the linear portion of the Michaelis-Menten curve.

The methodology was adjusted by increasing the concentrations of the triple-site GSM peptide while simultaneously reducing the enzyme concentration in the ITC cell. This approach was predicated on the understanding that a lower enzyme concentration would decelerate the reaction rate, potentially resulting in a broader peak. This modification was anticipated to facilitate a more accurate observation and fitting of the data to the Michaelis-Menten model by capturing a broader range of the enzyme kinetics involved.

Seven different concentrations of the triple-site GSM peptide (0.5mM, 1mM, 1.5mM, 2mM, 3mM, 4.5mM, and 6mM) in the ITC syringe were injected into a 0.5 μ M GSK3 β solution in the ITC cell. Exothermic peaks were observed for each reaction with an increase in DP change in a concentration-dependent manner (**Figure 6.5**). A lower enzyme concentration allowed for a broader exothermic peak in response to the reaction. We can distinguish this by comparing the raw ITC curves for the reaction of 1mM triple-site GSM peptide with 2 μ M GSK3 β in R#3247 (dark blue curve) with a DP change of -12.5 μ J/sec (**Figure 6.3**) against 0.5 μ M GSK3 β in R#3298 (green curve) with a DP change of -5.4 μ J/sec (**Figure 6.5**).

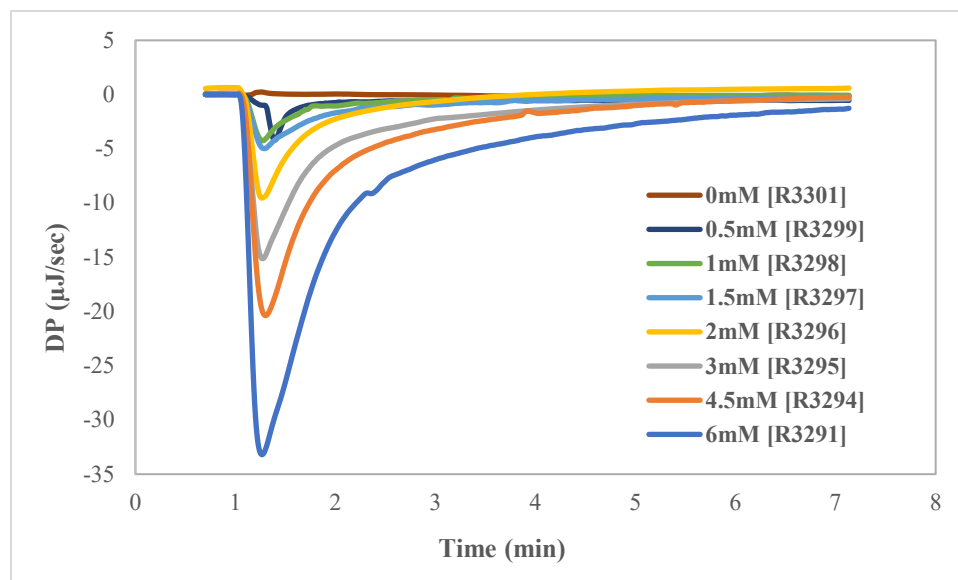


Figure 6.5. ITC Single-injection Analysis of Various Triple-site GSM (RG42) Peptide Concentrations with GSK3 β . Triple-site GSM peptide was injected at $t = 1$ min into the ITC cell containing $0.5\mu\text{M}$ GSK3 β and 1.5mM ATP in 50mM TRIS pH 8, 20mM NaCl, and 10mM MgCl $_2$ at 30°C .

The maximum initial Rate_{ITC} values were obtained from the raw ITC curves in **Figure 6.5**, using equation 6.9, and the unreacted substrate concentration in the ITC cell at the time point representing the calculated initial Rate_{ITC} was determined using equation 6.10. The maximum initial Rate_{ITC} values were plotted against the peptide substrate concentration in the ITC cell. The Excel Solver tool was utilized to analyze the measured or observed Rate_{ITC} data in relation to the Michaelis-Menten model. This feature enabled us to fit the Rate_{ITC} observed from the experiment to the theoretical model outlined by Michaelis-Menten kinetics. The fit was iterated by adjusting the parameters within Excel Solver to match the experimental data closely. (**Figure 6.6**). While the iterative fitting using Excel Solver closely aligned with the experimental data, the resulting curve did not conform to the expected Michaelis-Menten model. Instead of displaying the

characteristic hyperbolic shape of a Michaelis-Menten curve, the fit showed a slight curvature towards its end. This deviation indicates that, although the experimental observations are closely matched, the reaction kinetics observed from this experiment did not fully adhere to the traditional Michaelis-Menten kinetics.

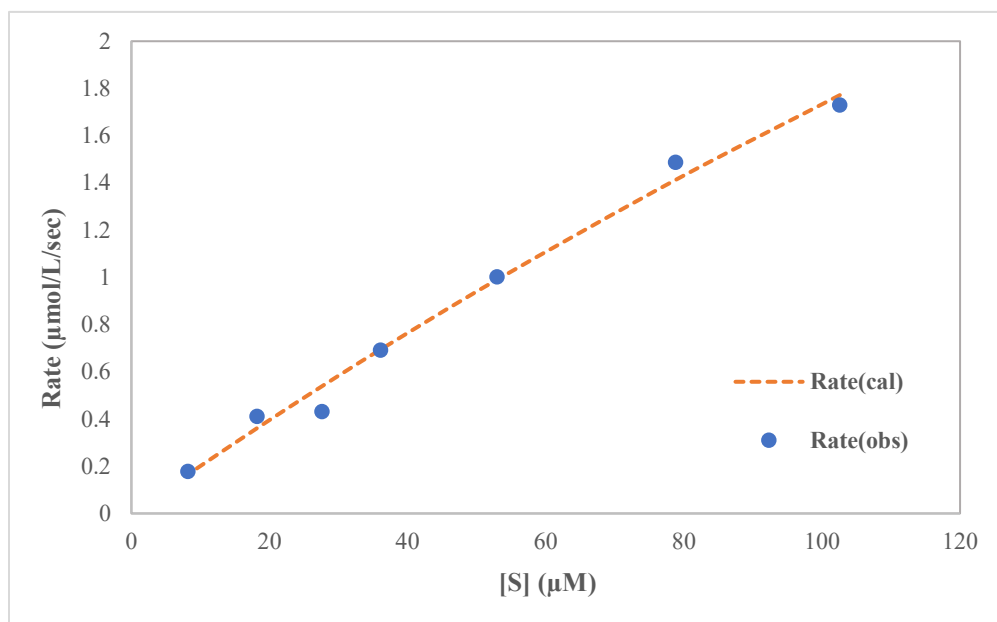


Figure 6.6: Michaelis-Menten Analysis for Triple-site GSM (RG42) Peptide with 0.5μM GSK3β. The initial rate_{ITC} calculated for each ITC raw plot was plotted as a function of each peptide concentration used and then fitted to the Michaelis-Menten equation for kinetic analysis using Microsoft Excel. Dots represent the initial rate_{ITC} derived for each peptide concentration, and the solid line represents the fit to the Michaelis-Menten equation.

Several limitations associated with using the maximum initial Rate_{ITC} for the analysis may lead to the experimental data not accurately reflecting the actual kinetics of an enzyme reaction. The ITC has a certain amount of thermal inertia, which is the resistance to changes in

temperature. This inertia can delay the instrument's ability to detect and accurately report rapid or large increases in heat flow.

This parameter is the instrument response time (τ) and depends on the make of different ITC models (Hagedoorn, 2022; Hansen et al., 2016; Transtrum et al., 2015). Our MicroCal PEAQ-ITC has an instrument response time of 8 seconds (Malvern). As the reaction progresses, the amount of heat generated increases, potentially leading to a larger deflection from the baseline on the ITC curve. When the heat change is significant (at or near the maximum deflection point), the instrument might take longer to adjust, leading to undershooting the actual heat flow rate (for exothermic reactions). This delay can make it harder to accurately capture the peak rates of reaction, especially if they change rapidly over a short period, as observed for triple-site GSM peptide phosphorylation reaction by GSK3 β .

To elucidate the effect of this impact, the DP change over time was corrected for the instrument response time using the Tian equation (Bäckman et al., 1995; Transtrum et al., 2015), which corrects for the instrument's response time, comparing measured DP values with those corrected for the 8 seconds response time in our ITC instrument.

Equation 6.12:

$$\Phi_{corrected} = \Phi_{measured} + \tau \left(\frac{d\Phi_{measured}}{dt} \right)$$

Where:

$\Phi_{corrected}$ = the actual heat flow from the reaction

$\Phi_{measured}$ = the measured heat flow from the reaction reported as DP

The initial period following substrate injection, where there is a delay before the ITC detects a significant change in heat flow, is called the lag phase. This delay is not purely a matter of instrument response time; it also involves the physical processes of mixing and thermal equilibration between the injected substrate, enzyme in the sample cell, and the calorimeter itself. The lag phase represents the time required for the enzyme and substrate to mix thoroughly and reach a uniform temperature distribution within the sample cell, setting the stage for the enzymatic reaction to proceed uniformly throughout the sample volume.

The measured DP for R3291, where 6mM triple-site GSM peptide was injected into the ITC cell with 0.5 μ M GSK3 β (**Figure 6.5**), was corrected for the instrument response time. The two ITC curves were compared (**Figure Appendix V.D**). Interestingly, in the initial time points following the lag phase, the corrected and measured DP values closely overlap, indicating minimal effect of the instrument's response time on the early measurements. At the same time, a discrepancy between measured and corrected DP is observed near the maximum deflection point for this GSK3 β catalyzed phosphorylation reaction.

The initial rate calorimetry (IrCal) method proposed by Ebrahimi et al. (2015) focuses on obtaining initial rates of enzyme activity from heat measurements during the early stages of a reaction, effectively bypassing the confounding effects of instrument response time on later measurements. The DP change in the first few time points post-lag phase shows a linear relationship with time (Honarmand Ebrahimi et al., 2015). The maximum deflection point often occurs outside the reaction's initial linear phase. Substrate depletion or product inhibition could also affect it more, misrepresenting the enzyme's initial rate. The IrCal method leverages the linear relationship between the early DP values unaffected by the instrument's lag.

Employing the IrCal method could address the problems identified in our initial analysis by ensuring that the calculated rates represent GSK3 β 's true activity under initial reaction conditions. This method's reliance on early, linear data points minimizes the distortion caused by the instrument's response time, potentially providing a more accurate and reliable measure of enzymatic kinetics. The evidence presented by demonstrating the alignment of measured and corrected DP in the initial reaction phase (**Figure Appendix V.D**) further supports the validity of adopting the IrCal approach for a more accurate assessment of enzyme activity and kinetics for the triple-site GSM peptide phosphorylation catalyzed by GSK3 β .

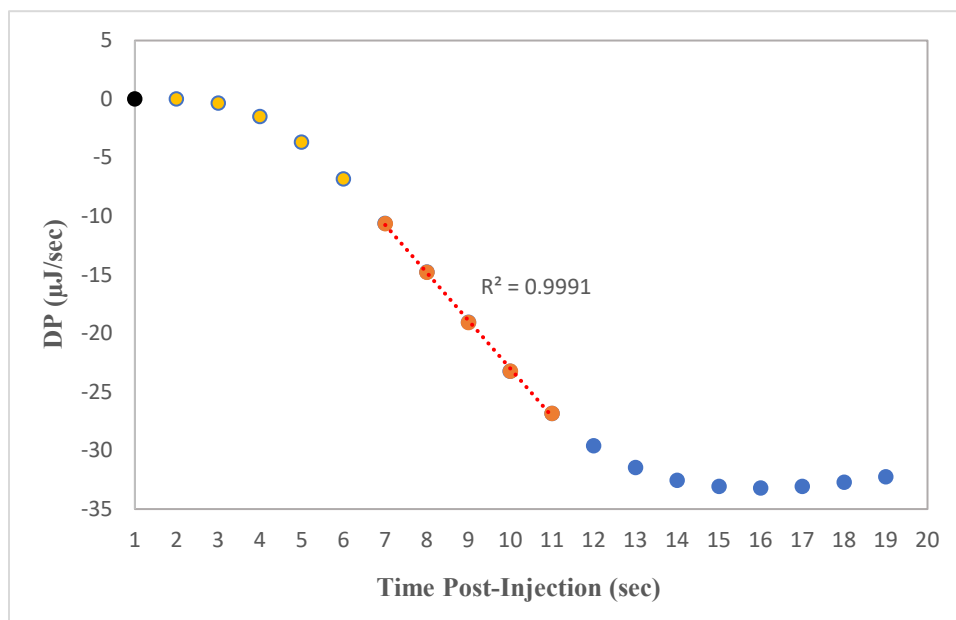


Figure 6.7: Example of a Graphical Analysis of Lag and Linear Phases. The DP change for the time points post-injection is plotted for R3291, where 6mM triple-site GSM peptide was injected into the ITC cell with 0.5 μ M GSK3 β . The black dot represents the point of injection. The yellow dots show the lag phase. The linear range for DP change is shown in orange dots with the best-fit trendline ($R^2 = 0.9991$). The linear range for DP change is used for the IrCal approach.

To apply the IrCal approach, we should observe the change in DP over time in the initial stages of the reaction across different substrate concentrations to identify the lag and linear phase (**Figure 6.7**). Rates are obtained right after the lag phase for each substrate concentration during the linear phase of the heat flow versus the time curve. This indicates a constant rate of the enzymatic reaction, free from the instrument response time, substrate depletion, or product inhibition effects.

The graphical representation of DP change over time for R3291, where 6mM triple-site GSM peptide was injected into the ITC cell with 0.5 μ M GSK3 β (**Figure 6.5**), showed the lag phase lasted until 6 seconds post-injection, and the linear range for DP change was observed between 7 and 12 seconds (**Figure 6.7**). The DP change between subsequent time points in the linear range $\Delta DP_{ITC}(t)$ was determined using equation 6.13 (Honarmand Ebrahimi et al., 2015).

Equation 6.13:

$$\Delta DP_{ITC}(t) = DP_t - DP_{t-n}$$

Where:

n = the sampling time (for MicroCal PEAQ-ITC instrument, n = 1 sec)

Equation 6.9 can be modified to determine the $Rate_{ITC}$ corresponding to each time point.

Equation 6.14:

$$Rate_{ITC}(t) = \frac{\Delta DP_{ITC}(t)}{\Delta H_{app} \cdot V_{cell}}$$

It is important to note that initial $Rate_{ITC}$ values derived from ITC require adjustment by a proportionality constant to account for the thermal and volumetric parameters of the instrument and reflect the actual enzyme reaction rates. The approach mentioned by Ebrahimi et al., 2015, involves using a standard reaction, such as the conversion of para-nitrophenyl phosphate (PNPP) to para-nitrophenol (PNP) by Alkaline Phosphatase, as a benchmark to determine a proportionality constant between initial $Rate_{ITC}$ obtained from ITC and the initial rate obtained from spectroscopic measurements using equation 6.15 (Honarmand Ebrahimi et al., 2015).

Equation 6.15:

$$initial\ Rate_{ITC}(t) = a_{CA} \cdot initial\ Rate_{enz}(t)$$

Where:

$Initial\ Rate_{ITC}(t)$ = the derivative of the ITC heat signal with respect to time, evaluated at an early time point, t

$Initial\ Rate_{enz}(t)$ = the rate change in product concentration or the rate of substrate depletion per unit time, measured at an early, specific time point, t

a_{CA} = proportionality constant

Since the a_{CA} is a constant for the ITC instrument, once determined using a standard assay, it can be applied to all other enzymatic reactions analyzed by ITC. Despite this adjustment requirement, the primary goal of our investigation was to assess whether the phosphorylation reaction of GSK3 β follows the Michaelis-Menten kinetics. For this purpose, we utilized the

unadjusted initial Rate_{ITC} values as a straightforward means to observe the reaction's overall behavior and determine its adherence to Michaelis-Menten kinetics. The $\text{Rate}_{\text{ITC}}(t)$, reflecting the enzyme's activity at the beginning of the reaction under steady-state conditions, can be measured for various substrate concentrations. The raw data from **Figure 6.5** was used to determine the $\Delta\text{DP}_{\text{ITC}}(t)$ and then the $\text{Rate}_{\text{ITC}}(t)$ for the 8-11 second time points from the linear phase and plotted against time post-substrate injection for each substrate concentration (**Figure 6.8**). The appearance of the fit's quality seems deceptive because of the effect of scaling. Ideally, the $\text{Rate}_{\text{ITC}}(t)$ should be near-constant across the linear DP range. However, the initial Rate_{ITC} values extrapolated from each trendline were plotted against the substrate concentrations, and the fit to the Michaelis-Menten equation was assessed (**Figure 6.9**).

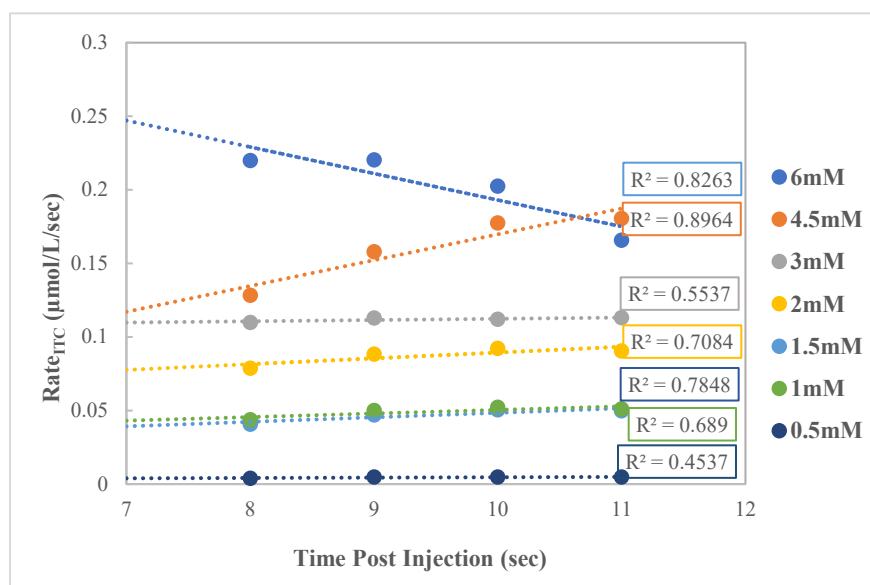


Figure 6:8: The Initial Rate_{ITC} Determination from Linear DP Range. The $\text{Rate}_{\text{ITC}}(t)$ was calculated from the linear DP range and was plotted against time post-injection for the single-injection assays with different triple-site GSM peptides (6mM, 4.5mM, 3mM, 2mM, 1.5mM, 1mM, and 0.5mM). Dots represent the Rate_{ITC} values calculated for each time point, and the dotted lines represent the extrapolation. Initial Rate_{ITC} for each substrate concentration is obtained from the y-axis intercept. The fit's quality seems deceptive due to scaling.

Although a linear range for DP change was observed for 7-12 seconds post-injection, the Rate_{ITC} calculated using the $\Delta\text{DP}_{\text{ITC}}(t)$ for subsequent time points and plotted against time post-injection did not provide good fits (poor R^2 values) for all substrate concentrations, suggesting the reaction kinetics might not be entirely linear within the chosen timeframe or that the reaction system exhibits complexity not fully captured by linear extrapolation. The poor fitting of the Initial Rate_{ITC} into the Michaelis-Menten equation (**Figure 6.9**) implies that the triple-site GSM phosphorylation reaction catalyzed by GSK3 β does not conform to the classical enzyme kinetics model.

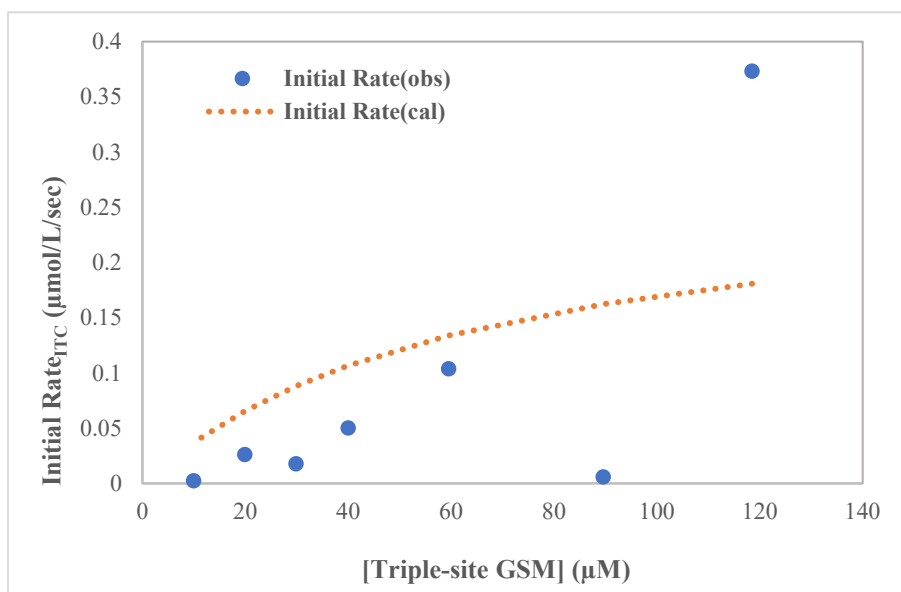


Figure 6.9: Comparison of Observed and Calculated Initial Rates for GSK3 β Catalysis of Triple-site GSM Peptide via IrCal: Poor Fit to Michaelis-Menten Model. The blue dots represent the initial Rate_{ITC} determined from the IrCal approach (Initial Rate_{obs}) for the catalysis of different peptide concentrations by GSK3 β . The dotted orange line represents the calculated initial Rate_{ITC} (initial Rate_{cal}) by fitting to the Michaelis-Menten equation. A large discrepancy is observed between the Initial Rate_{obs} and Initial Rate_{cal} , implying this reaction may not follow the Michaelis-Menten kinetics model.

Since the studied reaction involves a multi-site phosphorylation scenario, a kinase could adhere to its substrate and phosphorylate all target sites without detaching, following a processive mechanism. Alternatively, in a distributive mechanism, the kinase might bind, phosphorylate a single residue, detach, and then need to reattach to phosphorylate the following site (Patwardhan & Miller, 2007; Salazar & Höfer, 2009). To help explain how the individual phosphorylation events differ in these two mechanisms, the terminologies [MODE 1] and [MODE 2] were coined (**Figure 6.10**). [MODE 1] represents the case where the enzyme encounters the primed peptide, forming the ES complex, and then phosphorylation occurs. [MODE 2] is characterized by an enzyme already engaged with the substrate and poised to phosphorylate the target site without needing the ES complex formation step. Presumably, a 4 amino acid ratcheting step would be required to re-position the peptide substrate relative to the active site for [MODE 2]. If GSK3 β follows a 100% processive mechanism, then the #1 site on the peptide gets phosphorylated via [MODE 1], and the 2nd and 3rd sites get phosphorylated via [MODE 2]. Alternatively, if GSK3 β follows a 100% distributive mechanism, all sites are phosphorylated via [MODE 1], and there is no [MODE 2]. The kinetics for [MODE 1] and [MODE 2] are undoubtedly distinct, which means if GSK3 β is highly processive, the kinetics of the overall system would be a mixture of both modes. The simple single-site Michaelis-Menten model does not apply to this mixed-mode system. In contrast to the kinetic behavior, the ΔH_{app} may not differentiate between the models. If the observed heat release mainly reflects the chemical transformations associated with the phosphorylation events, the cumulative heat change could be quite similar for processive and distributive models.

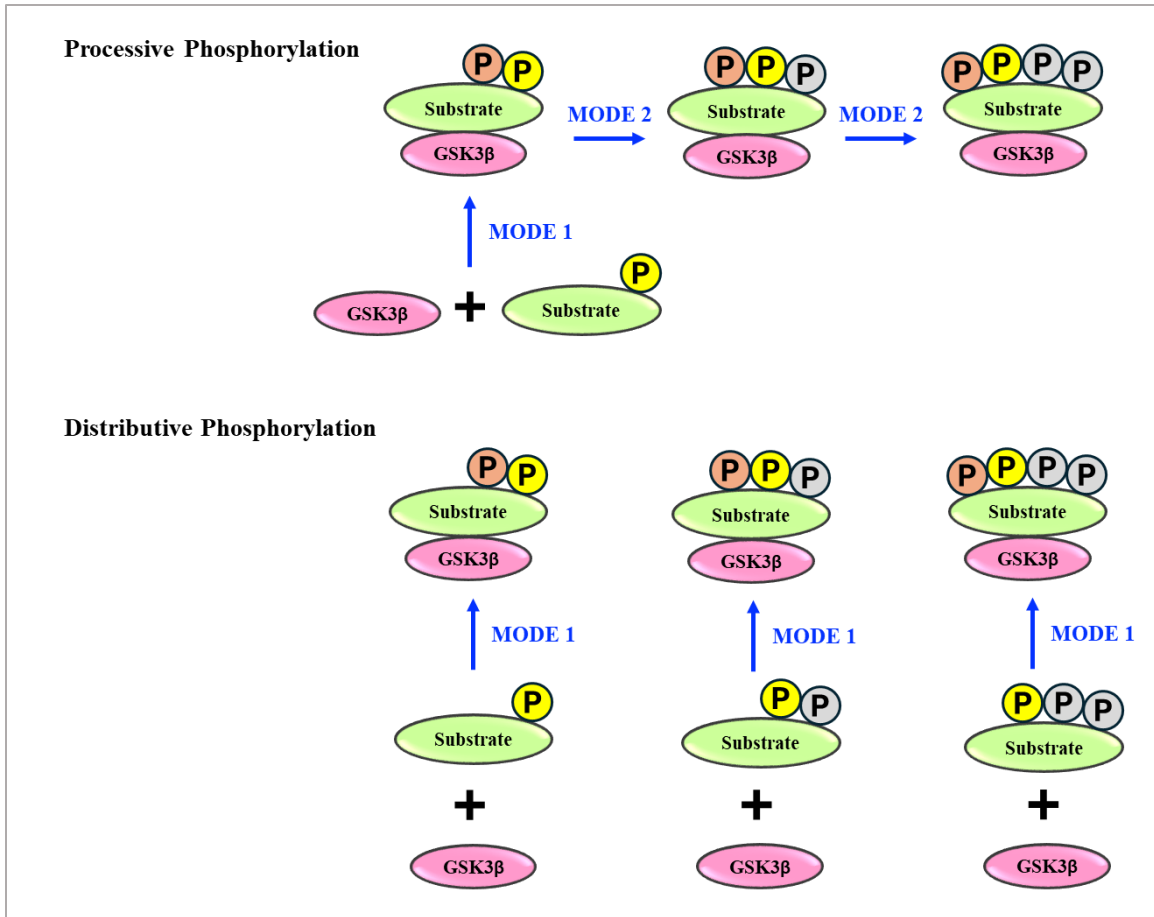


Figure 6.10: Mechanistic Models for Multi-Site Phosphorylation by GSK3β. The GSK3β kinase recognition sequence (SXXX{pS}) includes a phosphoserine residue that is called a "primed" site. Many natural substrates possess two or more adjacent sequences in tandem, creating the potential for a sequential phosphorylation cascade. Two distinct models of kinase action can be envisioned. **Processive Model:** The kinase may phosphorylate all 3 sites without detaching from the substrate by employing MODE 1 for the first phosphorylation and MODE 2 at the 2nd and 3rd sites. **Distributive Model:** The kinase may need to repeatedly bind, dissociate, and re-associate to phosphorylate the 3 sites, employing MODE 1-type interactions exclusively. The primed phosphorylated site (yellow), site of phosphorylation (orange), and previously phosphorylated sites (grey) are indicated.

The complexity introduced by multi-site phosphorylation can lead to behavior that does not conform neatly to the assumptions underlying the Michaelis-Menten equation derived from a single, simple enzymatic reaction. Previous Michaelis-Menten kinetics observed for this triple-site GSM phosphorylation by GSK3 β used discontinuous assays (Dajani et al., 2001, 2003; Ryves et al., 1998; Ryves & Harwood, 2001; Thornton et al., 2008), where the enzyme reaction rates were determined using the total concentration of peptide phosphorylated over a given time. These assays would not, therefore, capture dynamic changes associated with multi-site phosphorylation. Analyzing the kinetics of this type of reaction might require more sophisticated models that can account for the multi-step nature of the process.

Michaelis – Menten Analysis for the Phosphorylation of Mono-site GSM Peptide

A mono-site GSM peptide was derived by replacing the serine residues on the triple-site GSM peptide's second and third phosphorylation sites with alanine. GSK3 β will recognize the primed site and phosphorylate the serine residue on the first phosphorylation site. The phosphorylation of the mono-site GSM peptide catalyzed by GSK3 β was analyzed via the ITC single-injection assay. The mono-site peptide offers a relatively straightforward enzymatic process, where the enzyme-substrate interaction and the subsequent phosphorylation follow a single-path mechanism that is predicted to follow Michaelis-Menten kinetics. This simplicity would allow a more straightforward interpretation of the kinase activity and kinetic parameters for GSK3 β .

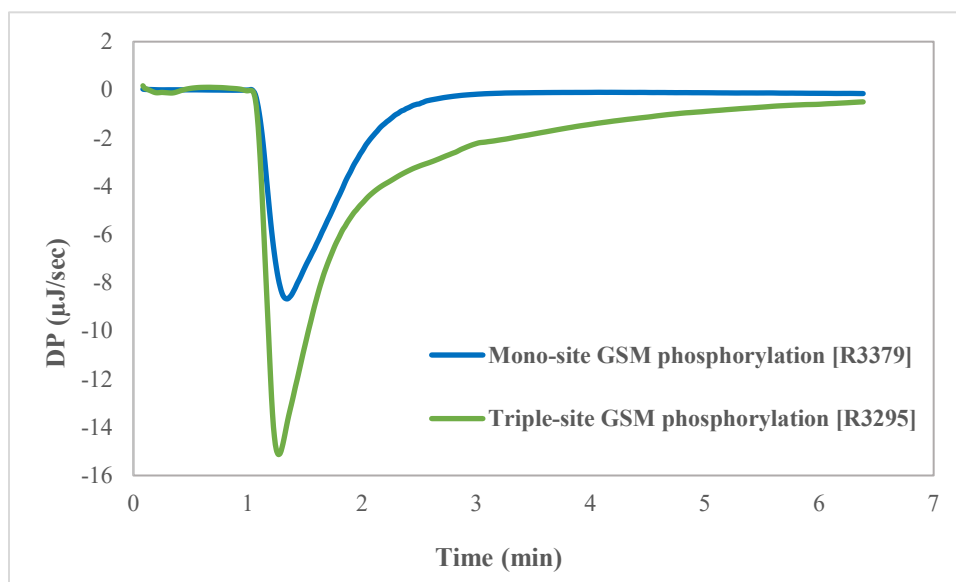


Figure 6.11: Comparing ITC Thermograms for the Phosphorylation of Triple-site GSM vs. Mono-site GSM Peptide Catalyzed by GSK3 β . 3mM peptide was injected at t = 1min into the ITC cell containing 0.5 μ M (R3295) or 0.66 μ M (R3379) GSK3 β and 1.5mM or 0.6mM ATP in 50mM TRIS pH 8, 20mM NaCl, 10mM MgCl₂ at 30 °C.

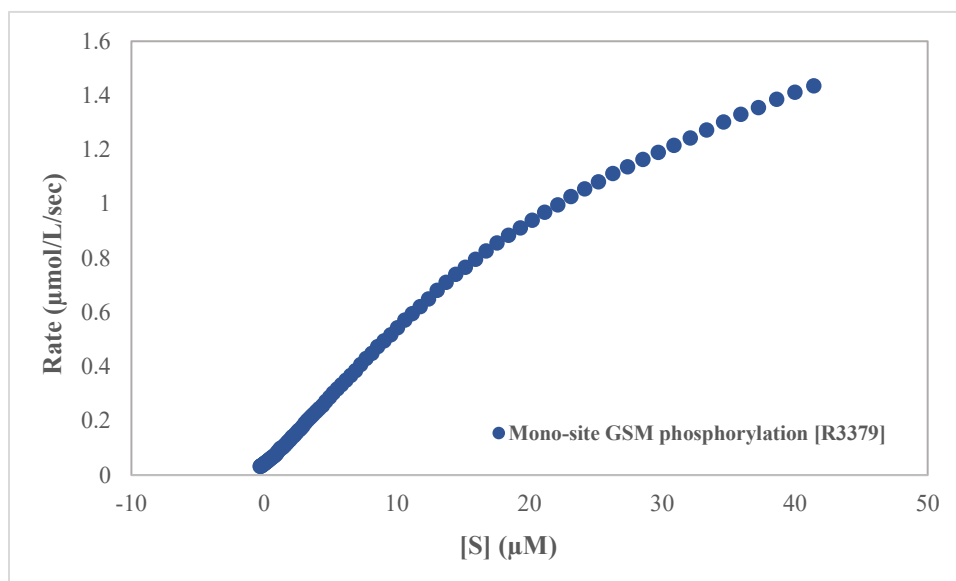


Figure 6.12: Rate of GSK3 β Activity vs. Increasing Mono-site GSM Peptide Concentrations. Enzyme rate vs. substrate concentration plot from the single injection analysis for the phosphorylation of the mono-site GSM peptide catalyzed by GSK3 β displays Michaelis-Menten behavior.

The raw ITC thermograms observed for the phosphorylation of the mono-site vs. triple-site GSM peptides showed that the exothermic peak for the mono-site peptide produced less heat compared to the triple-site GSM peptide (**Figure 6.11**). This would be expected since fewer phosphorylation events per molecule will be associated with the mono-site peptide. The Rate_{ITC} values derived from the DP change over time for the duration of the reaction (for each time point of the raw ITC curve) could be fitted to the Michaelis-Menten curve when plotted against the substrate concentration at the respective time point (**Figure 6.12**). This is a striking difference compared to the phosphorylation of the triple-site GSM peptide by GSK3 β , which did not adhere to the classical kinetics and further indicates a more complex reaction mechanism associated with sequential phosphorylation of multiple residues. The Michaelis-Menten constant, K_M , for the mono-site peptide phosphorylation by GSK3 β offers a measure of enzyme-substrate affinity, serving as a useful approximation for understanding the initial peptide-binding and phosphorylation dynamics at the first site of the triple-site GSM peptide. K_M inversely reflects enzyme affinity for its substrate, applicable to both mono- and initial multi-site phosphorylation events.

To obtain the kinetic parameters for the mono-site GSM phosphorylation by GSK3 β , the DP change throughout the reaction should be converted to Rate_{ITC} and plotted against the substrate concentration. The measured DP change for this reaction was corrected using the Tian equation (equation 6.12) to observe whether the instrument response time significantly affects the raw ITC curve. Although there was a discrepancy between the measured and corrected DP change near the deflection point, the measured DP change following the peak deflection was closely aligned with the corrected DP (**Figure Appendix V.E**). The MicroCal PEAQ analysis software allows the user to define the region of the raw ITC curve applicable to the Michaelis-

Menten analysis by adjusting “Enzyme Markers” to exclude the data most affected by the instrument response time (grey brackets in **Figure 6.13**). Therefore, the Tian correction minimally impacts the portion of the thermogram utilized for the Michaelis-Menten analysis. The measured DP corresponding to the selected region of the curve was used to determine the Rate_{ITC} and substrate concentrations using equations 6.9 and 6-10, respectively, for single-injection assays followed by injecting 3mM or 6mM mono-site GSM peptide into a 0.66 μM GSK3 β in 50mM TRIS pH 8, 20mM NaCl, 10mM MgCl_2 and ATP in excess. These Rate_{ITC} values (V_{obs}) were fitted to the Michaelis-Menten equation and iterated to obtain the best fit using Excel Solver. An example of this data analysis is shown in **Appendix V (Part B, Analysis 4)**.

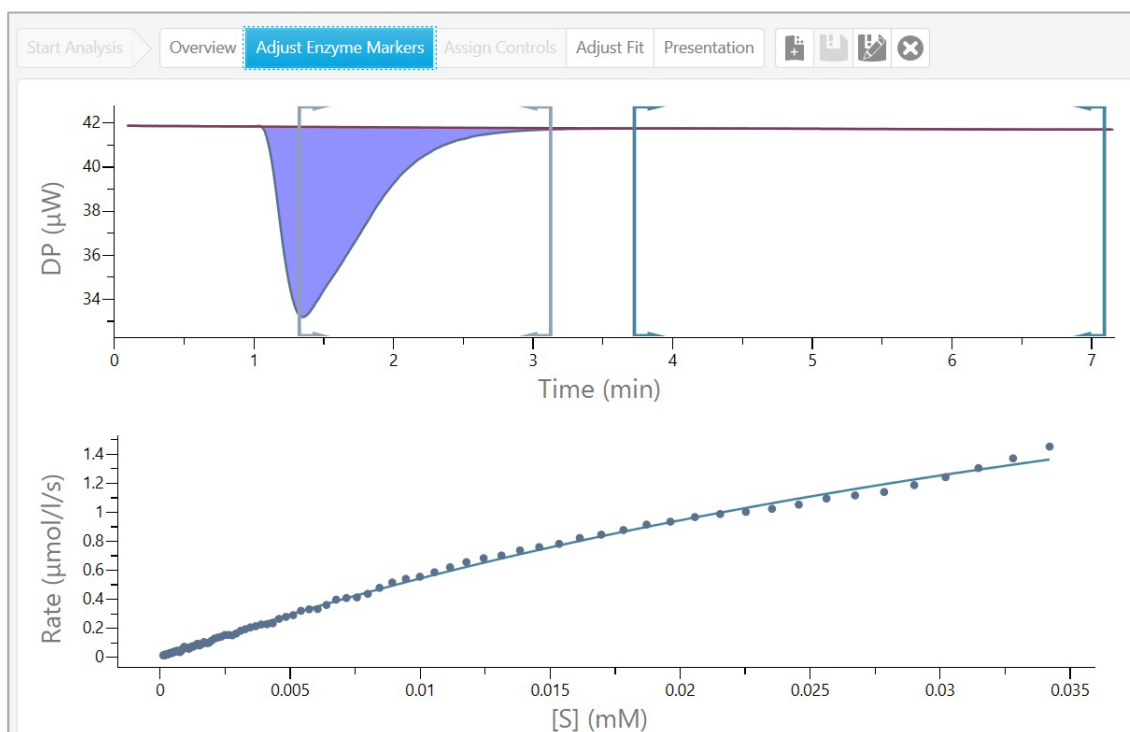


Figure 6.13: Sample Enzyme Marker Selection for the Single-injection Assay Analysis. The region of DP utilized by the MicroCal PEAQ analysis software for the Michaelis-Menten analysis is indicated in grey brackets.

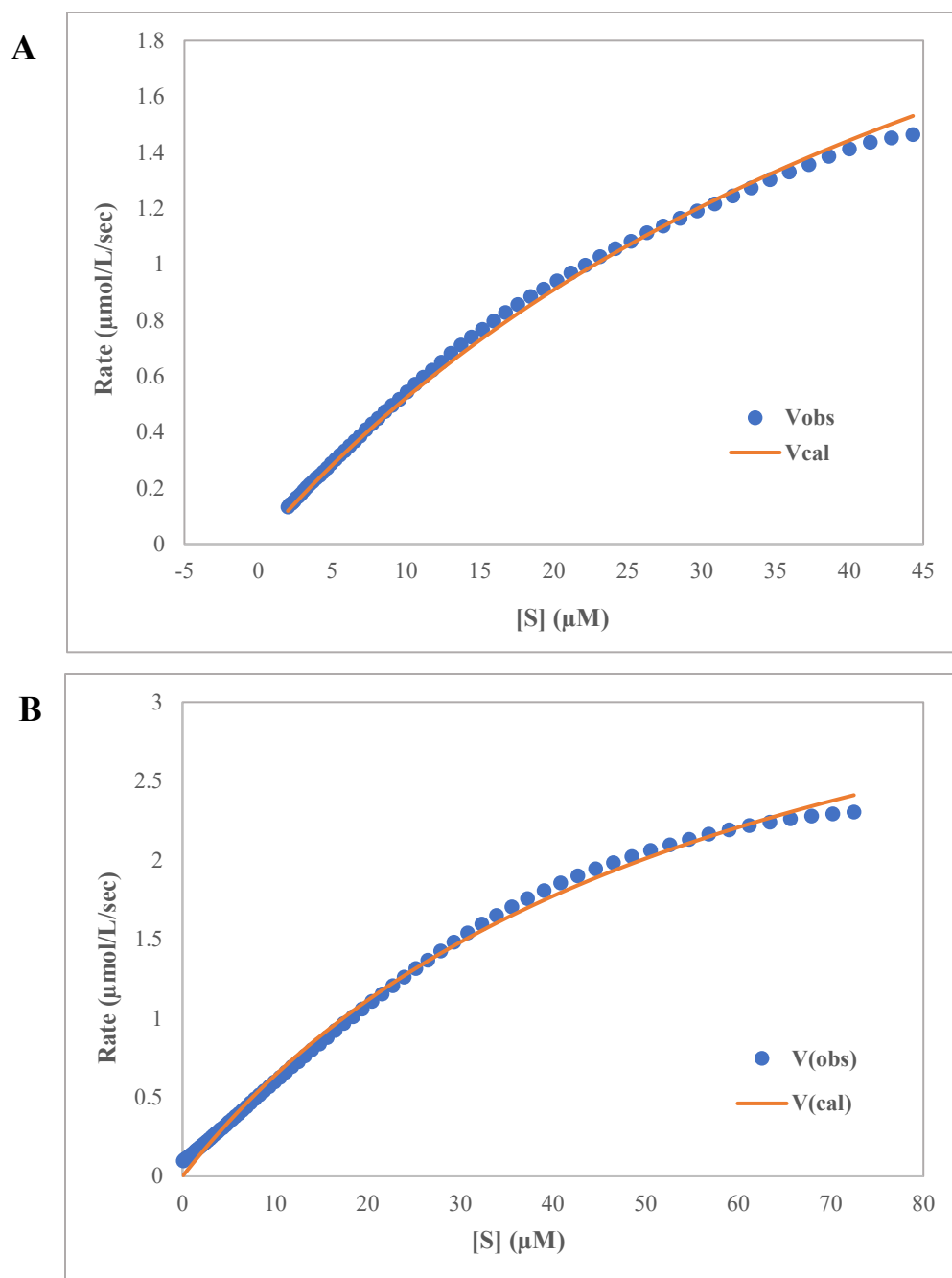


Figure 6.14: Michaelis-Menten Analysis Plots for Single-injection of Various Mono-site GSM Concentrations. Enzyme rate vs. substrate concentrations best fitted to the Michaelis-Menten equation for the phosphorylation of mono-site GSM peptide. A) 3mM peptide concentration in the syringe (0.06mM final), B) 6mM peptide concentration in the syringe (0.12mM final) catalyzed by 0.66μM GSK3β. Dots represent the rate measured based on DP change, and the solid line represents the fit to the Michaelis-Menten equation.

The Rate_{ITC} values calculated by fitting (V_{cal}) showed good alignment with the experimental rates for both 3mM (**Figure 6.14A**) and 6mM (**Figure 6.14B**) mono-site GSM phosphorylation by GSK3 β . The K_M , k_{cat} , and V_{max} were determined for each assay by manually fitting the data in Excel (**Table 6.2**), which agreed with the kinetic parameters reported by the MicroCal PEAQ analysis software (**Table 6.3**). The average K_M was $59.23 \pm 1.40 \mu\text{M}$, and the turnover number k_{cat} was $6.31 \pm 0.70 \text{ s}^{-1}$ (**Table 6.4**).

Table 6.2: Michaelis-Menten Analysis: Phosphorylation of Mono-Site GSM Peptide by GSK3 β Using Excel. The apparent reaction enthalpy, reported on MicroCal PEAQ-ITC analysis software, was used to manually calculate the rate observed vs. unreacted substrate over time. The rate observed and the rate calculated by fitting the Michaelis-Menten equation were iterated to the best fit using Excel Solver to obtain the Min Sum Square root for the rate calculated subtracted from the rate observed. k_{cat} was calculated using the V_{max} and enzyme concentration.

Exp Run#	GSM Conc. in ITC cell (μM)	ΔH_{app} (kJ/mol)	K_M (μM)	k_{cat} (s^{-1})	V_{max} ($\mu\text{M/s}$)
R3377	120	-41.2	55.81	5.85	3.86
R3378	120	-37.5	57.73	6.56	4.33
R3379	60	-29.6	57.0	5.30	3.50

Table 6.3: Michaelis-Menten Analysis: Phosphorylation of Mono-Site GSM Peptide by GSK3 β Using MicroCal PEAQ-ITC Analysis Software. The apparent reaction enthalpy, ΔH_{app} , Michaelis-Menten constant, K_M , and the turnover number, k_{cat} , obtained from the single injection of 3mM or 6mM peptide into 0.66 μ M GSK3 β . The parameters are reported from MicroCal PEAQ-ITC analysis software. V_{max} was calculated using the reported k_{cat} value and enzyme concentration.

Exp Run#	GSM Conc. in ITC cell (μ M)	ΔH_{app} (kJ/mol)	K_M (μ M)	k_{cat} (s ⁻¹)	V_{max} (μ M/s)
R3377	120	-41.2	59.3 \pm 0.928	6.26 \pm 0.06	4.13
R3378	120	-37.5	60.6 \pm 3.85	7.03 \pm 0.277	4.64
R3379	60	-29.6	57.8 \pm 2.37	5.64 \pm 0.170	3.72

Table 6.4: Average Michaelis-Menten Parameters for Mono-Site GSM Phosphorylation from MicroCal PEAQ-ITC Analysis. Mean \pm Std Deviation from n = 3 ITC runs.

ΔH_{app} (kJ/mol)	K_M (μ M)	k_{cat} (s ⁻¹)	V_{max} (μ M/s)
-36.1 \pm 5.93	59.23 \pm 1.40	6.31 \pm 0.70	4.16 \pm 0.46

Our study's K_M and k_{cat} values appear to be within a comparable range to the literature values for GSK3 β activity towards GSM peptides. (Dajani et al., 2001, 2003) studied the phosphorylation of the triple-site GSM peptide by human GSK3 β using a γ -P³²-ATP incorporation assay in a 50mM HEPES pH 8 buffer system with 12.5mM MgCl₂, 2mM DTT, and 0.05mM EDTA at 30 °C. K_M values of 70 μ M (Dajani et al., 2001), and K_M and k_{cat} values of 60 μ M and 0.7 s⁻¹ for GSK3 β without Tyr216 phosphorylation, and 85 μ M and 3.7 s⁻¹ for GSK3 β with Tyr216 phosphorylation (Dajani et al., 2003) were reported. The difference in the mono-site GSM peptide is the replacement of serine residues on the triple-site GSM's second and

third phosphorylation sites with alanine. Therefore, theoretically, both peptides should display similar enzyme-substrate interactions to bind the primed peptide and phosphorylate the first phosphorylation site. Our ITC study was followed in a 50mM TRIS pH 8 buffer system with 20mM NaCl, 10mM MgCl₂, and 10x ATP at 30 °C. In this context, the K_M of 59.23μM reported by our single-injection assay is comparable to the literature values, and the k_{cat} value of 6.3 s⁻¹ is also within the same order of magnitude.

Comparative Analysis of ΔH_{app} and ITC Curve Shapes for Mono- and Triple-Site GSM Suggests a Processive Phosphorylation Mechanism by GSK3 β on Multi-Site Substrates

A single-injection assay was utilized to compare the raw ITC thermograms for the GSK3 β catalyzed phosphorylation of 1mM (the final concentration in the ITC cell is 0.02mM) Triple-site, Mono-site, or Ser>Ala mutant GSM peptide in 50mM TRIS pH 8 buffer with 20mM NaCl, 10mM MgCl₂ and ATP in excess (**Figure 6.15**). As expected, the exothermic curve for the mono-site GSM phosphorylation was smaller than that for the triple-site GSM peptide. The Ser>Ala mutant GSM peptide has the serine residue in the first phosphorylation site replaced with an alanine residue. GSK3 β preferentially phosphorylates substrates with primed phosphorylation at the (+)4-position relative to the target serine/threonine. Therefore, we expect GSK3 β to bind Ser>Ala mutant GSM peptide but cannot catalyze the phosphotransfer, serving as a negative control. As expected, injection of 1mM Ser>Ala mutant GSM peptide into the GSK3 β generated a tiny peak attributed to the heat of dilution and peptide-enzyme binding.

Since GSK3 β needs a primed phosphorylated site to recognize and bind a substrate, its order of phospho-site phosphorylation in a multi-phospho-site substrate is expected to follow

sequential phosphorylation. This sequential phosphorylation by GSK3 β has been demonstrated for substrates with multi-phosphorylation sites such as Glycogen synthase where residues Ser-640, Ser-644, Ser-648, and Ser-652 are phosphorylated sequentially from C-terminus to N-terminus direction following the Ser-656 primed phosphorylation by Casein Kinase II (Fiol et al., 1987, 1990; Y. Wang & Roach, 1993), β -catenin at the residues Thr-41, Ser-37, and Ser-33 from C-terminus to N-terminus direction following the Ser-45 primed phosphorylation by Casein Kinase I (McCubrey et al., 2014; Stamos & Weis, 2013).

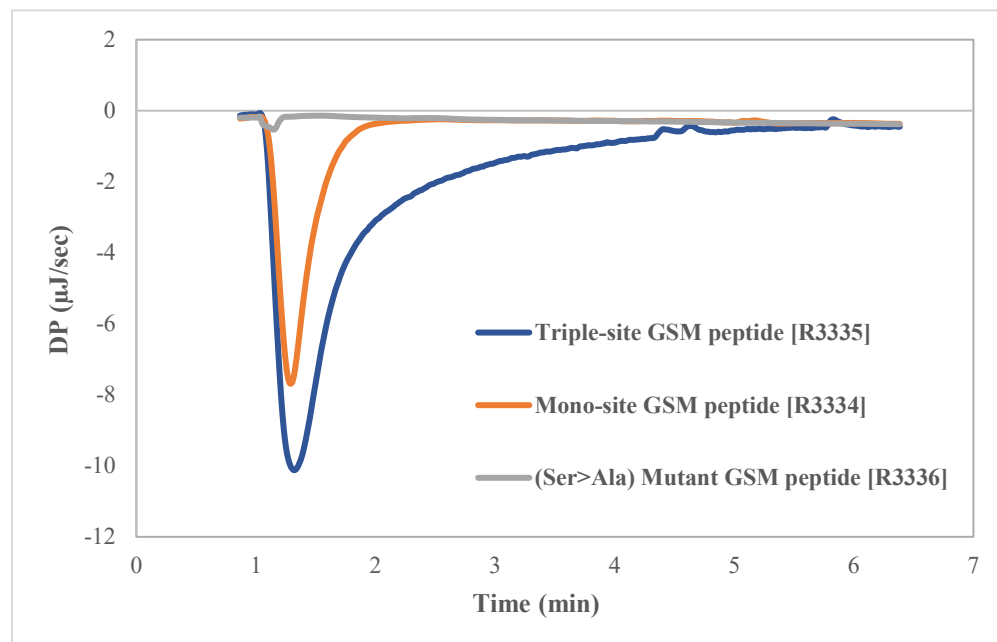


Figure 6.15: ITC Thermograms for GSK3 β Kinase Reaction with Different GSM Peptides.

The ITC thermograms for the phosphorylation of Triple-site GSM peptide (blue), Mono-site GSM peptide (orange), and (Ser>Ala) Mutant GSM peptide (grey) were compared. In each experiment, 1mM GSM peptide was catalyzed by 2 μ M GSK3 β in the reaction buffer: 50mM TRIS pH 8, 20mM NaCl, 10mM MgCl₂, and 0.2mM ATP.

A kinase can catalyze sequential phosphorylation in a processive or distributive manner. In a processive phosphorylation mechanism, the kinase binds to its substrate and phosphorylates multiple sites without releasing the substrate between phosphorylation events. Once the kinase-substrate complex is formed, the kinase can catalyze phosphotransfer to several sites in a single binding event. The distributive phosphorylation mechanism involves the kinase binding and phosphorylating a single site, then dissociating from the substrate before it can bind again to another site. This requires multiple rounds of binding and dissociation for the phosphorylation of multiple sites on the substrate.

Processive mechanisms are generally efficient, ensuring multiple phosphorylations occur rapidly and coordinated. However, the distributive mechanism may allow for greater regulation and integration of different signaling inputs (Patwardhan & Miller, 2007; Salazar & Höfer, 2009). Although the sequential pattern of GSK3 β phosphorylation has been reported, whether this reaction follows a processive or distributive mechanism is unknown. Understanding this mechanism for GSK3 β phosphorylation can have important implications for drug development. We intended to investigate this using the ITC single-injection assay. The single-injection assays were repeated to compare the ΔH_{app} and total heat produced from the phosphorylation of 1mM triple-site GSM against 1mM and 3mM of mono-site GSM peptide (**Figure 6.16A**). Each peptide sample was also injected into the buffer without the enzyme to demonstrate that the heat of dilution is negligible relative to the thermogram representing the reaction (**Figure 6.16B**). The ΔH_{app} values were derived from MicroCal PEAQ ITC analysis software, indicating differences in reaction enthalpies among the two peptides (**Table 6.5**).

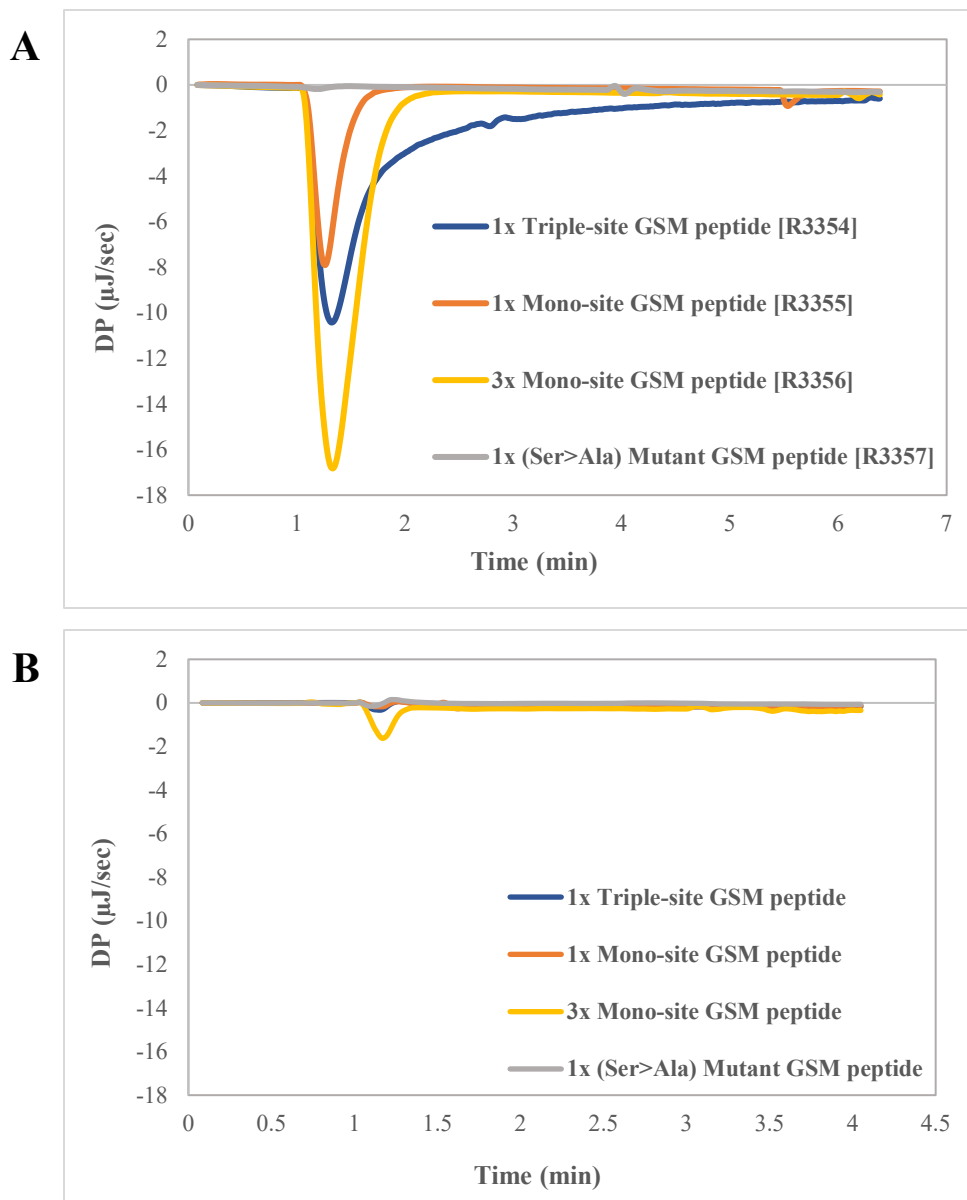


Figure 6.16: Comparison of ITC Thermograms for GSK3 β Phosphorylation of GSM Peptides at Varying Concentrations and Phosphorylation Sites. (A) The ITC thermograms for the phosphorylation of 1mM Triple-site GSM peptide (blue), 1mM Mono-site GSM peptide (orange), 3mM Mono-site GSM peptide (yellow), and 1mM (Ser>Ala) Mutant GSM peptide (grey) compared. In each experiment, the GSM peptides were catalyzed by 1 μM GSK3 β in the reaction buffer: 50mM TRIS pH 8, 20mM NaCl, 10mM MgCl₂, and 0.2mM ATP. (B) The ITC thermograms for peptide to buffer controls respective to the curves in (A).

Table 6.5: The Apparent Reaction Enthalpy from the Single-injection Analysis Comparing Triple-site GSM (RG42) vs. Mono-site GSM peptide (RG43) Phosphorylation by GSK3 β .

Triple-site GSM peptide at 1mM and mono-site peptide at 1mM or 3mM reacted with 0.5 μ M-2 μ M GSK3 β in 50mM TRIS pH 8, 20mM NaCl, 10mM MgCl₂, 0.2mM or 1mM ATP at 25 °C. The apparent reaction enthalpy values for n=2 runs are reported from MicroCal PEAQ ITC analysis software.

	1mM Triple-site GSM peptide	1mM Mono-site GSM peptide	3mM Mono-site GSM peptide
ΔH_{app} (kJ/mol)	-120 (R3335)	-30.1 (R3334)	-37.1 (R3356)
	-117 (R3354)	-33.4 (R3355)	-42.2 (R3394)
Mean \pm Std dev	-118.5 \pm 2.12	-31.75 \pm 2.33	-39.65 \pm 3.61

Phosphorylation of the triple-site GSM peptide exhibited a ΔH_{app} comparable to previous study observations, with an average value of -118.5 \pm 2.12 kJ/mol. The mono-site GSM peptide at 1mM and 3mM concentrations showed an average ΔH_{app} of -31.75 \pm 2.33 kJ/mol and -39.65 \pm 3.61 kJ/mol. Ideally, the substrate concentration should not affect the ΔH_{app} value reported because the total observed heat from the peak area is divided by the total moles of substrate injected for the reaction. The ΔH_{app} values observed for 1mM and 3mM mono-site GSM phosphorylation are still comparable, and the difference can be attributed to variations in solution preparation in experiments followed on different days. When 3mM of mono-site GSM peptide was injected for phosphorylation by GSK3 β , theoretically, the number of phosphorylation sites available for the reaction is the same as the number of phosphorylation sites available following injection of the 1mM triple-site GSM peptide. The total heat generated upon phosphorylation of 1mM triple-site GSM was = -118.5 kJ (-118.5 kJ/mol x 1mol), and the total heat generated upon

phosphorylation of 3mM mono-site GSM was = -118.95 kJ/mol (-39.65 kJ/mol x 3 mol). This result shows that the total heat released was similar when the number of phosphorylated sites available for the reaction was the same for triple-site GSM and mono-site GSM by concentration matching. This observation suggests that the amount of heat released per phosphorylation is consistent across both peptides, indicating that each phosphorylation event releases a similar amount of energy.

Next, the shape of the ITC curves is considered. If GSK3 β followed a fully distributive mechanism for multi-site phosphorylation, each phosphorylation step would follow [MODE 1] as discussed previously in the chapter. In this scenario, it would not matter whether the target sites were clustered on the same peptide molecule or dispersed among different peptide molecules, and the raw ITC curves for the phosphorylation of 1mM triple-site GSM and 3mM mono-site GSM would overlap perfectly. However, that did not appear to be the case. The raw ITC curves from **Figure 6.15** and **Figure 6.16** were scaled so they would appear to be the same size with respect to the y-axis to compare the shape of the curves (**Figure 6.17**). There appeared to be a consistent difference in the shape of the ITC thermograms for the triple-site and mono-site GSM phosphorylation across multiple ITC runs (**Figure 6.17A** and **Figure 6.17B**).

The scaled overlay of the thermograms for triple-site and mono-site GSM phosphorylation (**Figure 6.17C** and **Figure 6.17D**) shows that the initial portions of the curves overlap up to and immediately after the deflection point. The DP change over time is initially rapid, following both peptides' deflection points. However, while the curve for the mono-site peptide continues this trend and sharply returns to the baseline, the curve for the triple-site peptide appears to slow down and take longer to return to the baseline. This curve shape pattern is consistent at 25 °C (**Figure 6.17C**) and 30 °C (**Figure 6.17D**).

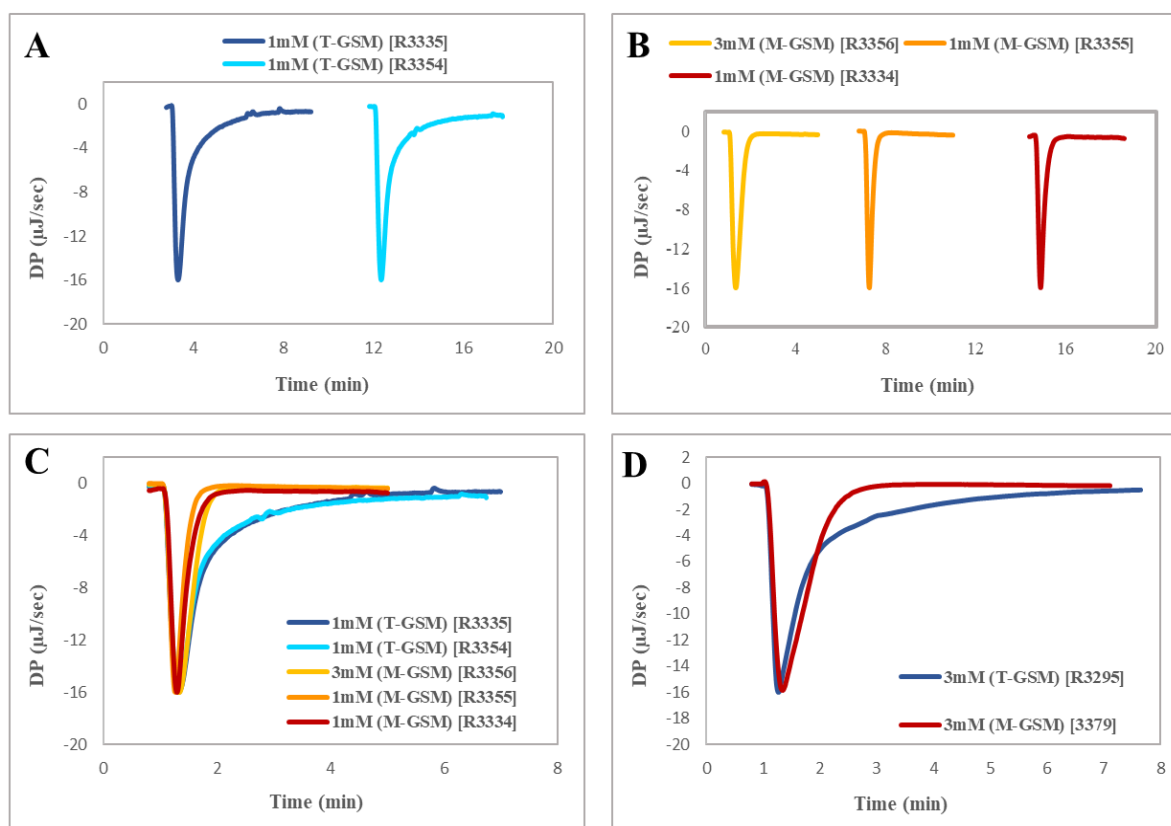


Figure 6.17: Thermogram Shape Comparison. (A–C) The raw ITC curves from **Figure 6.15** and **Figure 6.16** are scaled so they would appear to be the same size with respect to the y-axis. All reactions were followed at 25 °C. (A) Triple-site GSM peptide thermograms. (B) Mono-site GSM peptide thermograms. (C) Overlay of plots. (D) Overlay of the raw ITC curves from **Figure 6.11** scaled so they would appear to be the same size with respect to the y-axis. These reactions were followed at 30 °C for 3mM Triple-site and 3mM Mono-site peptides.

The difference in the shapes of the ITC thermograms indicates a biphasic nature in the phosphorylation of the triple-site peptide. Previously, it was discussed that if GSK3 β follows sequential phosphorylation of multiple sites in a processive manner, we can expect [MODE 1] where ES complex forms and the first site is phosphorylated, and [MODE 2] where subsequent sites are phosphorylated without the enzyme dissociating from the ES complex. The

thermograms for the phosphorylation of 1mM triple-site GSM and 3mM mono-site GSM do not entirely overlap (**Figure 6.16A**), providing evidence supporting a processive mechanism. Since the curve for mono-site GSM phosphorylation represents [MODE 1] kinetics, we can deduce that the part of the ITC curve for triple-site GSM phosphorylation that overlaps with the curve for mono-site GSM represents [MODE 1] and the portion of the curve with the slow return to the baseline predominantly represents [MODE 2].

The reaction rates for triple-site GSM and mono-site GSM phosphorylation by GSK3 β were compared for the raw ITC curves from **Figure 6.17D** to analyze the reaction rate's behavior in the curve post-deflection point (**Figure 6.18A**). These curves represent the phosphorylation of 3mM triple-site and mono-site GSM peptides by GSK3 β at 30 °C. The reaction rate for triple-site phosphorylation, immediately post-deflection, is expected to represent [MODE 1]. This phase demonstrated fast kinetics. In contrast, the latter part of the curve is expected to represent [MODE 2]. This phase demonstrated slow kinetics. The comparison of the reaction rate with substrate concentration for the triple-site and mono-site GSM peptides shows that the reaction rate demonstrates fast kinetics for the mono-site GSM phosphorylation and fast kinetics at the beginning and slow kinetics towards the end for the triple-site GSM phosphorylation (**Figure 6.18B**).

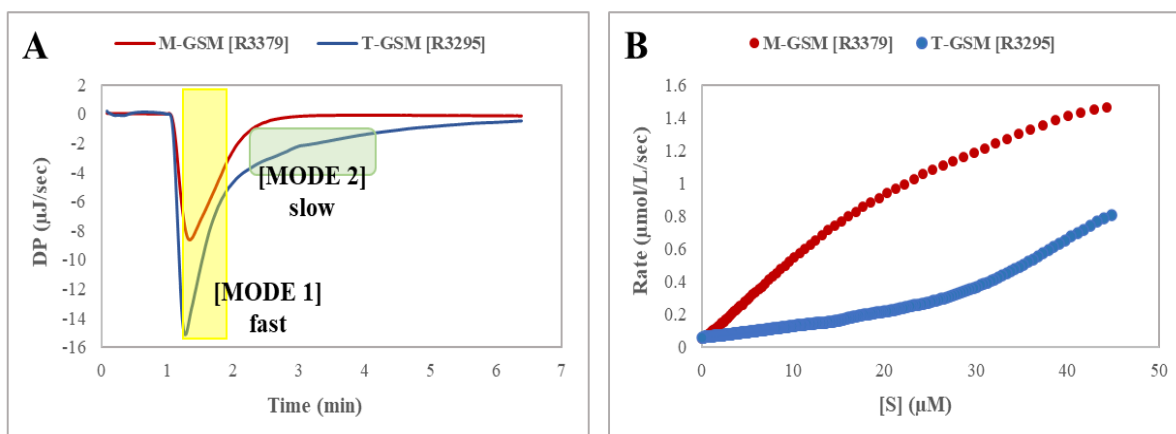


Figure 6.18: Comparison of Reaction Rates Demonstrate Biphasic Behavior for Multi-site Phosphorylation by GSK3 β . The reaction rates for the raw ITC curves from **Figure 6.17D** are plotted against the substrate concentration. All reactions were followed at 30 °C. (A) The raw ITC curves for triple-site GSM phosphorylation show biphasic behavior distinguishing between [MODE 1] and [MODE 2] mechanisms, and mono-site GSM phosphorylation only follows [MODE 1] (B) The reaction rates observed later in the reaction (at low [S]) are depressed for triple-site GSM relative to mono-site GSM.

Processivity might be considered a mechanism to increase the reaction rate of the secondary and tertiary phosphorylation sites. For GSK3 β , the converse seems to be the case: the initial rate at site #1 exhibits comparable kinetics to the mono-site substrate peptide, but kinetics seem slower at sites #2 and #3. A possible explanation for this observation would be that the reinitiation of the catalytic cycle requires the dissociation of product ADP. Due to steric hindrance or conformational changes, ADP may dissociate more readily from free enzymes and less readily from the ES complex. It may be that the absolute rate of phosphorylation at multiple sites in a sequence is not crucial, but what is biologically important is ensuring that when multiple tandem sites need phosphorylation, the process is complete, resulting in few, if any, partially phosphorylated sites. Wang and Roach (1993) demonstrated that phosphorylation of all the GSK3 target sites on the multiple tandem sequence of glycogen synthase was necessary to

inactivate it fully. Mutant forms of glycogen synthase were created where specific phosphorylation sites were altered to alanine, preventing phosphorylation at those sites. The mutants included changes at sites 3a (Ser640), 3b (Ser644), and 3c (Ser648). The study highlighted that GSK3 phosphorylation occurs sequentially. However, most importantly, partially phosphorylated forms of glycogen synthase resulted in only modest inactivation, and the phosphorylation of all tandem sites, including the final site 3a, was necessary to significantly decrease glycogen synthase activity by GSK3 (Y. Wang & Roach, 1993).

Our observations support the processive nature of GSK3 β activity. Once GSK3 β initiates phosphorylation, it remains associated with the substrate to ensure thorough and complete modification of all tandem phosphorylation sites, following a mechanism designed to ensure reliability rather than speed. Many GSK3 β substrates feature multiple tandem phosphorylation sites (**Table 6.6**). In cellular signaling, the complete phosphorylation of substrates might be crucial for achieving a proper regulatory outcome, as was the case for glycogen synthase inactivation. Prevention of incomplete substrate modification may ensure that the full regulatory intentions of the phosphorylation (activation or inactivation) are met. The need for complete and sequential phosphorylation by GSK3 β underlines the kinase's role in tightly controlled signaling pathways. Understanding the processive kinetics of GSK3 β might also have therapeutic implications. In diseases where GSK3 β activity is dysregulated, such as Alzheimer's disease, diabetes, or cancer, targeting the processivity of the specific phosphorylation sites could provide a means to modulate GSK3 β activity more precisely.

Table 6.6: GSK3 β Substrates Featuring Multiple Tandem Phosphorylation Sites. A list of GSK3 β substrates reported with multi-phosphorylation sites (Sutherland, 2011). Some substrates contain more GSK3 β target residues; only tandem sites are listed.

Substrate	Target Residues	Priming Residue (kinase)	Effect of Phosphorylation	Reference
Axin	Ser322, Ser326	Ser330	Stabilization of Axin	(Ikeda et al., 1998; Yamamoto et al., 1999)
β -catenin	Ser33, Ser37, Thr41	Ser45 (CK I)	Targets β -catenin for proteasomal degradation	(Ikeda et al., 1998)
CLASP2 (Cytoplasmic linker-associated protein 2)	Ser533, Ser537	Ser541 (CDK5)	Abolish microtubule association in metaphase	(Pemble et al., 2017)
CRMP2 (Collapsin response mediator protein 2)	Thr509, Thr514, Ser518	Ser522 (CDK5)	Impaired neuronal polarization	(Yoshimura et al., 2005)
Glycogen Synthase	Ser640, Ser644, Ser648, Ser652	Ser656 (CK II)	Reduces activity and regulates glycogen synthesis	(Parker et al., 1983; Rylatt et al., 1980)
Hif1 α	Ser551, Thr555 ----- Ser589	Not determined	Targets for proteasomal degradation	(Flügel et al., 2007)
Presenilin 1 (PS1)	Thr320, Ser324 ----- Ser353, Ser357 ----- Ser397, Ser401	Unprimed substrate	Downregulate efficiency of PS1/n-cadherin/ β -catenin complex	(Lauretti et al., 2020; Twomey & McCarthy, 2006; Uemura et al., 2007)
snail	Ser97, Ser101 ----- Ser108, Ser112, Ser116, Ser120	Not determined	Regulates proteasomal degradation and nuclear exclusion	(Zhou et al., 2004)
Substrate	Target Residues	Priming Residue (kinase)	Effect of Phosphorylation	Reference
Tau (microtubule-associated protein)	Ser46, Thr50 ----- Thr149, Thr153 ----- Thr217, Thr220 ----- Thr231, Ser235 ----- Ser258, Ser262	PKA, CDK5, CK1, CK2	Hyperphosphorylation reduces affinity to microtubules, leading to microtubule destabilization	(Hanger et al., 1992; Sayas & Ávila, 2021; Yang & Yuan, 1999)

	----- Ser409, Ser413 (Only tandem phosphorylation sites are included here)			
TSC2 (Tuberous sclerosis complex 2)	Ser1337, Ser1341	Ser1345 (AMPK)	Inhibit mTOR by TSC2 activation	(Inoki et al., 2006)

Determining Buffer-Independent Reaction Enthalpy for the Phosphorylation of Mono-site GSM Peptide by GSK3 β

In the single-injection ITC experiment, the observed total heat change (ΔH_{app}) encompasses the cumulative effect of all processes involved in the reaction, including those associated with the movement of protons to or from the buffer solution. The uptake or release of protons from the buffer during the reaction contributes additional heat within the reaction cell. The following relationship in equation 6.16 can determine the intrinsic enthalpy of the reaction (ΔH_{rxn}).

Equation 6.16:

$$\Delta H_{app} = \Delta H_{rxn} + n\Delta H_{ion}$$

Where:

n = the average number of protons exchanged

ΔH_{ion} = the ionization enthalpy of the specific buffer

ΔH_{rxn} = the buffer-independent enthalpy intrinsic to the enzymatic reaction

The analysis can be performed across different buffers at the same pH to determine the intrinsic reaction enthalpy and the number of protons exchanged. Each buffer is characterized by a distinct ionization enthalpy (ΔH_{ion}), which indicates the heat absorbed or released when a proton is added to or removed from the buffer molecule. By plotting the ΔH_{app} against the known ΔH_{ion} of the buffers in which the reaction is performed, the ΔH_{rxn} and the moles of protons exchanged can be determined through linear regression using the relationship described by equation 6.16.

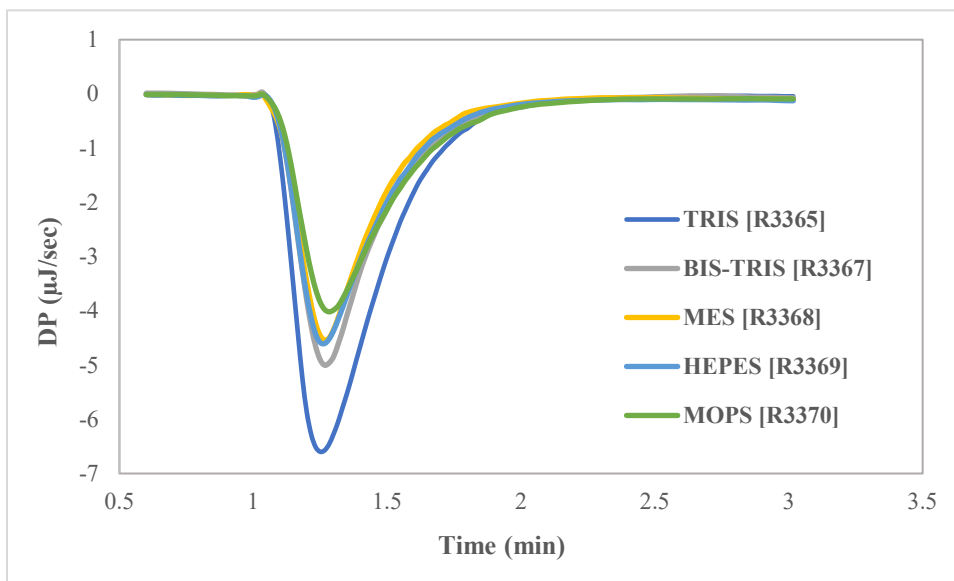


Figure 6.19: ITC thermograms for GSK3 β Kinase Reaction with Mono-site GSM Peptide in Different Buffers at pH 7 and 30 °C.

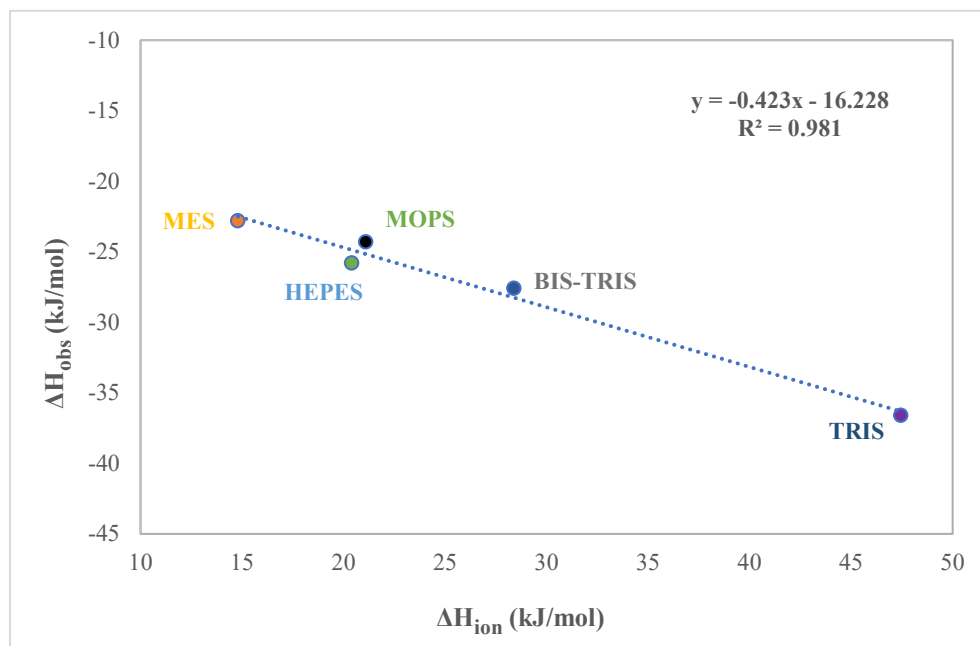


Figure 6.20: Buffer-independent ΔH for GSK3 β Kinase Reaction with Mono-site GSM peptide. The ΔH_{app} values are plotted against ΔH_{ion} for each buffer. The dotted line represents the line of the best fit. The slope of the line represents the number of protons released from the reaction, and the y-intercept indicates the ΔH_{rxn} for the phosphorylation of mono-site GSM peptide by GSK3 β .

A negative slope indicates protons are being released by the substrates or reaction system and accepted by the buffer. This proton transfer contributes to the overall heat change measured for the reaction on ITC. Likewise, a positive slope indicates that the substrates or the reaction system accepts protons during the reaction, and the buffer releases them (Bianconi, 2003; Mazzei et al., 2014; Todd & Gomez, 2001). Single-injection assays were followed in 5 different buffers: MES, HEPES, MOPS, BIS-TRIS, and TRIS for the phosphorylation of the mono-site GSM peptide by GSK3 β at pH 7 (Figure 6.19). The pH 7 was chosen for this experiment because it is within the optimal buffering capacity of TRIS, BIS-TRIS and HEPES buffers used for ITC

binding and kinase assays performed for GSK3 β in this study. The ΔH_{ion} values for each buffer were obtained from **Goldberg et al., 2002 (Table 6.7)**. The ΔH_{app} measured for the reaction in each buffer was plotted on the y-axis against the ΔH_{ion} for each buffer (**Figure 6.20**). The slope from linear regression was negative, indicating protons are released during the phosphorylation reaction catalyzed by GSK3 β for the GSM peptide. Approximately 0.4 moles of protons were released during this reaction, and the buffer-independent reaction enthalpy was -16 kJ/mol (**Figure 6.20**).

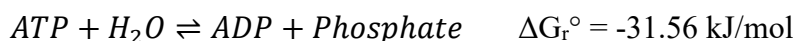
Table 6.7: ΔH_{app} Values for Mono-site GSM Phosphorylation by GSK3 β and ΔH_{ion} in Different Buffers at pH 7. The apparent reaction enthalpy was obtained from 1mM mono-site GSM peptide (RG43) injection into 1 μ M GSK3 β in the buffers listed. The ΔH_{app} is reported from MicroCal PEAQ-ITC analysis software. The ionization enthalpy for each buffer was obtained from **Goldberg et al., 2002**.

Buffer	ΔH_{ion} (kJ/mol)	ΔH_{obs} (kJ/mol)
MES	14.8	-22.8
HEPES	20.4	-25.8
MOPS	21.1	-24.3
BIS-TRIS	28.4	-27.6
TRIS	47.45	-36.6

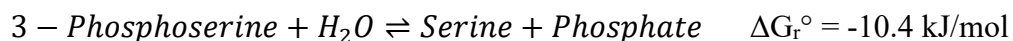
There are no reported values for the reaction enthalpy in literature for the phosphorylation of serine to phosphoserine to evaluate the reasonableness of the experimentally determined intrinsic enthalpy for this reaction. Instead, the intrinsic enthalpy is considered in the context provided by Gibbs free energy (ΔG_r°) values for ATP hydrolysis and the hydrolysis of 3-

phosphoserine (Alberty, 1998, 2003). The Gibbs free energy and enthalpy change describe different aspects of reaction energetics. The Gibbs free energy reflects the spontaneity and the maximal work the reaction at constant temperature and pressure can do. In contrast, the enthalpy reflects the heat absorbed or released during the reaction. Hess's law states that the total enthalpy change for a reaction is the same, regardless of whether it occurs in one step or a series of steps. Using Hess's law, the Gibbs free energy for the phosphorylation of a serine can be estimated using the following reactions.

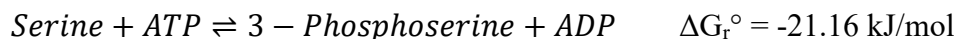
Scheme 6-2:



Scheme 6-3:



Scheme 6-4:

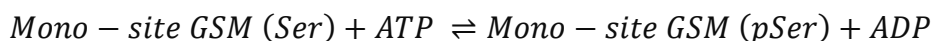


The Gibbs free energy for ATP hydrolysis is exergonic and is the driving force of many biological reactions, including phosphorylation. The hydrolysis of 3-phosphoserine to serine is exergonic, which means adding a phosphate group onto serine is endergonic. The overall ΔG_r° for the phosphorylation is exergonic, implying the reaction is spontaneous. Also, $\Delta G_r^\circ = -21.16 \text{ kJ/mol}$ implies a $K_{eq} = 5000$ (because $\Delta G = -RT \ln(K_{eq})$), which supports that the kinase reaction goes nearly to completion, suggesting the magnitude of experimental ΔH_{rxn} of -16 kJ/mol is within a plausible range. These comparisons are approximations since the values from the

literature were obtained under conditions of 298K, pH 7, pMg 3, and ionic strength of 0.1M. In comparison, the experimental conditions in our study are 303K, pH 7, pMg 2, and ionic strength 0.09M (without considering contributions from ATP ionization).

Determining the moles of protons released or absorbed during a chemical reaction involves looking at the change in the number of H⁺ ions between the reactants and products. This can be done theoretically by comparing the sum of charges for the species involved, specifically focusing on how these charges reflect changes in proton numbers. **Alberty, 2001**, explained how the conservation of mass principle applies differently in the context of biochemical reactions when conditions such as pH and pMg are specified (Alberty, 2001). Hydrogen ions' activity (or effective concentration) is kept constant when the pH is held constant in a biochemical system. Similarly, specifying pMg means holding the activity of Mg²⁺ constant. Hydrogen and magnesium ions are effectively buffered in such a controlled environment. They are not conserved in the traditional sense because their concentrations are fixed externally. Due to the presence of buffering agents or systems, the system can absorb or release hydrogen and magnesium ions without changing the overall pH or pMg. Due to the non-conservation of H⁺ and Mg²⁺ under these conditions, biochemical equations are often written to reflect the state of reactants and products as sums of species. This means that instead of writing out each form of a molecule that might exist at a given pH or pMg, the molecules are represented in terms that encompass all of their protonated, deprotonated, or complexed forms that are relevant at the specified pH and pMg. The reaction for the phosphorylation of the mono-site GSM peptide by GSK3β can be written as follows.

Scheme 6-5:



Here, ATP represents the sum of all ionized species of ATP predominantly existing at pH 7, like ATP^{-4} and HATP^{-3} ; ADP represents HADP^{-2} and ADP^{-3} ; the phosphate group on the phosphorylated serine residue of the product would represent only HPO_4^{-2} species. Considering the speciation of ATP and ADP relevant to pH 7, each could be represented as a diprotic reagent H_2A , and the fraction of each species α , for the reagent can be given as follows (Harris, 2007).

Scheme 6-6:

$$\alpha_{A^{-2}} = \frac{K_{a1} K_{a2}}{[H^+]^2 + K_{a1}[H^+] + K_{a1}K_{a2}}$$

$$\alpha_{HA^{-1}} = \frac{K_{a1} [H^+]}{[H^+]^2 + K_{a1}[H^+] + K_{a1}K_{a2}}$$

$$\alpha_{H_2A} = \frac{[H^+]^2}{[H^+]^2 + K_{a1}[H^+] + K_{a1}K_{a2}}$$

Where:

$\alpha_{A^{-2}}$ = fraction of fully deprotonated species

$\alpha_{HA^{-}}$ = fraction of 1 proton-bound species

α_{H_2A} = fraction of 2 proton-bound species

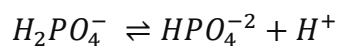
$[H^+]$ = Concentration of H^+ at pH 7

$K_{a1} = 10^{-pK_a}$ of the species of H_2A

$K_{a2} = 10^{-pK_a}$ of the species of HA^{-}

No dissociation constants are specifically available for the deprotonation of the phosphate group added to the serine residue of the peptide; therefore, the dissociation constants can be considered for one deprotonation at pH 7 for the following scheme.

Scheme 6-7:



Scheme 6-8:

$$\alpha_{HPO_4^{2-}} = \left(\frac{K_{a1}}{[H^+] + K_{a1}} \right)$$

The pKa for dissociating the serine hydroxyl group in the serine residue of mono-site GSM participating in the phosphorylation reaction is quite high (pKa 12-14). Therefore, at pH 7, this serine's hydroxyl group is almost entirely in the protonated form. The OH group, however, does undergo deprotonation when the reaction is catalyzed by GSK3 β , which would provide the specific environment to facilitate the deprotonation, which makes oxygen a stronger nucleophile and thereby able to follow a nucleophilic attack on the gamma phosphate group of ATP to follow the phosphotransfer. Since it is difficult to determine the context of this particular deprotonation, it is not considered in this analysis. The weighted average of the charged for each reactant and product can be calculated by equation 6.17.

Equation 6.17:

$$\text{Weighted average charge} = \alpha_A^{-n} (-n) + \alpha_A^{-n+1} (-n + 1) + \alpha_A^{-n+2} (-n + 2)$$

Where:

n = the charge for the fully deprotonated species or the charge of the most deprotonated species considered at pH 7 for this phosphorylation reaction.

Table 6.8: The Association Constant for H₂PO₄⁻ and the Fully Deprotonated ATP and ADP. The dissociation constants at T = 298.15K and I = 0.25 from **Alberty & Goldberg et al., 1992** (Alberty & Goldberg, 1992).

	K _{a1}	K _{a2}
ATP	1.483E-04	3.426E-07
ADP	1.612E-04	4.689E-07
Phosphoserine (H ₂ PO ₄ ⁻)	2.225E-07	-

The equilibrium constants for the dissociation of ATP (for the species ATP⁻⁴ and HATP⁻³), ADP (for the species HADP⁻² and ADP⁻³), and H₂PO₄⁻ (for HPO₄⁻²) were obtained from Alberty & Goldberg (1992). The fraction of each charged species was determined using [H⁺] as 1 x 10⁷ M since the reactions were followed at pH 7. The weighted average charge for each reagent and product was then determined by applying equation 6.17. A sample calculation for ATP is shown below.

$$\alpha_{ATP^{-4}} = \frac{K_{a1} K_{a2}}{[H^+]^2 + K_{a1}[H^+] + K_{a1}K_{a2}} = 0.7739$$

$$\alpha_{HATP^{-3}} = \frac{K_{a1} [H^+]}{[H^+]^2 + K_{a1}[H^+] + K_{a1}K_{a2}} = 0.226$$

$$\text{Weighted average charge} = 0.7739 (-4) + 0.226 (-3) = -3.7736$$

The weighted average charges calculated for ATP, ADP, and phosphoserine (H_2PO_4^-) were -3.7736, -2.8239, and -1.3798, respectively. The sum of the charges of the reactants is -3.7736, and the sum of the charges of the products is -4.2037. The net charge of the reaction would be +0.43. The theoretical analysis indicates the reaction would release 0.43 protons per mole of substrate phosphorylated. The experimental value observed for the phosphorylation of the mono-site peptide by GSK3 β from the linear regression was 0.423 (**Figure 6.19**), which is in good agreement with the value estimated theoretically.

Single-injection Analysis for Dose-Dependent Inhibition of GSK3 β Phosphorylation by Inhibitors LiCl and BeSO₄

Lithium (Li^+) is a classical inhibitor of GSK3 β , and beryllium ions (Be^{2+}) have also been characterized as a potent inhibitor of GSK3 β . Single-injection assays were performed with 1mM triple-site GSM peptide and 0.5 μM GSK3 β , in the presence of varying concentrations of LiCl (1mM, 10mM, and 30mM) or BeSO₄ (1 μM , 3 μM , 10 μM , 30 μM , and 100 μM). The enzyme and inhibitor were loaded into the ITC cell, and the reaction was initiated by injecting the peptide substrate. An assay without the inhibitor was performed as the control. Both inhibitors have demonstrated dose-dependent inhibition of GSK3 β kinase activity studied via a FRET assay, with BeSO₄ displaying 1000-fold potency compared to LiCl inhibition (Mudireddy et al., 2014). Our single-injection experiments were in agreement with previous observations demonstrating dose-dependent inhibition. The ITC thermogram declined with increasing inhibitor concentration

for LiCl treatment (**Figure 6.21**) and BeSO₄ treatment (**Figure 6.22**). The apparent enthalpy of the reaction varied significantly with inhibitor concentration, indicating direct inhibition of the GSK3 β phosphorylation reaction (**Table 6.9**). BeSO₄ exhibited a potent inhibitory effect, as expected, and interestingly showed nearly 1000-fold higher potency than LiCl. In LiCl treatment, the influence on ΔH_{app} was minimal at lower concentrations and became prominent when 30mM was used. At the same time, BeSO₄ showed potent inhibition at low concentrations like 3 μ M, demonstrating a much stronger inhibition of GSK3 β activity.

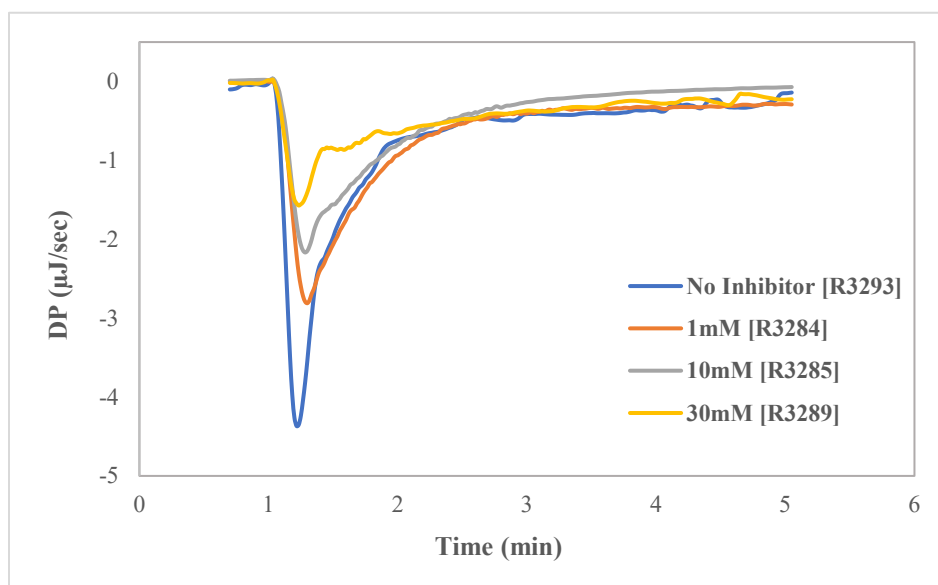


Figure 6.21: ITC Thermograms for GSK3 β Phosphorylation with Various LiCl Inhibitor Concentrations. Single-injection analysis for the reaction of 0.02mM triple-site GSM with 0.5 μ M GSK3 β and 0.2mM ATP in various LiCl inhibitor concentrations. All reactions followed in 50mM BIS-TRIS pH 6.5, 20mM NaCl, and 10mM MgCl₂ at 30 °C.

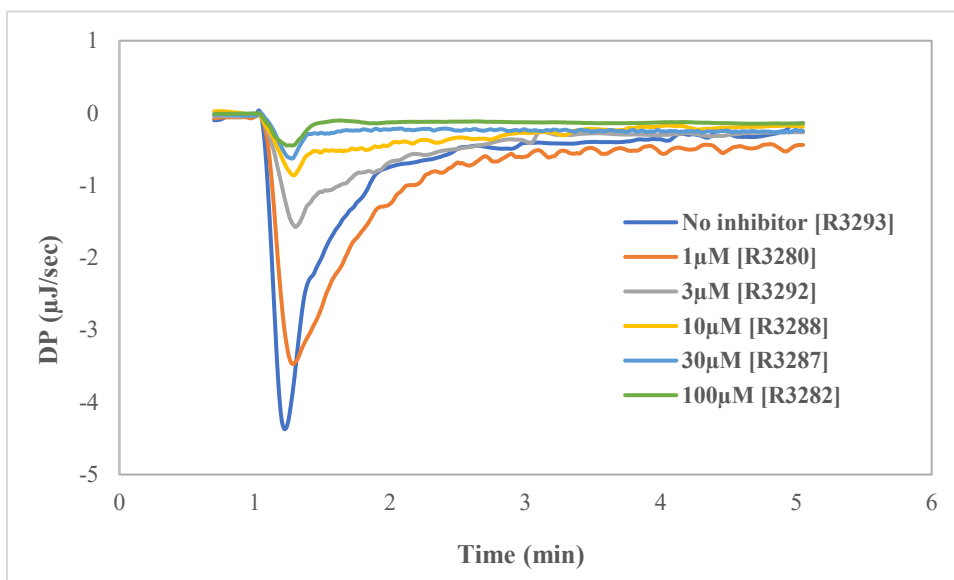


Figure 6.22: ITC Thermograms for GSK3 β Phosphorylation with Various BeSO₄ Inhibitor Concentrations. Single injection analysis for the reaction of 0.02mM GSM with 0.5 μ M GSK3 β and 0.2mM ATP in various BeSO₄ inhibitor concentrations. All reactions followed in 50mM BIS-TRIS pH 6.5, 20mM NaCl, and 10mM MgCl₂ at 30 °C.

Table 6.9: Dose-dependent Decrease in ΔH_{app} for GSK3 β Phosphorylation in the Presence of LiCl and BeSO₄. Inhibition of GSK3 β activity via Be²⁺ was ~1000-fold more potent than Li⁺.

LiCl Conc. (mM)	ΔH_{app} (kJ/mol)	BeSO ₄ Conc. (μ M)	ΔH_{app} (kJ/mol)
0	-43.3	0	-43.3
1	-40.3	1	-41.2
10	-33.3	3	-21.9
30	-28.3	10	-12.7
		30	-10
		100	-9.84

Reversibility of LiCl and BeSO₄ Inhibition of GSK3 β Phosphorylation

This study aimed to investigate the reversibility of the inhibition of GSK3 β activity by LiCl and BeSO₄. Initial FRET-based assays suggested Be²⁺ exerted a near irreversible inhibitory effect on GSK3 β (**Figure 6.23**), a hypothesis further explored using the ITC single-injection assay. For the FRET assay, GST-GSK3 β fusion protein attached to Glutathione beads was treated with 100 μ M BeSO₄ or 100mM LiCl. The kinase activity was assessed post-inhibitor wash, suggesting the possible near-irreversible inhibition by Be²⁺. The ITC single-injection assay was performed pre- and post-wash after GSK3 β was treated with 30 μ M BeSO₄ or 30mM LiCl (**Figure 6.24**). These concentrations were chosen to maintain the 1000-fold difference in inhibitor concentration between BeSO₄ and LiCl, and also 100mM LiCl produces a large heat of dilution, which obscures heat released due to the kinase reaction (Data not shown). The ITC data revealed a nuanced view of inhibitor reversibility. After washing, a recovery in GSK3 β activity was observed for both Li⁺ and Be²⁺, indicating that the inhibition by both Li⁺ and Be²⁺ is reversible (**Figure 6.24 and Figure 6.25**). Although the inhibition from Be²⁺ appears to persist slightly more than inhibition by Li⁺, the effect is not as pronounced as observed in the FRET study.

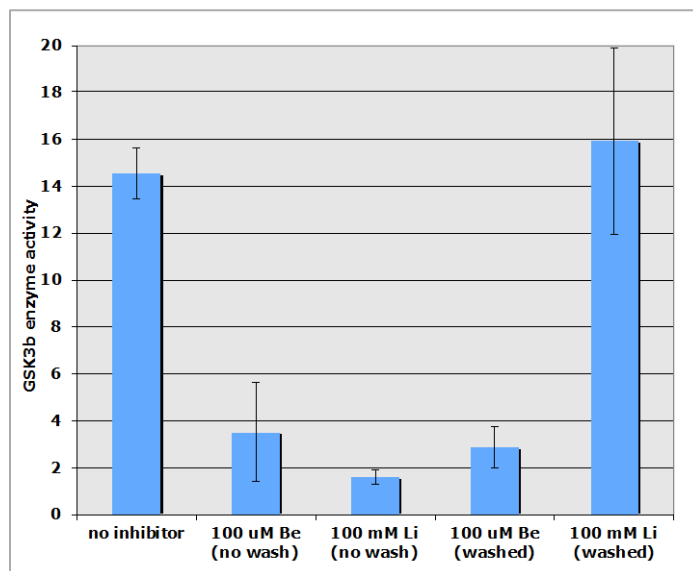


Figure 6.23: Near Irreversibility of Be²⁺ Inhibition. GST-GSK3b fusion protein bound to glutathione beads was treated with an inhibitor (100 μ M Be²⁺ or 100 mM Li⁺). Then, the beads were washed to remove the unbound inhibitor (right pair) or not washed to allow the inhibitor to remain (left pair). Enzyme activity was measured using a FRET-based assay (Mudireddy et al., 2014). Ronald Gary conducted these experiments. These results motivated follow-up studies using ITC by Bhagya De Silva.

In the pre-wash GSK3 β activity, it appears that inhibition by 30mM LiCl was slightly more potent, at least by one method of quantification (**Figure 6.25**). In this presentation, the enzyme activity was measured by the Rate_{ITC} at the peak point of the raw thermogram. The apparent enthalpy is proportional to the extent of product formation, so the ΔH_{app} value can be used as a surrogate for reaction progress in the inhibitor studies. If the apparent enthalpy of each assay is compared, it can be seen that Be²⁺ affected the overall phosphorylation reaction of GSK3 β more than Li⁺. The ΔH_{app} for no inhibitor, 30mM LiCl, and 30 μ M BeSO₄ pre-wash -53.3 kJ/mol, -36.7 kJ/mol, and -14.8 kJ/mol, respectively. ΔH_{app} for no inhibitor, 30mM LiCl, and 30 μ M BeSO₄ post-wash -54.1 kJ/mol, --49.2 kJ/mol, and -43.1 kJ/mol, respectively.

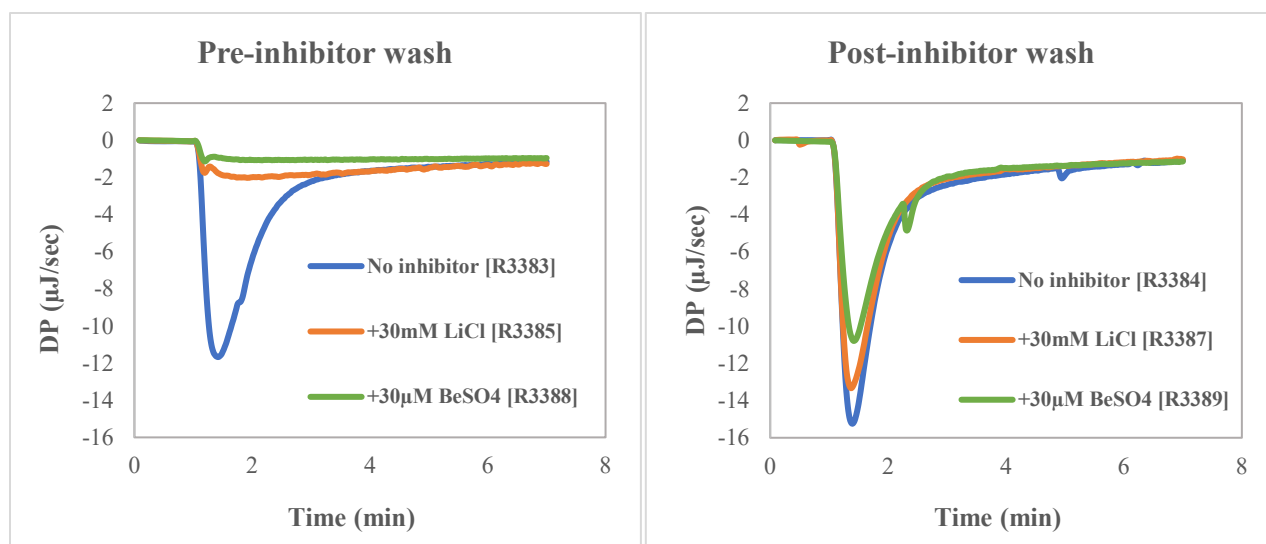


Figure 6.24: Single-injection Analysis Testing the Reversibility of GSK3 β Phosphorylation by LiCl and BeSO₄. A single-injection analysis for the phosphorylation of 0.08mM mono-site GSM peptide (RG43) by 0.5 μ M GSK3 β in the presence of 30mM LiCl or 30 μ M BeSO₄ was performed before (left panel) and after washing (right panel) the inhibitor to observe reversibility. All reactions were performed in 50mM BIS-TRIS pH 6.5, 20mM NaCl, and 10mM MgCl₂ at 25 °C.

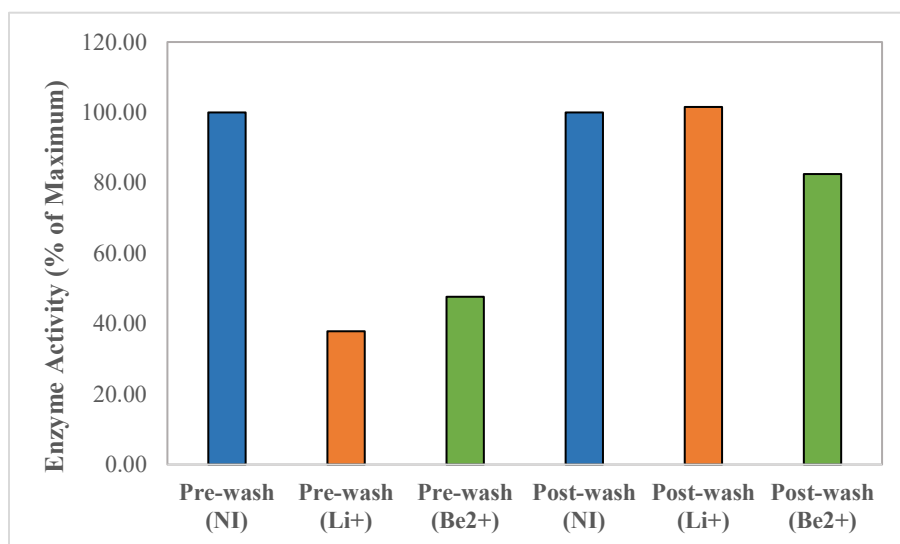


Figure 6.25: Enzyme Activity for GSK3 β Phosphorylation Pre- and Post-inhibitor Wash. GSK3 β activity pre- and post-washing, with treatment of LiCl or BeSO₄ inhibitors. The data are presented as a single experimental result (n=1) for each condition, and error bars are omitted due to the absence of replicates.

Although the FRET results could not be fully replicated via the ITC experiment, both the FRET and the ITC experiments did demonstrate some degree of resistance to washout by Be^{2+} but not Li^+ . These were single-concentration studies, with 100 μM BeSO_4 in the FRET experiment and 30 μM BeSO_4 in the ITC experiment, so it is possible that this is a relevant variation in the comparison. Further experiments would be needed to test the effect on the kinetics of the enzyme vs. overall product formation between Li^+ and Be^{2+} mediated inhibition. Using the mono-site GSM peptide would allow a more comprehensive study of these inhibitory effects as it simplifies the kinetic analysis.

The apparently higher reversibility of LiCl compared to BeSO_4 could be attributed to the ionic nature and binding affinity of these metal ion inhibitors to $\text{GSK3}\beta$. Be^{2+} , with its smaller ionic radius and higher charge density, might form a stronger interaction with $\text{GSK3}\beta$, making its inhibition more resilient to reversal. IC_{50} values from a FRET-based assay was 5 μM for BeSO_4 and 12mM for LiCl (Mudireddy et al., 2014). Furthermore, Be^{2+} has been shown to be capable of competing for both the Mg^{2+} and Mg : ATP binding sites, while Li^+ was shown to compete only with the Mg^{2+} binding site (Ryves et al., 2002). This dual binding disrupts the Mg^{2+} -dependent stabilization of ATP. It directly interferes with the ATP binding site, enhancing the inhibitory effect of BeSO_4 on $\text{GSK3}\beta$, explaining the higher potency and resilience to reversibility observed during Be^{2+} inhibition. In contrast, LiCl 's near-complete reversible inhibition and its dependence on higher concentrations for a similar inhibitory effect align with Li^+ interaction with a single Mg^{2+} site, which does not directly interfere with ATP binding.

Chapter 7: Summary and Future Directions

Summary

GSK3 β is a serine/threonine kinase with crucial roles in many biological functions, including regulating cell metabolism and homeostasis, guiding the developmental biology process, and modulating neuronal pathways. Thus, it is a pivotal enzyme in both health and disease. GSK3 β is an unusual kinase regulated by inhibition rather than activation and prefers substrates with primed phosphorylation. GSK3 β has about 100 confirmed and putative substrates (Sutherland, 2011), and many of these substrates have multiple tandem phosphorylation sites following the Ser/Thr-X-X-X-(pSer/pThr) sequence. Hyperphosphorylation of Tau by GSK3 β , leading to the formation of neurofibrillary tangles, is a hallmark pathology of Alzheimer's disease. Previous studies in our research group demonstrated evidence of pathway-specific and cell-type specific inhibition of GSK3 β by beryllium ions, which is 1000-fold more potent than lithium, classically used as a GSK3 β inhibitor and used to treat bipolar disorder. This study intended to explore ligand-binding interactions involving GSK3 β using isothermal titration calorimetry (ITC) and microscale thermophoresis (MST).

ITC is a label-free technique for determining thermodynamic parameters for protein-ligand binding and studying enzyme kinetics. This dissertation explored the affinity of beryllium ions against carboxylate-rich chelators and peptides, GSK3 β ligand binding, and analyzed the kinase activity of GSK3 β using ITC. The study also explored different protein expression systems to prepare GSK3 β for ITC experiments. A summary of the findings follows:

- ITC binding experiments for beryllium and magnesium (and lithium) ions using model chelators featuring carboxylate groups (EDTA, NTA, 4,5-IDA, and Salicylic acid) and tetrapeptides featuring carboxylate groups (composed of aspartic acid residues (D) or versions where various residues were replaced with glycine (G)), demonstrated that beryllium ions display a higher affinity and preference for structured carboxylate-rich binding sites than magnesium and lithium ions. The stoichiometry for the binding event between beryllium ions and DDDD peptide was $n = 2$. The thermodynamic profile for this binding event demonstrated a significant gain in entropy. This shows that the binding events involving beryllium and carboxylate groups of aspartic acid residues are entropically driven. Binding studies repeated with MST corroborated that beryllium has a higher affinity against carboxylate-rich peptides than magnesium. This study demonstrated that the unique aqueous chemistry of beryllium due to its high charge density, preference for tetrahedral coordination geometry, and ability to form strong electrostatic interactions with carboxylate groups contribute to its ability to displace magnesium from both solvated and non-solvated magnesium binding sites on GSK3 β .
- Recombinant GST-GSK3 β was attempted to be expressed in bacterial cells and via the baculovirus expression system in Sf9 and Hi5 insect cells. The bacterial expression did not yield full-length GST-GSK3 β , and the glutathione-purified protein sample predominantly contained degraded versions. Utilizing a Codon Plus *E. coli* strain did not improve this result. Full-length GST-GSK3 β was expressed in Sf9 cells. However, the protein expression levels largely varied, and the overall yield was insufficient for ITC binding experiments. Using Sf9 cells for baculovirus amplification and Hi5 cells for protein expression yielded the best results. GST-GSK3 β was successfully expressed in

Hi5 cells and could be isolated at high purity following glutathione affinity purification and ion exchange chromatography.

- ITC binding experiments for ATP vs. GSK3 β initially showed broad exothermic peaks more akin to an enzymatic reaction rather than a binding event, suggesting basal ATP hydrolysis might occur. Therefore, a non-hydrolyzable ATP analog AMP-PNP was utilized for binding experiments with GSK3 β . A distinct exothermic peak was observed for the first injection when AMP-PNP was titrated into GSK3 β in the ITC cell. This observation was reproducible and concluded as a representation of binding. However, thermodynamic parameters could not be derived since a binding isotherm could not be obtained under the tested experimental conditions.
- This dissertation presents the first kinetic analysis of a protein kinase using an ITC enzymatic assay. The ITC single-injection assay was utilized to study the phosphorylation of a primed GSK3 β substrate, the GSM phosphopeptide. The GSM phosphopeptide has three consecutive phosphorylation sites. Mutated versions of GSM were developed to create mono-site (serine residues on the second and third phosphorylation sites mutated) and zero-site (serine residue on the first phosphorylation site mutated) GSM substrates in which serine residues in specific phosphorylation sites were changed to alanine. Phosphorylation of the mono-site GSM by GSK3 β was an exothermic reaction and followed Michaelis-Menten kinetics, with a K_M of 59 μ M and k_{cat} of 6.3 s⁻¹. The intrinsic enthalpy of the reaction was -16 kJ/mol. The kinetic analysis for triple-site GSM phosphorylation did not conform to classical Michaelis-Menten kinetics and instead displayed a biphasic behavior. This novel observation could not be uncovered via conventional kinase assays.

- GSK3 β sequentially phosphorylates substrates that contain multiple phosphorylation sites arranged in tandem. Comparative studies of reaction enthalpies and the shapes of the raw ITC thermograms for both mono-site and triple-site GSM indicated that GSK3 β employs a processive phosphorylation mechanism. This processive action displays two phases: rapid kinetics in ES complex formation and phosphorylation at the initial site, followed by slower kinetics at the secondary and subsequent sites. This pattern suggests that once GSK3 β starts the phosphorylation process, it remains bound to the substrate, ensuring complete modification across all tandem sites, adopting a mechanism that prioritizes accuracy over speed. This behavior underlines the importance of GSK3 β 's role in precisely regulated signaling pathways, highlighting the necessity for complete and sequential phosphorylation.
- The ITC single-injection assay compared beryllium and lithium-mediated inhibition of GSK3 β kinase activity. The enthalpy of the reaction decreased in a dose-dependent manner for both beryllium and lithium. Additionally, inhibition of GSK3 β activity by beryllium was 1000-fold more potent than lithium, similar to published data (Mudireddy et al., 2014). The reversibility of GSK3 β inhibition by beryllium and lithium was tested. Inhibition by both metal ions was reversible. Inhibition by lithium was completely reversible, and inhibition by beryllium was moderately but not completely reversible under the tested experimental conditions.

Future Directions

Enhancing Kinetic Analysis in ITC: Implementing the Empirical Response Model for Rapid Reaction Dynamics

Although the ITC single-injection assay offers significant advantages over traditional discontinuous kinase assays, its capability to analyze rapid kinetic events can still be enhanced. In our study, the ITC single injection assay revealed distinct kinetic phases in the phosphorylation of the triple-site GSM peptide by GSK3 β , which were not discernible in conventional assays that rely on endpoint measurements and thus miss the real-time dynamics of the kinase activity. Specifically, while the phosphorylation of the first site by GSK3 β exhibited rapid kinetics, the subsequent phosphorylation events were considerably slower. This nuanced observation highlights the critical insights provided by the ITC method.

However, the rapid kinetics of the initial phosphorylation site presents a challenge in accurately capturing the complete kinetic profile due to the limitations in the calorimeter's response time. The empirical response model (ERM) can be applied to address this and improve the accuracy of our measurements for such fast reactions (Di Trani et al., 2017). By empirically determining the calorimeter's response function, $f(t)$, through a series of calibration experiments using known rapid reactions (such as Ca²⁺ vs. EDTA) under the same experimental conditions, we can deconvolute this response from the observed calorimetric data $g(t)$. This allows us to reconstruct the true heat change curve $h(t)$, thereby more accurately depicting the reaction kinetics.

Equation 7.1:

$$g(t) = h(t) * f(t)$$

Implementing the ERM can enhance our understanding of fast-acting biochemical processes and could unveil further mechanistic insights into kinase activity regulation.

Exploring the ITC Multiple-Injection Assay for the Kinetic Analysis for Multi-site Phosphorylation

Several studies using conventional γ -P³²-ATP incorporation assay to measure GSK3 β kinase activity with the triple-site GSM peptide reported data fitting the Michaelis-Menten model (Dajani et al., 2001, 2003; Ryves et al., 1998; Ryves & Harwood, 2001; Thornton et al., 2008). It would be interesting to explore whether a similar result and kinetic parameters can be obtained utilizing the ITC multiple-injection assay. Multiple-injection assay measures the DP change with respect to the initial baseline following incremental substrate injections. Firstly, the DP change is measured when the raw curve approaches the baseline, so the effect of the instrument response time on the measurement would be minimal. Secondly, the phosphorylation of the first and subsequent sites on the peptide will be complete as the raw curve approaches the baseline. Since this assay measures the DP change between the initial baseline and respective baselines following each injection, it will simulate a discontinuous assay. If the application of the ITC multiple-injection assay for multi-site phosphorylation by GSK3 β yields data conforming to the classical enzyme kinetics model, we can propose that utilizing both the ITC single-injection and multiple-injection assay to investigate the kinetics of complex enzymatic reactions as a method to derive comprehensive information about the mechanism and conventional kinetic parameters.

Using MALDI-TOF MS to Support Processive Kinetics by GSK3 β

To substantiate the processive kinetics of GSK3 β in phosphorylating GSM substrate peptides, MALDI-TOF MS can directly observe the sequential and site-specific phosphorylation events. By preparing phosphorylation reactions with mono-site and multi-site GSM peptides under consistent conditions and analyzing the treated samples using MALDI-TOF MS, we can identify the mass/charge ratios corresponding to unphosphorylated and various phosphorylated forms. The analysis will focus on detecting a progression of phosphorylation states, particularly evident in multi-site peptides, indicating a processive mechanism. This approach will help correlate the equivalent heat generation observed in ITC studies for different substrate configurations with a biochemical pattern of successive phosphorylations, providing compelling evidence of GSK3 β 's processive action. Such findings will confirm the enzyme's kinetic behavior and enhance our understanding of its regulatory role in cellular pathways, supporting the development of targeted therapeutic strategies.

Preliminary MALDI-TOF MS experiments were attempted with the CHCA (α -Cyano-4-hydroxycinnamic acid) matrix; however, the GSM peptide did not appear to ionize sufficiently with this matrix. Subsequent attempts with the SA (Sinapinic acid) matrix were successful; however, the assay conditions must be optimized to obtain reproducible data.

Microscale Thermophoresis (MST) for GSK3 β Ligand Binding Studies

The characterization of GSK3 β -ligand interactions using ITC did not successfully produce discernible binding curves, likely because the interactions did not generate sufficient detectable heat under the experimental conditions and because of protein solubility issues. MST

offers a sensitive alternative to detect binding interactions by measuring changes in the movement of fluorescently labeled molecules within a temperature gradient, which occurs in response to binding events. For this purpose, we plan to use a RED-NHS labeling kit to label GSK3 β . RED-NHS contains a red fluorescent label linked to an N-hydroxy succinimide (NHS) ester that covalently attaches to primary amine groups, typically found on the lysine residues of the protein. This labeling will facilitate the fluorescent detection necessary for MST analysis. One published study has reported MST data for GSK3 β -ligand interactions (Balboni et al., 2022) with RED-NHS labeled GSK3 β and fluorine compounds. MST can be applied to study interactions with AMP-PNP, GSM substrate peptides, inhibitors like Alsterpaullone, and metal ions beryllium and lithium. These MST experiments will not only complement our existing data but are expected to provide deeper insights into the kinetic and thermodynamic properties of GSK3 β -ligand interactions.

Appendix I

Capillary Electrophoresis Analysis of Phosphorylation in β -catenin and Ser9 Phosphorylation in GSK3 β Following the Treatment of Lithium and Beryllium in A172 Cells.

A172 cells were utilized for the lithium chloride (LiCl) or beryllium sulfate (BeSO₄) dose treatment experiment. The cells were cultured to 80-90% confluency in RPMI medium supplemented with 10% fetal bovine serum and 1% PSF (penicillin-streptomycin-fungizone), then treated with varying LiCl concentrations (0, 1, 5, 10, 20, 30, and 50 mM) or with varying BeSO₄ concentrations (0, 10, 30, 100, 1000 μ M) and incubated in a CO₂ incubator at 37 °C for 24h to assess protein expression changes. Post-treatment, cells were harvested using 0.25% trypsin, centrifuged, and the pellets lysed using MPER with protease and phosphatase inhibitors. Lysis was conducted on ice with gentle shaking and subsequent centrifugation to clear cell debris. Protein concentrations in the lysates were determined using the BCA (bicinchoninic acid assay), with standards prepared from a 2000 μ g/mL albumin solution, ensuring accuracy in protein quantification for further analysis.

The WES (12-230 kDa) Master Kit and WES HRP-conjugated rabbit secondary antibodies were obtained from ProteinSimple, San Jose, CA, for Capillary electrophoresis experiments. The same amount of protein was loaded into each capillary for a specific antigen (optimized for best antigen: antibody ratio in preliminary experiments). Lysates were combined with SDS Sample Buffer to achieve a 1 \times concentration and included fluorescent internal control size markers (1 kD, 29 kD, 230 kD) from ProteinSimple, San Jose, CA, USA. The sample mixture was then heated at 95 °C for 5 minutes. The samples were analyzed using 12-230 kD

size assay capillaries on a Wes capillary electrophoresis system from ProteinSimple, always incorporating a capillary with a biotinylated size ladder (12, 40, 66, 116, 180, and 230 kD) in each run. Primary antibody concentrations applied for each antigen tested were optimized in preliminary experiments. Primary antibodies utilized in the capillary electrophoresis were applied at specific dilutions: GAPDH rabbit polyclonal at 1:500 (#sc-25778, Santa Cruz Biotechnology), GSK3 β rabbit polyclonal at 1:100 (#sc-9166, Santa Cruz Biotechnology), phospho-Ser9-GSK3 β rabbit polyclonal at 1:50 (#9336, Cell Signaling Technology), β -catenin rabbit monoclonal at 1:250 (clone D10A8, #8480, Cell Signaling Technology), phospho-Ser33/Ser37- β -catenin rabbit polyclonal at 1:50 (#2009, Cell Signaling Technology), and phospho-Ser33/Ser37/Thr41- β -catenin rabbit polyclonal at 1:50 (#9561, Cell Signaling Technology). Capillary electrophoresis data, including peak area calculations, were processed using Compass software from ProteinSimple. The electropherograms were analyzed to quantify protein levels, with results normalized against GAPDH to ensure an accurate assessment of protein expressions across samples.

The LiCl dose-response effects on P- β -Catenin were observed in U251 and U87MG Glioblastoma cells (Data Not Shown).

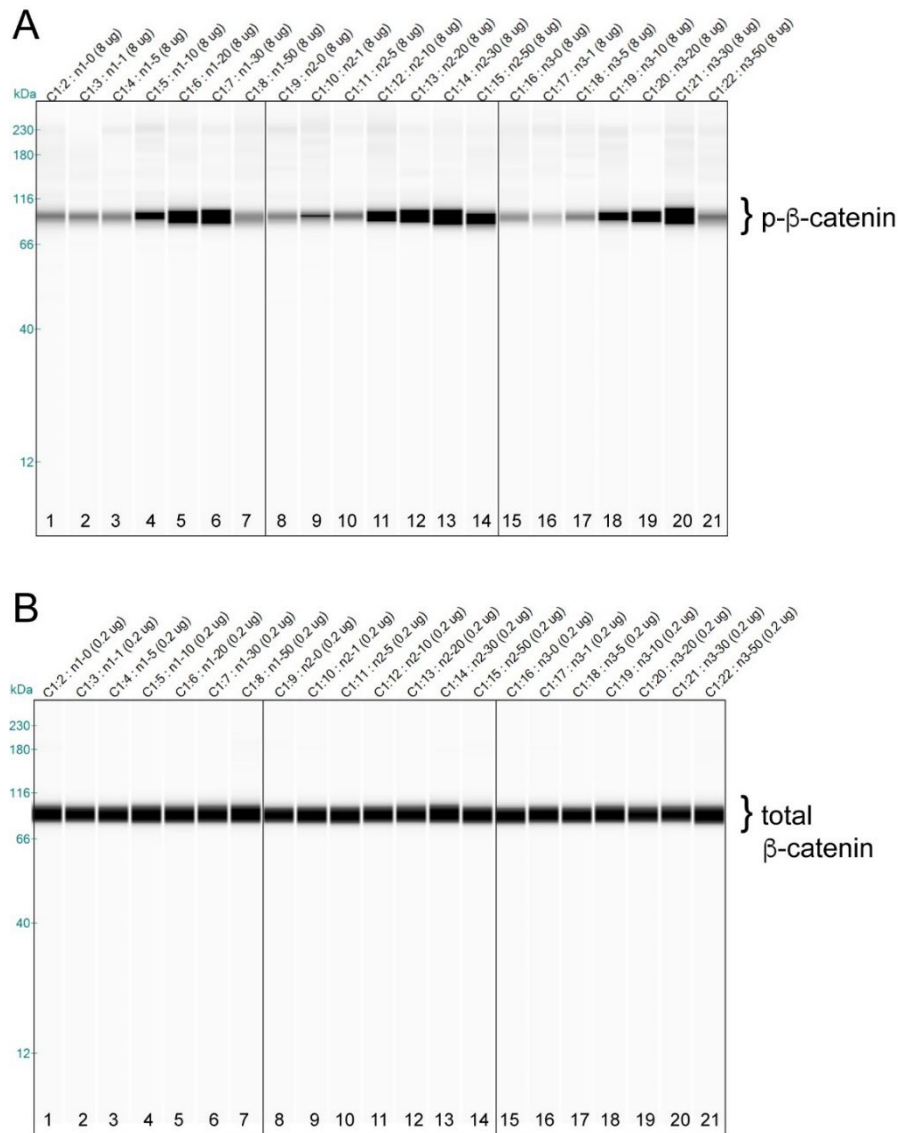


Figure Appendix I.A: Effect of LiCl on P-β-Catenin and Total-β-Catenin Levels. A172 cells underwent treatment with LiCl concentrations of 0, 1, 5, 10, 20, 30, and 50 mM for a duration of 24 hours. Post-treatment, the samples were analyzed through capillary electrophoresis and were probed with either phospho-Ser33/Ser37-β-catenin antibody (A) or total β-catenin antibody (B), generating a chemiluminescent output. The results were presented in a format akin to a virtual Western blot. For each lithium concentration, three separate samples were prepared and the corresponding capillaries were assigned as follows: 0 mM (Lanes 1, 8, 15), 1 mM (Lanes 2, 9, 16), 5 mM (Lanes 3, 10, 17), 10 mM (Lanes 4, 11, 18), 20 mM (Lanes 5, 12, 19), 30 mM (Lanes 6, 13, 20), and 50 mM (Lanes 7, 14, 21) LiCl.

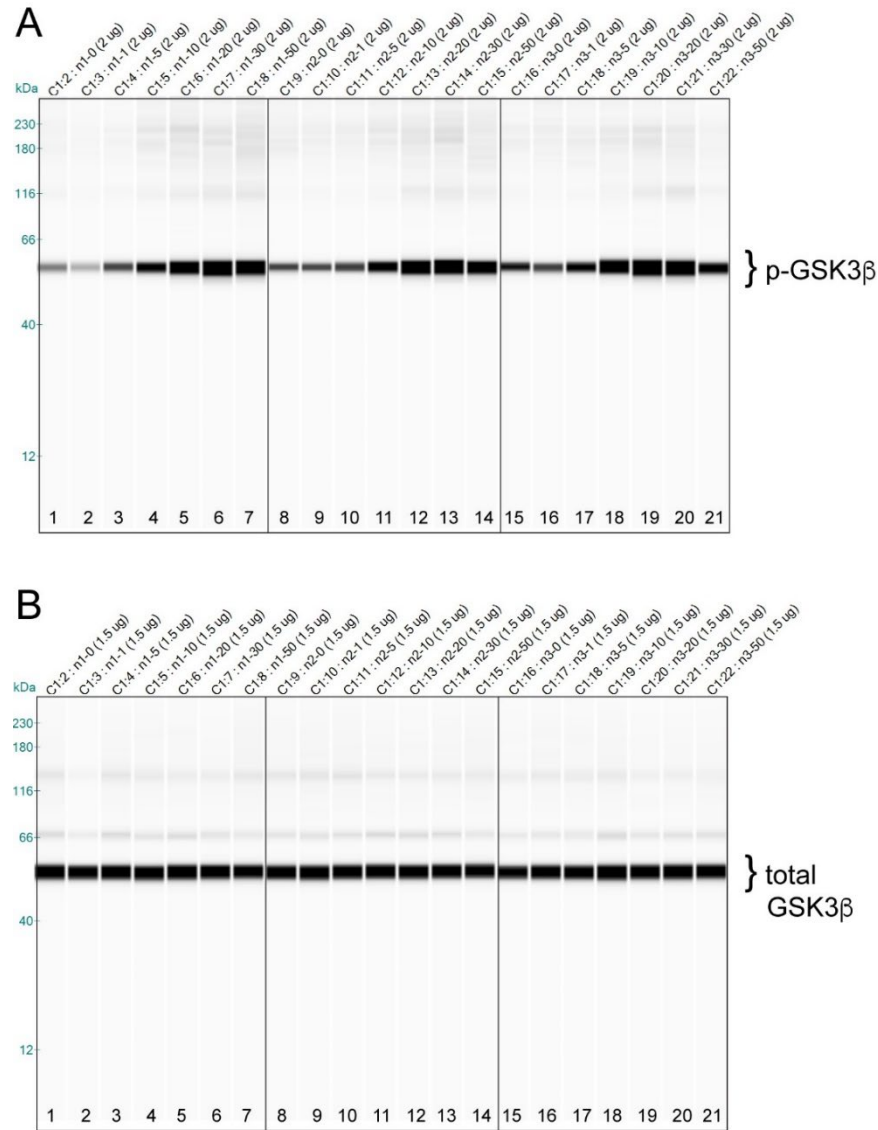


Figure Appendix I.B: Effect of LiCl on P-Ser9-GSK3β and Total-GSK3β Levels. A172 cells underwent treatment with LiCl concentrations of 0, 1, 5, 10, 20, 30, and 50 mM for a duration of 24 hours. Post-treatment, the samples were analyzed through capillary electrophoresis and were probed with either phospho-Ser9-GSK3β antibody (A) or total GSK3β antibody (B), generating a chemiluminescent output. The results were presented in a format akin to a virtual Western blot. For each lithium concentration, three separate samples were prepared and the corresponding capillaries were assigned as follows: 0 mM (Lanes 1, 8, 15), 1 mM (Lanes 2, 9, 16), 5 mM (Lanes 3, 10, 17), 10 mM (Lanes 4, 11, 18), 20 mM (Lanes 5, 12, 19), 30 mM (Lanes 6, 13, 20), and 50 mM (Lanes 7, 14, 21) LiCl.

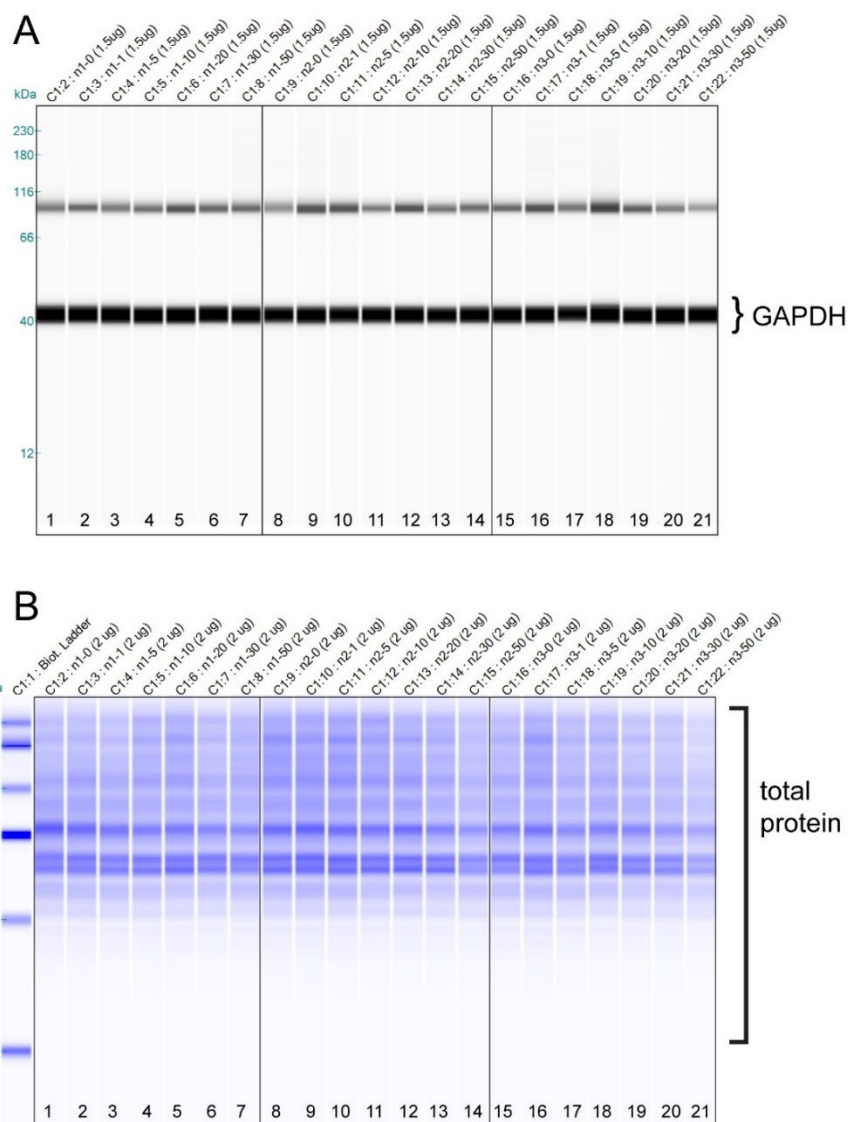


Figure Appendix I.C: GAPDH Level and Total Protein Panel with LiCl Treatment. A172 cells underwent a 24-hour treatment with various concentrations of LiCl (0, 1, 5, 10, 20, 30, or 50 mM). The samples were then processed using capillary electrophoresis, during which they were probed with a GAPDH antibody (A) or a total protein labeling reagent (B), and a secondary reagent was applied to generate a chemiluminescent signal. The resulting electropherograms were presented as a virtual Western blot (A) or a simulated Coomassie-stained SDS-PAGE gel (B). Each lithium concentration was represented in three independent samples, with capillaries designated as follows: 0 mM (Lanes 1, 8, 15), 1 mM (Lanes 2, 9, 16), 5 mM (Lanes 3, 10, 17), 10 mM (Lanes 4, 11, 18), 20 mM (Lanes 5, 12, 19), 30 mM (Lanes 6, 13, 20), and 50 mM (Lanes 7, 14, 21). Additionally, a capillary containing size markers was included for reference.

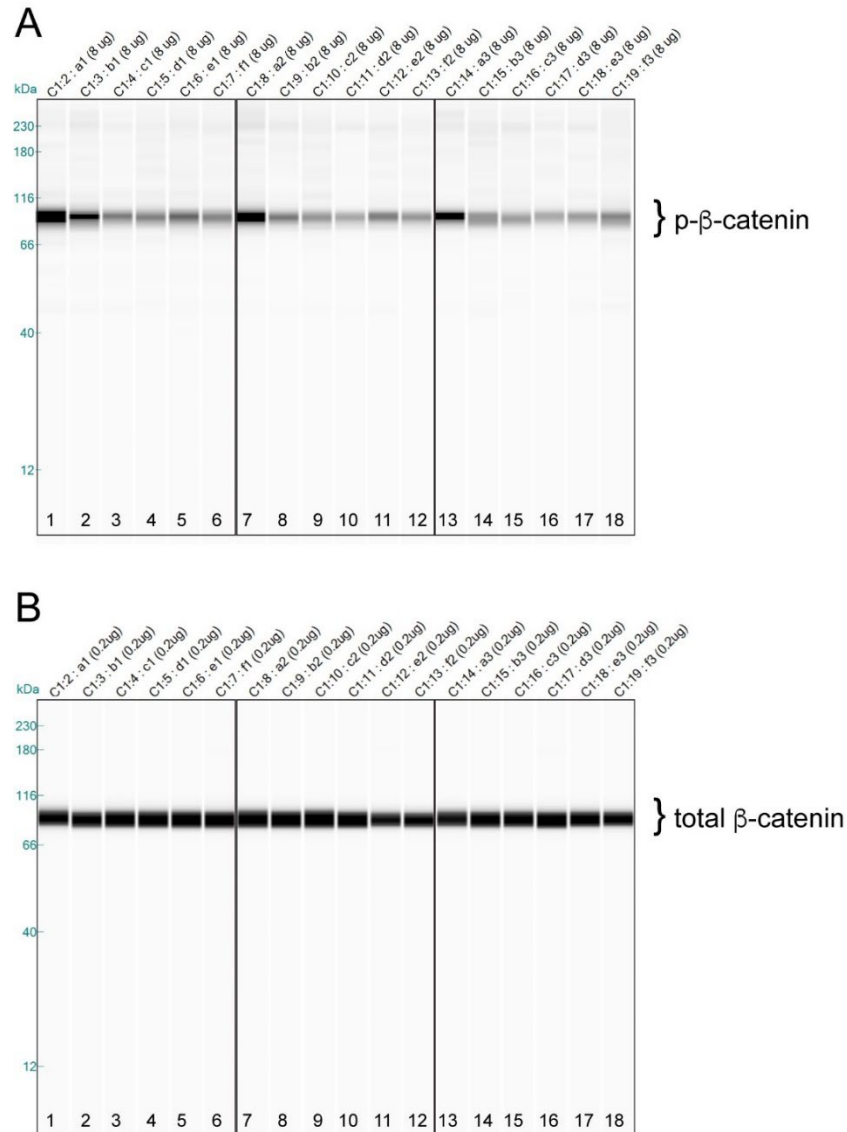


Figure Appendix I.D: Effect of BeSO₄ on P-β-Catenin and Total-β-Catenin Levels. A172 cells underwent treatment with either 3 nM Calyculin A for one hour or various concentrations of BeSO₄ (0, 10, 100, 300, or 1000 μM) for 24 hours. After treatment, the samples were analyzed using capillary electrophoresis and probed with either phospho-Ser33/Ser37-β-catenin antibody (A) or total β-catenin antibody (B), generating a chemiluminescent output. The results were visualized as a virtual Western blot. Three independent samples were produced for each treatment condition. The corresponding capillaries were marked as follows: 3 nM Calyculin A (Lanes 1, 7, 13), 0 μM BeSO₄ (Lanes 2, 8, 14), 10 μM BeSO₄ (Lanes 3, 9, 15), 100 μM BeSO₄ (Lanes 4, 10, 16), 300 μM BeSO₄ (Lanes 5, 11, 17), and 1000 μM BeSO₄ (Lanes 6, 12, 18).

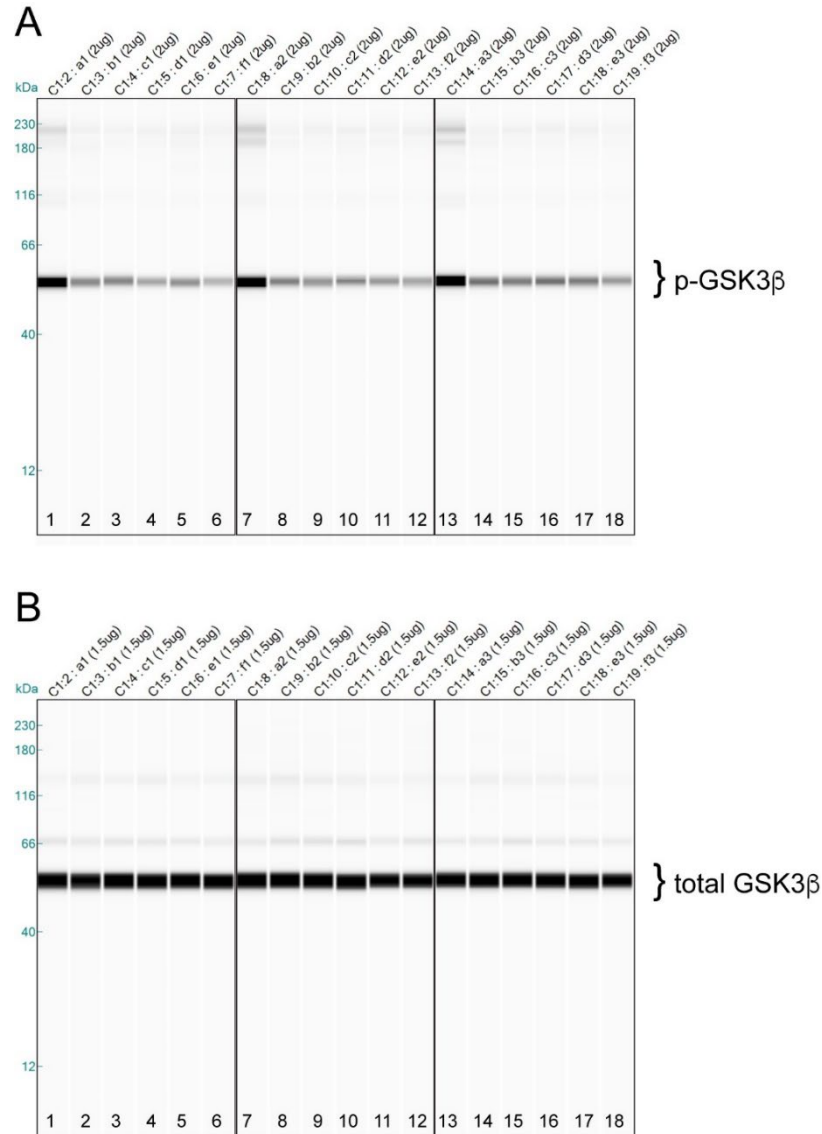


Figure Appendix I.E: Effect of BeSO₄ on P-Ser9-GSK3β and Total-GSK3β Levels. A172 cells underwent treatment with either 3 nM Calyculin A for one hour or various concentrations of BeSO₄ (0, 10, 100, 300, or 1000 μM) for 24 hours. After treatment, the samples were analyzed using capillary electrophoresis and probed with either phospho-Ser33/Ser37-β-catenin antibody (A) or total β-catenin antibody (B), generating a chemiluminescent output. The results were visualized as a virtual Western blot. Three independent samples were produced for each treatment condition. The corresponding capillaries were marked as follows: 3 nM Calyculin A (Lanes 1, 7, 13), 0 μM BeSO₄ (Lanes 2, 8, 14), 10 μM BeSO₄ (Lanes 3, 9, 15), 100 μM BeSO₄ (Lanes 4, 10, 16), 300 μM BeSO₄ (Lanes 5, 11, 17), and 1000 μM BeSO₄ (Lanes 6, 12, 18).

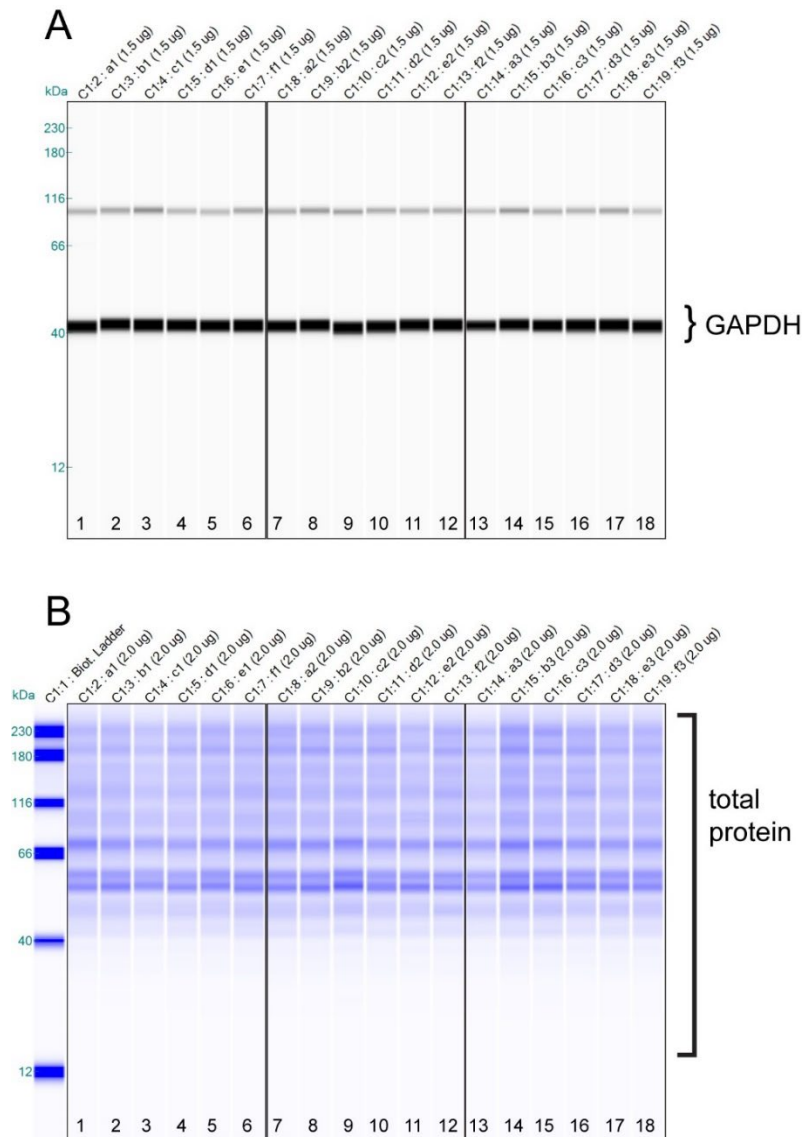


Figure Appendix I.F: GAPDH Level and Total Protein Panel with BeSO₄ Treatment. A172 cells were exposed to either 3 nM Calyculin A for one hour or varying concentrations of BeSO₄ (0, 10, 100, 300, or 1000 μ M) for 24 hours. Following treatment, the samples underwent capillary electrophoresis and were labeled with either a GAPDH antibody (A) or a total protein reagent (B) to generate a chemiluminescent output. The results were visualized as a virtual Western blot (A) or a simulated Coomassie-stained SDS-PAGE gel (B). Additionally, a capillary featuring size markers was included in the display. For each treatment condition, three independent samples were created. Their respective capillaries were identified as follows: 3 nM Calyculin A (Lanes 1, 7, 13), 0 μ M BeSO₄ (Lanes 2, 8, 14), 10 μ M BeSO₄ (Lanes 3, 9, 15), 100 μ M BeSO₄ (Lanes 4, 10, 16), 300 μ M BeSO₄ (Lanes 5, 11, 17), and 1000 μ M BeSO₄ (Lanes 6, 12, 18).

Appendix II

ITC Runs for Chapter 3

ITC Runs for Metal Ion and Chelator Binding Studies: EDTA

Run#	ITC Cell	ITC Syringe	Buffer	Temp.
R133	0.1mM EDTA	2mM BeSO ₄	100mM MES pH 6.0	25 °C
R224		2mM MgSO ₄		
R348		1mM CaSO ₄		

ITC Runs for Metal Ion and Chelator Binding Studies: 4,5-IDA

Run#	ITC Cell	ITC Syringe	Buffer	Temp.
R074	1mM 4,5-IDA	10mM BeSO ₄	100mM MES pH 6.0	25 °C
R077		10mM MgSO ₄		
R094		20mM MgSO ₄		

ITC Runs for Metal Ion and Chelator Binding Studies: NTA

Run#	ITC Cell	ITC Syringe	Buffer	Temp.
R279	0.2mM NTA	2mM BeSO ₄	100mM MES pH 6.0	25 °C
R301		2mM MgSO ₄		
R130	1mM NTA	5mM BeSO ₄		
R177		5mM MgSO ₄		

ITC Runs for Metal Ion and Chelator Binding Studies: SA

Run#	ITC Cell	ITC Syringe	Buffer	Temp.
R189	0.2mM SA	2mM BeSO ₄	100mM MES pH 6.0	25 °C
R190	0.5mM SA	5mM BeSO ₄		
R197		5mM MgSO ₄		
R198		10mM MgSO ₄		

ITC Runs for Metal Ion and Model Peptide Binding Studies at pH 6.

Run#	ITC Cell	ITC Syringe	Buffer	Temp.
R482	Buffer	Buffer	100mM MES pH 6.0	25 °C
R549	0.2mM DDDD	Buffer		
R550	0.2mM DDDD	5mM BeSO ₄		
R551	Buffer	5mM BeSO ₄		
R552	0.2mM DDDD	5mM MgSO ₄		
R556	Buffer	5mM MgSO ₄		
R554	0.2mM KKKK	5mM BeSO ₄		
R555	0.2mM KKKK	5mM MgSO ₄		
R570	0.2mM KKKK	Buffer		
R564	0.2mM GGGG	5mM BeSO ₄	100mM MES pH 6.0, 5% DMSO	
R565	Buffer	5mM BeSO ₄		
R566	0.2mM GGGG	5mM MgSO ₄		
R567	Buffer	5mM MgSO ₄		
R568	Buffer	Buffer		
R569	0.2mM GGGG	Buffer		

ITC Runs for BeSO₄, MgSO₄, and LiCl vs. DDDD Peptide Binding at pH 5.80.

Run#	ITC Cell	ITC Syringe	Buffer	Temp.
R1581	0.2mM DDDD	5mM BeSO ₄	100mM MES pH 5.80	25 °C
R1572		5mM MgSO ₄		
R1598		5mM LiCl		

ITC Runs for MgSO₄ and LiCl vs. DDDD Peptide Binding at pH 7.0.

Run#	ITC Cell	ITC Syringe	Buffer	Temp.
R1576	0.2mM DDDD	5mM MgSO ₄	100mM HEPES pH 7.0	25 °C
R1579		5mM MgSO ₄		
R1578		5mM LiCl		
R1580		5mM LiCl		

ITC Runs for BeSO₄ vs. Peptide Binding at pH 5.80

Peptides: FITC-DDDD, FITC-GDDD, FITC-GGDD, FITC-GGGGDDDD, FITC-GGGGKKKK, Cy5-CDDDD, and Cy5-CKKKK.

Run#	ITC Cell	ITC Syringe	Buffer	Temp.
R1708	Buffer	5mM BeSO ₄	100mM MES pH 5.80	25 °C
R1710	0.2mM FITC-GGGGDDDD			
R1711	0.2mM FITC-GGGGKKKK			
R1712	0.2mM Cy5-CDDDD			
R1713	0.2mM Cy5-CKKKK			
R2360	0.2mM FITC-DDDD		100mM MES pH 5.80, 1% DMSO	

Appendix III

GST-GSK3 β Extraction and Purification from Sf9 Cells and Experimental Challenges

Experiment 1

GenScript developed the P2 baculovirus stock for expressing the isoform 1 of human GSK3 β , tagged with N-terminal GST. The cDNA of human GSK3 β isoform 1 was synthesized and inserted into the pFastBacGST expression vector. This vector was transformed into the DH10Bac strain, leading to the creation of a recombinant bacmid. The presence of the recombinant bacmid with the GSK3 β isoform 1 gene was verified through PCR. Subsequently, Sf9 cells were transfected with this bacmid, and the resultant supernatant, known as the P1 viral stock, was used to produce the P2 viral stock. For the expression process, 100 mL of Sf9 cell culture was infected with the P2 virus and incubated at 27 °C in Sf-900 II SFM medium for three days before being harvested. The presence of GST-tagged GSK3 β protein was validated using SDS-PAGE and Western Blot techniques. Protein concentration was determined using the Bradford protein assay, BSA as the standard, with a reported concentration of 0.12 mg/ml by GenScript. We compared the GST-GSK3 β protein expressed and purified from Sf9 cells by GenScript with those obtained from the BL21(Gold) *E.coli* bacterial expression system.

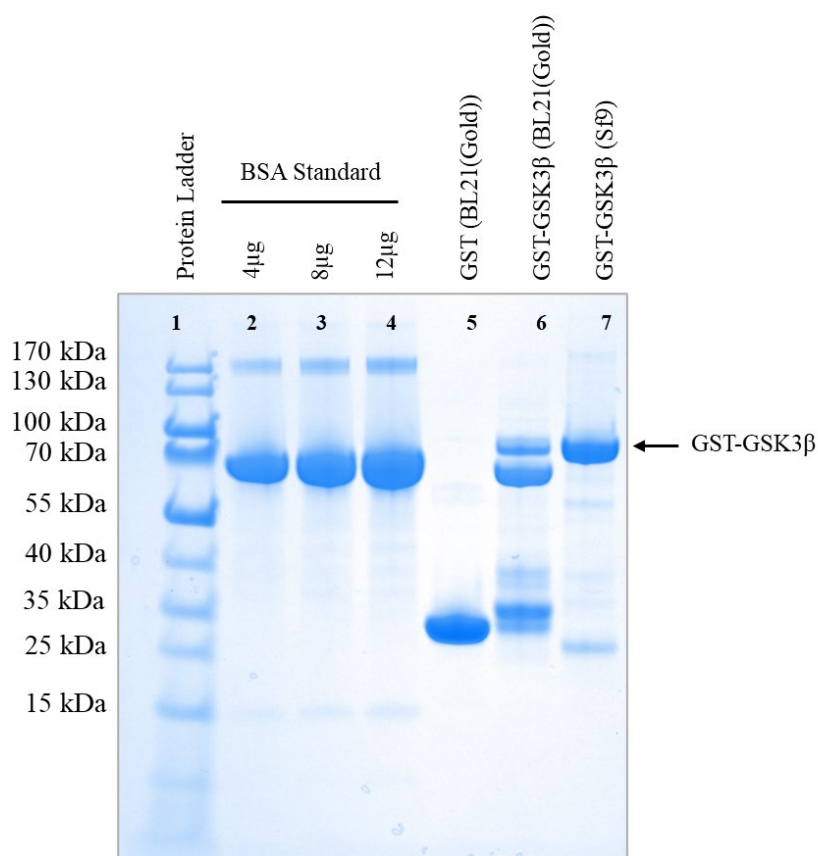
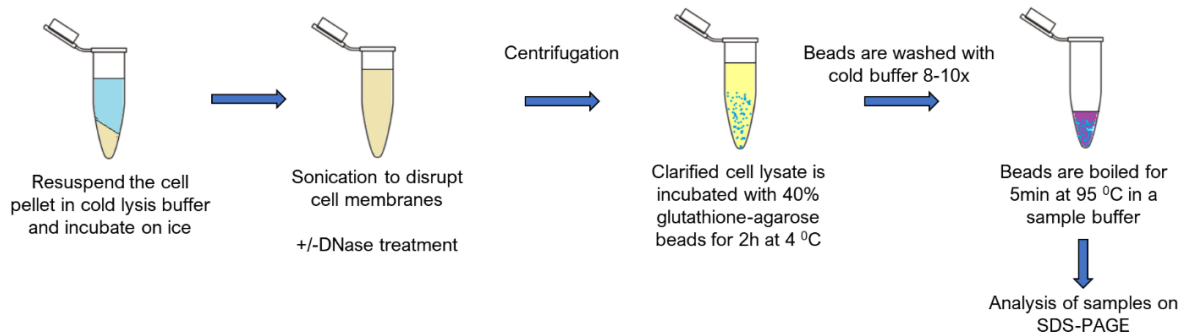


Figure Appendix III.A: GST-GSK3 β Expression in Sf9 Cells from GenScript Compared Against GST-GSK3 β Expression in BL21 (Gold) *E. coli* Cells. SDS_PAGE analysis showing GST-GSK3 β expressed and purified from Sf9 cells by GenScript (lane 7) compared against GST (lane 5) and GST-GSK3 β (lane 6) expressed in BL21(Gold) *E.coli*. In lanes 5-7, 8 μ g of total protein is loaded per lane. The predominant protein band in lane 7 is the 74kDa band for full-length GST-GSK3 β . Lanes 2-4 have 4, 8, and 12 μ g of BSA loaded for comparison.

Experiment 2

GST-GSK3 β extraction and FPLC protein purification from a 100mL Sf9 + P4 amplified baculovirus pellet. A 5mL pellet from this 100mL culture was first tested with a Glutathione-Mini-Pulldown Assay (MPD). Figure 2. B shows a schematic diagram of this assay setup. The screening with the smaller pellet confirmed the presence of a 74kDa protein band indicative of GST-GSK3 β expression in this Sf9 culture (Data not shown). The larger Sf9 pellet was lysed and sonicated in a lysis buffer with 50mM TRIS-HCl pH 8, 50mM NaCl, 3mM EDTA & 1x Protease/Phosphatase inhibitors. MgCl₂ was added to a final concentration of 5mM to the cell lysate for DNase activation. 25U/mL DNase (Pierce Universal Nuclease #88701) was added to the lysate and incubated at room temperature for 10 min to degrade genomic DNA. EDTA was added to the lysate to a final concentration of 7mM to quench the DNase activity by chelating the Mg²⁺. The lysate was clarified by centrifugation at 15 000 rpm and 4 °C for 15 min, and the clarified lysate was filtered through a 0.45 μ m syringe filter before purifying the lysate via a 1mL GSTrap HP column on FPLC with 50mM TRIS-HCl pH 8.0, 50mM NaCl and 1mM EDTA as the FPLC buffer. The column was equilibrated, and the protein-bound fractions were collected post-elution via GSH-elution. These fractions were analyzed through gel electrophoresis. Additionally, a Glutathione MPD test was conducted on both the lysate and the FPLC unbound fraction to verify the presence of the target protein.

A



B

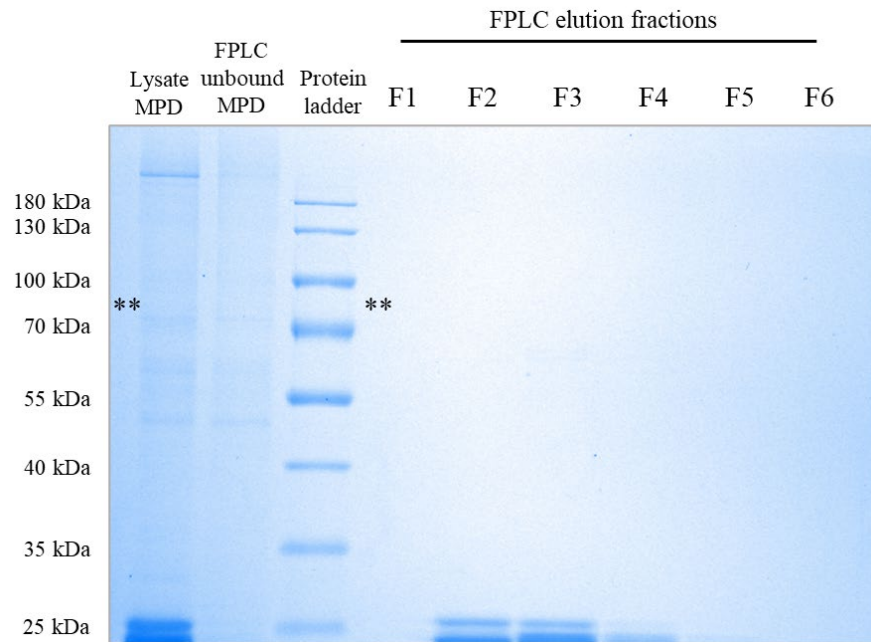


Figure Appendix III.B: Extraction and Isolation of GST-GSK3 β from Sf9 via Glutathione-sepharose Column on FPLC Lacked the 74kDa Protein Band. The prep utilized a 100mL Sf9 culture infected with P4 amplified baculovirus at an M.O.I. = 10 and incubated at 27 °C /100rpm for 48h. A) Schematic diagram of the Glutathione-Mini-Pulldown Assay. B)SDS-PAGE analysis of the GSH-eluted fractions F1-F6 did not show a 74kDa protein band as expected for GST-GSK3 β . A Glutathione-Mini-Pulldown (labeled as MPD) test was conducted on the lysate applied on the Glutathione-sepharose column on FPLC and the FPLC unbound lysate to observe whether a GST-GSK3 β band was present. The absence of the 74kDa band in the lysate applied on the affinity column and the FPLC unbound lysate suggested that the GST-fusion protein may have undergone degradation.

Experiment 3

The experiment aimed to optimize protein extraction from Sf9+P4 pellets by testing various DNA degradation conditions to prevent recombinant protein degradation during cell lysis and protein extraction. The procedure involved preparing a lysis buffer with 50mM TRIS-HCl, 50mM NaCl, 3mM EDTA, and 1x protease and phosphatase inhibitors. A 100mL Sf9 + P4 pellet was used for the experiment. The cell pellet was resuspended in lysis buffer and subjected to sonication. Five aliquots of the cell lysate were then treated differently: one was left untreated, one was mechanically sheared using an 18 G $\frac{1}{2}$ needle, and the remaining three were treated with DNase at 25U/mL under different conditions (incubated in ice for 10 min, at room temperature for 10 min, and room temperature for 60 min). After DNase treatment, EDTA was added to quench DNase activity. The lysates were centrifuged, and the supernatants were collected for a Glutathione mini-pull-down assay. The beads from the pull-down assay were washed, mixed with sample buffer, boiled, and prepared for analysis via PAGE. The analysis aimed to evaluate the effectiveness of DNA degradation treatments in preserving the integrity of the GST-GSK3 β protein during extraction. Despite the different treatments, the results were inconclusive regarding the impact of DNase treatments on protein degradation, with all samples showing signs of protein degradation. This led to considerations of alternative DNA removal methods, such as using polyethyleneimine (PEI).

Experiment 4

The experiment evaluated the effectiveness of adding Triton X-100, PEI (Polyethyleneimine), and DNA shearing versus filtration of cell lysate from Sf9+P4 pellets, aiming to enhance the filtration process before FPLC application. This process is crucial as particles in the lysate could clog FPLC tubing and columns. The experiment investigated the use of Triton X-100 in the lysis buffer to improve the solubilization of cellular components, the substitution of DNase treatment with PEI to precipitate DNA, and the mechanical shearing of DNA using 18G 1½ or 22G needles. Two lysis buffers were prepared, one with and one without 0.25% (w/v) Triton X-100, containing 50mM TRIS-HCl, 50mM NaCl, 5mM EDTA, and 0.1mM PMSF. The experiment used two pooled 100mL Sf9+P4 pellets, subjected to five different treatment conditions to assess filtration ease: untreated, DNA shearing with 18 G ½ or 22G needles, DNase treatment, and DNA precipitation with 0.2% PEI. The results indicated that adding Triton X-100 did not significantly facilitate filtration. In contrast, DNA shearing with needles slightly improved filtration for the buffer without Triton X-100, and adding 0.2% PEI for DNA precipitation notably enhanced filtration ease, especially in the buffer without Triton X-100, making it the most effective approach among the tested methods. This finding suggests PEI as a preferable alternative to DNase treatment for preparing cell lysate for filtration before FPLC analysis.

Table Appendix III.A: The Effect of Various Treatments on Cell Lysate Viscosity. The effectiveness of adding Triton X-100, PEI (Polyethyleneimine), and DNA shearing versus filtration of cell lysate from Sf9 + P3/P4 pellets to enhance the filtration process before FPLC application is compared. Ease of filtration on a scale of 1-5: 1) Very hard to filter, 2) Hard to filter, 3) Not hard or easy, 4) Easier to filter, 5) Very easy to filter.

DNA treatment	Lysis buffer -0.25% (w/v) Triton x-100	Lysis buffer +0.25% (w/v) Triton x-100
No treatment	3	1
DNA shearing with 18G 1 ½ needle	3 – 4 more towards 4 but might get difficult when there's a larger volume to filter	1
DNA shearing with 22G needle	3 – 4 more towards 4 but might get difficult when there's a larger volume to filter	2
25U/mL DNase treatment for 10min in ice	3	2
Adding 0.2% PEI for DNA precipitation	4 – 5 was much easier to filter	3

Experiment 5

A modified protocol for protein extraction and FPLC protein purification from a 100mL Sf9+P4 pellet was tested, incorporating higher EDTA concentrations and using PEI to precipitate DNA from the cell lysate. The FPLC buffer was adjusted to include 3 mM EDTA, and the lysis buffer was formulated with 5 mM EDTA and 0.2% (w/v) PEI, with other components 50mM TRIS-HCl, 50mM NaCl, and 0.1mM PMSF. This adjustment aimed to enhance the purification process by mitigating potential DNA presence and protein degradation issues. The protocol involved thawing the pellet, resuspending it in the lysis buffer, sonication, and allowing DNA precipitation with PEI. The lysate was centrifuged, filtered through a 0.45µm syringe filter, and subjected to FPLC using a GSTrap-HP. The filtered cell lysate was loaded onto the FPLC, and after washing the column, GSH-elution was performed, collecting fractions for analysis. Glutathione-mini-pulldown tests were conducted for both the lysate and FPLC unbound fractions to assess the presence of the target protein. Despite detecting the target protein in the lysate, it appeared not to bind to the column efficiently, as indicated by its presence in the unbound lysate rather than in the elution fractions. The experiment raised considerations regarding the level of GST-GSK3β expression in the Sf9 cultures.

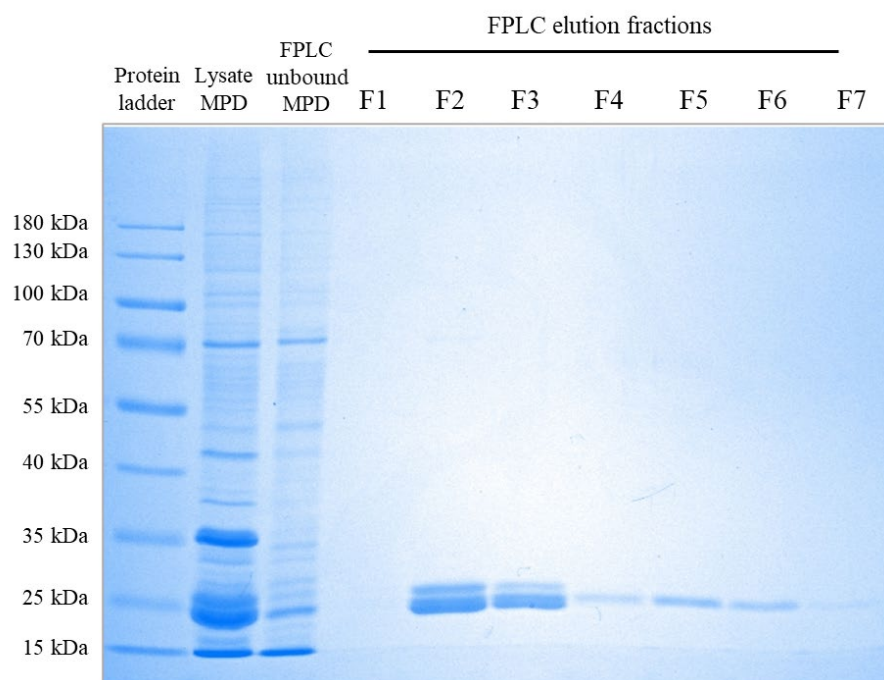


Figure Appendix III.C: Extraction and Isolation of GST-GSK3 β from Sf9 via Glutathione-sepharose Column on FPLC Lacked the 74kDa Protein Band in the GSH-eluted Fractions. The prep utilized a 100mL Sf9 culture infected with P4 amplified baculovirus at an M.O.I. = 10 and incubated at 27 °C /100rpm for 48h. SDS-PAGE analysis of the GSH-eluted fractions F1-F7 did not show a 74kDa protein band as expected for GST-GSK3 β . Glutathione-Mini-Pulldown (labeled as MPD) test was conducted on the lysate applied on the Glutathione-sepharose column on FPLC, and the FPLC unbound lysate showed the 74kDa protein band for GST-GSK3 β was present, suggesting in this case the protein had not bound the Glutathione-sepharose column on FPLC.

Experiment 6

The experiment aimed to investigate the observed discrepancies in protein expression levels in Sf9 cells infected with baculovirus, focusing on the presence of the 74kDa GST-GSK3 β protein band and an unexplained 35 kDa protein band binding to glutathione. Utilizing new source vials of Sf9/Millipore cells, the study involved culture expansion, baculovirus infection, protein extraction, and subsequent analysis via Glutathione-Mini-pulldown assays. Findings revealed the 35 kDa band's presence across all Sf9 cultures, irrespective of baculovirus infection status, identifying it as an endogenous protein with Glutathione affinity. This observation, coupled with inconsistent interference of baculovirus infection on the 35 kDa protein's expression, indicated that the mysterious band did not result from inadvertent viral infection. Despite somewhat improved expression in new cell cultures, the study noted persistent low levels of recombinant protein expression and found no correlation between the 35 kDa band's appearance and factors like cell viability or contamination. The conclusion suggests further investigations, including using different glutathione concentrations during GSH elution to isolate the recombinant protein more effectively.

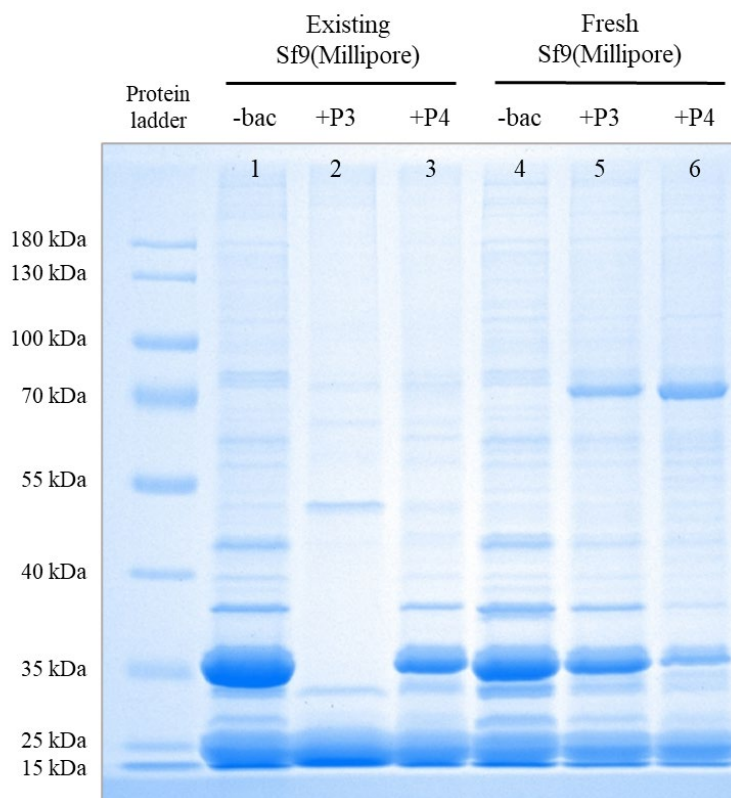


Figure Appendix III.D: Comparing the Glutathione-bound Protein Profiles in Fresh vs. Old Sf9 Cells Treated With +/- Amplified Baculovirus. Each prep utilized a 50mL Sf9 culture grown to a cell density of 1.5×10^6 cells/mL and amplified baculovirus P3 or P4 added +/- at an M.O.I. = ~ 5 and incubated at 27 °C/100rpm for 48h. Glutathione-Mini-pulldown assays were performed on the harvested Sf9 pellets for each condition and analyzed on SDS-PAGE. The ~ 35 kDa Glutathione-binding protein was present in all cultures irrespective of the absence or presence of baculovirus and regardless of using Sf9 cells cultured from older cryo-stocks or freshly purchased cell stocks. The abundance of the 35kDa protein varied between different cultures and infection with baculovirus.

Experiment 7

This experiment was designed to address the co-elution of GST-GSK3 β with the ~35kDa endogenous Glutathione-binding protein observed in Sf9 cell cultures. Different concentrations of glutathione (GSH) were tested in the elution buffer to achieve selective elution. Utilizing new Sf9 cell pellets, both with and without P4 baculovirus infection, the study employed lysis, sonication, and incubation with Glutathione slurry, followed by elution with buffers containing varied GSH concentrations (5mM, 10mM, 20mM). The experiment showed that the GST-fusion protein primarily eluted at 5mM GSH, while the 35 kDa protein started eluting at 10mM GSH. However, significant quantities of both proteins remained bound to the beads until forcibly eluted by boiling with sample buffer (Lane #7 in each gel).

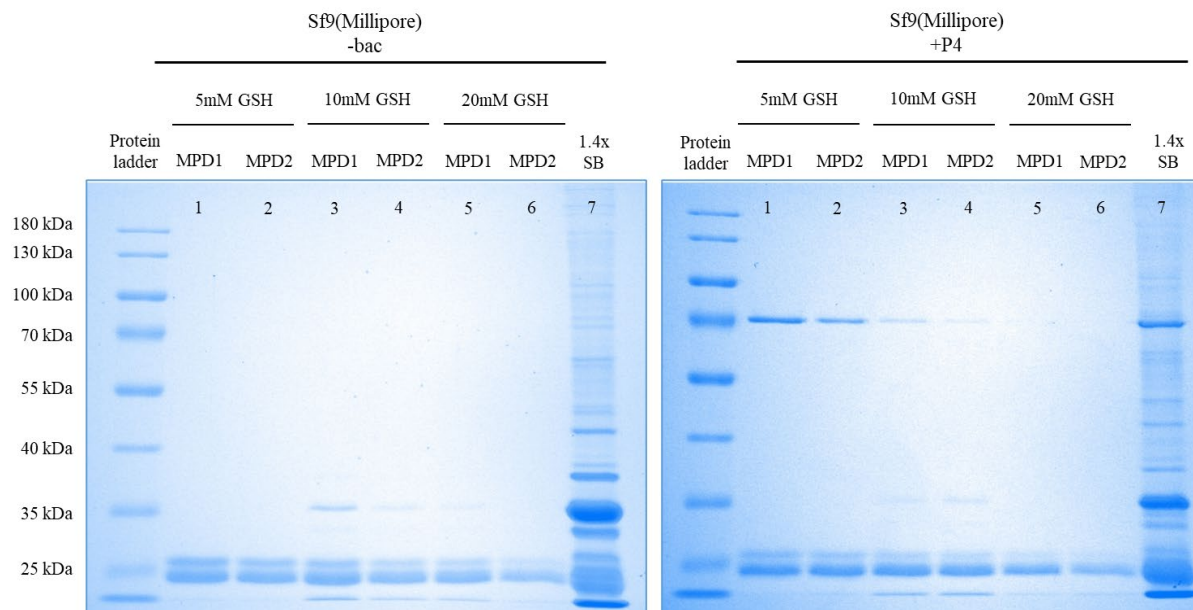


Figure Appendix III.E: Elution of Glutathione-bound Protein from Sf9 Lysates with Different GSH Concentrations in the Elution Buffer. MPD refers to Glutathione-Mini-Pulldown assay, with MPD1 and 2 representing repeated elution at the specified GSH concentration. The 35kDa endogenous Glutathione-binding protein is present in Sf9 lysates treated with or without amplified baculovirus. The recombinant protein of interest, GST-GSK3 β , largely eluted with 5mM GSH. In contrast, the 35kDa protein started eluting at 10mM GSH, showing that using different GSH concentrations, we can separate the co-elution of these proteins during GST-GSK3 β purification from Glutathione-affinity purification.

Experiment 8

To enhance the elution efficiency of GST-GSK3 β recombinant protein from Sf9 cell pellets, an experiment was conducted to assess the effects of including 0.1% (w/v) Triton X-100, and increasing NaCl concentration to 150mM in lysis, wash, and elution buffers. The objective was to mitigate protein aggregation, potentially induced during sonication or through disulfide bond formation, which was hypothesized to impede protein elution. Previous attempts with DTT to address disulfide-related aggregation did not yield improvements (Data not shown), leading to the exploration of Triton X-100, a nonionic detergent, to reduce sonication-induced aggregation and the hypothesis that increased ionic strength would favor specific interaction dynamics during binding and elution. Results revealed that the inclusion of 0.1% (w/v) Triton X-100 significantly enhanced GST-GSK3 β elution across all fractions, with reduced protein remaining bound to the Glutathione beads, indicating more complete elution compared to samples without Triton X-100. In contrast, increasing NaCl concentration to 150mM did not independently make a noticeable difference, suggesting that the presence of Triton X-100 was the critical factor in improving protein recovery. This experiment provided insight into the effectiveness of Triton X-100 in mitigating aggregation and enhancing the GSH-elution process of GST-GSK3 β .

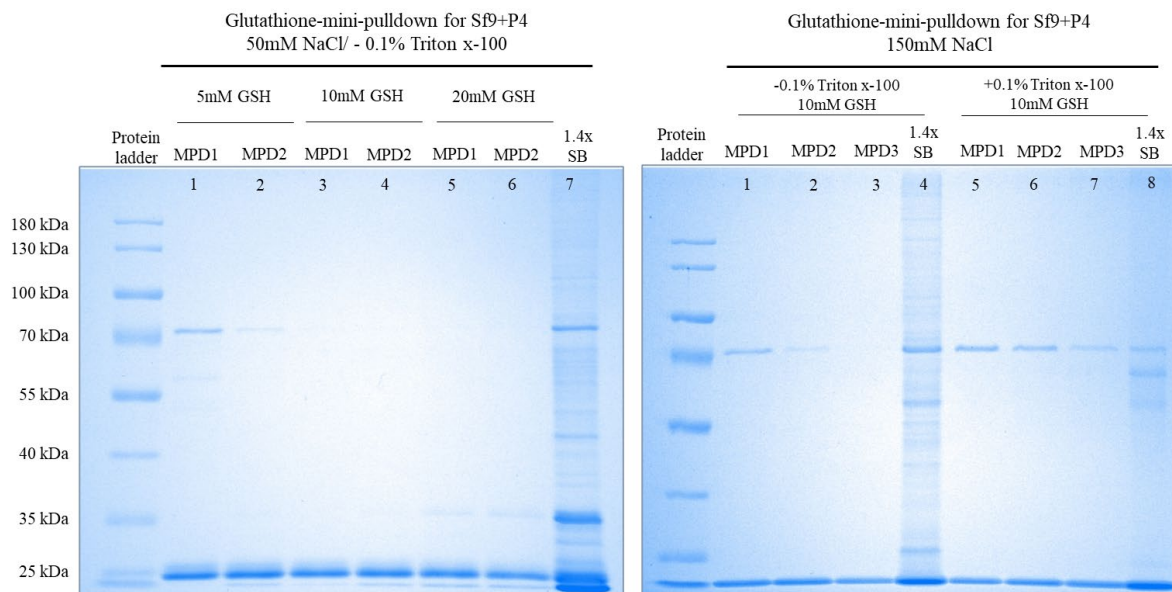


Figure Appendix III.F: SDS-PAGE Analysis of GST-GSK3 β Elution Efficiency with and without 0.1% Triton X-100 in Lysis, Wash, and Elution Buffers. These SDS-PAGE gel images illustrate the elution profiles of GST-GSK3 β recombinant protein from Sf9 cell pellets treated with (+) and without (-) 0.1% Triton X-100 across three elution fractions following Glutathione-Mini-pulldown (MPD 1,2 and 3) and a final boil-off fraction (1.4x SB). Lysis, wash, and elution buffers were modified by including 150 mM NaCl to assess the combined effect of increased ionic strength and the presence of the nonionic detergent on protein elution efficiency. For samples treated with Triton X-100, a notable improvement in protein elution is observed, with distinct bands visible across all elution fractions, indicating a more complete recovery of GST-GSK3 β . In contrast, samples without Triton X-100 show diminished elution by MPD3, with a significant amount of protein only released during the boil-off in Lane 7 of Gel 1. These results demonstrate that including 0.1% Triton X-100 significantly mitigates protein aggregation, potentially induced by sonication, thereby enhancing the elution process and overall protein yield.

Appendix IV

Part A: ITC Experiments Exploring GSK3 β Ligand Binding

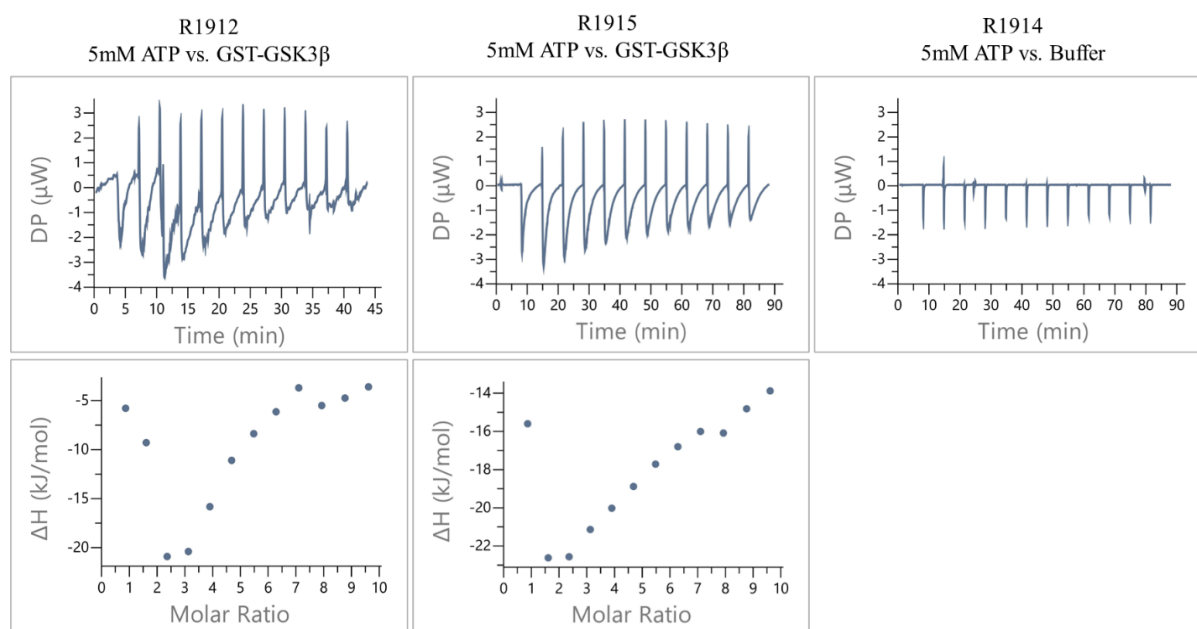


Figure Appendix IV.A: ITC Thermograms for ATP vs. GST-GSK3 β Interactions. (R1912 and R1915) 5mM ATP titrated against bacterial expressed and purified 0.1mM GST-GSK3 β in 25mM HEPES pH 7, 150mM NaCl and 10mM MgCl₂. Broad exothermic peaks were observed in R1912. The spacing between injections increased in R1915 to avoid peak overlap and baseline shift. R1914 shows ATP vs. buffer titration for the heat of dilution. The difference between the exothermic peaks for ATP vs. GSK3 β and buffer shows binding interactions between ATP-GSK3 β ; however, the plots for integrated heat against molar ratio (bottom panels) would not fit a binding model.

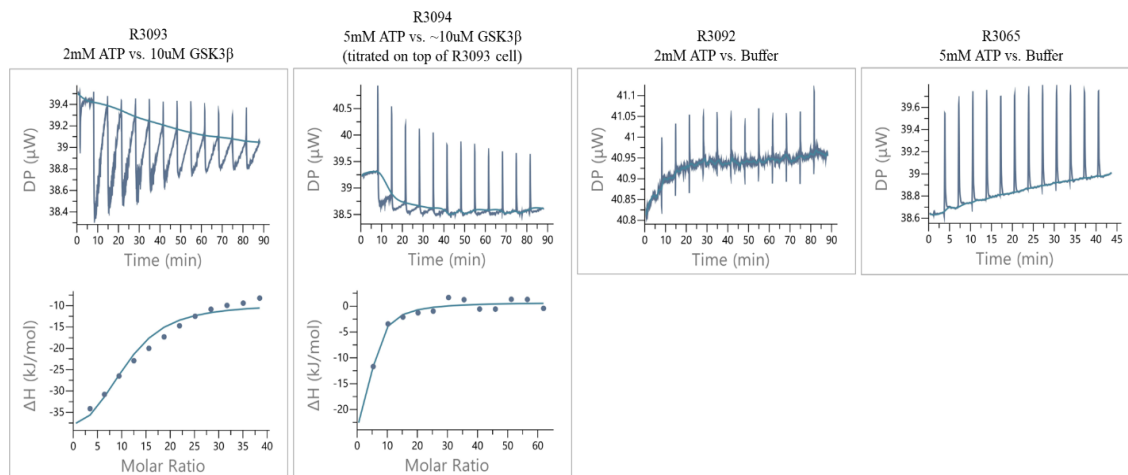


Figure Appendix IV.B: ITC Thermograms for ATP vs. GSK3 β Interactions. (R2093) 2mM ATP titrated against 10 μ M GSK3 β (Hi5 expressed and purified) in 50mM HEPES pH 7, 50mM NaCl, and 20mM MgCl₂ displayed the broad exothermic peaks that slowly returned to the baseline. The exothermic peaks are decreasing in size with incremental injection of ATP, simulating a binding behavior. (R3094) 5mM ATP titrated against the GSK3 β in the ITC cell from R3093. The exothermic peaks diminished in size, with the last injections reflecting peaks similar to that of 5mM ATP vs. buffer (R3065). 2mM ATP vs. buffer titration (R3092) shown for comparison.

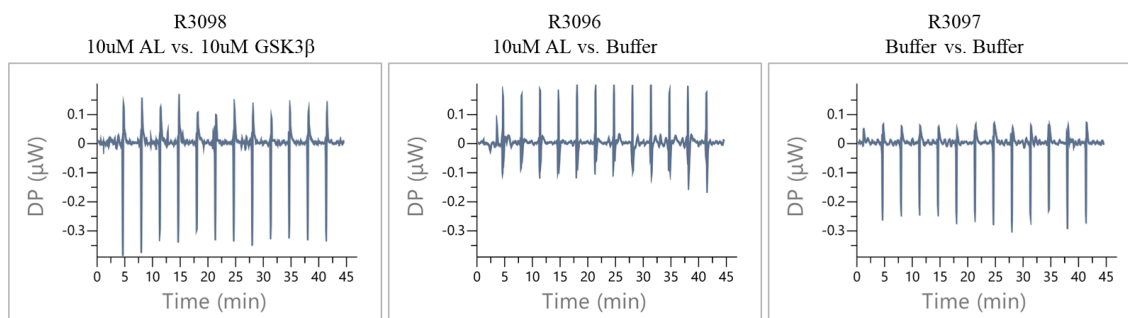


Figure Appendix IV.C: ITC Thermograms for AL vs. GSK3 β Interactions. (R2098) 10 μ M Alsterpaullone (AL) titrated against 10 μ M GSK3 β in 50mM HEPES pH 7, 50mM NaCl, and 20mM MgCl₂ and 2% DMSO (R3096) 10 μ M AL vs. Buffer (R3097) Buffer vs. Buffer. The titrations show no detectable binding.

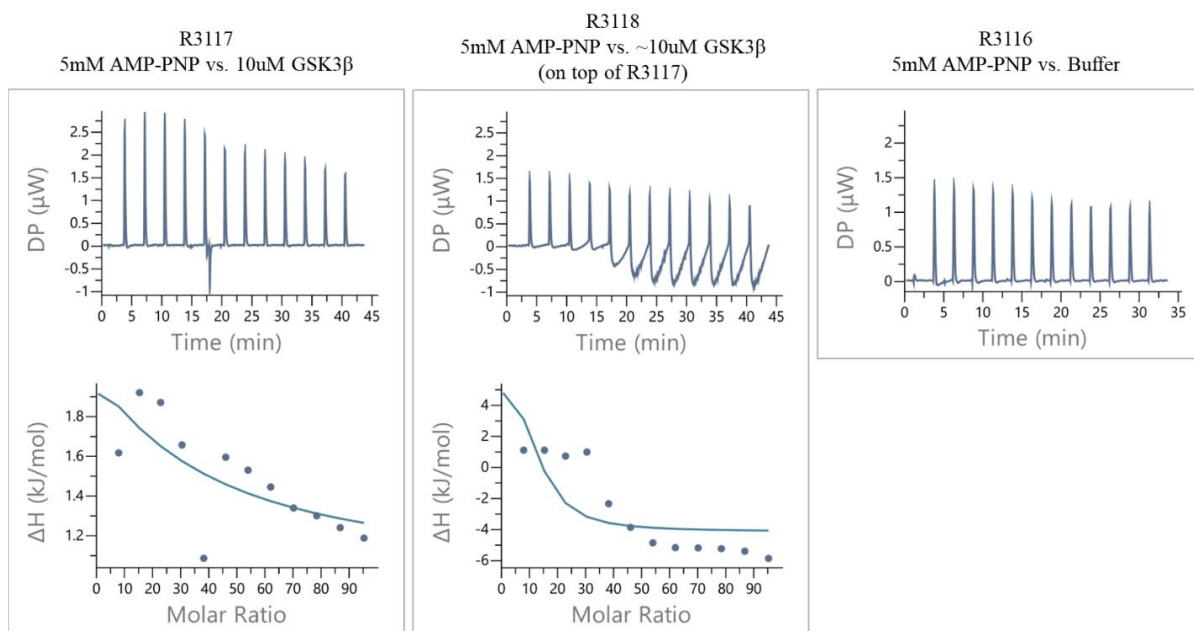


Figure Appendix IV.D: ITC Thermograms for AMP-PNP vs. GSK3β Interactions. (R3117) 5mM AMP-PNP titration against 10μM GSK3β in 50mM HEPES pH 7, 50mM NaCl, and 20mM MgCl₂ showed endothermic peaks slightly larger than (R3116) the AMP-PNP vs. buffer peaks, and the size of the peaks appeared to decrease with incremental injections of AMP-PNP gradually. (R3118) Titration with 5mM AMP-PNP continued against the R3117 cell to observe whether saturation is possible. Halfway in R3118, exothermic peaks were produced, displaying a biphasic behavior. The shape and magnitude of the exothermic peaks were similar to those observed in the ATP vs. GSK3β titrations.

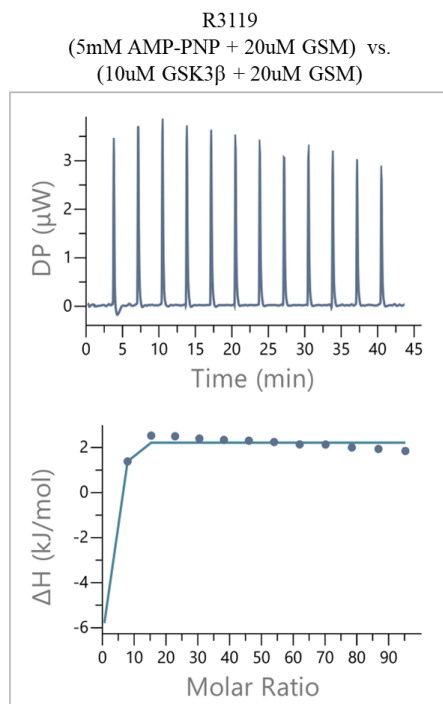


Figure Appendix IV.E: ITC Thermograms for AMP-PNP vs. GSK3 β Interactions in the Presence of Peptide Substrate. (R3119) 20 μM GSM peptide substrate was included in syringe and cell solutions for 5mM AMP-PNP titration against 10 μM GSK3 β in 50mM HEPES pH 7, 50mM NaCl, and 20mM MgCl_2 . The observed endothermic peaks did not show binding.

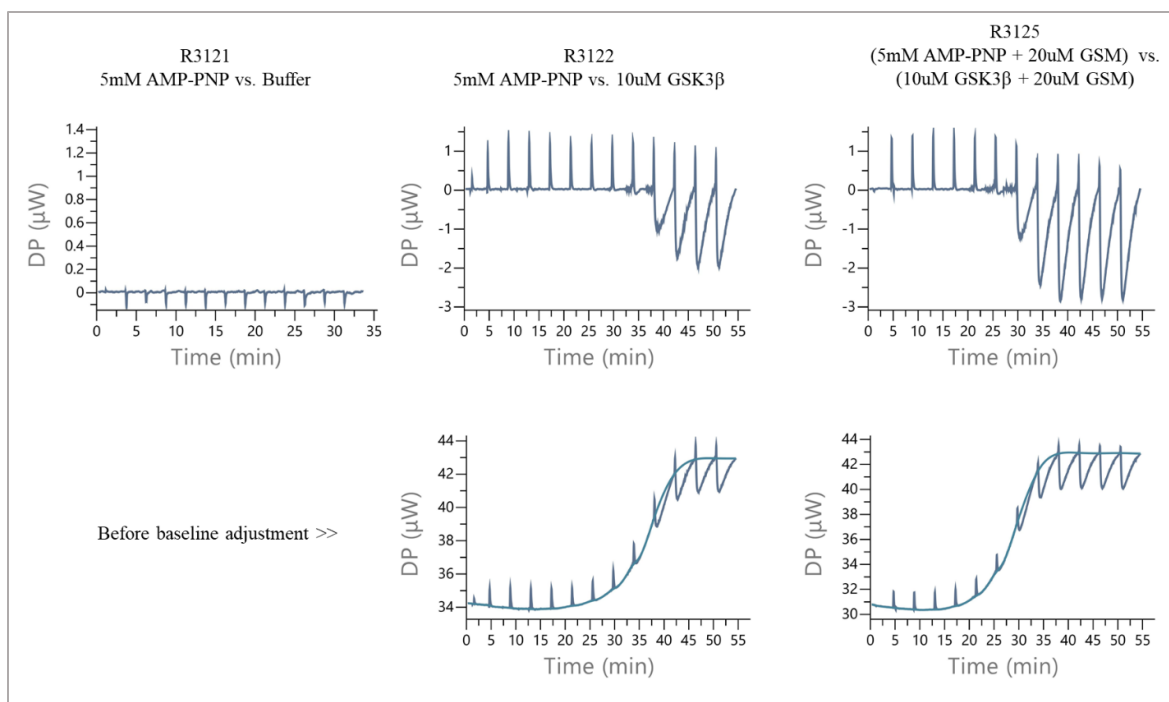


Figure Appendix IV.F: Unusual Baseline Shift in ITC Thermograms. A significant baseline shift was observed when AMP-PNP in the syringe was titrated into the cell containing GSK3β. (R3121) 5mM AMP-PNP vs. buffer showing small exothermic peaks for the heat of dilution. (R3122) 5mM AMP-PNP vs. 10μM GSK3β (R3125) 5mM AMP-PNP vs. GSK3β with 20μM GSM peptide in both syringe and cell samples. Both titrations with protein led to a significant shift in the thermogram baseline. When the baseline was normalized, the thermograms displayed a biphasic behavior with endothermic peaks in the beginning and broad exothermic peaks in the later injections.

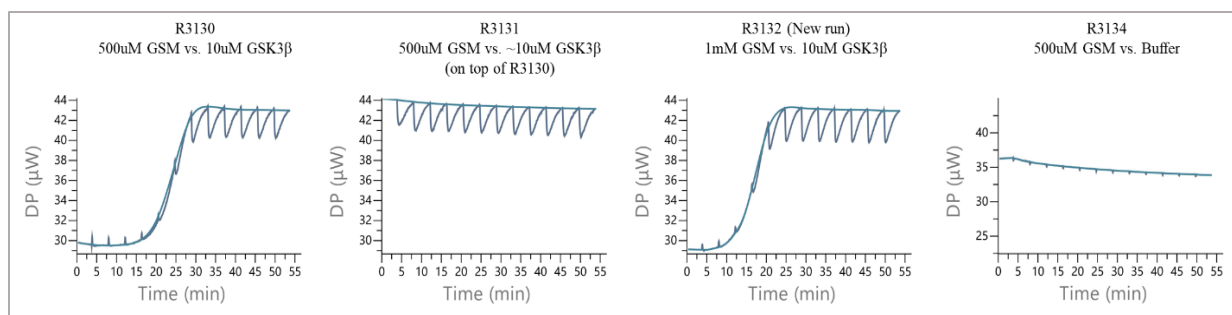


Figure Appendix IV.G: Unusual Baseline Shift in ITC Thermograms for Peptide vs. GSK3 β Interactions. A significant baseline shift was observed when the GSM peptide in the syringe was titrated into the cell containing GSK3 β . (R3130) 500 μM GSM vs. 10 μM GSK3 β displayed a baseline shift in the raw thermogram. (R3131) 500 μM GSM titrated into the cell solution of R3130, which followed the latter baseline established in R3130. (R3132) a new ITC run with 1mM GSM vs. 10 μM GSK3 β displayed a baseline shift. The nature of the peaks was not affected by increasing the GSM peptide concentration in the syringe. (R3134) 500 μM GSM vs. buffer shows small peaks representing the heat of dilution. The starting baseline for this ITC run appeared similar to the low starting baseline observed for the ITC runs with the protein.

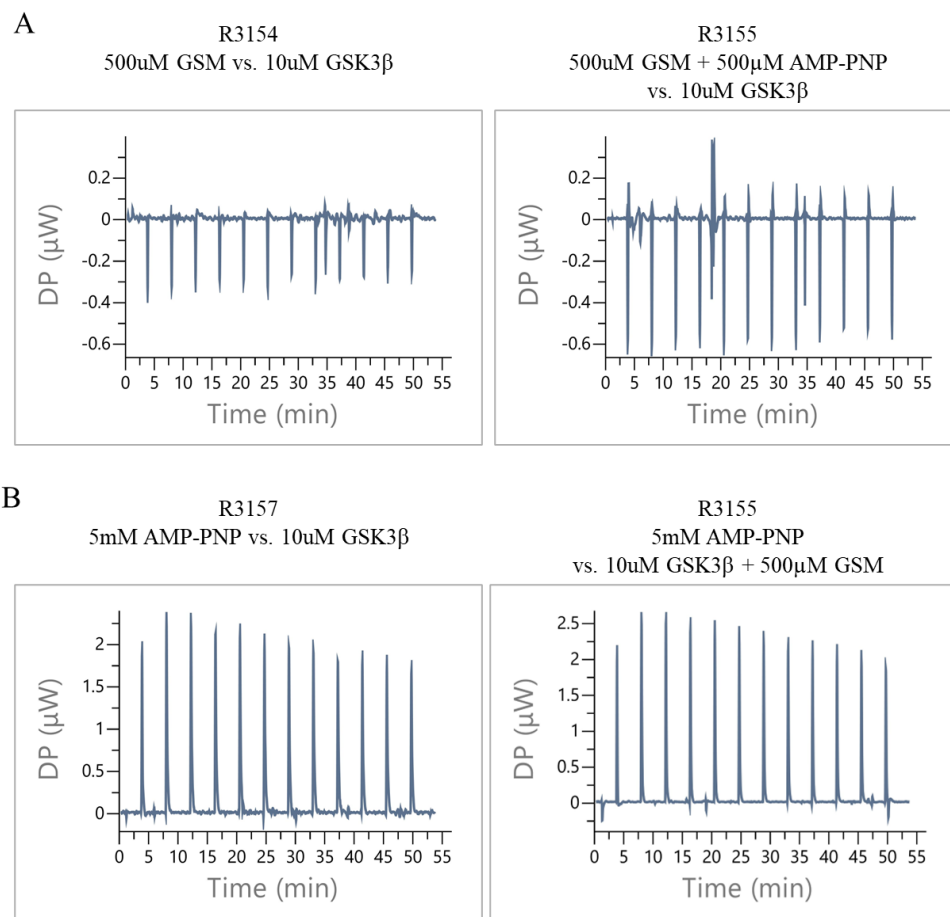


Figure Appendix IV.H: No Binding Observed Against 10 μ M GSK3 β . (A) The GSM peptide was titrated against GSK3 β (R3154) 500 μ M GSM vs. 10 μ M GSK3 β (R3155) 500 μ M GSM and 500 μ M AMP-PNP vs. 10 μ M GSK3 β . Both experiments showed no binding behavior. (B) AMP-PNP titrated against GSK3 β (R3157) 5mM AMP-PNP vs. 10 μ M GSK3 β (R3158) 5mM AMP-PNP vs. vs. vs. 10 μ M GSK3 β and 500 μ M GSM in cell. Both experiments showed no binding behavior.

Part B: ITC Runs for Chapter 5 and Appendix IV

ITC Runs for ATP vs. GST-GSK3 β (Bacterial Expressed)

Run#	ITC Cell	ITC Syringe	Buffer	Temp.
R1912	0.1mM GST-GSK3 β	5mM ATP	25mM HEPES pH 7, 150mM NaCl, 10mM MgCl ₂	25 °C
R1914	Buffer			
R1915	0.1mM GST-GSK3 β			

ITC Runs for ATP vs. GSK3 β (Hi5 Expressed)

Run#	ITC Cell	ITC Syringe	Buffer	Temp.
R3065	Buffer	5mM ATP	50mM HEPES pH 7, 50mM NaCl, 20mM MgCl ₂ , 0.125mM DTT	25 °C
R3092	Buffer	2mM ATP		
R3093	10 μ M GSK3 β	2mM ATP		
R3094	10 μ M GSK3 β (R3093 cell)	5mM ATP		

ITC Runs for Alsterpaullone (AL) vs. GSK3 β (Hi5 Expressed)

Run#	ITC Cell	ITC Syringe	Buffer	Temp.
R3096	Buffer	50 μ M AL	50mM HEPES pH 7, 50mM NaCl, 20mM MgCl ₂ , 2% DMSO	25 °C
R3097				
R3098	10 μ M GSK3 β			

ITC Runs for AMP-PNP vs. GSK3 β (Hi5 Expressed)

Run#	ITC Cell	ITC Syringe	Buffer	Temp.
R3116	Buffer	5mM AMP-PNP	50mM HEPES pH 7, 50mM NaCl, 20mM MgCl ₂ , 0.125mM DTT	25 °C
R3117	10μM GSK3β			
R3118	10μM GSK3β (R3117 cell)			
R3119	10μM GSK3β + 20μM GSM	5mM AMP-PNP + 20μM GSM		
R3121	Buffer	5mM AMP-PNP	50mM TRIS pH 8, 50mM NaCl, 10mM MgCl ₂ (2.5mM HEPES & 0.125mM DTT carry over from GSK3β stock)	
R3122	10μM GSK3β			
R3125	10μM GSK3β + 20μM GSM	5mM AMP-PNP + 20μM GSM		

ITC Runs for GSM peptide vs. GSK3 β (Hi5 Expressed)

Run#	ITC Cell	ITC Syringe	Buffer	Temp.
R3130	10 μ M GSK3 β	500 μ M GSM	50mM TRIS pH 8, 20mM NaCl, 10mM MgCl ₂ (2.5mM HEPES & 0.125mM DTT carry over from GSK3 β stock)	25 °C
R3131	10 μ M GSK3 β (R3130 cell)	500 μ M GSM		
R3132	10 μ M GSK3 β	1mM GSM		
R3134	Buffer	500 μ M GSM		

ITC Runs (post-stringent cleaning of ITC cell)

Run#	ITC Cell	ITC Syringe	Buffer	Temp.
R3154	10μM GSK3β	500μM GSM	50mM HEPES pH 7, 50mM NaCl, 10mM MgCl ₂	25 °C
R3155		500μM GSM + 500μM AMP-PNP		
R3157		5mM AMP-PNP	50mM TRIS pH 8, 20mM NaCl, 10mM MgCl ₂	
R3158	10μM GSK3β + 500μM GSM	5mM AMP-PNP		

ITC Runs for AMP-PNP vs. GSK3 β (Hi5 Expressed)

Run#	ITC Cell	ITC Syringe	Buffer	Temp.	Stir Speed
R3200	Buffer	5mM AMP-PNP	50mM TRIS pH 8, 20mM NaCl, 10mM MgCl ₂	15 °C	750rpm
R3201	43.9 μ M GSK3 β				
R3209	42.45 μ M GSK3 β				
R3210	Buffer				

ITC Runs for AMP-PNP vs. GSK3 β (Hi5 Expressed)

Run#	ITC Cell	ITC Syringe	Buffer	Temp.	Stir Speed
R3225	Buffer	2.5mM AMP-PNP	50mM TRIS pH 8, 20mM NaCl, 10mM MgCl ₂	15 °C	500rpm
R3227	57.9μM GSK3β				
R3261	Buffer		50mM BIS-TRIS pH 6.5, 20mM NaCl, 10mM MgCl ₂ (+L-Arg/L-Glu), 0.5mM β-ME		
R3262	52.3μM GSK3β				

Appendix V

Part A

ITC Single-injection Thermograms for GSK3 β Kinase Reaction in the Presence and Absence of Known GSK3 β Inhibitors.

LiCl is a classical inhibitor of GSK3 β . Alsterpaullone is a synthetic potent inhibitor of GSK3 β . The triple-site GSM peptide (RG42) phosphorylation by GSK3 β was observed in the presence or absence of these inhibitors. A single injection of 5mM ATP in 50mM HEPES pH 7, 50mM NaCl, 20mM MgCl₂, 0.125mM DTT, and 2% DMSO was injected into the ITC cell containing 2 μ M GSK3 β , 100 μ M GSM peptide substrate in 50mM HEPES pH 7, 50mM NaCl, 20mM MgCl₂, 0.125mM DTT and 2% DMSO with +/- 5 μ M Alsterpaullone (AL) or +/- 10mM LiCl. An exothermic peak was observed for the phosphorylation of the GSM peptide catalyzed by GSK3 β , and the exothermic signal was significantly reduced in the presence of the known GSK3 β inhibitors, confirming that the ITC measures and detects the actual kinase reaction catalyzed by GSK3 β with the GSM peptide as the substrate.

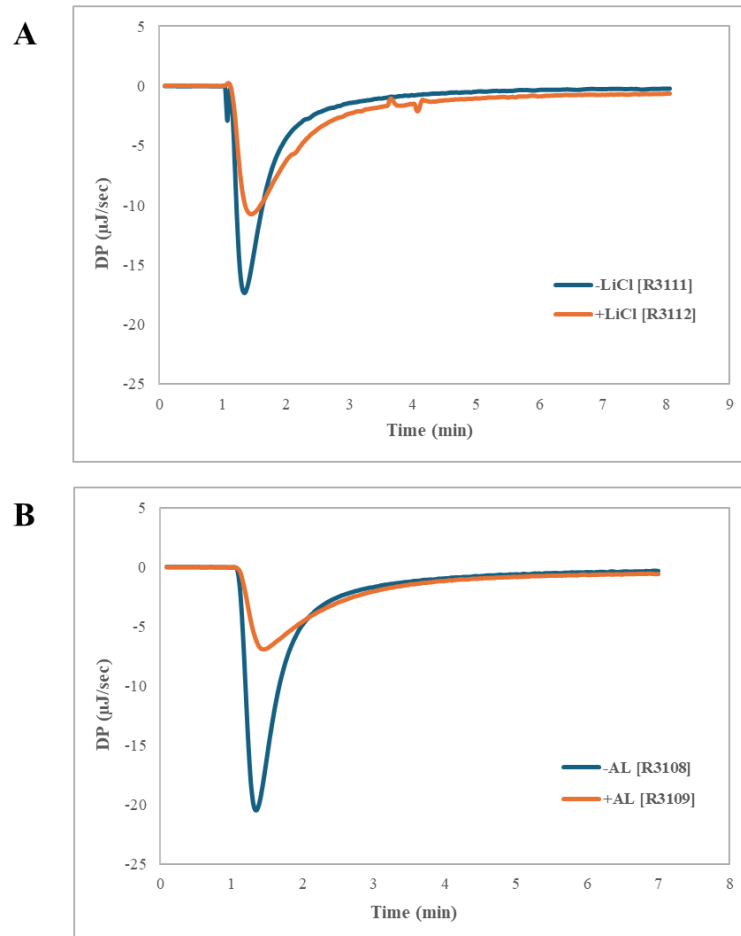


Figure Appendix V.A: ITC Single-injection Assay Thermograms for GSK3 β Kinase Reaction +/- Inhibitors. The phosphorylation of 100 μ M triple-site GSM peptide (RG42) catalyzed by 2 μ M GSK3 β in the reaction buffer: 50mM HEPES pH 7, 50mM NaCl, 20mM MgCl₂, 0.125mM DTT and 2% DMSO with A) +/- 10mM LiCl a classical inhibitor of GSK3 β or B) +/- 5 μ M Alsterpaullone (AL) a potent synthetic inhibitor of GSK3 β . The reaction was initiated by injecting 4 μ L of 5mM ATP in the matching buffer. The blue curves represent the ITC thermogram for the GSK3 β kinase reaction in the absence of an inhibitor, and the orange curve for the reaction in the presence of an inhibitor.

GSK3 β Kinase Reaction in Different Buffers and pH

The phosphorylation of the triple-site GSM peptide (RG42) catalyzed by GSK3 β was observed in four biological buffers: MES buffer pH 6, BIS-TRIS buffer pH 6.5, HEPES buffer pH 7, and TRIS buffer pH 8. This experiment was done mainly to observe which buffer yielded the largest thermogram signal in response to the GSK3 β catalyzed phosphorylation. Suppose a specific buffer system yields a significantly larger thermogram. In that case, it can be inferred that such conditions not only support the enzymatic activity of GSK3 β but also likely foster optimal substrate-protein interactions preceding the phosphorylation event. A single injection of 5mM ATP in 50mM choice buffer, 50mM NaCl, 20mM MgCl₂, was injected into the ITC cell containing 2 μ M GSK3 β , 100 μ M GSM peptide substrate prepared in the same buffer conditions. The results demonstrated that the exothermic signal representing GSK3 β catalyzed phosphorylation was significantly higher in the TRIS-HCl pH 8 buffer, suggesting that this condition was most favorable for the kinase reaction.

The exothermic signal was the second largest for the BIS-TRIS pH 6.5 buffer, followed by the MES pH 6 buffer and HEPES pH 7 buffer. Due to the sulfonate groups in the buffer structures of the latter two, we hypothesize that the HEPES and MES buffers could compete for the ATP binding site on the kinase.

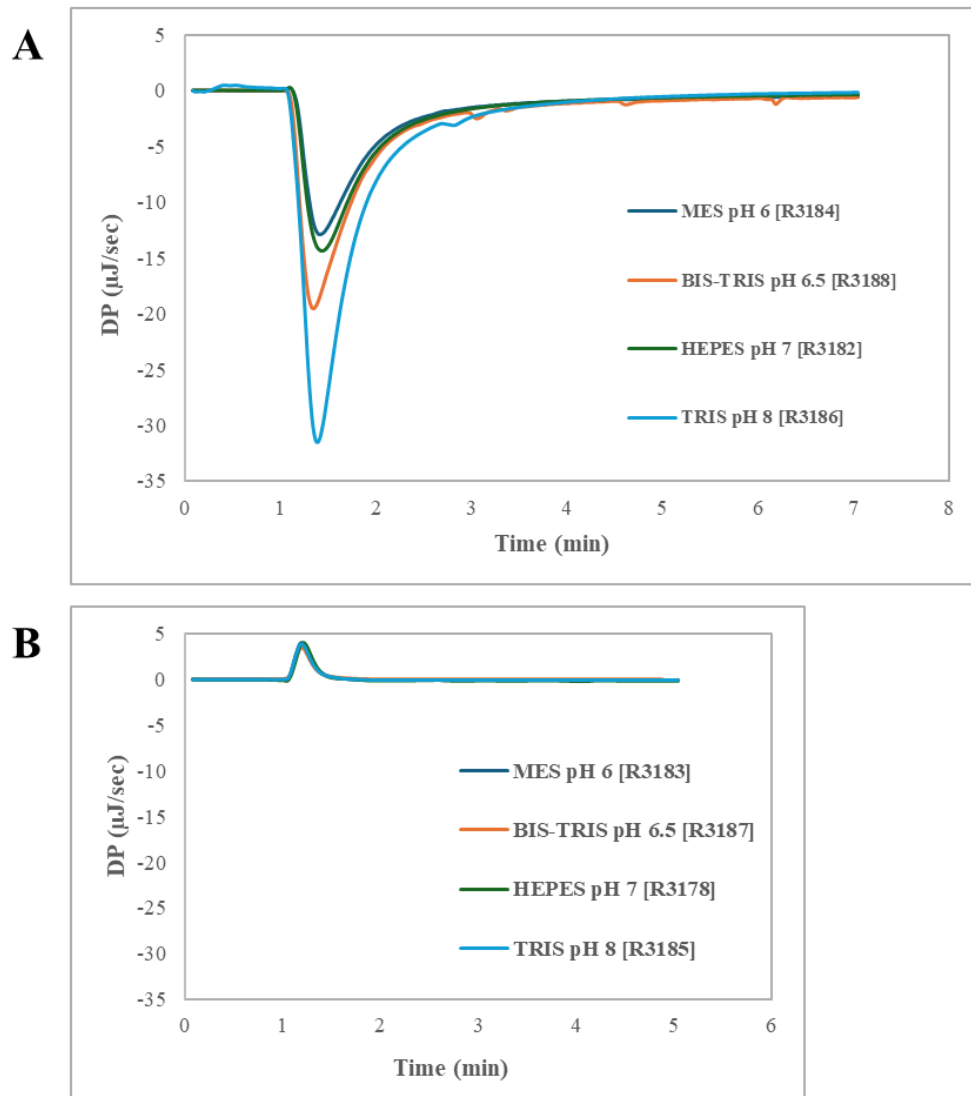


Figure Appendix V.B: ITC Single-injection Analysis Thermogram for GSK3 β Kinase Reaction in Different Buffers and pH. The phosphorylation of 100 μM triple-site GSM peptide (RG42) catalyzed by 2 μM GSK3 β in four different biological buffers: 50mM MES pH 6, 50mM BIS-TRIS pH 6.5, 50mM HEPES pH 7, and 50mM TRIS pH 8 supplemented with 20mM NaCl and 10mM MgCl₂. The reaction was initiated by injecting 4 μL of 5mM ATP in the matching buffer. A) Raw ITC curves for GSK3 β phosphorylation reaction in different buffers show that TRIS pH 8 buffer facilitates the most significant heat release followed by BIS-TRIS pH 6.5, MES pH 6, and HEPES pH 7 in decreasing order B) shows the heat of dilution following the injection of ATP into the respective buffer, in the absence of enzyme. Both figures are adjusted to the same scale on the y-axis for comparison.

Part B

Analysis 1: An Example of Determining the Maximum Initial Rate of ITC ($Rate_{ITC}$) for an ITC Single-injection Assay using Excel.

ITC R3247 is used for this example to demonstrate the calculation of the initial $Rate_{ITC}$ data. The initial $Rate_{ITC}$ calculated according to this manner was plotted against the respective substrate concentrations tested to assess the fit to the Michaelis-Menten curve for the triple-site GSM peptide phosphorylation by GSK3 β . The DP values for each time point were exported from the MicroCal PEAQ analysis software as a CSV file. The DP values were normalized to a DP of 0 using Excel. The DP change for each time point represents the heat generation rate due to enzymatic activity.

The apparent enthalpy (ΔH_{app}) for this reaction (R3247) was = -117 kJ/mol. The active reaction volume was = 200 μ L.

Using equation 6-10, the initial $Rate_{ITC}$ for each 1-sec interval could be calculated in Excel.

Equation 6.9:

$$Rate_{ITC} = \frac{DP}{V_{cell} \cdot \Delta H_{app}}$$

An example is shown for calculating initial Rate_{ITC} at t = 16-sec post-substrate injection where the maximum DP change was -12.5736 μJ/sec:

$$V_{0(ITC)} = \left(\frac{1}{(0.0002L) \left(117 \times \frac{10^3 J}{mol} \right)} \right) \times \left(\left(-12.5736 \mu \frac{J}{sec} \right) \times (-1) \right)$$

$$V_{0(ITC)} = 0.537333 \mu \frac{mol}{L} / sec$$

Using equation 6-11, the substrate concentration in the ITC cell at each time point can be determined. A segment of the Excel analysis to determine [S]_t is shown (concentrations are in μM). The highlighted row shows the reaction rate for the largest DP change and the calculation of the substrate concentration corresponding to that time point.

Equation 6.10:

$$[S]_t = [S]_0 - \frac{\left(\int_0^t DP dt \right)}{V_{cell} \cdot \Delta H_{app}}$$

Table Appendix V.A: Determining Rate_{ITC} for ITC Run R3247. The table shows the setup for the calculation in Excel. Substrate concentrations are calculated from the point of injection at 1min. The row with the bolded font represents the maximum DP change and corresponding Rate_{ITC} vs. substrate concentration.

Time (min)	DP Change (μJ/sec)	d[S]/dt (μM/sec)	(d[S]/dt)*(1-sec)	[S] _t (μM)	d[P]/dt (μM/sec)
1	-0.18045	-0.00771	-0.007711581	20	0.007712
1.016667	-0.13477	-0.00576	-0.00575953	19.99424	0.00576
1.033333	-0.07243	-0.0031	-0.003095385	19.99115	0.003095
1.05	-0.08399	-0.00359	-0.003589231	19.98756	0.003589
1.066667	-0.23429	-0.01001	-0.010012564	19.97754	0.010013
1.083333	-0.64359	-0.0275	-0.02750406	19.95004	0.027504
1.1	-1.36749	-0.05844	-0.058439872	19.8916	0.05844
1.116667	-2.41068	-0.10302	-0.103020342	19.78858	0.10302
1.133333	-3.70013	-0.15813	-0.158125085	19.63045	0.158125
1.15	-5.14562	-0.2199	-0.219898248	19.41056	0.219898
1.166667	-6.71655	-0.28703	-0.287032009	19.12352	0.287032
1.183333	-8.28321	-0.35398	-0.353983205	18.76954	0.353983
1.2	-9.74252	-0.41635	-0.41634688	18.35319	0.416347
1.216667	-10.9444	-0.46771	-0.467710299	17.88548	0.46771
1.233333	-11.8191	-0.50509	-0.505090897	17.38039	0.505091
1.25	-12.3533	-0.52792	-0.527917906	16.85247	0.527918
1.266667	-12.5736	-0.53733	-0.537332863	16.31514	0.537333
1.283333	-12.5153	-0.53484	-0.534842265	15.7803	0.534842
1.3	-12.2097	-0.52178	-0.52178265	15.25852	0.521783

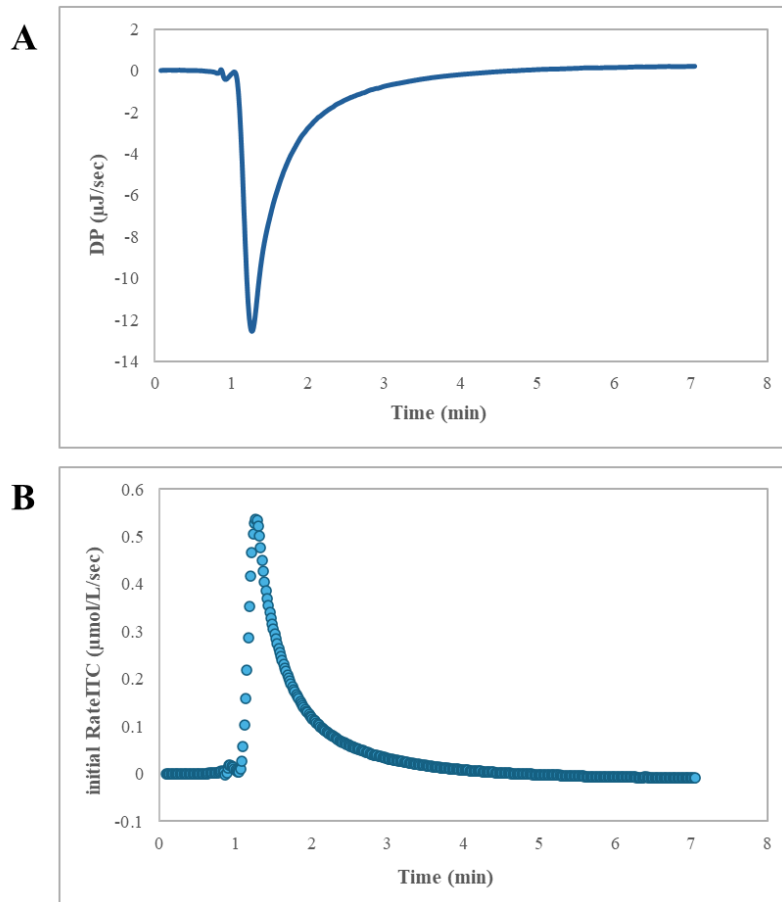


Figure Appendix V.C: The Rate_{ITC} vs. Time for DP Values from the Reaction Course for R3247. A) The raw ITC curve for R3247 shows the DP change over time during the reaction for the phosphorylation of 0.02mM triple-site GSM [RG42] by 2μM GSK3β in 50mM TRIS pH 8, 20mM NaCl, 10mM MgCl₂, and 0.2mM ATP. B) Rate_{ITC} calculated for all DP values during the reaction plotted as a function of time. The highest Rate_{ITC} was noted at the early stages of the reaction following complete mixing to be the peak of the plot and extracted as the initial Rate_{ITC} value for the phosphorylation reaction at this peptide concentration.

Analysis 2: Example of DP Correction for the Instrument Response Time for GSK3 β Catalyzed Phosphorylation of the Triple-site GSM peptide

The measured DP values can be corrected for the ITC instrument's thermal inertia using the Tian equation (equation 6-12).

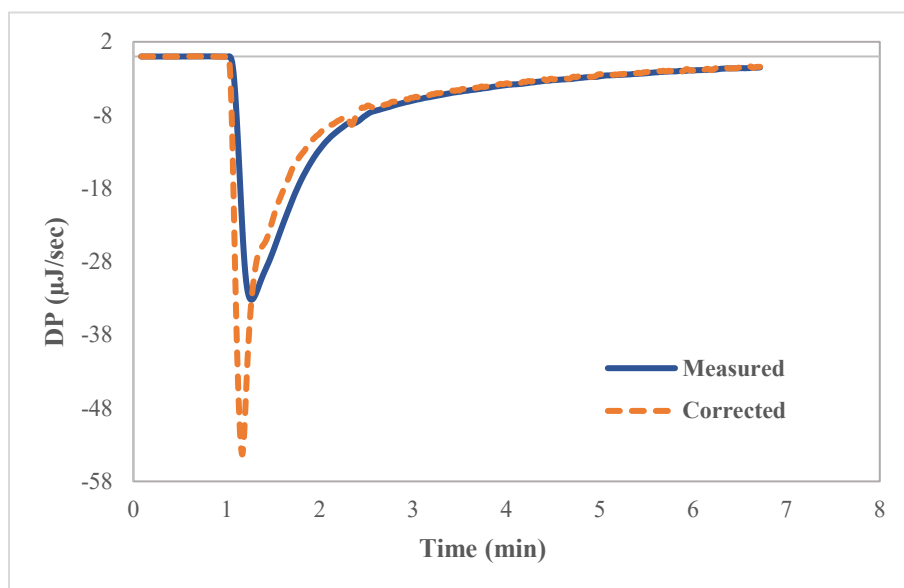


Figure Appendix V.D: Comparison between the Measured Thermogram and the Tian Equation Corrected Thermogram. This comparison used the raw ITC curve from the single injection assay R3291, where 6mM triple-site GSM peptide was injected into 0.5 μ M GSK3 β . The raw thermogram measured by ITC is shown in blue, and the thermogram corrected for the instrument response time with the Tian equation is shown in orange.

Analysis 3: Example of DP Correction for the Instrument Response Time for GSK3 β Catalyzed Phosphorylation of the Mono-site GSM peptide

The measured DP values can be corrected for the ITC instrument's thermal inertia using the Tian equation (equation 6-12).

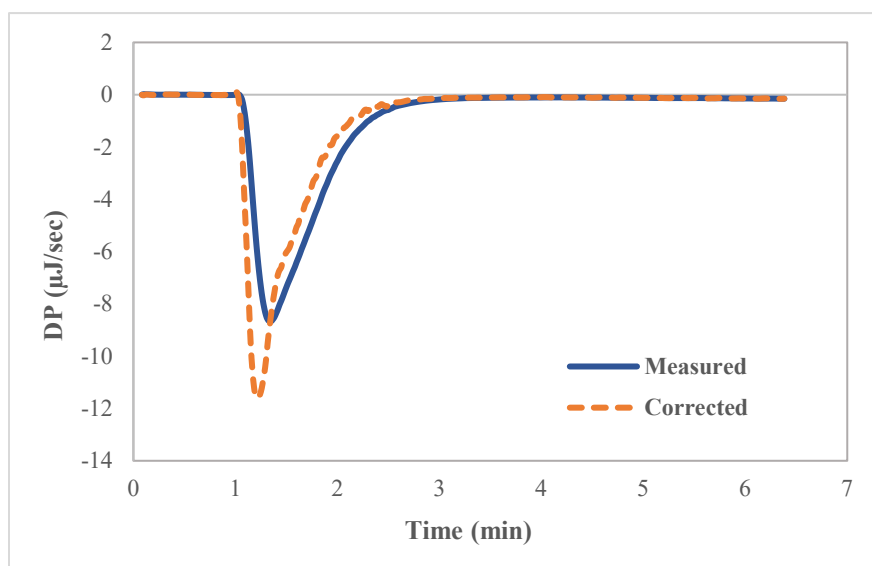


Figure Appendix V.E: Comparison between the Measured Thermogram and the Tian Equation Corrected Thermogram. This comparison used the raw ITC curve from the single injection assay R3379, where 3mM mono-site GSM peptide was injected into 0.66 μ M GSK3 β . The raw thermogram measured by ITC is shown in blue, and the thermogram corrected for the instrument response time with the Tian equation is shown in orange.

Analysis 4: Michaelis-Menten Analysis for Mono-site GSM Phosphorylation Catalyzed by GSK3 β Using Excel

All data points, including and downward from the boxed values, are derived from the raw ITC curve segment selected on MicroCal PEAQ-ITC analysis software by “Enzyme Marker” brackets and are used for kinetic analysis on Excel. Vcal represents the calculated reaction velocity based on the Michaelis-Menten equation using the indicated [S] with the fitted parameters $K_m = 57 \mu\text{M}$ and $V_{\text{max}} = 3.5 \mu\text{M}/\text{sec}$.

[S] ⁰		0.06 mM		60		K _M		57 (μM)		
ΔH _{app} (kJ/mol)		-29.6		29600		V _{max}		3.5 (μM/sec)		
V _{cell} (L)		200μL		0.0002						
Time (min)	DP Change (μJ/sec)	Rate (-d[S]/dt) μmol/L/sec	Rate*dt μM	[S] _t μM	d[P]/dt	[S] _t	V _{obs}	V _{cal}	V _{obs} -V _{cal}	
1	-0.006637	-0.001121195	-0.001121195	59.99888	0.001121195	44.30087	1.464047	1.530619	-0.06657	
1.016667	0.0003545	5.98864E-05	5.98864E-05	59.99894	-5.98864E-05	42.8485	1.452364	1.501973	-0.04961	
1.033333	0.0131245	0.002216981	0.002216981	60.00116	-0.002216981	41.41206	1.436444	1.472809	-0.03637	
1.05	-0.056376	-0.009523053	-0.009523053	59.99163	0.009523053	39.9999	1.412158	1.443297	-0.03114	
1.066667	-0.197555	-0.033370857	-0.033370857	59.95826	0.033370857	38.61352	1.386386	1.413475	-0.02709	
1.083333	-0.514914	-0.086978796	-0.086978796	59.87128	0.086978796	37.25723	1.356286	1.383451	-0.02717	
1.1	-0.951011	-0.16064383	-0.16064383	59.71064	0.16064383	35.92647	1.303755	1.353141	-0.02239	
1.116667	-1.507688	-0.254677107	-0.254677107	59.45596	0.254677107	34.62387	1.302601	1.32262	-0.02002	
1.133333	-2.173808	-0.367197377	-0.367197377	59.08876	0.367197377	33.35108	1.272791	1.291947	-0.01916	
1.15	-2.966411	-0.501083019	-0.501083019	58.58768	0.501083019	32.10686	1.244226	1.261115	-0.01689	
1.166667	-3.811977	-0.643915114	-0.643915114	57.94377	0.643915114	30.89044	1.216418	1.230129	-0.01371	
1.183333	-4.644397	-0.7845266	-0.7845266	57.15924	0.7845266	29.69945	1.190993	1.198947	-0.00795	
1.2	-5.452156	-0.920972377	-0.920972377	56.23827	0.920972377	28.53476	1.164691	1.167615	-0.00292	
1.216667	-6.172872	-1.042714945	-1.042714945	55.19555	1.042714945	27.39722	1.137533	1.136178	0.001355	
1.233333	-6.807214	-1.149867309	-1.149867309	54.04569	1.149867309	26.28468	1.11254	1.104602	0.007938	
1.25	-7.352754	-1.242019337	-1.242019337	52.80367	1.242019337	25.20208	1.082603	1.073054	0.009549	
1.266667	-7.810581	-1.319354978	-1.319354978	51.48431	1.319354978	24.14634	1.055742	1.041479	0.014263	
1.283333	-8.164449	-1.379129978	-1.379129978	50.10518	1.379129978	23.11902	1.027318	1.009955	0.017364	
1.3	-8.436005	-1.42500924	-1.42500924	48.68018	1.42500924	22.12213	0.996893	0.978581	0.018312	
1.316667	-8.59682	-1.45216562	-1.45216562	47.22801	1.45216562	21.15235	0.969771	0.947294	0.022478	
1.333333	-8.661548	-1.463099404	-1.463099404	45.76492	1.463099404	20.2114	0.940952	0.916185	0.024767	
1.35	-8.667158	-1.464047039	-1.464047039	44.30087	1.464047039	19.29967	0.911736	0.88531	0.026462	
1.366667	-8.597992	-1.452363593	-1.452363593	42.8485	1.452363593	18.41451	0.885158	0.85462	0.030538	
1.383333	-8.503747	-1.43644383	-1.43644383	41.41206	1.43644383	17.55821	0.856296	0.824238	0.032058	
1.4	-8.359973	-1.412157681	-1.412157681	39.9999	1.412157681	16.73084	0.827371	0.794212	0.033158	
1.416667	-8.207406	-1.386386228	-1.386386228	38.61352	1.386386228	15.93398	0.796861	0.76465	0.032211	
1.433333	-8.029215	-1.356286397	-1.356286397	37.25723	1.356286397	15.16681	0.767171	0.735571	0.0316	
1.45	-7.878072	-1.330755485	-1.330755485	35.92647	1.330755485	14.42632	0.740495	0.706912	0.033583	
1.466667	-7.711395	-1.302600587	-1.302600587	34.62387	1.302600587	13.71456	0.711753	0.678799	0.032954	
1.483333	-7.534922	-1.272790958	-1.272790958	33.35108	1.272790958	13.03233	0.682233	0.651316	0.030917	
1.5	-7.365817	-1.244225924	-1.244225924	32.10686	1.244225924	12.38216	0.650167	0.624621	0.025546	
1.516667	-7.201192	-1.216417647	-1.216417647	30.89044	1.216417647	11.76053	0.62163	0.598626	0.023004	
1.533333	-7.050677	-1.190992816	-1.190992816	29.69945	1.190992816	11.16421	0.596319	0.573244	0.023074	
1.55	-6.894669	-1.164690789	-1.164690789	28.53476	1.164690789	10.59244	0.571778	0.548486	0.023291	
1.566667	-6.734196	-1.137533188	-1.137533188	27.39722	1.137533188	10.04895	0.543489	0.524562	0.018927	
1.583333	-6.586235	-1.112539776	-1.112539776	26.28468	1.112539776	9.531061	0.517887	0.501401	0.016486	
1.6	-6.409008	-1.082602782	-1.082602782	25.20208	1.082602782	9.035084	0.495977	0.478879	0.017098	
1.616667	-6.249993	-1.055742141	-1.055742141	24.14634	1.055742141	8.561144	0.47394	0.457039	0.016901	
1.633333	-6.081725	-1.027318492	-1.027318492	23.11902	1.027318492	8.111272	0.449873	0.436014	0.013858	
1.65	-5.901609	-0.996893492	-0.996893492	22.12213	0.996893492	7.68106	0.430212	0.415635	0.014577	
1.666667	-5.741046	-0.969771364	-0.969771364	21.15235	0.969771364	7.27497	0.408563	0.396028	0.012535	
1.683333	-5.570433	-0.9409516	-0.9409516	20.2114	0.9409516	6.886636	0.385861	0.377281	0.00858	
1.7	-5.397477	-0.911736059	-0.911736059	19.29967	0.911736059	6.518667	0.367968	0.359191	0.008777	
1.716667	-5.240137	-0.885158357	-0.885158357	18.41451	0.885158357	6.168359	0.350309	0.341773	0.008555	
1.733333	-5.069273	-0.856296195	-0.856296195	17.55821	0.856296195	5.834627	0.333731	0.324999	0.008732	
1.75	-4.898033	-0.827370519	-0.827370519	16.73084	0.827370519	5.516236	0.318391	0.308829	0.009562	
1.766667	-4.717415	-0.796860722	-0.796860722	15.93398	0.796860722	5.213538	0.302698	0.293302	0.009396	
1.783333	-4.541653	-0.767171195	-0.767171195	15.16681	0.767171195	4.925211	0.288327	0.278372	0.009955	
1.8	-4.383727	-0.740494505	-0.740494505	14.42632	0.740494505	4.653298	0.271912	0.264163	0.007749	
1.816667	-4.213575	-0.711752614	-0.711752614	13.71456	0.711752614	4.395587	0.257711	0.250581	0.00713	
1.833333	-4.038818	-0.68223285	-0.68223285	13.03233	0.68223285	4.149694	0.245893	0.237514	0.008379	
1.85	-3.848989	-0.650167141	-0.650167141	12.38216	0.650167141	3.914628	0.235066	0.224925	0.010141	
1.866667	-3.680051	-0.621630316	-0.621630316	11.76053	0.621630316	3.691571	0.223057	0.212888	0.010169	
1.883333	-3.530206	-0.596318661	-0.596318661	11.16421	0.596318661	3.478076	0.213495	0.201284	0.012211	
1.9	-3.384924	-0.571777782	-0.571777782	10.59244	0.571777782	3.275401	0.202675	0.190192	0.012482	
1.916667	-3.217452	-0.543488593	-0.543488593	10.04895	0.543488593	3.083703	0.191698	0.179632	0.012066	
1.933333	-3.06589	-0.517886904	-0.517886904	9.531061	0.517886904	2.903822	0.17988	0.169662	0.010219	
1.95	-2.936183	-0.495976938	-0.495976938	9.035084	0.495976938	2.732811	0.171012	0.160127	0.010885	
1.966667	-2.805722	-0.473939607	-0.473939607	8.561144	0.473939607	2.56892	0.16389	0.150938	0.012952	
1.983333	-2.663245	-0.449872546	-0.449872546	8.111272	0.449872546	2.415024	0.153897	0.142263	0.011633	
2	-2.546852	-0.430211566	-0.430211566	7.68106	0.430211566	2.268906	0.146117	0.133985	0.012132	
2.016667	-2.418694	-0.408563255	-0.408563255	7.272497	0.408563255	2.127506	0.1414	0.125936	0.015464	
2.033333	-2.284298	-0.385861228	-0.385861228	6.886636	0.385861228	1.994592	0.132913	0.118334	0.014579	
2.05	-2.178372	-0.367968323	-0.367968323	6.518667	0.367968323	1.867471	0.127121	0.111032	0.01609	
2.066667	-2.073827	-0.350308695	-0.350308695	6.168359	0.350308695	1.746425	0.121046	0.104049	0.016997	
2.083333	-1.975689	-0.33373133	-0.33373133	5.834627	0.33373133	1.632374	0.114052	0.097443	0.016706	
2.1	-1.884877	-0.318391465	-0.318391465	5.516236	0.318391465	1.524496	0.107877	0.091171	0.016706	
2.116667	-1.791972	-0.302698053	-0.302698053	5.213538	0.302698053	1.420565	0.103931	0.085107	0.018825	
2.133333	-1.706896	-0.288327107	-0.288327107	4.925211	0.288327107	1.32051	0.100055	0.079248	0.020807	
2.15	-1.609721	-0.271912411	-0.271912411	4.653298	0.271912411	1.222081	0.098429	0.073465	0.024964	
2.166667	-1.52565	-0.257711228	-0.257711228	4.395587	0.257711228	1.129953	0.092127	0.068034	0.024093	
2.183333	-1.455688	-0.245893323	-0.245893323	4.149694	0.245893323	1.042302	0.087651	0.062852	0.024799	
2.2	-1.391588	-0.23506562	-0.23506562	3.914628	0.23506562	0.960741	0.081561	0.058015	0.023546	
2.216667	-1.320497	-0.223057005	-0.223057005	3.691571	0.223057005	0.883868	0.076873	0.053444	0.023429	
2.233333	-1.263891	-0.213495181	-0.213495181	3.478076	0.213495181	0.809775	0.074093	0.049027	0.025067	
2.25	-1.199833	-0.202674573	-0.202674573	3.275401	0.202674573	0.738695	0.07108	0.044778	0.026302	
2.266667	-1.134854	-0.191698391	-0.191698391	3.083703	0.191698391	0.670019	0.068676	0.040664	0.028012	
2.283333	-1.064892	-0.179								

Appendix VI

ITC Runs for Chapter 6

ITC single injection analysis thermogram for GSK3 β kinase reaction:

Run#	ITC Cell	ITC Syringe	Buffer	Temp.
R3335	2 μ M GSK3 β	1mM Triple-site GSM	50mM TRIS pH 8, 20mM NaCl, 10mM MgCl ₂ , 0.2mM ATP	25 °C
R3337	2 μ M GSK3 β		50mM TRIS pH 8, 20mM NaCl, 10mM MgCl ₂ , 0.2mM AMP-PNP	
R3338	Buffer		50mM TRIS pH 8, 20mM NaCl, 10mM MgCl ₂	

ITC single Injection analysis for the phosphorylation of triple-site GSM peptide (RG42) catalyzed with various concentrations of GSK3 β .

Run#	ITC Cell	ITC Syringe	Buffer	Temp.
R3202	2 μ M GSK3 β + 100 μ M triple-site GSM	5mM ATP	50mM TRIS pH 8, 20mM NaCl, 10mM MgCl ₂	30 °C
R3276	Buffer			
R3277	0.5 μ M GSK3 β + 100 μ M triple-site GSM			
R3278	0.125 μ M GSK3 β + 100 μ M triple-site GSM			

Run#	ITC Cell	ITC Syringe	Buffer	Temp.
R3291	0.5 μ M GSK3 β + 1.5mM ATP	6mM RG42	50mM TRIS pH 8, 20mM NaCl, 10mM MgCl ₂	30 °C
R3294		4.5mM RG42		
R3295		3mM RG42		
R3296		2mM RG42		
R3297		1.5mM RG42		
R3298		1mM RG42		
R3299		0.5mM RG42		
R3301		0mM RG42		

ITC single Injection analysis for the phosphorylation of mono-site GSM peptide (RG43) catalyzed with 0.66 μ M GSK3 β .

Run#	ITC Cell	ITC Syringe	Buffer	Temp.
R3377	0.66 μ M GSK3 β	6mM Mono-site GSM	50mM TRIS pH 8, 20mM NaCl, 10mM MgCl ₂ , 1.2mM ATP	30 °C
R3378		6mM Mono-site GSM	50mM TRIS pH 8, 20mM NaCl, 10mM MgCl ₂ , 1.2mM ATP	
R3379		3mM Mono-site GSM	50mM TRIS pH 8, 20mM NaCl, 10mM MgCl ₂ , 0.6mM ATP	

Comparing Apparent Reaction Enthalpy from the Single-injection Assay for the Phosphorylation of Various Concentrations of Triple-site GSM (RG42) vs. Mono-site GSM (RG43) by GSK3 β .

Run#	ITC Cell	ITC Syringe	Buffer	Temp.
R3335	2 μ M GSK3 β	1mM Triple-site GSM	50mM TRIS pH 8, 20mM NaCl, 10mM MgCl ₂ , 0.2mM ATP	25 °C
R3334	2 μ M GSK3 β	1mM Mono-site GSM		
R3336	2 μ M GSK3 β	1mM (Ser>Ala) Mutant GSM		
R3354	1 μ M GSK3 β	1mM Triple-site GSM		
R3355	1 μ M GSK3 β	1mM Mono-site GSM		
R3356	1 μ M GSK3 β	3mM Mono-site GSM		
R3357	1 μ M GSK3 β	1mM (Ser>Ala) Mutant GSM		
R3358	Buffer	1mM Triple-site GSM		
R3359	Buffer	1mM Mono-site GSM		
R3360	Buffer	3mM Mono-site GSM		
R3361	Buffer	1mM (Ser>Ala) Mutant GSM		
R3394	0.5 μ M GSK3 β	3mM Mono-site GSM	50mM TRIS pH 8, 20mM NaCl, 10mM MgCl ₂ , 1mM ATP	

Determining the Buffer Independent Reaction Enthalpy for GSK3 β Phosphorylation of Mono-site GSM peptide

Run#	ITC Cell	ITC Syringe	Buffer	Temp.
R3365	1 μ M GSK3 β	1mM Mono-site GSM	50mM TRIS pH 7, 20mM NaCl, 10mM MgCl ₂ , 1.9mM ATP	30 °C
R3367			50mM BIS-TRIS pH 7, 20mM NaCl, 10mM MgCl ₂ , 1.9mM ATP	
R3368			50mM MES pH 7, 20mM NaCl, 10mM MgCl ₂ , 1.9mM ATP	
R3369			50mM HEPES pH 7, 20mM NaCl, 10mM MgCl ₂ , 1.9mM ATP	
R3370			50mM MOPS pH 7, 20mM NaCl, 10mM MgCl ₂ , 1.9mM ATP	
R3371	Buffer		50mM TRIS pH 7, 20mM NaCl, 10mM MgCl ₂ , 1.9mM ATP	
R3373	Buffer		50mM BIS-TRIS pH 7, 20mM NaCl, 10mM MgCl ₂ , 1.9mM ATP	
R3374	Buffer		50mM MES pH 7, 20mM NaCl, 10mM MgCl ₂ , 1.9mM ATP	
R3375	Buffer		50mM HEPES pH 7, 20mM NaCl, 10mM MgCl ₂ , 1.9mM ATP	
R3376	Buffer		50mM MOPS pH 7, 20mM NaCl, 10mM MgCl ₂ , 1.9mM ATP	

Single-injection Assays for the Study of Effect of Inhibitors: BeSO₄ and LiCl

Run#	ITC Cell	ITC Syringe	Buffer	Temp.
R3384	0.5μM GSK3β + 1mM LiCl	1mM Triple-site GSM	50mM BIS-TRIS pH 6.5, 20mM NaCl, 10mM MgCl ₂ , 0.2mM ATP	30 °C
R3385	0.5μM GSK3β + 10mM LiCl			
R3289	0.5μM GSK3β + 30mM LiCl			
R3280	0.5μM GSK3β + 1μM BeSO ₄			
R3292	0.5μM GSK3β + 3μM BeSO ₄			
R3288	0.5μM GSK3β + 10μM BeSO ₄			
R3287	0.5μM GSK3β + 30μM BeSO ₄			
R3282	0.5μM GSK3β + 100μM BeSO ₄			

Single-injection Assays for Inhibitor Reversibility for the Inhibition of GSK3 β Phosphorylation by LiCl and BeSO₄

Run#	ITC Cell	ITC Syringe	Buffer	Temp.
R3383	0.5 μ M GSK3 β + No-inhibitor (pre-wash)	4mM Triple-site GSM	50mM BIS-TRIS pH 6.5, 20mM NaCl, 10mM MgCl ₂ , 0.8mM ATP	25 °C
R3384	0.5 μ M GSK3 β + No-inhibitor (post-wash)			
R3385	0.5 μ M GSK3 β + 30mM LiCl (pre-wash)			
R3387	0.5 μ M GSK3 β + 30mM LiCl (post-wash)			
R3388	0.5 μ M GSK3 β + 30 μ M BeSO ₄ (pre-wash)			
R3389	0.5 μ M GSK3 β + 30 μ M BeSO ₄ (post-wash)			

References

- Abdul, A. U. R. M., De Silva, B., & Gary, R. K. (2018). The GSK3 kinase inhibitor lithium produces unexpected hyperphosphorylation of β -catenin, a GSK3 substrate, in human glioblastoma cells. *Biology Open*, 7(1), bio030874. <https://doi.org/10.1242/bio.030874>
- Ahrens, L. H. (1952). The use of ionization potentials Part 1. Ionic radii of the elements. *Geochimica et Cosmochimica Acta*, 2(3), 155–169. [https://doi.org/10.1016/0016-7037\(52\)90004-5](https://doi.org/10.1016/0016-7037(52)90004-5)
- Alberty, R. A. (1998). Calculation of Standard Transformed Gibbs Energies and Standard Transformed Enthalpies of Biochemical Reactants. *Archives of Biochemistry and Biophysics*, 353(1), 116–130. <https://doi.org/10.1006/abbi.1998.0638>
- Alberty, R. A. (2001). Standard Apparent Reduction Potentials for Biochemical Half Reactions as a Function of pH and Ionic Strength. *Archives of Biochemistry and Biophysics*, 389(1), 94–109. <https://doi.org/10.1006/abbi.2001.2318>
- Alberty, R. A. (2003). Thermodynamics of the Hydrolysis of Adenosine Triphosphate as a Function of Temperature, pH, pMg, and Ionic Strength. *The Journal of Physical Chemistry B*, 107(44), 12324–12330. <https://doi.org/10.1021/jp030576l>
- Alberty, R. A., & Goldberg, R. N. (1992). Standard thermodynamic formation properties for the adenosine 5'-triphosphate series. *Biochemistry*, 31(43), 10610–10615. <https://doi.org/10.1021/bi00158a025>
- Alderighi, L., Gans, P., Midollini, S., & Vacca, A. (2000). Aqueous solution chemistry of beryllium. In *Advances in Inorganic Chemistry* (Vol. 50, pp. 109–172). Academic Press. [https://doi.org/10.1016/S0898-8838\(00\)50003-8](https://doi.org/10.1016/S0898-8838(00)50003-8)

- Ali, A., Hoeflich, K. P., & Woodgett, J. R. (2001). Glycogen synthase kinase-3: Properties, functions, and regulation. *Chemical Reviews*, 101(8), 2527–2540.
<https://doi.org/10.1021/cr000110o>
- Asuni, A. A., Hooper, C., Reynolds, C. H., Lovestone, S., Anderton, B. H., & Killick, R. (2006). GSK3alpha exhibits beta-catenin and tau directed kinase activities that are modulated by Wnt. *The European Journal of Neuroscience*, 24(12), 3387–3392.
<https://doi.org/10.1111/j.1460-9568.2006.05243.x>
- Attwood, M. M., Fabbro, D., Sokolov, A. V., Knapp, S., & Schiöth, H. B. (2021). Trends in kinase drug discovery: Targets, indications and inhibitor design. *Nature Reviews. Drug Discovery*, 20(11), 839–861. <https://doi.org/10.1038/s41573-021-00252-y>
- Bäckman, P., Breidenbach, R. W., Johansson, P., & Wadsö, I. (1995). A gas perfusion microcalorimeter for studies of plant tissue. *Thermochimica Acta*, 251, 323–333.
[https://doi.org/10.1016/0040-6031\(94\)02144-D](https://doi.org/10.1016/0040-6031(94)02144-D)
- Balboni, B., Tripathi, S. K., Veronesi, M., Russo, D., Penna, I., Giabbai, B., Bandiera, T., Storici, P., Girotto, S., & Cavalli, A. (2022). Identification of Novel GSK-3 β Hits Using Competitive Biophysical Assays. *International Journal of Molecular Sciences*, 23(7), 3856. <https://doi.org/10.3390/ijms23073856>
- Behrens, J., Jerchow, B. A., Würtele, M., Grimm, J., Asbrand, C., Wirtz, R., Kühl, M., Wedlich, D., & Birchmeier, W. (1998). Functional interaction of an axin homolog, conductin, with beta-catenin, APC, and GSK3beta. *Science (New York, N.Y.)*, 280(5363), 596–599.
<https://doi.org/10.1126/science.280.5363.596>
- Bertrand, J. A., Thieffine, S., Vulpetti, A., Cristiani, C., Valsasina, B., Knapp, S., Kalisz, H. M., & Flocco, M. (2003). Structural characterization of the GSK-3beta active site using

- selective and non-selective ATP-mimetic inhibitors. *Journal of Molecular Biology*, 333(2), 393–407. <https://doi.org/10.1016/j.jmb.2003.08.031>
- Beurel, E., Grieco, S. F., & Jope, R. S. (2015). Glycogen synthase kinase-3 (GSK3): Regulation, actions, and diseases. *Pharmacology & Therapeutics*, 0, 114–131. <https://doi.org/10.1016/j.pharmthera.2014.11.016>
- Bianconi, M. L. (2003). Calorimetric determination of thermodynamic parameters of reaction reveals different enthalpic compensations of the yeast hexokinase isozymes. *The Journal of Biological Chemistry*, 278(21), 18709–18713. <https://doi.org/10.1074/jbc.M211103200>
- Bianconi, M. L. (2007). Calorimetry of enzyme-catalyzed reactions. *Biophysical Chemistry*, 126(1–3), 59–64. <https://doi.org/10.1016/j.bpc.2006.05.017>
- Bichet, P., Mollat, P., Capdevila, C., & Sarubbi, E. (2000). Endogenous glutathione-binding proteins of insect cell lines: Characterization and removal from glutathione S-transferase (GST) fusion proteins. *Protein Expression and Purification*, 19(1), 197–201. <https://doi.org/10.1006/prep.2000.1239>
- Bilic, J., Huang, Y.-L., Davidson, G., Zimmermann, T., Cruciat, C.-M., Bienz, M., & Niehrs, C. (2007). Wnt induces LRP6 signalosomes and promotes dishevelled-dependent LRP6 phosphorylation. *Science (New York, N.Y.)*, 316(5831), 1619–1622. <https://doi.org/10.1126/science.1137065>
- Bowley, E., Mulvihill, E., Howard, J. C., Pak, B. J., Gan, B. S., & O’Gorman, D. B. (2005). A novel mass spectrometry-based assay for GSK-3 β activity. *BMC Biochemistry*, 6, 29. <https://doi.org/10.1186/1471-2091-6-29>

- Buchner, M. R. (2020). Correction: Beryllium coordination chemistry and its implications on the understanding of metal induced immune responses. *Chemical Communications (Cambridge, England)*, 56(90), 14102. <https://doi.org/10.1039/d0cc90479a>
- Case, D. R., Zubietta, J., & P. Doyle, R. (2020). The Coordination Chemistry of Bio-Relevant Ligands and Their Magnesium Complexes. *Molecules*, 25(14), 3172. <https://doi.org/10.3390/molecules25143172>
- Clayton, G. M., Wang, Y., Crawford, F., Novikov, A., Wimberly, B. T., Kieft, J. S., Falta, M. T., Bowerman, N. A., Marrack, P., Fontenot, A. P., Dai, S., & Kappler, J. W. (2014). Structural basis of chronic beryllium disease: Linking allergic hypersensitivity and autoimmunity. *Cell*, 158(1), 132–142. <https://doi.org/10.1016/j.cell.2014.04.048>
- Cohen, P. (2002). Protein kinases—The major drug targets of the twenty-first century? *Nature Reviews. Drug Discovery*, 1(4), 309–315. <https://doi.org/10.1038/nrd773>
- Colombet, J., Robin, A., Lavie, L., Bettarel, Y., Cauchie, H. M., & Sime-Ngando, T. (2007). Virioplankton “pegylation”: Use of PEG (polyethylene glycol) to concentrate and purify viruses in pelagic ecosystems. *Journal of Microbiological Methods*, 71(3), 212–219. <https://doi.org/10.1016/j.mimet.2007.08.012>
- Cowan, J. A. (1998). Metal Activation of Enzymes in Nucleic Acid Biochemistry. *Chemical Reviews*, 98(3), 1067–1088. <https://doi.org/10.1021/cr960436q>
- Cross, D. A., Alessi, D. R., Cohen, P., Andjelkovich, M., & Hemmings, B. A. (1995). Inhibition of glycogen synthase kinase-3 by insulin mediated by protein kinase B. *Nature*, 378(6559), 785–789. <https://doi.org/10.1038/378785a0>
- Cross, D. A., Watt, P. W., Shaw, M., van der Kaay, J., Downes, C. P., Holder, J. C., & Cohen, P. (1997). Insulin activates protein kinase B, inhibits glycogen synthase kinase-3 and

- activates glycogen synthase by rapamycin-insensitive pathways in skeletal muscle and adipose tissue. *FEBS Letters*, 406(1–2), 211–215. [https://doi.org/10.1016/s0014-5793\(97\)00240-8](https://doi.org/10.1016/s0014-5793(97)00240-8)
- Dajani, R., Fraser, E., Roe, S. M., Yeo, M., Good, V. M., Thompson, V., Dale, T. C., & Pearl, L. H. (2003). Structural basis for recruitment of glycogen synthase kinase 3 β to the axin–APC scaffold complex. *The EMBO Journal*, 22(3), 494–501. <https://doi.org/10.1093/emboj/cdg068>
- Dajani, R., Fraser, E., Roe, S. M., Young, N., Good, V., Dale, T. C., & Pearl, L. H. (2001). Crystal structure of glycogen synthase kinase 3 beta: Structural basis for phosphate-primed substrate specificity and autoinhibition. *Cell*, 105(6), 721–732. [https://doi.org/10.1016/s0092-8674\(01\)00374-9](https://doi.org/10.1016/s0092-8674(01)00374-9)
- Davis, T. R., Wickham, T. J., McKenna, K. A., Granados, R. R., Shuler, M. L., & Wood, H. A. (1993). Comparative Recombinant Protein Production of Eight Insect Cell Lines. *In Vitro Cellular & Developmental Biology. Animal*, 29A(5), 388–390.
- De Sarno, P., Li, X., & Jope, R. S. (2002). Regulation of Akt and glycogen synthase kinase-3 beta phosphorylation by sodium valproate and lithium. *Neuropharmacology*, 43(7), 1158–1164. [https://doi.org/10.1016/s0028-3908\(02\)00215-0](https://doi.org/10.1016/s0028-3908(02)00215-0)
- Di Trani, J. M., Moitessier, N., & Mittermaier, A. K. (2017). Measuring Rapid Time-Scale Reaction Kinetics Using Isothermal Titration Calorimetry. *Analytical Chemistry*, 89(13), 7022–7030. <https://doi.org/10.1021/acs.analchem.7b00693>
- Ding, V. W., Chen, R. H., & McCormick, F. (2000). Differential regulation of glycogen synthase kinase 3beta by insulin and Wnt signaling. *The Journal of Biological Chemistry*, 275(42), 32475–32481. <https://doi.org/10.1074/jbc.M005342200>

- Doble, B. W., Patel, S., Wood, G. A., Kockeritz, L. K., & Woodgett, J. R. (2007). Functional redundancy of GSK-3 α and GSK-3 β in Wnt/ β -catenin signaling shown by using an allelic series of embryonic stem cell lines. *Developmental Cell*, 12(6), 957–971. <https://doi.org/10.1016/j.devcel.2007.04.001>
- Doble, B. W., & Woodgett, J. R. (2003). GSK-3: Tricks of the trade for a multi-tasking kinase. *Journal of Cell Science*, 116(7), 1175–1186. <https://doi.org/10.1242/jcs.00384>
- Draczkowski, P., Tomaszuk, A., Halczuk, P., Strzemiński, M., Matosiuk, D., & Jozwiak, K. (2016). Determination of affinity and efficacy of acetylcholinesterase inhibitors using isothermal titration calorimetry. *Biochimica Et Biophysica Acta*, 1860(5), 967–974. <https://doi.org/10.1016/j.bbagen.2015.11.006>
- Dudev, T., Cowan, J. A., & Lim, C. (1999). Competitive Binding in Magnesium Coordination Chemistry: Water versus Ligands of Biological Interest. *Journal of the American Chemical Society*, 121(33), 7665–7673. <https://doi.org/10.1021/ja984470t>
- Dudev, T., & Lim, C. (2011). Competition between Li⁺ and Mg²⁺ in metalloproteins. Implications for lithium therapy. *Journal of the American Chemical Society*, 133(24), 9506–9515. <https://doi.org/10.1021/ja201985s>
- Eldar-Finkelman, H., & Martinez, A. (2011). GSK-3 Inhibitors: Preclinical and Clinical Focus on CNS. *Frontiers in Molecular Neuroscience*, 4, 32. <https://doi.org/10.3389/fnmol.2011.00032>
- Embi, N., Rylatt, D. B., & Cohen, P. (1980). Glycogen synthase kinase-3 from rabbit skeletal muscle. Separation from cyclic-AMP-dependent protein kinase and phosphorylase kinase. *European Journal of Biochemistry*, 107(2), 519–527.

- Entzian, C., & Schubert, T. (2016). Studying small molecule-aptamer interactions using MicroScale Thermophoresis (MST). *Methods (San Diego, Calif.)*, 97, 27–34.
<https://doi.org/10.1016/j.ymeth.2015.08.023>
- Falconer, R. J., Schuur, B., & Mittermaier, A. K. (2021). Applications of isothermal titration calorimetry in pure and applied research from 2016 to 2020. *Journal of Molecular Recognition: JMR*, 34(10), e2901. <https://doi.org/10.1002/jmr.2901>
- Fiol, C. J., Mahrenholz, A. M., Wang, Y., Roeske, R. W., & Roach, P. J. (1987). Formation of protein kinase recognition sites by covalent modification of the substrate. Molecular mechanism for the synergistic action of casein kinase II and glycogen synthase kinase 3. *The Journal of Biological Chemistry*, 262(29), 14042–14048.
- Fiol, C. J., Wang, A., Roeske, R. W., & Roach, P. J. (1990). Ordered multisite protein phosphorylation. Analysis of glycogen synthase kinase 3 action using model peptide substrates. *Journal of Biological Chemistry*, 265(11), 6061–6065.
[https://doi.org/10.1016/S0021-9258\(19\)39291-9](https://doi.org/10.1016/S0021-9258(19)39291-9)
- Flügel, D., Görlach, A., Michiels, C., & Kietzmann, T. (2007). Glycogen Synthase Kinase 3 Phosphorylates Hypoxia-Inducible Factor 1 α and Mediates Its Destabilization in a VHL-Independent Manner. *Molecular and Cellular Biology*, 27(9), 3253–3265.
<https://doi.org/10.1128/MCB.00015-07>
- Forstner, M., Berger, C., & Wallimann, T. (1999). Nucleotide binding to creatine kinase: An isothermal titration microcalorimetry study. *FEBS Letters*, 461(1–2), 111–114.
[https://doi.org/10.1016/s0014-5793\(99\)01431-3](https://doi.org/10.1016/s0014-5793(99)01431-3)
- Frame, S., & Cohen, P. (2001). GSK3 takes centre stage more than 20 years after its discovery. *The Biochemical Journal*, 359(Pt 1), 1–16. <https://doi.org/10.1042/0264-6021:3590001>

- Frasca, V. (2016). Using Isothermal Titration Calorimetry Techniques to Quantify Enzyme Kinetics. *Industrial Biotechnology*, 12(4), 207–211.
<https://doi.org/10.1089/ind.2016.29040.vfr>
- Fraser, E., Young, N., Dajani, R., Franca-Koh, J., Ryves, J., Williams, R. S. B., Yeo, M., Webster, M.-T., Richardson, C., Smalley, M. J., Pearl, L. H., Harwood, A., & Dale, T. C. (2002). Identification of the Axin and Frat binding region of glycogen synthase kinase-3. *The Journal of Biological Chemistry*, 277(3), 2176–2185.
<https://doi.org/10.1074/jbc.M109462200>
- Gao, C., Hölscher, C., Liu, Y., & Li, L. (2011). GSK3: A key target for the development of novel treatments for type 2 diabetes mellitus and Alzheimer disease. *Reviews in the Neurosciences*, 23(1), 1–11. <https://doi.org/10.1515/rns.2011.061>
- Gavagan, M., Fagnan, E., Speltz, E. B., & Zalatan, J. G. (2020). The Scaffold Protein Axin Promotes Signaling Specificity within the Wnt Pathway by Suppressing Competing Kinase Reactions. *Cell Systems*, 10(6), 515-525.e5.
<https://doi.org/10.1016/j.cels.2020.05.002>
- Gavagan, M., Jameson, N., & Zalatan, J. G. (2023). The Axin scaffold protects the kinase GSK3 β from cross-pathway inhibition. *eLife*, 12, e85444.
<https://doi.org/10.7554/eLife.85444>
- Ghai, R., Falconer, R. J., & Collins, B. M. (2012). Applications of isothermal titration calorimetry in pure and applied research—Survey of the literature from 2010. *Journal of Molecular Recognition: JMR*, 25(1), 32–52. <https://doi.org/10.1002/jmr.1167>
- Ginger, R. S., Dalton, E. C., Ryves, W. J., Fukuzawa, M., Williams, J. G., & Harwood, A. J. (2000). Glycogen synthase kinase-3 enhances nuclear export of a Dictyostelium STAT

- protein. *The EMBO Journal*, 19(20), 5483–5491.
<https://doi.org/10.1093/emboj/19.20.5483>
- Gitlin, M. (2016). Lithium side effects and toxicity: Prevalence and management strategies. *International Journal of Bipolar Disorders*, 4(1), 27. <https://doi.org/10.1186/s40345-016-0068-y>
- Godemann, R., Biernat, J., Mandelkow, E., & Mandelkow, E. M. (1999). Phosphorylation of tau protein by recombinant GSK-3 β : Pronounced phosphorylation at select Ser/Thr-Pro motifs but no phosphorylation at Ser262 in the repeat domain. *FEBS Letters*, 454(1–2), 157–164. [https://doi.org/10.1016/s0014-5793\(99\)00741-3](https://doi.org/10.1016/s0014-5793(99)00741-3)
- Hagedoorn, P.-L. (2022). Isothermal Titration Calorimetry in Biocatalysis. *Frontiers in Catalysis*, 2. <https://doi.org/10.3389/fctls.2022.906668>
- Hagen, T., Di Daniel, E., Culbert, A. A., & Reith, A. D. (2002). Expression and characterization of GSK-3 mutants and their effect on beta-catenin phosphorylation in intact cells. *The Journal of Biological Chemistry*, 277(26), 23330–23335.
<https://doi.org/10.1074/jbc.M201364200>
- Hanger, D. P., Hughes, K., Woodgett, J. R., Brion, J. P., & Anderton, B. H. (1992). Glycogen synthase kinase-3 induces Alzheimer's disease-like phosphorylation of tau: Generation of paired helical filament epitopes and neuronal localisation of the kinase. *Neuroscience Letters*, 147(1), 58–62. [https://doi.org/10.1016/0304-3940\(92\)90774-2](https://doi.org/10.1016/0304-3940(92)90774-2)
- Hanks, S. K., & Hunter, T. (1995). The eukaryotic protein kinase superfamily: Kinase (catalytic) domain structure and classification1. *The FASEB Journal*, 9(8), 576–596.
<https://doi.org/10.1096/fasebj.9.8.7768349>

- Hansen, L. D., Transtrum, M. K., Quinn, C., & Demarse, N. (2016). Enzyme-catalyzed and binding reaction kinetics determined by titration calorimetry. *Biochimica Et Biophysica Acta*, 1860(5), 957–966. <https://doi.org/10.1016/j.bbagen.2015.12.018>
- Harper, S., & Speicher, D. W. (2011). Purification of proteins fused to glutathione S-transferase. *Methods in Molecular Biology (Clifton, N.J.)*, 681, 259–280. https://doi.org/10.1007/978-1-60761-913-0_14
- Harris, T. K., & Keshwani, M. M. (2009). Chapter 7 Measurement of Enzyme Activity. In R. R. Burgess & M. P. Deutscher (Eds.), *Methods in Enzymology* (Vol. 463, pp. 57–71). Academic Press. [https://doi.org/10.1016/S0076-6879\(09\)63007-X](https://doi.org/10.1016/S0076-6879(09)63007-X)
- Hoeflich, K. P., Luo, J., Rubie, E. A., Tsao, M. S., Jin, O., & Woodgett, J. R. (2000). Requirement for glycogen synthase kinase-3 β in cell survival and NF- κ B activation. *Nature*, 406(6791), 86–90. <https://doi.org/10.1038/35017574>
- Honarmand Ebrahimi, K., Hagedoorn, P., Jacobs, D., & Hagen, W. R. (2015). Accurate label-free reaction kinetics determination using initial rate heat measurements. *Scientific Reports (Nature Publisher Group)*, 5, 16380. <https://doi.org/10.1038/srep16380>
- Hopkins, R., & Esposito, D. (2009). A rapid method for titrating baculovirus stocks using the Sf-9 Easy Titer cell line. *BioTechniques*, 47(3), 785–788. <https://doi.org/10.2144/000113238>
- Hughes, K., Nikolakaki, E., Plyte, S. E., Totty, N. F., & Woodgett, J. R. (1993). Modulation of the glycogen synthase kinase-3 family by tyrosine phosphorylation. *The EMBO Journal*, 12(2), 803–808. <https://doi.org/10.1002/j.1460-2075.1993.tb05715.x>
- Ikeda, S., Kishida, S., Yamamoto, H., Murai, H., Koyama, S., & Kikuchi, A. (1998). Axin, a negative regulator of the Wnt signaling pathway, forms a complex with GSK-3 β and

- beta-catenin and promotes GSK-3 β -dependent phosphorylation of beta-catenin. *The EMBO Journal*, 17(5), 1371–1384. <https://doi.org/10.1093/emboj/17.5.1371>
- Inoki, K., Ouyang, H., Zhu, T., Lindvall, C., Wang, Y., Zhang, X., Yang, Q., Bennett, C., Harada, Y., Stankunas, K., Wang, C., He, X., MacDougald, O. A., You, M., Williams, B. O., & Guan, K.-L. (2006). TSC2 Integrates Wnt and Energy Signals via a Coordinated Phosphorylation by AMPK and GSK3 to Regulate Cell Growth. *Cell*, 126(5), 955–968. <https://doi.org/10.1016/j.cell.2006.06.055>
- Jerabek-Willemsen, M., Wienken, C. J., Braun, D., Baaske, P., & Duhr, S. (2011). Molecular Interaction Studies Using Microscale Thermophoresis. *Assay and Drug Development Technologies*, 9(4), 342–353. <https://doi.org/10.1089/adt.2011.0380>
- Johnson, K. A., & Goody, R. S. (2011). The Original Michaelis Constant: Translation of the 1913 Michaelis-Menten Paper. *Biochemistry*, 50(39), 8264–8269. <https://doi.org/10.1021/bi201284u>
- Joep, R. S. (2003). Lithium and GSK-3: One inhibitor, two inhibitory actions, multiple outcomes. *Trends in Pharmacological Sciences*, 24(9), 441–443. [https://doi.org/10.1016/S0165-6147\(03\)00206-2](https://doi.org/10.1016/S0165-6147(03)00206-2)
- Joep, R. S., & Johnson, G. V. W. (2004). The glamour and gloom of glycogen synthase kinase-3. *Trends in Biochemical Sciences*, 29(2), 95–102. <https://doi.org/10.1016/j.tibs.2003.12.004>
- Juhaszova, M., Zorov, D. B., Yaniv, Y., Nuss, H. B., Wang, S., & Sollott, S. J. (2009). Role of glycogen synthase kinase-3 β in cardioprotection. *Circulation Research*, 104(11), 1240–1252. <https://doi.org/10.1161/CIRCRESAHA.109.197996>

- Kaidanovich-Beilin, O., & Woodgett, J. R. (2011). GSK-3: Functional Insights from Cell Biology and Animal Models. *Frontiers in Molecular Neuroscience*, 4, 40.
<https://doi.org/10.3389/fnmol.2011.00040>
- Kalidas, C., & Sangaranarayanan, M. V. (2023). Applications of Isothermal Calorimetry in the Study of Biochemical Reactions. In C. Kalidas & M. V. Sangaranarayanan (Eds.), *Biophysical Chemistry: Techniques and Applications* (pp. 375–385). Springer Nature Switzerland. https://doi.org/10.1007/978-3-031-37682-5_23
- Kane, J. F. (1995). Effects of rare codon clusters on high-level expression of heterologous proteins in *Escherichia coli*. *Current Opinion in Biotechnology*, 6(5), 494–500.
[https://doi.org/10.1016/0958-1669\(95\)80082-4](https://doi.org/10.1016/0958-1669(95)80082-4)
- Kim, D.-S., Qiao, L., Lee, K.-J., & Ko, K. (2015). Optimization of colorectal cancer vaccine candidate protein GA733-Fc expression in a baculovirus–insect cell system. *Entomological Research*, 45(1), 39–48. <https://doi.org/10.1111/1748-5967.12092>
- King, M. K., Pardo, M., Cheng, Y., Downey, K., Jope, R. S., & Beurel, E. (2014). Glycogen synthase kinase-3 inhibitors: Rescuers of cognitive impairments. *Pharmacology & Therapeutics*, 141(1), 1–12. <https://doi.org/10.1016/j.pharmthera.2013.07.010>
- Klein, P. S., & Melton, D. A. (1996). A molecular mechanism for the effect of lithium on development. *Proceedings of the National Academy of Sciences of the United States of America*, 93(16), 8455–8459. <https://doi.org/10.1073/pnas.93.16.8455>
- Knight, Z. A., & Shokat, K. M. (2005). Features of selective kinase inhibitors. *Chemistry & Biology*, 12(6), 621–637. <https://doi.org/10.1016/j.chembiol.2005.04.011>
- Kunick, C., Lauenroth, K., Wieking, K., Xie, X., Schultz, C., Gussio, R., Zaharevitz, D., Leost, M., Meijer, L., Weber, A., Jørgensen, F. S., & Lemcke, T. (2004). Evaluation and

- comparison of 3D-QSAR CoMSIA models for CDK1, CDK5, and GSK-3 inhibition by paullones. *Journal of Medicinal Chemistry*, 47(1), 22–36.
<https://doi.org/10.1021/jm0308904>
- Kwiatkowski, A. P., Huang, C. Y., & King, M. M. (1990). Kinetic mechanism of the type II calmodulin-dependent protein kinase: Studies of the forward and reverse reactions and observation of apparent rapid-equilibrium ordered binding. *Biochemistry*, 29(1), 153–159. <https://doi.org/10.1021/bi00453a019>
- Lauretti, E., Dincer, O., & Praticò, D. (2020). Glycogen synthase kinase-3 signaling in Alzheimer's disease. *Biochimica Et Biophysica Acta. Molecular Cell Research*, 1867(5), 118664. <https://doi.org/10.1016/j.bbamcr.2020.118664>
- Li, L., Yuan, H., Weaver, C. D., Mao, J., Farr, G. H., Sussman, D. J., Jonkers, J., Kimelman, D., & Wu, D. (1999). Axin and Frat1 interact with dvl and GSK, bridging Dvl to GSK in Wnt-mediated regulation of LEF-1. *The EMBO Journal*, 18(15), 4233–4240.
<https://doi.org/10.1093/emboj/18.15.4233>
- Liang, S. H., Chen, J. M., Normandin, M. D., Chang, J. S., Chang, G. C., Taylor, C. K., Trapa, P., Plummer, M. S., Para, K. S., Conn, E. L., Lopresti-Morrow, L., Lanyon, L. F., Cook, J. M., Richter, K. E. G., Nolan, C. E., Schachter, J. B., Janat, F., Che, Y., Shanmugasundaram, V., ... Vasdev, N. (2016). Discovery of a Highly Selective Glycogen Synthase Kinase-3 Inhibitor (PF-04802367) That Modulates Tau Phosphorylation in the Brain: Translation for PET Neuroimaging. *Angewandte Chemie (International Ed. in English)*, 55(33), 9601–9605. <https://doi.org/10.1002/anie.201603797>

- Liang, Y. (2008). Applications of isothermal titration calorimetry in protein science. *Acta Biochimica Et Biophysica Sinica*, 40(7), 565–576. <https://doi.org/10.1111/j.1745-7270.2008.00437.x>
- Lim, R. (2022). Characterization of the Isothermal Titration Calorimetry Single Injection Method Using T4 Polynucleotide Kinase as a Model System for Kinases. *UNLV Theses, Dissertations, Professional Papers, and Capstones*. <https://digitalscholarship.unlv.edu/thesesdissertations/4601>
- Lim, R. C., De Silva, B., Park, J. H., Hodge, V. F., & Gary, R. K. (2020). Aqueous solubility of beryllium(II) at physiological pH: Effects of buffer composition and counterions. *Preparative Biochemistry & Biotechnology*, 50(6), 585–591. <https://doi.org/10.1080/10826068.2020.1719514>
- Lonhienne, T. G. A., Reilly, P. E. B., & Winzor, D. J. (2003). Further evidence for the reliance of catalysis by rabbit muscle pyruvate kinase upon isomerization of the ternary complex between enzyme and products. *Biophysical Chemistry*, 104(1), 189–198. [https://doi.org/10.1016/S0301-4622\(02\)00366-6](https://doi.org/10.1016/S0301-4622(02)00366-6)
- Lopez-zavala, A. A., Sotelo-mundo, R. R., Hernandez-flores, J. M., Lugo-sanchez, M. E., Sugich-miranda, R., & Garcia-orozco, K. D. (2016). Arginine kinase shows nucleoside diphosphate kinase-like activity toward deoxythymidine diphosphate. *Journal of Bioenergetics and Biomembranes*, 48(3), 301–308. <https://doi.org/10.1007/s10863-016-9660-1>
- L. Scott, B., Mark McCleskey, T., Chaudhary, A., Hong-Geller, E., & Gnanakaran, S. (2008). The bioinorganic chemistry and associated immunology of chronic beryllium disease. *Chemical Communications*, 0(25), 2837–2847. <https://doi.org/10.1039/B718746G>

- Lu, S.-Y., Jiang, Y.-J., Zou, J.-W., & Wu, T.-X. (2011). Molecular modeling and molecular dynamics simulation studies of the GSK3 β /ATP/substrate complex: Understanding the unique P+4 primed phosphorylation specificity for GSK3 β substrates. *Journal of Chemical Information and Modeling*, 51(5), 1025–1036.
<https://doi.org/10.1021/ci100493j>
- Ly, P. T. T., Wu, Y., Zou, H., Wang, R., Zhou, W., Kinoshita, A., Zhang, M., Yang, Y., Cai, F., Woodgett, J., & Song, W. (2013). Inhibition of GSK3 β -mediated BACE1 expression reduces Alzheimer-associated phenotypes. *The Journal of Clinical Investigation*, 123(1), 224–235. <https://doi.org/10.1172/JCI64516>
- Mandelkow, E. M., Drewes, G., Biernat, J., Gustke, N., Van Lint, J., Vandenheede, J. R., & Mandelkow, E. (1992). Glycogen synthase kinase-3 and the Alzheimer-like state of microtubule-associated protein tau. *FEBS Letters*, 314(3), 315–321.
[https://doi.org/10.1016/0014-5793\(92\)81496-9](https://doi.org/10.1016/0014-5793(92)81496-9)
- Mao, Y., Yu, L., Yang, R., Qu, L., & Harrington, P. de B. (2015). A novel method for the study of molecular interaction by using microscale thermophoresis. *Talanta*, 132, 894–901.
<https://doi.org/10.1016/j.talanta.2014.09.038>
- Maqbool, M., Mobashir, M., & Hoda, N. (2016). Pivotal role of glycogen synthase kinase-3: A therapeutic target for Alzheimer's disease. *European Journal of Medicinal Chemistry*, 107, 63–81. <https://doi.org/10.1016/j.ejmech.2015.10.018>
- Marmol, F. (2008). Lithium: Bipolar disorder and neurodegenerative diseases Possible cellular mechanisms of the therapeutic effects of lithium. *Progress in Neuro-Psychopharmacology & Biological Psychiatry*, 32(8), 1761–1771.
<https://doi.org/10.1016/j.pnpbp.2008.08.012>

- Mazzei, L., Ciurli, S., & Zambelli, B. (2014). Hot biological catalysis: Isothermal titration calorimetry to characterize enzymatic reactions. *Journal of Visualized Experiments: JoVE*, 86, 51487. <https://doi.org/10.3791/51487>
- McCubrey, J. A., Steelman, L. S., Bertrand, F. E., Davis, N. M., Sokolosky, M., Abrams, S. L., Montalto, G., D'Assoro, A. B., Libra, M., Nicoletti, F., Maestro, R., Basecke, J., Rakus, D., Gizak, A., Demidenko, Z., Cocco, L., Martelli, A. M., & Cervello, M. (2014). GSK-3 as potential target for therapeutic intervention in cancer. *Oncotarget*, 5(10), 2881–2911.
- Meares, G. P., & Jope, R. S. (2007). Resolution of the nuclear localization mechanism of glycogen synthase kinase-3: Functional effects in apoptosis. *The Journal of Biological Chemistry*, 282(23), 16989–17001. <https://doi.org/10.1074/jbc.M700610200>
- Mederos, A., Domínguez, S., Chinae, E., Brito, F., & Cecconi, F. (2001). REVIEW: NEW ADVANCES IN THE COORDINATION CHEMISTRY OF THE BERYLLIUM(II). *Journal of Coordination Chemistry*. <https://doi.org/10.1080/00958970108022906>
- Metcalf, C., & Bienz, M. (2011). Inhibition of GSK3 by Wnt signalling—Two contrasting models. *Journal of Cell Science*, 124(Pt 21), 3537–3544. <https://doi.org/10.1242/jcs.091991>
- Mudireddy, S. R., Abdul, A. R. M., Gorjala, P., & Gary, R. K. (2014). Beryllium is an inhibitor of cellular GSK-3 β that is 1,000-fold more potent than lithium. *Biometals: An International Journal on the Role of Metal Ions in Biology, Biochemistry, and Medicine*, 27(6), 1203–1216. <https://doi.org/10.1007/s10534-014-9783-y>
- Murai, H., Okazaki, M., & Kikuchi, A. (1996). Tyrosine dephosphorylation of glycogen synthase kinase-3 is involved in its extracellular signal-dependent inactivation. *FEBS Letters*, 392(2), 153–160. [https://doi.org/10.1016/0014-5793\(96\)00806-x](https://doi.org/10.1016/0014-5793(96)00806-x)

- Nagar, S., Argikar, U. A., & Tweedie, D. J. (2014). Enzyme kinetics in drug metabolism: Fundamentals and applications. *Methods in Molecular Biology (Clifton, N.J.)*, 1113, 1–6. https://doi.org/10.1007/978-1-62703-758-7_1
- Naglav, D., Buchner, M. R., Bendt, G., Kraus, F., & Schulz, S. (2016). Off the Beaten Track-A Hitchhiker's Guide to Beryllium Chemistry. *Angewandte Chemie (International Ed. in English)*, 55(36), 10562–10576. <https://doi.org/10.1002/anie.201601809>
- Ng, S. S., Mahmoudi, T., Danenberg, E., Bejaoui, I., de Lau, W., Korswagen, H. C., Schutte, M., & Clevers, H. (2009). Phosphatidylinositol 3-kinase signaling does not activate the wnt cascade. *The Journal of Biological Chemistry*, 284(51), 35308–35313. <https://doi.org/10.1074/jbc.M109.078261>
- Olsen, S. N. (2006). Applications of isothermal titration calorimetry to measure enzyme kinetics and activity in complex solutions. *Thermochimica Acta*, 448(1), 12–18. <https://doi.org/10.1016/j.tca.2006.06.019>
- Olsher, Uriel., Izatt, R. M., Bradshaw, J. S., & Dalley, N. Kent. (1991). Coordination chemistry of lithium ion: A crystal and molecular structure review. *Chemical Reviews*, 91(2), 137–164. <https://doi.org/10.1021/cr00002a003>
- Oruch, R., Elderbi, M. A., Khattab, H. A., Pryme, I. F., & Lund, A. (2014). Lithium: A review of pharmacology, clinical uses, and toxicity. *European Journal of Pharmacology*, 740, 464–473. <https://doi.org/10.1016/j.ejphar.2014.06.042>
- Palmer, A., Begres, B. N., Van Houten, J. M., Snider, M. J., & Fraga, D. (2013). Characterization of a putative oomycete taurocyamine kinase: Implications for the evolution of the phosphagen kinase family. *Comparative Biochemistry and Physiology. Part B*,

- Biochemistry & Molecular Biology*, 166(3–4), 173–181.
<https://doi.org/10.1016/j.cbpb.2013.08.003>
- Pap, M., & Cooper, G. M. (1998). Role of glycogen synthase kinase-3 in the phosphatidylinositol 3-Kinase/Akt cell survival pathway. *The Journal of Biological Chemistry*, 273(32), 19929–19932. <https://doi.org/10.1074/jbc.273.32.19929>
- Parker, P. J., Caudwell, F. B., & Cohen, P. (1983). Glycogen Synthase from Rabbit Skeletal Muscle; Effect of Insulin on the State of phosphorylation of the Seven Phosphoserine Residues in vivo. *European Journal of Biochemistry*, 130(1), 227–234.
<https://doi.org/10.1111/j.1432-1033.1983.tb07140.x>
- Patwardhan, P., & Miller, W. T. (2007). Processive phosphorylation: Mechanism and biological importance. *Cellular Signalling*, 19(11), 2218–2226.
<https://doi.org/10.1016/j.cellsig.2007.06.006>
- Pemble, H., Kumar, P., van Haren, J., & Wittmann, T. (2017). GSK3-mediated CLASP2 phosphorylation modulates kinetochore dynamics. *Journal of Cell Science*, 130(8), 1404–1412. <https://doi.org/10.1242/jcs.194662>
- Pierce, M. M., Raman, C. S., & Nall, B. T. (1999). Isothermal Titration Calorimetry of Protein–Protein Interactions. *Methods*, 19(2), 213–221. <https://doi.org/10.1006/meth.1999.0852>
- Primot, A., Baratte, B., Gompel, M., Borgne, A., Liabeuf, S., Romette, J. L., Jho, E. H., Costantini, F., & Meijer, L. (2000). Purification of GSK-3 by affinity chromatography on immobilized axin. *Protein Expression and Purification*, 20(3), 394–404.
<https://doi.org/10.1006/prep.2000.1321>

- Quinn, C. F., & Hansen, L. D. (2019). Enzyme Kinetics Determined by Single-Injection Isothermal Titration Calorimetry. *Methods in Molecular Biology (Clifton, N.J.), 1964*, 241–249. https://doi.org/10.1007/978-1-4939-9179-2_17
- Rankin, C. A., Sun, Q., & Gamblin, T. C. (2007). Tau phosphorylation by GSK-3 β promotes tangle-like filament morphology. *Molecular Neurodegeneration*, 2, 12. <https://doi.org/10.1186/1750-1326-2-12>
- Richeldi, L., Sorrentino, R., & Saltini, C. (1993). HLA-DPB1 glutamate 69: A genetic marker of beryllium disease. *Science (New York, N.Y.)*, 262(5131), 242–244. <https://doi.org/10.1126/science.8105536>
- Riegel, K., Vijayarangakannan, P., Kechagioglou, P., Bogucka, K., & Rajalingam, K. (2022). Recent advances in targeting protein kinases and pseudokinases in cancer biology. *Frontiers in Cell and Developmental Biology*, 10, 942500. <https://doi.org/10.3389/fcell.2022.942500>
- Rohatgi, N., Guðmundsson, S., & Rolfsson, Ó. (2015). Kinetic analysis of gluconate phosphorylation by human gluconokinase using isothermal titration calorimetry. *FEBS Letters*, 589(23), 3548–3555. <https://doi.org/10.1016/j.febslet.2015.10.024>
- Roskoski, R. (2015). A historical overview of protein kinases and their targeted small molecule inhibitors. *Pharmacological Research*, 100, 1–23. <https://doi.org/10.1016/j.phrs.2015.07.010>
- Rylatt, D. B., Aitken, A., Bilham, T., Condon, G. D., Embi, N., & Cohen, P. (1980). Glycogen synthase from rabbit skeletal muscle. Amino acid sequence at the sites phosphorylated by glycogen synthase kinase-3, and extension of the N-terminal sequence containing the site

- phosphorylated by phosphorylase kinase. *European Journal of Biochemistry*, 107(2), 529–537.
- Ryves, W. J., Dajani, R., Pearl, L., & Harwood, A. J. (2002). Glycogen synthase kinase-3 inhibition by lithium and beryllium suggests the presence of two magnesium binding sites. *Biochemical and Biophysical Research Communications*, 290(3), 967–972.
<https://doi.org/10.1006/bbrc.2001.6305>
- Ryves, W. J., Fryer, L., Dale, T., & Harwood, A. J. (1998). An Assay for Glycogen Synthase Kinase 3 (GSK-3) for Use in Crude Cell Extracts. *Analytical Biochemistry*, 264(1), 124–127. <https://doi.org/10.1006/abio.1998.2832>
- Ryves, W. J., & Harwood, A. J. (2001). Lithium inhibits glycogen synthase kinase-3 by competition for magnesium. *Biochemical and Biophysical Research Communications*, 280(3), 720–725. <https://doi.org/10.1006/bbrc.2000.4169>
- Saarinen, M. A., Troutner, K. A., Gladden, S. G., Mitchell-Logean, C. M., & Murhammer, D. W. (1999). Recombinant protein synthesis in *Trichoplusia ni* BTI-Tn-5B1-4 insect cell aggregates. *Biotechnology and Bioengineering*, 63(5), 612–617.
[https://doi.org/10.1002/\(SICI\)1097-0290\(19990605\)63:5<612::AID-BIT11>3.0.CO;2-C](https://doi.org/10.1002/(SICI)1097-0290(19990605)63:5<612::AID-BIT11>3.0.CO;2-C)
- Salazar, C., & Höfer, T. (2009). Multisite protein phosphorylation – from molecular mechanisms to kinetic models. *The FEBS Journal*, 276(12), 3177–3198.
<https://doi.org/10.1111/j.1742-4658.2009.07027.x>
- Sami, F., Gary, R. K., Fang, Y., & Sharma, S. (2016). Site-directed mutants of human RECQ1 reveal functional importance of the zinc binding domain. *Mutation Research*, 790, 8–18.
<https://doi.org/10.1016/j.mrfmmm.2016.05.005>

- Sayas, C. L., & Ávila, J. (2021). GSK-3 and Tau: A Key Duet in Alzheimer's Disease. *Cells*, 10(4), 721. <https://doi.org/10.3390/cells10040721>
- Schwartz, P. A., & Murray, B. W. (2011). Protein kinase biochemistry and drug discovery. *Bioorganic Chemistry*, 39(5–6), 192–210. <https://doi.org/10.1016/j.bioorg.2011.07.004>
- Schweitzer, G. K., & Pesterfield, L. L. (2010). *The Aqueous Chemistry of the Elements*. Oxford University Press. <https://doi.org/10.1093/oso/9780195393354.001.0001>
- Seibert, E., & Tracy, T. S. (2014). Fundamentals of enzyme kinetics. *Methods in Molecular Biology (Clifton, N.J.)*, 1113, 9–22. https://doi.org/10.1007/978-1-62703-758-7_2
- Shao, W., Sharma, R., Clausen, M. H., & Scheller, H. V. (2020). Microscale thermophoresis as a powerful tool for screening glycosyltransferases involved in cell wall biosynthesis. *Plant Methods*, 16, 99. <https://doi.org/10.1186/s13007-020-00641-1>
- Shaw, M., Cohen, P., & Alessi, D. R. (1997). Further evidence that the inhibition of glycogen synthase kinase-3 β by IGF-1 is mediated by PDK1/PKB-induced phosphorylation of Ser-9 and not by dephosphorylation of Tyr-216. *FEBS Letters*, 416(3), 307–311. [https://doi.org/10.1016/s0014-5793\(97\)01235-0](https://doi.org/10.1016/s0014-5793(97)01235-0)
- Shimura, T. (2011). Acquired radioresistance of cancer and the AKT/GSK3 β /cyclin D1 overexpression cycle. *Journal of Radiation Research*, 52(5), 539–544. <https://doi.org/10.1269/jrr.11098>
- Snitow, M. E., Bhansali, R. S., & Klein, P. S. (2021). Lithium and Therapeutic Targeting of GSK-3. *Cells*, 10(2), 255. <https://doi.org/10.3390/cells10020255>
- Srinivasan, B. (2023). A guide to enzyme kinetics in early drug discovery. *The FEBS Journal*, 290(9), 2292–2305. <https://doi.org/10.1111/febs.16404>

- Stambolic, V., Ruel, L., & Woodgett, J. R. (1996). Lithium inhibits glycogen synthase kinase-3 activity and mimics wingless signalling in intact cells. *Current Biology: CB*, 6(12), 1664–1668. [https://doi.org/10.1016/s0960-9822\(02\)70790-2](https://doi.org/10.1016/s0960-9822(02)70790-2)
- Stambolic, V., & Woodgett, J. R. (1994). Mitogen inactivation of glycogen synthase kinase-3 beta in intact cells via serine 9 phosphorylation. *Biochemical Journal*, 303(Pt 3), 701–704.
- Stamos, J. L., Chu, M. L.-H., Enos, M. D., Shah, N., & Weis, W. I. (2014). Structural basis of GSK-3 inhibition by N-terminal phosphorylation and by the Wnt receptor LRP6. *eLife*, 3, e01998. <https://doi.org/10.7554/eLife.01998>
- Stamos, J. L., & Weis, W. I. (2013). The β -Catenin Destruction Complex. *Cold Spring Harbor Perspectives in Biology*, 5(1), a007898. <https://doi.org/10.1101/cshperspect.a007898>
- Streeter, J., Schickling, B. M., Jiang, S., Stanic, B., Thiel, W. H., Gakhar, L., Houtman, J. C. D., & Miller, F. J. (2014). Phosphorylation of Nox1 regulates association with NoxA1 activation domain. *Circulation Research*, 115(11), 911–918. <https://doi.org/10.1161/CIRCRESAHA.115.304267>
- Su, H., & Xu, Y. (2018). Application of ITC-Based Characterization of Thermodynamic and Kinetic Association of Ligands With Proteins in Drug Design. *Frontiers in Pharmacology*, 9, 1133. <https://doi.org/10.3389/fphar.2018.01133>
- Sun, B., Wibowo, D., Middelberg, A. P. J., & Zhao, C.-X. (2018). Cost-effective downstream processing of recombinantly produced pexiganan peptide and its antimicrobial activity. *AMB Express*, 8, 6. <https://doi.org/10.1186/s13568-018-0541-3>

- SUN, H., JIANG, Y.-J., YU, Q.-S., & GAO, H. (2011). Molecular Dynamics Simulations on the Role of Structural Mg²⁺ Ions in Phosphoryl Transfer Catalyzed by GSK-3 β . *Acta Physico-Chimica Sinica*, 27(1), 207–212.
- Sutherland, C. (2011). What Are the bona fide GSK3 Substrates? *International Journal of Alzheimer's Disease*, 2011, 505607. <https://doi.org/10.4061/2011/505607>
- Sutherland, C., Leighton, I. A., & Cohen, P. (1993). Inactivation of glycogen synthase kinase-3 beta by phosphorylation: New kinase connections in insulin and growth-factor signalling. *The Biochemical Journal*, 296 (Pt 1)(Pt 1), 15–19. <https://doi.org/10.1042/bj2960015>
- Taelman, V. F., Dobrowolski, R., Plouhinec, J.-L., Fuentealba, L. C., Vorwald, P. P., Gumper, I., Sabatini, D. D., & De Robertis, E. M. (2010). Wnt signaling requires sequestration of glycogen synthase kinase 3 inside multivesicular endosomes. *Cell*, 143(7), 1136–1148. <https://doi.org/10.1016/j.cell.2010.11.034>
- Takahashi-Yanaga, F. (2013). Activator or inhibitor? GSK-3 as a new drug target. *Biochemical Pharmacology*, 86(2), 191–199. <https://doi.org/10.1016/j.bcp.2013.04.022>
- Tejeda-Muñoz, N., González-Aguilar, H., Santoyo-Ramos, P., Castañeda-Patlán, M. C., & Robles-Flores, M. (2016). Glycogen Synthase Kinase 3 β Is Positively Regulated by Protein Kinase C ζ -Mediated Phosphorylation Induced by Wnt Agonists. *Molecular and Cellular Biology*, 36(5), 731–741. <https://doi.org/10.1128/MCB.00828-15>
- ter Haar, E., Coll, J. T., Austen, D. A., Hsiao, H. M., Swenson, L., & Jain, J. (2001). Structure of GSK3beta reveals a primed phosphorylation mechanism. *Nature Structural Biology*, 8(7), 593–596. <https://doi.org/10.1038/89624>
- Thomas, G. M., Frame, S., Goedert, M., Nathke, I., Polakis, P., & Cohen, P. (1999). A GSK3-binding peptide from FRAT1 selectively inhibits the GSK3-catalysed phosphorylation of

- axin and beta-catenin. *FEBS Letters*, 458(2), 247–251. [https://doi.org/10.1016/s0014-5793\(99\)01161-8](https://doi.org/10.1016/s0014-5793(99)01161-8)
- Thornton, T. M., Pedraza-Alva, G., Deng, B., Wood, C. D., Aronshtam, A., Clements, J. L., Sabio, G., Davis, R. J., Matthews, D. E., Doble, B., & Rincon, M. (2008). Phosphorylation by p38 MAPK as an Alternative Pathway for GSK3 β Inactivation. *Science (New York, N.Y.)*, 320(5876), 667–670. <https://doi.org/10.1126/science.1156037>
- Todd, M. J., & Gomez, J. (2001). Enzyme kinetics determined using calorimetry: A general assay for enzyme activity? *Analytical Biochemistry*, 296(2), 179–187. <https://doi.org/10.1006/abio.2001.5218>
- Transtrum, M. K., Hansen, L. D., & Quinn, C. (2015). Enzyme kinetics determined by single-injection isothermal titration calorimetry. *Methods (San Diego, Calif.)*, 76, 194–200. <https://doi.org/10.1016/j.ymeth.2014.12.003>
- Twomey, C., & McCarthy, J. V. (2006). Presenilin-1 is an unprimed glycogen synthase kinase-3 β substrate. *FEBS Letters*, 580(17), 4015–4020. <https://doi.org/10.1016/j.febslet.2006.06.035>
- Uemura, K., Kuzuya, A., Shimozone, Y., Aoyagi, N., Ando, K., Shimohama, S., & Kinoshita, A. (2007). GSK3 β Activity Modifies the Localization and Function of Presenilin 1*. *Journal of Biological Chemistry*, 282(21), 15823–15832. <https://doi.org/10.1074/jbc.M610708200>
- Valvezan, A. J., & Klein, P. S. (2012). GSK-3 and Wnt Signaling in Neurogenesis and Bipolar Disorder. *Frontiers in Molecular Neuroscience*, 5. <https://doi.org/10.3389/fnmol.2012.00001>

- Velazquez-Campoy, A., Leavitt, S. A., & Freire, E. (2015). Characterization of Protein-Protein Interactions by Isothermal Titration Calorimetry. In C. L. Meyerkord & H. Fu (Eds.), *Protein-Protein Interactions* (Vol. 1278, pp. 183–204). Springer New York.
https://doi.org/10.1007/978-1-4939-2425-7_11
- Wang, Q. M., Fiol, C. J., DePaoli-Roach, A. A., & Roach, P. J. (1994). Glycogen synthase kinase-3 beta is a dual specificity kinase differentially regulated by tyrosine and serine/threonine phosphorylation. *The Journal of Biological Chemistry*, 269(20), 14566–14574.
- Wang, Y., Guan, J., Di Trani, J. M., Auclair, K., & Mittermaier, A. K. (2019). Inhibition and Activation of Kinases by Reaction Products: A Reporter-Free Assay. *Analytical Chemistry*, 91(18), 11803–11811. <https://doi.org/10.1021/acs.analchem.9b02456>
- Wang, Y., Hanrahan, G., Azar, F. A., & Mittermaier, A. (2022). Binding interactions in a kinase active site modulate background ATP hydrolysis. *Biochimica Et Biophysica Acta. Proteins and Proteomics*, 1870(1), 140720. <https://doi.org/10.1016/j.bbapap.2021.140720>
- Wang, Y., & Roach, P. J. (1993). Inactivation of rabbit muscle glycogen synthase by glycogen synthase kinase-3. Dominant role of the phosphorylation of Ser-640 (site-3a). *The Journal of Biological Chemistry*, 268(32), 23876–23880.
- Wang, Y., Wach, J.-Y., Sheehan, P., Zhong, C., Zhan, C., Harris, R., Almo, S. C., Bishop, J., Haggarty, S. J., Ramek, A., Berry, K. N., O’Herin, C., Koehler, A. N., Hung, A. W., & Young, D. W. (2016). Diversity-Oriented Synthesis as a Strategy for Fragment Evolution against GSK3 β . *ACS Medicinal Chemistry Letters*, 7(9), 852–856.
<https://doi.org/10.1021/acsmedchemlett.6b00230>

- Wang, Y., Wang, G., Moitessier, N., & Mittermaier, A. K. (2020). Enzyme Kinetics by Isothermal Titration Calorimetry: Allostery, Inhibition, and Dynamics. *Frontiers in Molecular Biosciences*, 7, 583826. <https://doi.org/10.3389/fmolb.2020.583826>
- Ward, W. H. J., & Holdgate, G. A. (2001). 7 Isothermal Titration Calorimetry in Drug Discovery. In F. D. King & A. W. Oxford (Eds.), *Progress in Medicinal Chemistry* (Vol. 38, pp. 309–376). Elsevier. [https://doi.org/10.1016/S0079-6468\(08\)70097-3](https://doi.org/10.1016/S0079-6468(08)70097-3)
- Wei, J., Wang, J., Zhang, J., Yang, J., Wang, G., & Wang, Y. (2022). Development of inhibitors targeting glycogen synthase kinase-3 β for human diseases: Strategies to improve selectivity. *European Journal of Medicinal Chemistry*, 236, 114301. <https://doi.org/10.1016/j.ejmech.2022.114301>
- Wharton, C. W., & Eisenthal, R. (1981). Simple Enzyme Kinetics. In C. W. Wharton & R. Eisenthal (Eds.), *Molecular Enzymology* (pp. 73–98). Springer US. https://doi.org/10.1007/978-1-4615-8532-9_4
- Wickham, T. J., Davis, T., Granados, R. R., Shuler, M. L., & Wood, H. A. (1992). Screening of insect cell lines for the production of recombinant proteins and infectious virus in the baculovirus expression system. *Biotechnology Progress*, 8(5), 391–396. <https://doi.org/10.1021/bp00017a003>
- Wickham, T. J., Nemerow, G. R., Wood, H. Az., & Shuler, M. L. (1995). Comparison of Different Cell Lines for the Production of Recombinant Baculovirus Proteins. In C. D. Richardson (Ed.), *Baculovirus Expression Protocols* (pp. 385–395). Humana Press. <https://doi.org/10.1385/0-89603-272-8:385>

- Wiseman, T., Williston, S., Brandts, J. F., & Lin, L. N. (1989). Rapid measurement of binding constants and heats of binding using a new titration calorimeter. *Analytical Biochemistry*, 179(1), 131–137. [https://doi.org/10.1016/0003-2697\(89\)90213-3](https://doi.org/10.1016/0003-2697(89)90213-3)
- Wolf, F. I., & Cittadini, A. (2003). Chemistry and biochemistry of magnesium. *Molecular Aspects of Medicine*, 24(1–3), 3–9. [https://doi.org/10.1016/s0098-2997\(02\)00087-0](https://doi.org/10.1016/s0098-2997(02)00087-0)
- Woodgett, J. R. (1990). Molecular cloning and expression of glycogen synthase kinase-3/factor A. *The EMBO Journal*, 9(8), 2431–2438.
- Wood-Kaczmar, A., Kraus, M., Ishiguro, K., Philpott, K. L., & Gordon-Weeks, P. R. (2009). An alternatively spliced form of glycogen synthase kinase-3 β is targeted to growing neurites and growth cones. *Molecular and Cellular Neurosciences*, 42(3), 184–194. <https://doi.org/10.1016/j.mcn.2009.07.002>
- Yamamoto, H., Kishida, S., Kishida, M., Ikeda, S., Takada, S., & Kikuchi, A. (1999). Phosphorylation of axin, a Wnt signal negative regulator, by glycogen synthase kinase-3 β regulates its stability. *The Journal of Biological Chemistry*, 274(16), 10681–10684. <https://doi.org/10.1074/jbc.274.16.10681>
- Yang, L., & Yuan, Z. (1999). Determination of dissociation constants of amino acids by capillary zone electrophoresis. *Electrophoresis*, 20(14), 2877–2883. [https://doi.org/10.1002/\(SICI\)1522-2683\(19991001\)20:14<2877::AID-ELPS2877>3.0.CO;2-Q](https://doi.org/10.1002/(SICI)1522-2683(19991001)20:14<2877::AID-ELPS2877>3.0.CO;2-Q)
- Yoshimura, T., Kawano, Y., Arimura, N., Kawabata, S., Kikuchi, A., & Kaibuchi, K. (2005). GSK-3 β regulates phosphorylation of CRMP-2 and neuronal polarity. *Cell*, 120(1), 137–149. <https://doi.org/10.1016/j.cell.2004.11.012>

- Zhang, F., Phiel, C. J., Spece, L., Gurvich, N., & Klein, P. S. (2003). Inhibitory phosphorylation of glycogen synthase kinase-3 (GSK-3) in response to lithium. Evidence for autoregulation of GSK-3. *The Journal of Biological Chemistry*, 278(35), 33067–33077.
<https://doi.org/10.1074/jbc.M212635200>
- Zhou, B. P., Deng, J., Xia, W., Xu, J., Li, Y. M., Gunduz, M., & Hung, M.-C. (2004). Dual regulation of Snail by GSK-3 β -mediated phosphorylation in control of epithelial–mesenchymal transition. *Nature Cell Biology*, 6(10), 931–940.
<https://doi.org/10.1038/ncb1173>

Curriculum Vitae

Bhagya De Silva

wabnilu@gmail.com

Education

Master of Science in Biochemistry

Kansas State University, KS

August 2015

Bachelor of Science in Biochemistry and Molecular Biology

University of Colombo, Sri Lanka

November 2011

Publications

Lim, R. C., De Silva, B., Park, J. H., Hodge, V. F., & Gary, R. K. (2020). Aqueous solubility of beryllium (II) at physiological pH: effects of buffer composition and counterions. *Preparative Biochemistry & Biotechnology*, 50(6), 585–591. <https://doi.org/10.1080/10826068.2020.1719514>

Abdul, A. U. R. M., De Silva, B., & Gary, R. K. (2018). The GSK3 kinase inhibitor lithium produces unexpected hyperphosphorylation of β -catenin, a GSK3 substrate, in human glioblastoma cells. *Biology Open*. <https://doi.org/10.1242/bio.030874>

Adhikari, B., De Silva, B., Molina, J. A., Allen, A., Peck, S. H., & Lee, S. Y. (2019). Neuronal ceroid lipofuscinosis-related ER membrane protein CLN8 regulates PP2A activity and ceramide levels. *Biochimica et Biophysica Acta (BBA) - Molecular Basis of Disease*, 1865(2), 322–328. <https://doi.org/10.1016/j.bbadis.2018.11.011>

De Silva, B., Adams, J., & Lee, S. Y. (2015). Proteolytic processing of the neuronal ceroid lipofuscinosis-related lysosomal protein CLN5. *Experimental Cell Research*, 338(1), 45–53. <https://doi.org/10.1016/j.yexcr.2015.08.021>

Abstracts and Presentations

De Silva, B., Rattanasopa, C., Kleiger, G., Gary, R.K. (2023, August). Kinetic characterization of glycogen synthase kinase 3 β (GSK3 β) via isothermal titration calorimetry. Poster presented at the American Chemical Society Fall National Meeting, San Francisco, CA, Division of Biological Chemistry.

De Silva, B., & Gary, R.K. (2018, April). Preferential interaction of Beryllium ion with carboxylate-rich peptides. Poster session presented at the Annual National Meeting of the American Society for Biochemistry and Molecular Biology, San Diego, CA.

De Silva, B., & Lee, S. Y. (2015, January). Identifying interacting proteins and the functional role of CLN8, a neurodegenerative disorder-related protein. Paper presented at the 13th K-INBRE Symposium, Topeka, KS.

Selected Awards and Fellowships

Summer Doctoral Research Fellowship – Graduate College, University of Nevada, Las Vegas (2023 – 2019, 2017)

Love of Learning Award – Phi Kappa Phi (2023, 2020, 2018)

College of Science Scholarship (Wolzinger Family Research Science Scholarship) – University of Nevada, Las Vegas (2020)

Outstanding Graduate Teaching Assistant Award (First place award) – University of Nevada, Las Vegas (2020)

Research Foundation Scholarship – Kansas State University, KS (2013 – 2015)

Teaching Experience

Graduate Teaching Assistant (Organic Chemistry Lab) – University of Nevada, Las Vegas (2015 – 2024)

Graduate Teaching Assistant (Organic and Biochemistry Lab) – Kansas State University (2013 – 2015)

Academic Outreach and Mentorship

Resident Scientist (Resident Scientists-in-Schools Program with STEM Teacher Development Academy) – College of Sciences, University of Nevada, Las Vegas

(2022 – 2023)

Graduate Student Mentor (Grad Rebel Advantage Program) – Graduate College, University of Nevada, Las Vegas

(2020 – 2019)

Graduate Student Mentor (Louis Stokes Alliance for Minority Participation (LSAMP) in Southern Nevada and Northern Arizona (SNNA)) – Center for Academic Enrichment and Outreach, University of Nevada, Las Vegas

(2019 – 2018)